

CHRISTIAN-ALBRECHTS-UNIVERSITÄT ZU KIEL
INSTITUT FÜR THEORETISCHE PHYSIK UND ASTROPHYSIK

MASTER THESIS

**Non-Markovian quantum kinetic simulations of
relaxation processes in spatially uniform
nonequilibrium plasmas**

Author:
Christopher MAKAIT

Supervisor:
Prof. Dr. Michael BONITZ

Second examiner:
Prof. Dr. Nahid TALEBI

Kiel, October 2022

Abstract

Warm dense matter (WDM) has been an active research field in the past decades. It is an exotic state of matter with densities at and beyond that of a solid but temperatures around $1,000,000\text{ K}$. Besides its natural occurrence in astrophysical objects it can be generated in laboratories today. It is even of high economic and ecologic interest since this state of matter appears in a hydrogen fusion approach, the inertial confinement fusion (ICF). Its theoretical treatment is very challenging since it shares properties with both solids and plasmas. In particular, WDM produced in laboratories demands a nonequilibrium quantum description as it is usually generated using shock waves or similarly drastic methods, where it is driven far out of equilibrium, and quickly expands afterwards.

In quantum kinetic theory, in particular nonequilibrium Green functions and reduced density matrices, non-Markovian equations that accurately include nonideality and dynamical screening effects (GW , or also known as RPA) have been known for many decades. These remain numerically challenging due to the occurrence of memory. The recently found G1–G2 scheme gives an equivalent description of GW and even better approximations, but can even treat the correlation effects time-locally.

In this work the presently known formulations of the GW approximation are discussed first and compared regarding feasibility for uniform Coulomb systems, a commonly used model for plasmas. It is found that the computational demands of the G1–G2 scheme for 3D systems are too high for present computers, especially if the system is not isotropic. In the numerical section of this thesis methods are discussed that reduce the RAM demand, the bottleneck of these methods, and allow quick computations. In contrast to earlier implementations the methods discussed allow to make most efficient use of the assumed symmetries of the system. An algorithm to solve the GW approximations is presented. Its implementation is used to study the stopping power of a warm dense plasma that is experienced by a proton or an electron projectile. The non-Markovian GW results are compared to prevalent Markovian methods, in particular the Markovian RPA linear response stopping power. The proton results agree well with the linear response data, whereas the electron result is reduced significantly. The key differences leading to this behavior is the projectile mass. The mechanism behind this is derived from the non-Markovian GW collision integral.

Kurzfassung

Warme dichte Materie (WDM) war in den letzten Jahrzehnten ein sehr aktives Forschungsfeld. Sie ist ein Materiezustand mit Dichten eines Festkörpers und noch höheren, mit zugleich Temperaturen von etwa 1.000.000 K. Neben ihrem natürlichen Auftreten in astrophysikalischen Objekten kann sie heutzutage in Laboren erzeugt werden. Sie ist sogar von hohem ökonomischen und ökologischen Interesse, da dieser Materiezustand in einem Wasserstoffusionsansatz, der Trägheitsfusion (ICF), auftritt. Die theoretische Beschreibung ist außerordentlich schwierig, da WDM sowohl Eigenschaften von Festkörpern als auch Plasmen besitzt. Künstliche WDM auf der Erde benötigt insbesondere eine Nichtgleichgewichtsbeschreibung mit Berücksichtigung von Quanteneffekten, da sie üblicherweise mittels Schockwellen oder ähnlich drastischen Methoden erzeugt wird, wobei das System weit aus dem Gleichgewicht getrieben wird, und anschließend schnell expandiert.

In der Quanten-kinetischen Theorie, zu der u.a. Nichtgleichgewichtsgreenfunktionen (NEGF) und reduzierte Dichtematrizen zählen, sind bereits seit Jahrzehnten nicht-Markov'sche Gleichungen bekannt, welche Nichtidealität und dynamische Abschirmung präzise beschreiben (GW, auch bekannt als RPA). Diese bleiben aber weiterhin numerisch aufwendig wegen des Auftretens von Gedächtniseffekten. Das vor Kurzem aufgestellte G1–G2-Schema ist eine äquivalente Umformulierung der GW-Näherung und noch besserer Näherungen, aber kann die Korrelationseffekte sogar zeitlokal behandeln.

In dieser Arbeit werden zunächst die bekannten Formulierungen der GW-Näherung diskutiert und im Hinblick auf ihre numerische Umsetzbarkeit auf einem Computer untersucht. Das betrachtete Modell ist dabei das homogene Coulomb-Gas, welches oft zur Beschreibung von Plasmen verwendet wird. Es stellt sich heraus, dass das G1–G2-Schema in 3D-Plasmen für heutige Computer noch zu aufwendig ist, vor allem, wenn das System nicht isotrop ist. Der numerische Abschnitt dieser Arbeit behandelt numerische Neuerungen, welche den RAM-Bedarf, welcher die Größe der Rechnungen begrenzt, senken und schnelle Berechnungen erlauben. Im Vergleich zu früheren Implementierungen nutzen die vorgestellten Methoden die angenommene Zylindersymmetrie des Systems voll aus. Ein Algorithmus zur Lösung der GW-Gleichungen wird vorgestellt. Seine Implementierung in einem Computerprogramm wird genutzt, um das Bremsvermögen eines warmen dichten Plasmas auf ein Protonen- oder Elektronenprojektil zu untersuchen. Die so berechneten nicht-Markov'schen Ergebnisse werden mit dem weiter verbreiteten Markov'schen Grenzfall, nämlich der RPA im Rahmen der linear-response-Theorie, verglichen. Die Ergebnisse für das Protonenprojektil stimmen gut überein, bei den Elektronenprojektile gibt es hingegen starke Abweichungen. Der zentrale Unterschied zwischen den Projektilsorten ist die Masse. Der Mechanismus, der zu den unterschiedlichen Ergebnissen führt, wird aus dem nicht-Markov'schen GW-Stoßintegral abgeleitet.

Contents

1	Introduction	1
1.1	Thesis outline	3
2	Nonequilibrium many-body theory	5
2.1	Nonequilibrium Green functions (NEGF)	5
2.1.1	Time-dependent Schrödinger equation	5
2.1.2	Second quantization	6
2.1.3	Heisenberg picture	8
2.1.4	Nonequilibrium Green functions	9
2.1.5	Selfenergy approximations	16
2.1.6	Generalized Kadanoff–Baym ansatz (GKBA)	22
2.2	The G1–G2 scheme	24
2.3	Spatially uniform systems	26
2.3.1	The Jellium Hamiltonian	26
2.3.2	Plasma parameters	29
2.3.3	NEGF for the uniform electron gas	30
2.3.4	Thermodynamic limit	31
2.3.5	Observables in uniform systems using NEGF	31
2.3.6	Lindhard theory for static screening	33
2.3.7	G1–G2 equations for the uniform multi-component gas	34
2.3.8	Initial correlations, adiabatic switching	35
3	Simulation variants for spatially uniform systems	39
3.1	Another reformulation of GW	39
3.2	Uniform plasmas	41
3.2.1	Scaling of SOA, GW in different dimensions, symmetries, reformulations	42
3.2.2	Test simulation of G1–G2 in 2D, isotropic	44
3.3	Dephasing and aliasing	45
3.3.1	Aliasing in GKBA-type algorithms	46
3.3.2	Aliasing in G1–G2 type algorithms	47
3.3.3	A revision of the scalings for long simulation durations	48
4	Numerical implementation (cylinder symmetric plasma)	51
4.1	Fourier transformation in cylindric symmetry	51

4.1.1	Fourier-Hankel transform	52
4.1.2	Discrete Hankel transform, k-point grid	52
4.1.3	A library for Discrete Hankel transforms	54
4.2	Discretization in momentum space and time	55
4.2.1	Discretization in momentum space	55
4.2.2	Discretization in time, stepper and quadrature	57
4.3	Real-time equations of motion for GW in the uniform gas	59
4.4	Second-Order Approximation	60
4.4.1	Necessary data structures	61
4.4.2	Computing HF energies	62
4.4.3	Computing collision integrals	62
4.4.4	Application of h^{HF} and I	63
4.5	GW Approximation	64
4.5.1	Discretization of the Dyson Equation	64
4.5.2	Numerical solution scheme for the Dyson equation	65
4.5.3	Computing collision integrals and HF energies	67
4.5.4	Flowchart of the program	69
4.5.5	Parallelization	72
4.6	Convergence parameters	74
5	Application to stopping power	75
5.1	Simulation setup	75
5.1.1	Plasma target velocity scale separation	75
5.1.2	Simulation procedure to compute stopping powers	76
5.2	Distinction between projectile and target electrons	78
5.3	Relaxation of the projectile momentum distribution function	80
5.4	Non-Markovian and time-dependent stopping power	82
5.4.1	Description of the findings, comparison between proton and electron projectiles	82
5.4.2	Quantum Lenard-Balescu equation	84
5.4.3	Comparisons	86
6	Conclusion and outlook	93
	Appendices	97
	Appendix A Useful NEGF relations in uniform systems	99
A.1	Relations for one-particle Green function	99
A.2	Relations for zeroth order polarization function	100
A.3	Relations for GW screened potential W	101
	Appendix B Uniform lattice models	103
B.1	Homogeneous rectangular lattices	103

B.2 The honeycomb lattice	105
Appendix C Semianalytical Euler stepper	113
Appendix D Numerical energy conservation	115
Appendix E Time-dependent plasmon-occupation	117
Appendix F Complete time-dependent stopping data in SOA	119
References	121
Important used tools	129
Danksagung	130
Erklärung nach Prüfungsverfahrensordnung	132

1. Introduction

Warm dense matter [1–3] (WDM) has been a very active research field in the past two decades. It is an exotic state of matter that occurs at densities at and above that of a solid and temperatures around 1,000,000 K, cf. also Fig. 1.1. In nature, WDM can be found in astrophysical objects [4–6], such as brown and white dwarfs, neutron stars or the interior of our sun. On earth, it can be generated and investigated in laboratories under tremendous effort, for example by means of Z-pinch [7] or shock compression using free electron lasers such as LINAC [8] or the European XFEL [9]. Understanding WDM is also of high economic and ecologic interest since the inertial confinement fusion (ICF) [10, 11], a promising approach to hydrogen fusion, involves matter in this state. As one of the most recent breakthroughs, ignition has been achieved [12].

The theoretical description of warm dense matter is highly challenging, since its density and temperature domain is such that neither classical plasma nor pure solid state theory yield accurate results. In this state, electrons exert quantum behavior and the interaction energy is on the scale of the kinetic energy. An accurate description thus needs to account for both dynamical screening and strong coupling at the same time. Among the most used theoretical approaches are Quantum Kinetic Theory [13, 14], Quantum Hydrodynamics [15], Density Functional Theory [16, 17], Time-Dependent Density Functional Theory [18] and Quantum Monte Carlo (QMC) simulations [19, 20]. Most of these methods are also applicable to solids. Out of these, QMC yields the most precise *ab initio* results for warm dense matter but is, so far, limited to equilibrium. Laboratory WDM, on the other hand, is generated using shock waves of some form and expands afterwards. The description of these experiments thus requires a nonequilibrium formalism to describe the ever-changing conditions. The development of new methods that are applicable to nonequilibrium has thus been very active since.

In particular, the stopping of fast particles in these plasmas is an interesting quantity: Superthermal particles, e.g. helium cores generated by hydrogen fusion, are stopped by the surrounding medium, which in turn is heated up. In fact, there is a well-researched strategy that revolves around using a dense particle beam to ignite a plasma, cf. Refs. [21–23]. Being dependent on a lot of parameters of the plasma, such as density, temperature, ionization state, the stopping power serves as a useful diagnostic tool.

The stopping power has been investigated over many decades in many density and temperature regions. Most approaches however, such as linear response, are *Markovian* [24–26]. This means that stationarity of the target system is implicitly assumed. In order to account for effects due to the nonequilibrium nature of laboratory WDM, the dynamics of the correlations of target particles, especially the electrons, must be regarded.

Quantum Kinetic Theories, in particular Reduced Density Matrices and Nonequilibrium Green functions, allow a precise non-Markovian description of the correlation dynamics mentioned above via their collision integrals that contain information about all previous single-particle

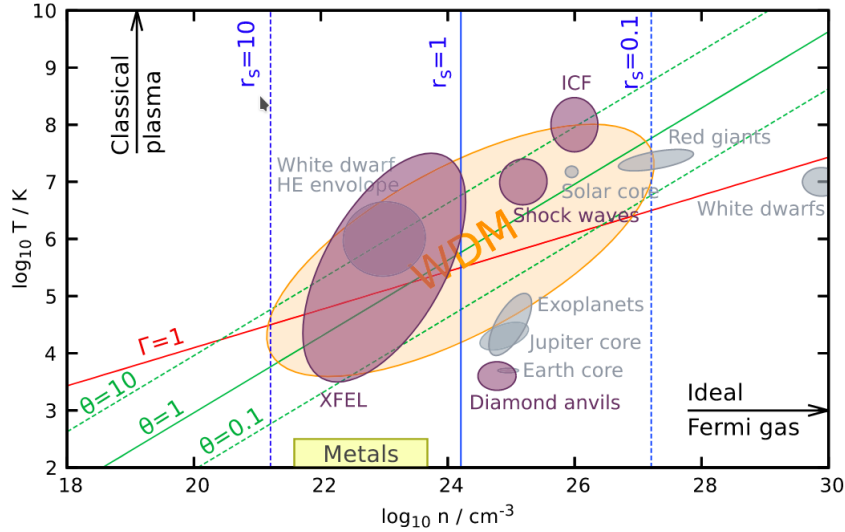


Figure 1.1.: Sketch of the occurrence of warm dense matter in the density/temperature plane, taken from Ref. [3]. Given are also the isolines of the Brückner parameter r_s and the quantum degeneracy parameter Θ , both defined in sect. 2.3.2. WDM approximately spans the region $r_s = 0.1 \dots 10$, $\Theta = 0.1 \dots 10$.

distributions. Expressions for the description of nonequilibrium screening dynamics (GW approximation) and for the description of strong coupling (T-matrix) exist and can even easily be combined [27] in the G1–G2 scheme, a reformulation, which drastically reduces the computational cost in some systems, cf. Refs. [28, 29]. Quantum kinetic approaches can be applied to a variety of system geometries and symmetries, but are often applied to finite systems [30, 31] or to uniform systems. Uniform plasmas can be modelled using the uniform electron gas model and generalizations to the multi-component case.

This thesis focuses on the application of Nonequilibrium Green functions using the Generalized Kadanoff–Baym ansatz [32] to uniform systems. As it turns out, the G1–G2 scheme is actually computationally quite expensive for 3D systems, especially if isotropy is not assumed. Scaling considerations give insight into which method is the least expensive to tackle a given system geometry. 3D cylinder symmetric systems in particular allow the investigation of many interesting physical situations, e.g. one-sided particle beams impinging on the system or time-dependent electric fields. Numerical techniques that are useful for the efficient computation of dynamics using the GW selfenergy are introduced. These techniques are used in a computer program to calculate the stopping power of a uniform warm dense plasma acting on a proton projectile or on an electron projectile, the results of which are compared to corresponding RPA linear response stopping powers [25].

1.1. Thesis outline

Chapter 1 Introduction

Chapter 2 Nonequilibrium many-body theory

After a short introduction into second quantization the Nonequilibrium Green functions are defined. Their physical meaning and contained information is discussed. Their equations of motion are derived, which couple to higher-order Green functions. The self-energy is defined, for which approximations, in particular Hartree–Fock, second order approximation, and the *GW* approximation are explained. The Generalized Kadanoff–Baym ansatz (GKBA) for a simplification of the equations and a time-local reformulation, the G1–G2 scheme, are introduced. This chapter ends with an introduction into spatially uniform systems and the specification of all needed quantities for this type of system.

Chapter 3 Simulation variants for spatially uniform systems

The most used selfenergy approximations in the past, SOA and GWA, are available in equivalent forms with very different numerical scalings. For GWA, a third reformulation exists which is sketched in this chapter. The scalings of all methods are compared for different system dimensions and symmetries, showing that 3D cylinder symmetric plasmas are least expensive using the 'old' method. Long time GKBA simulations are perturbed by aliasing. The final section of this chapter revisits the scalings in view of this problem.

Chapter 4 Numerical implementation (cylinder symmetric plasma)

The selfenergies considered can be computed efficiently using Fourier transformations. The assumed cylinder symmetry can be used to reduce memory demand and computational cost by means of a Hankel transform, of which the numerical treatment is described. After some general remarks regarding discretization and quadrature formulas used, the *GW* simulation procedure is explained in two steps: The computation of collision integrals in second order approximation already contains a lot of the subprocedures of *GW*, but is a bit more clear. Then the additional complexity of the *GW* Dyson integral is introduced and it is explained, how it modifies the SOA algorithm.

Chapter 5 Application to stopping power

The previously described computer program is used to compute the time-dependent stopping power. At first, the setup to model the stopping process in a NEGF calculation is explained. In particular, we are interested in proton projectiles and electron projectiles. Electron projectiles, due to their indistinguishability with electrons of the target, need modified equations of motion, in comparison to proton projectiles. Next, the simulation results are presented: time-dependent distribution functions, their time-derivatives, and the change of observables over time. Stopping power is extracted from the result and compared to static RPA results. Agreement and disagreement can be explained analytically.

Chapter 5 Conclusion and outlook

2. Nonequilibrium many-body theory

Abstract: This chapter gives an introduction to the Nonequilibrium Green functions. In particular, it covers their definition, the information contained in them, their equations of motion including approximations to the effective two-particle interaction (selfenergy) and another useful approximation, the Generalized Kadanoff–Baym ansatz (GKBA). The G1–G2 scheme, a novel reformulation of the GKBA with different numerical scalings, is introduced next. This chapter closes with an introduction into uniform systems and their implications for Green functions calculations and the G1–G2 scheme.

2.1. Nonequilibrium Green functions (NEGF)

2.1.1. Time-dependent Schrödinger equation

Dynamics of quantum systems follow the Schrödinger equation [33]

$$i\hbar \frac{d}{dt} |\Psi(t)\rangle = \hat{H} |\Psi(t)\rangle, \quad (2.1)$$

where $|\Psi(t)\rangle$ is a state vector, and \hat{H} is the Hamiltonian of the system. A relativistic generalization is the Dirac equation [34]. These equations can be solved analytically only in the simplest cases. With growing particle number the numerical treatment becomes exponentially more involved. This can be seen in spatial coordinate representation,

$$\Psi(t, \mathbf{r}_1\sigma_1, \dots, \mathbf{r}_n\sigma_n) = \langle \mathbf{r}_1\sigma_1, \dots, \mathbf{r}_n\sigma_n | \Psi(t) \rangle. \quad (2.2)$$

The solution on a discretized spatial grid of N grid points involves in total N^n values of Ψ for each spin configuration, making this approach viable only for few-particle systems. In practice, the Schrödinger equation is solved using the Configuration Interaction (CI) method. Another severe limitation of this approach is that it allows only pure states, whereas for finite temperature problems, statistical ensembles [35] are relevant.

Various methods have been developed to reduce the computational effort needed to treat quantum-many-body problems numerically. While the underlying theories are exact, they all depend on quantities, e.g. exchange-correlation potential or selfenergy. These quantities capture the many-body effects, whose exact forms are unknown and thus are approximated in practical calculations. The most common methods are

- Density Functional Theory (DFT) [36, 37]: DFT was initially a pure ground-state theory, but it has been generalized to finite temperature [38]. The core idea behind practical

DFT is to map the interacting (ground) state in an external potential onto a noninteracting state in an effective potential, introducing the exchange-correlation potential. It is often combined with a molecular dynamics simulation for the ions. Due to its low computational cost DFT is suitable to simulate rather large sections of a solid. This is especially true in comparison to the following methods.

- Time-Dependent Density Functional Theory (TDDFT) [39]: In a time-dependent external field, the interacting many-body state is mapped onto a noninteracting state in a time-dependent effective potential, which depends on all previous times. In most applications, adiabatic approximations are used. That means, a time-local exchange-correlation potential from DFT is applied instead. Just as DFT, TDDFT is often combined with molecular dynamics and can be used for rather large system sizes.
- Reduced Density Matrices (RDMs) [14, 40]: RDMs simplify the description of the full N -particle density matrix, but retain the ability to describe ensembles and can be used to compute expectation values of few-particle observables. Their equations of motion couple to higher-order RDMs, yielding the BBGKY hierarchy [41]. While being highly accurate, their computational scaling makes them viable only for smaller system sizes. RDMs can be applied to nonequilibrium or to equilibrium, where simplifications occur.
- Nonequilibrium Green functions (NEGF) [14, 42–44]: NEGF can be understood as a two-time dependent generalization to the RDMs, which also grants access to spectral information. NEGF are computationally even more expensive than RDMs. As the most general approach, NEGF also yield the most accurate results out of the many-body methods mentioned, but simulations are limited to small system sizes and ultrashort time scales. NEGF are related to equilibrium Green functions. Their theory provides a method to systematically construct more accurate selfenergy approximations that are applicable in both cases.

2.1.2. Second quantization

Throughout this thesis, the following in principle applies: if \pm or \mp is used in a formula, the upper sign is valid for bosons and the lower sign is valid for fermions.

Second quantization is a way to formulate quantum mechanics for an unfixed number of particles and it is also the approach that leads to field quantization, which forms the basis for many more advanced quantum theories such as quantization of electromagnetism, Klein–Gordon field, Dirac field, Quantum Chromodynamics, and the Yang–Mills theory.

Wave functions of multiple indistinguishable particles are (anti-)symmetric under particle exchange, i.e.

$$\Psi(\mathbf{r}_1\sigma_1, \dots, \mathbf{r}_i\sigma_i, \dots, \mathbf{r}_j\sigma_j, \dots, \mathbf{r}_n\sigma_n) = \pm\Psi(\mathbf{r}_1\sigma_1, \dots, \mathbf{r}_j\sigma_j, \dots, \mathbf{r}_i\sigma_i, \dots, \mathbf{r}_n\sigma_n). \quad (2.3)$$

The n -particle space of (anti-)symmetric states is denoted as $\mathcal{H}_{\pm}^{(n)}$. The Hilbert space needed to

formulate second quantization, the Fock space [45], is defined as

$$\mathcal{F}_{\pm}(H) = \overline{\bigoplus_{n=0}^{\infty} \mathcal{H}_{\pm}^{(n)}}. \quad (2.4)$$

This means, it is defined as the Hilbert space completion of the direct sum of all (anti-)symmetric n -particle Hilbert spaces. The 0-particle Hilbert space contains only $|0\rangle$, the vacuum state, and is isomorphic to \mathbb{C} .

Let $\{|\phi_n\rangle\}$ be a complete orthonormal basis of the one-particle Hilbert space. Then the (anti-)symmetrized product states (Slater determinants[46] or permanents) form an orthonormal basis of the (anti-)symmetrized Fock space. These normalized basis states are usually written in *occupation number representation*. This means that the product state consisting of single particle orbitals $|\phi_{n_1}\rangle, \dots, |\phi_{n_m}\rangle$ with multiplicities $\alpha_1, \dots, \alpha_m$ is written as

$$|0, \dots, 0, \underset{\substack{\uparrow \\ \text{index:}}}{n_1}, 0, \dots, 0, \underset{\substack{\uparrow \\ n_2}}{\alpha_2}, 0, \dots, 0, \underset{\substack{\uparrow \\ n_m}}{\alpha_m}, 0, 0, \dots\rangle, \quad (2.5)$$

with α_i in the positions n_i and 0's everywhere else. For fermions only $\alpha_i \in \{0, 1\}$ is possible due to Pauli blocking, which is why there also the notations $|n_1, n_2, \dots, n_m\rangle$ and $|\{n\}\rangle$ are common. In the bosonic case all natural numbers are allowed. Such states are called Fock states.

On this basis, we define the annihilation operator \hat{a}_i and the creation operator \hat{a}_i^\dagger , which link the n -particle subspace to the $n + 1$ and the $n - 1$ -particle subspace respectively, which is why they are also called ladder operators. Through linearity these operators are defined on the whole Fock space. The actions of these operators on a Fock state are given by

$$\hat{a}_i^\dagger |n_1, n_2, \dots, n_i, \dots\rangle = (\pm 1)^\alpha \sqrt{1 \pm n_i} |n_1, n_2, \dots, n_i + 1, \dots\rangle \quad (2.6)$$

$$\hat{a}_i |n_1, n_2, \dots, n_i, \dots\rangle = (\pm 1)^\alpha \sqrt{n_i} |n_1, n_2, \dots, n_i - 1, \dots\rangle, \quad (2.7)$$

where $\alpha = \sum_{j=1}^i n_j$ induces (anti-)symmetry of the states. The factor $\sqrt{1 - n_i}$ for the creator in the fermionic case already introduces Pauli blocking: The creation of a particle in an occupied orbital yields 0. The occupancy number operator is a simple combination of the two ladder operators,

$$\hat{n}_i |n_1, n_2, \dots, n_i, \dots\rangle := \hat{a}_i^\dagger \hat{a}_i |n_1, n_2, \dots, n_i, \dots\rangle = n_i |n_1, n_2, \dots, n_i, \dots\rangle. \quad (2.8)$$

All Fock states are eigenstates of this operator and n_i is the eigenvalue.

The ladder operators obey the following commutator (anti-commutator) relations for bosons (fermions):

$$\begin{aligned} [\hat{a}_i^\dagger, \hat{a}_j^\dagger]_{\mp} &= 0, \\ [\hat{a}_i, \hat{a}_j]_{\mp} &= 0, \\ [\hat{a}_i, \hat{a}_j^\dagger]_{\mp} &= \delta_{i,j} \end{aligned} \quad (2.9)$$

with $[\hat{A}, \hat{B}]_{\mp} \equiv \hat{A}\hat{B} \mp \hat{B}\hat{A}$. These relations are valid on the whole Fock space and not just simple Fock states, which is why they are usually used in formal derivations, instead of Eqs. (2.6) and (2.7).

Using these two operators, we can easily write down any n -particle operator $\hat{A}^{(n)}$ in a form that is defined on the whole Fock space. For arbitrary 1-particle operators $\hat{A}^{(1)}$ and 2-particle operators $\hat{A}^{(2)}$ we get

$$\hat{A}^{(1)} = \sum_{i,j} \langle i | \hat{A}^{(1)} | j \rangle \hat{a}_i^{\dagger} \hat{a}_j =: \sum_{i,j} A_{ij}^{(1)} \hat{a}_i^{\dagger} \hat{a}_j, \quad (2.10)$$

$$\hat{A}^{(2)} = \sum_{i,j,k,l} \langle ij | \hat{A}^{(2)} | kl \rangle \hat{a}_i^{\dagger} \hat{a}_j^{\dagger} \hat{a}_l \hat{a}_k =: \sum_{i,j} A_{ijkl}^{(2)} \hat{a}_i^{\dagger} \hat{a}_j^{\dagger} \hat{a}_l \hat{a}_k, \quad (2.11)$$

where $A_{ij}^{(1)}$ and $A_{ijkl}^{(2)}$ are the matrix elements of the operators.

If we apply this to a general Hamiltonian, we get the second quantized version

$$\hat{H}(t) = \underbrace{\sum_{ij} h_{ij}^{(0)} \hat{a}_i^{\dagger} \hat{a}_j}_{\hat{H}^{(0)}} + \frac{1}{2} \underbrace{\sum_{ijkl} w_{ijkl} \hat{a}_i^{\dagger} \hat{a}_j^{\dagger} \hat{a}_l \hat{a}_k}_{\hat{W}} + \underbrace{\sum_{ij} U_{ij}^{\text{ext}}(t) \hat{a}_i^{\dagger} \hat{a}_j}_{\hat{U}^{\text{ext}}}, \quad (2.12)$$

where the first term, $\hat{H}^{(0)}$, accounts for single-particle contributions, such as kinetic energy and some static external field, the second term \hat{W} accounts for two-particle interactions. The third term, $\hat{U}^{\text{ext}}(t)$, adds the possibility for a time-dependent perturbation, e.g. given by a time-dependent external field.

2.1.3. Heisenberg picture

In the Schrödinger picture physical states are time-dependent according to the Schrödinger equation. Using the unitary time propagation Operator, $\hat{U}(t, t')$, which satisfies

$$i\hbar \frac{d}{dt} \hat{U}(t, t') = \hat{H}(t) \hat{U}(t, t'), \quad \hat{U}(t, t_1) \hat{U}(t_1, t') = \hat{U}(t, t'), \quad (2.13)$$

the time-dependence of a state can be written as $|\psi(t)\rangle = \hat{U}(t, t_0) |\psi_0\rangle$. We compute the time-dependent expectation value of some Schrödinger operator according to

$$\langle \hat{A} \rangle(t) = \langle \psi(t) | \hat{A}_S(t) | \psi(t) \rangle = \langle \psi_0 | \hat{U}(t_0, t) \hat{A}_S(t) \hat{U}(t, t_0) | \psi_0 \rangle =: \langle \psi_0 | \hat{A}_H(t) | \psi_0 \rangle, \quad (2.14)$$

where we combined $\hat{A}_S(t)$ with the time propagation operators into a Heisenberg operator $\hat{A}_H(t)$, and instead $|\psi_0\rangle$ is treated as time-independent. Its equation of motion, the Heisenberg equation, is derived by computing the time derivative

$$\frac{d}{dt} \hat{A}_H(t) = \frac{i}{\hbar} [\hat{A}_H, \hat{H}_H]_- + \left(\frac{\partial \hat{A}_S}{\partial t} \right)_H, \quad (2.15)$$

where Eq. (2.13) and its adjoint were used.

Of particular interest for NEGF theory are the Heisenberg equations of motion for the annihilation and creation operator, where in the following the index H is omitted. From the second quantized version of the Hamiltonian, Eq. (2.12), and using the (anti-)commutator relation in Eq. (2.9), we find the equations of motion of the ladder operators,

$$i\hbar \frac{d}{dt} \hat{a}_i(t) = \sum_j \left\{ h_{ij}^{(0)} + U_{ij}^{\text{ext}}(t) \right\} \hat{a}_j(t) + \sum_{jkl} w_{ijkl} \hat{a}_j^\dagger(t) \hat{a}_l(t) \hat{a}_k(t), \quad (2.16)$$

$$-i\hbar \frac{d}{dt} \hat{a}_i^\dagger(t) = \sum_j \hat{a}_j(t) \left\{ h_{ji}^{(0)} + U_{ji}^{\text{ext}}(t) \right\} + \sum_{jkl} \hat{a}_j^\dagger(t) \hat{a}_k^\dagger(t) \hat{a}_l(t) w_{jkil}. \quad (2.17)$$

2.1.4. Nonequilibrium Green functions

Motivation

Let $\hat{\rho}_0$ be the density operator describing an ensemble at t_0 . Then the density operator at time t is given by $\hat{\rho}(t) = \hat{U}(t, t_0) \hat{\rho}_0 \hat{U}(t_0, t)$ and we can compute the time-dependent ensemble expectation value of some observable \hat{A} via

$$\langle \hat{A} \rangle(t) = \text{Tr} \left\{ \hat{U}(t, t_0) \hat{\rho}_0 \hat{U}(t_0, t) \hat{A} \right\} = \text{Tr} \left\{ \hat{\rho}_0 \hat{U}(t_0, t) \hat{A} \hat{U}(t, t_0) \right\} = \text{Tr} \left\{ \hat{\rho}_0 \hat{A}_H(t) \right\}, \quad (2.18)$$

where we have used the cyclic invariance of the trace operator and identified the Heisenberg variant of the observable \hat{A} . Now consider for example a one-particle operator \hat{A} in second quantization in this expression

$$\langle \hat{A} \rangle(t) = \text{Tr} \left\{ \hat{\rho}_0 \sum_{ij} A_{ij} \hat{a}_i^\dagger(t) \hat{a}_j(t) \right\} = \sum_{ij} A_{ij} \text{Tr} \left\{ \hat{\rho}_0 \hat{a}_i^\dagger(t) \hat{a}_j(t) \right\} = \sum_{ij} A_{ij} \left\langle \hat{a}_i^\dagger(t) \hat{a}_j(t) \right\rangle_{\hat{\rho}_0}. \quad (2.19)$$

This shows that the time-dependent expectation values of all single-particle observables can be computed, given that $\left\langle \hat{a}_i^\dagger(t) \hat{a}_j(t) \right\rangle_{\hat{\rho}_0}$ for all combinations of i and j are known.

Definition of the NEGF

The NEGF are a generalization of the correlators mentioned above, in three ways:

- Arbitrary even numbers of ladder operators are allowed, half of them annihilators and half of them creators. These quantities naturally appear in the equations of motion.
- Each ladder operator depends on its own time argument t_j . Through this, the NEGF give access to spectral information by Fourier transforming with respect to the time difference.
- Time arguments t_i are generalized to times on the *Keldysh time contour* [47] z_i . Through this generalization of times, time integrals and time ordering, Wick's theorem and the diagram techniques known from equilibrium Green function theory remain valid in nonequilibrium. However, this is not within the scope of this thesis.

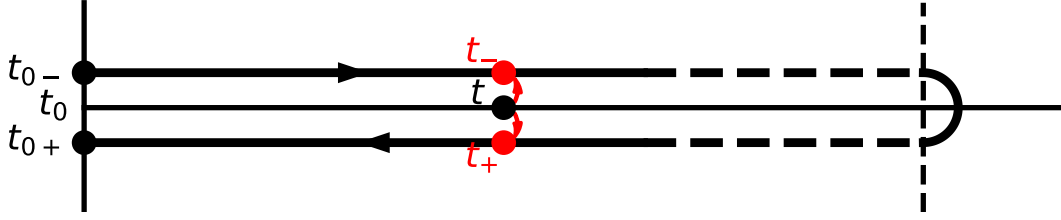


Figure 2.1.: The Keldysh contour. For every physical time t there is one contour time on the forward branch, t_- , and one on the backward branch, t_+ . The contour starts at t_{0-} , the forward branch variant of the initial time t_0 . It goes to $t = \infty$ and then back to t_{0+} , the backward branch variant of t_0 .

In addition all operators are ordered along the time contour by the *contour ordering operator* \mathcal{T}_C . The definition of the N -particle NEGF is given by

$$G_{i_1, \dots, i_N, j_1, \dots, j_N}^{(N)}(z_1, \dots, z_N, z'_1, \dots, z'_N) := \frac{1}{(i\hbar)^N} \left\langle \mathcal{T}_C \left\{ \hat{a}_{i_1}(z_1) \dots \hat{a}_{i_N}(z_N) \hat{a}_{j_N}^\dagger(z'_N) \dots \hat{a}_{j_1}^\dagger(z'_1) \right\} \right\rangle_{\hat{\rho}_0}. \quad (2.20)$$

The Keldysh time contour, see Fig. 2.1, splits any physical time t into two times, one on the forward branch t_- and one on the backward branch t_+ . The operator \mathcal{T}_C orders the operators according to their contour time arguments, with later times moved to the left. For example, all times on the backward branch are later than times on the forward branch. In that sense, the times from Fig. 2.1 are ordered $t_{0-} \leq t_- < t_+ \leq t_{0+}$.

In the following we write $\langle \dots \rangle \equiv \langle \dots \rangle_{\hat{\rho}_0}$ and use z, z' for contour times, where it does not matter which branch they are on.

Equations of motion (Martin–Schwinger hierarchy)

The equations of motion of the NEGF are acquired by partial differentiation of Eq. (2.20) with respect to a contour time z_i or z'_i and using the equations of motion for the ladder operators, Eqs. (2.16) and (2.17). The most important case is that of the one-particle NEGF (1pNEGF), which we will just call G .

$$\begin{aligned}
i\hbar \frac{\partial}{\partial z} G_{ij}(z, z') &= i\hbar \frac{\partial}{\partial z} \frac{1}{i\hbar} \left\langle \mathcal{T}_C \{ \hat{a}_i(z) \hat{a}_j^\dagger(z') \} \right\rangle \\
&= \delta_C(z, z') \delta_{ij} + \left\langle \mathcal{T}_C \{ [\partial_z \hat{a}_i(z)] \hat{a}_j^\dagger(z') \} \right\rangle \\
&= \delta_C(z, z') \delta_{ij} + \sum_k h_{ik}^{(0)}(z) \frac{1}{i\hbar} \underbrace{\left\langle \mathcal{T}_C \{ \hat{a}_k(z) \hat{a}_j^\dagger(z') \} \right\rangle}_{G_{kj}(z, z')} \\
&\quad + \sum_{kmn} w_{ikmn} \frac{1}{i\hbar} \left\langle \mathcal{T}_C \{ \hat{a}_k^\dagger(z^+) \hat{a}_n(z) \hat{a}_m(z) \hat{a}_j^\dagger(z') \} \right\rangle \\
&= \delta_C(z, z') \delta_{ij} + \sum_k h_{ik}^{(0)}(z) G_{kj}(z, z') \pm \sum_{kmn} w_{ikmn} \frac{1}{i\hbar} \underbrace{\left\langle \mathcal{T}_C \{ \hat{a}_m(z) \hat{a}_n(z) \hat{a}_k^\dagger(z') \hat{a}_j^\dagger(z^+) \} \right\rangle}_{i\hbar G_{mnjk}^{(2)}(z, z, z', z^+)} \\
&= \delta_C(z, z') \delta_{ij} + \sum_k h_{ik}^{(0)}(z) G_{kj}(z, z') \pm i\hbar \sum_{kmn} w_{ikmn} G_{mnjk}^{(2)}(z, z, z', z^+). \quad (2.21)
\end{aligned}$$

The $\delta_C(z, z')$ is a generalization of the Dirac delta distribution to the Keldysh contour. It accounts for the case, where the two operators change their ordering and their expectation value instantly changes due to the (anti-)commutator relations. Then the time derivative of the ladder operators was inserted, introducing two additional ladder operators in the last term. The 1pNEGF is identified easily. In order to find an expression containing the 2pNEGF, the ladder operators were swapped, which also gave rise to the ± 1 factor. To ensure the correct ordering, an infinitesimally shifted time $z^\pm = z \pm \epsilon$, $\epsilon \rightarrow 0$ was introduced. In a similar way one can treat the derivative with respect to the second time argument, z' , which can also be acquired by taking the Hermitian conjugate of the expression above,

$$-i\hbar \frac{\partial}{\partial z'} G_{ij}(z, z') = \delta_C(z, z') \delta_{ij} + \sum_k G_{ik}(z, z') h_{kj}^{(0)}(z') \pm i\hbar \sum_{kmn} G_{ikmn}^{(2)}(z, z'^-, z', z') w_{mnjk}. \quad (2.22)$$

We see that the dynamics of the 1pNEGF couple to the two-particle NEGF $G^{(2)}$.

In textbook discussions the interaction is often generalized to be dependent on two times: $w \rightarrow w(z, z') = w \delta_C(z, z')$. In this notation the equations of motion for the N -particle NEGF are given, see Ref. [44], by

$$\begin{aligned}
\sum_l \left(i\hbar \delta_{kl} \frac{\partial}{\partial z_k} - h_{kl}^{(0)}(z_k) \right) G_{i_1 \dots i_N, j_1 \dots j_N}^{(N)}(z_1 \dots z_k \dots z_N, z'_1 \dots z'_N) &= \\
&= \pm i\hbar \sum_{lmn} \int_C d\bar{z} w_{klmn}(z_k, \bar{z}) G_{i_1 \dots m \dots i_N n, j_1 \dots j_N}^{(N+1)}(z_1 \dots \bar{z} \dots z_N \bar{z}, z'_1 \dots z_N \bar{z}^+) \\
&\quad + \sum_{l=1}^N (-1)^{l+k} \delta(z'_l, z_k) G_{i_1 \dots \cancel{i_l} \dots i_N, j_1 \dots \cancel{j_k} \dots j_N}^{(N-1)}(z_1 \dots \cancel{z_l} \dots z_N, z'_1 \dots \cancel{z'_k} \dots z'_N), \quad (2.23)
\end{aligned}$$

$$\begin{aligned}
\sum_l \left(-i\hbar \delta_{lk} \frac{\partial}{\partial z'_k} - h_{lk}^{(0)}(z'_k) \right) G_{i_1 \dots i_N, j_1 \dots j_N}^{(N)}(z_1 \dots z_N, z'_1 \dots z'_k \dots z'_N) = \\
= \mp i\hbar \sum_{lmn} \int_C d\bar{z} G_{i_1 \dots i_N, l, j_1 \dots j_N}^{(N+1)}(z_1 \dots z_N \bar{z}^-, z'_1 \dots \bar{z} \dots z_N \bar{z}) w_{mnl}(\bar{z}, z'_k) \\
+ \sum_{l=1}^N (-1)^{l+k} \delta(z'_k, z_l) G_{i_1 \dots \cancel{j_k} \dots i_N, j_1 \dots \cancel{j_l} \dots j_N}^{(N-1)}(z_1 \dots \cancel{z_k} \dots z_N, z'_1 \dots \cancel{z'_l} \dots z'_N). \quad (2.24)
\end{aligned}$$

Again, the dynamics of the N -particle NEGF couple to the $N + 1$ -particle NEGF. The term coupling to the $N - 1$ -particle NEGF is due to operator swapping and the commutators. These equations are known as the *Martin–Schwinger hierarchy*. The solution of the complete hierarchy is equivalent to the solution of the time-dependent Schrödinger equation, but unfortunately not less costly. In practical solution the hierarchy is usually truncated and only the 1-particle NEGF is kept. Correlation effects are included in the selfenergy Σ , as introduced in the following.

The selfenergy

We define the *selfenergy* Σ as that two-contour-time matrix that fulfills the equations

$$i\hbar \frac{\partial}{\partial z} G_{ij}(z, z') = \delta_C(z, z') \delta_{ij} + \sum_k h_{ik}^{(0)}(z) G_{kj}(z, z') + \sum_k \int_C d\bar{z} \Sigma_{ik}(z, \bar{z}) G_{kj}(\bar{z}, z'), \quad (2.25)$$

$$-i\hbar \frac{\partial}{\partial z'} G_{ij}(z, z') = \delta_C(z, z') \delta_{ij} + \sum_k G_{ik}(z, z') h_{kj}^{(0)}(z') + \sum_k \int_C d\bar{z} G_{ik}(z, \bar{z}) \Sigma_{kj}(\bar{z}, z'), \quad (2.26)$$

i.e. effectively replacing $G^{(2)}$ and substituting it with a simpler quantity. The selfenergy is a unique functional of G and is dependent on all previous physical times (causality), but in most situations its exact form is unknown. There are however systematic methods to in principle construct approximations of arbitrary accuracy, see Ref. [44] for a textbook introduction. These approximations quickly become computationally highly expensive. In practice thus only a few approximations are used, where the cost could be reduced by means of special resummation techniques. Some of those will be discussed in section 2.1.5.

Let G^0 be the noninteracting 1pNEGF. Then the integral equations

$$G_{ij}(z, z') = G_{ij}^0(z, z') + \sum_{kl} \int_C d\bar{z} d\bar{\bar{z}} G_{ik}^0(z, \bar{z}) \Sigma_{kl}(\bar{z}, \bar{\bar{z}}) G_{lj}(\bar{\bar{z}}, z'), \quad (2.27)$$

$$G_{ij}(z, z') = G_{ij}^0(z, z') + \sum_{kl} \int_C d\bar{z} d\bar{\bar{z}} G_{ik}(z, \bar{z}) \Sigma_{kl}(\bar{z}, \bar{\bar{z}}) G_{lj}^0(\bar{\bar{z}}, z') \quad (2.28)$$

are called *Dyson equations* for the 1pNEGF and they are equivalent to the integro-differential equations (2.25) and (2.26). The Dyson equations are especially useful if one is interested in equilibrium properties: Then all functions are only dependent on the difference between the time arguments. In this case, the Dyson equation can be simplified through Fourier transform with respect to the difference between its two time arguments.

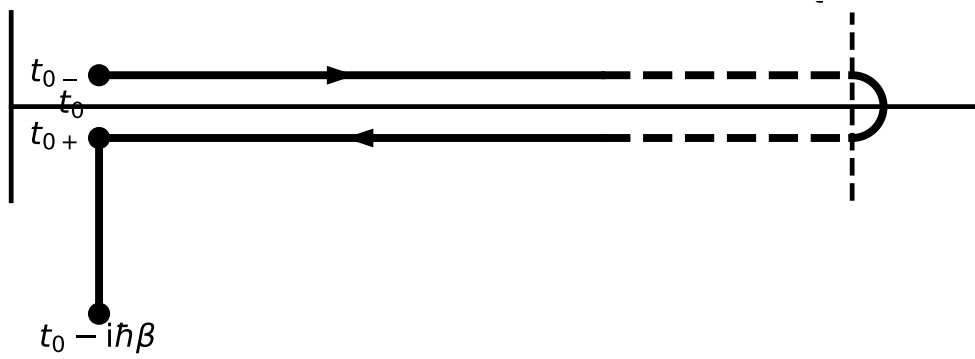


Figure 2.2.: Initial correlations in the *Konstantinov-Perel* formalism. Two times on the vertical track correspond to a pure equilibrium Green function calculation. Starting from thermal equilibrium, perturbations can be introduced and the response of the system can be studied.

Initial correlations

There are mainly two ways to incorporate initial **equilibrium** correlations into NEGF calculations:

- Extend the Keldysh contour and introduce an imaginary time branch, cf. Fig. 2.2
- Start from an uncorrelated ideal thermal distribution and *adiabatically switch on* the interaction, cf. Fig. 2.3

The first kind of extension, the *Konstantinov-Perel* formalism, links the NEGF theory to the theory of imaginary time equilibrium Green functions, the so-called Matsubara Green functions. Given the formal exponential expression for the time evolution operator, $\hat{U}(t, t')$,

$$\hat{U}(t, t') = \hat{T} \exp \left(\frac{1}{i\hbar} \int_{t'}^t d\bar{t} \hat{H}(\bar{t}) \right), \quad (2.29)$$

the canonical density operator can be formally written as

$$\hat{\rho}_0 = \frac{1}{Z} \exp(-\beta \hat{H}) = \frac{1}{Z} \hat{U}(t_0 - i\hbar\beta, t_0), \quad (2.30)$$

as a propagation in imaginary time. Here $Z = \text{Tr}(\exp -\beta \hat{H})$ is the canonical partition function. Such a calculation typically starts with solving the equilibrium Green function problem, i.e. the Matsubara formalism. Then a time-dependent perturbation is switched on and the response of the system can be investigated, starting from the equilibrium state. This nonequilibrium formalism is also called the *Konstantinov-Perel* formalism. In this thesis another necessary approximation, the Generalized Kadanoff–Baym ansatz (GKBA), is used, which is not compatible with this formalism.

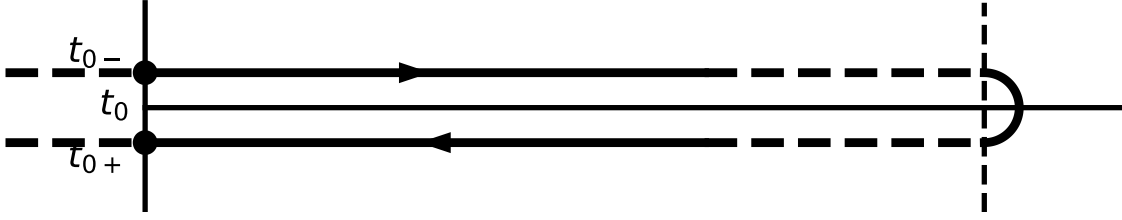


Figure 2.3.: Initial correlations using adiabatic switching. At $t \rightarrow -\infty$ the system is in some noninteracting thermal state. Then the interaction is switched on and reaches its full value at t_0 , generating an interacting initial state.

The second approach to initial correlations is called *adiabatic switching*, with an extension of the contour as sketched in Fig. 2.3. We start at $t = -\infty$, where the system is noninteracting and in thermal equilibrium. Then the interaction strength is switched on adiabatically, i.e. $w \rightarrow w(t) = w \cdot f(t)$ for a smooth switching function [48] with $\lim_{t \rightarrow -\infty} f(t) = 0$, $f(t \geq t_0) = 1$, which reaches its full strength at $t = t_0$. The ideal switching function is increasing infinitely slowly, thereby not introducing any additional excitation into the system at any time. The applicability of this procedure is supported by the *Gell-Mann and Low* theorem [49], which states that eigenstates of the noninteracting Hamiltonian, using this procedure, evolve into an eigenstate of the interacting Hamiltonian.

This formalism, i.e. without the explicit vertical track, is also called the *Keldysh formalism*. It is compatible with the GKBA and thus the only possible choice for this work.

Real-time components

Quantities on the Keldysh contour are mathematically difficult objects. In practice, we make a transition to components depending on two real times. Let $k(z, z')$ be a contour quantity, e.g. a 1pNEGF. We define the greater " $>$ " and less " $<$ " components by fixing the times to branches on the contour:

$$k^>(t, t') := k(t_+, t'_-), \quad k^<(t, t') := k(t_-, t'_+). \quad (2.31)$$

In the case of $k = G$, the orders of the ladder operators are now fixed, i.e. we define

$$G_{ij}^>(t, t') := \frac{1}{i\hbar} \langle \hat{a}_i(t) \hat{a}_j^\dagger(t') \rangle, \quad G_{ij}^<(t, t') := \pm \frac{1}{i\hbar} \langle \hat{a}_j^\dagger(t') \hat{a}_i(t) \rangle. \quad (2.32)$$

N -particle quantities would have $N!$ such components, but those are not studied in this work. The " $>$ " (" $<$ ") component of G_{ij} can be interpreted as complex transition amplitudes: A particle (hole) is created in state j (i) at time t' (t). This modified system is then propagated to time t (t'), where a particle (hole) in state i (j) is annihilated again. As discussed before, for equal times this probes the occupation of the states in the system. The analysis of the Green function at two different times, especially after a transition into the frequency domain, contains a lot of information about the dynamical response of the system to the added particle (hole).

The *retarded* and *advanced* components, $k^{\mathcal{R}/\mathcal{A}}$, are in general given by the expressions

$$k^{\mathcal{R}}(t, t') := k^\delta(t) \delta(t - t') + \Theta(t - t') [k^>(t, t') - k^<(t, t')] , \quad (2.33)$$

$$k^{\mathcal{A}}(t, t') := k^\delta(t) \delta(t - t') - \Theta(t' - t) [k^>(t, t') - k^<(t, t')] . \quad (2.34)$$

However, the $k^\delta(t)$ component of the relevant 1-particle functions, which appear in this thesis, vanishes, so that only the difference term remains. For the methods used in this thesis these components are the most important. The latter components are also called *spectral components*. The *spectral function*, $A(T, \omega)$, is accessible from the spectral Green function components by first making a transition to center of mass times and relative times, $G^{\mathcal{R}/\mathcal{A}}(T, \Delta t)$, taking its Fourier transform with respect to Δt , $G^{\mathcal{R}/\mathcal{A}}(T, \omega)$ and then computing

$$A(T, \omega) = i\hbar [G^{\mathcal{R}}(T, \omega) - G^{\mathcal{A}}(T, \omega)] . \quad (2.35)$$

The entry $A_{jj}(T, \omega)$ of the spectral function describes the probability that an added or removed fermion¹ with the single-particle state j at time T has the energy ω . The *density of states* (DOS) is also directly accessible from the spectral function by tracing over all single-particle states, i.e.

$$D(T, \omega) = \sum_j A_{jj}(T, \omega) , \quad (2.36)$$

which describes the number of existing single-particle states for a given energy $\hbar\omega$.

Many products in contour calculus are of *convolution type*². i.e. for two contour quantities a, b we compute $c = a \cdot b$ as

$$c(z, z') = \int_C d\bar{z} a(z, \bar{z}) b(\bar{z}, z') . \quad (2.37)$$

The Langreth-Wilkins rules, see Ref. [50], state that the components of c can be computed from the components of a and b by using non-contour integrals. In the Keldysh formalism, i.e. without imaginary branch, we have

$$c^{\geq}(t, t') = \int_{t_0}^{\infty} d\bar{t} a^{\mathcal{R}}(t, \bar{t}) b^{\geq}(\bar{t}, t') + \int_{t_0}^{\infty} d\bar{t} a^{\geq}(t, \bar{t}) b^{\mathcal{A}}(\bar{t}, t') , \quad (2.38)$$

$$c^{\mathcal{R}/\mathcal{A}}(t, t') = \int_{t_0}^{\infty} d\bar{t} a^{\mathcal{R}/\mathcal{A}}(t, \bar{t}) b^{\mathcal{R}/\mathcal{A}}(\bar{t}, t') . \quad (2.39)$$

¹This is more complex for bosons.

²Of course, Eq. (2.37) or Eqs. (2.38) and (2.39) do not contain the usual convolution expression. This form however can be achieved in the equilibrium case where only the time difference $\Delta t = t' - t$ matters.

In particular, when applied to the first hierarchy equation, we find the *real-time Kadanoff–Baym equations* (KBE):

$$i\hbar \frac{\partial}{\partial t} G_{ij}^{\geq}(t, t') = \sum_k h_{ik}^{(0)}(t) G_{kj}^{\geq}(t, t') + \sum_k \int_{t_0}^t d\bar{t} \Sigma_{ik}^{\mathcal{R}}(t, \bar{t}) G_{kj}^{\geq}(\bar{t}, t') + \sum_k \int_{t_0}^{t'} d\bar{t} \Sigma_{ik}^{\geq}(t, \bar{t}) G_{kj}^A(\bar{t}, t'), \quad (2.40)$$

$$-i\hbar \frac{\partial}{\partial t} G_{ij}^{\leq}(t, t') = \sum_k G_{ik}^{\leq}(t, t') h_{kj}^{(0)}(t') + \sum_k \int_{t_0}^t d\bar{t} G_{ik}^{\mathcal{R}}(t, \bar{t}) \Sigma_{kj}^{\leq}(\bar{t}, t') + \sum_k \int_{t_0}^{t'} d\bar{t} G_{ik}^{\leq}(t, \bar{t}) \Sigma_{kj}^A(\bar{t}, t'). \quad (2.41)$$

In the Konstantinov–Perel formalism we have three more components: the Matsubara component k^M with both times on the imaginary branch, and the k^{\lceil} and k^{\lfloor} components with one time on the real and one time on the imaginary branch. Accordingly, the Langreth–Wilkins in this formalism contain additional integrals.

2.1.5. Selfenergy approximations

The exact selfenergy Σ from Eq. (2.25),(2.26) contains the full information about the many-body system. Since this exact information is only known in very special model situations, in practice many-body approximations are needed. The selfenergy is usually split into the time-local Hartree–Fock part, $\Sigma^{\text{HF}}(z, z') \sim \delta_C(z, z')$, and the correlation part Σ^{corr}

$$\Sigma(z, z') = \Sigma^{\text{HF}}(z, z') + \Sigma^{\text{corr}}(z, z'). \quad (2.42)$$

While the Hartree–Fock part is known exactly, the correct description of correlation poses a much more difficult task and is usually only possible in an approximate manner.

Any approximation to the many-body effects should fulfill basic conservation laws (given the corresponding symmetries), i.e. particle number conservation, energy conservation, momentum conservation and angular momentum conservation. If one chooses the strategy of finding an approximate $G^{(2)}$, a sufficient criterion for conservation found by Kadanoff and Baym, cf. Refs. [51, 52], is that $G^{(2)}$ is symmetrical under particle exchange, i.e.

$$G_{ijkl}^{(2)}(z_1, z_2, z_1^+, z_2^+) = G_{jilk}^{(2)}(z_2, z_1, z_2^+, z_1^+). \quad (2.43)$$

In particular, this applies to the Hartree–Fock approximation, where we write

$$G_{ijkl}^{(2)}(z_1, z_2, z_3, z_4) = G_{ik}(z_1, z_3) G_{jl}(z_2, z_4) \pm G_{il}(z_1, z_4) G_{jk}(z_2, z_3) = G_{jilk}^{(2)}(z_2, z_1, z_4, z_3). \quad (2.44)$$

It turns out that finding an approximate $G^{(2)}$ is not the most natural approach to many-body dynamics. A derivation similar to that of Eq. (2.43) yields four conditions that Σ has to fulfill to be conserving. The particle number should be conserved in any closed system. The affiliated condition is that

$$\sum_k \int_C d\bar{z} [\Sigma_{ik}(z_1, \bar{z}) G_{ki}(\bar{z}, z_1^+) - G_{ik}(z_1, \bar{z}) \Sigma_{ki}(\bar{z}, z_1^+)] = 0. \quad (2.45)$$

Momentum is only conserved in spatially uniform systems, which is why the condition is written in spatial coordinate representation,

$$\int_{\mathbb{R}^n} d\mathbf{x}_1 d\mathbf{x}_2 \int_C d\bar{z} \left[\Sigma(\mathbf{x}_1 z_1, \mathbf{x}_2 \bar{z}) \nabla_1 G(\mathbf{x}_2 \bar{z}, \mathbf{x}_1 z_1^+) - G(\mathbf{x}_1 z_1, \mathbf{x}_2 \bar{z}) \nabla_1 \Sigma(\mathbf{x}_2 \bar{z}, \mathbf{x}_1 z_1^+) \right] = 0, \quad (2.46)$$

where ∇_1 acts on the first coordinate argument, i.e. \mathbf{x}_2 . Angular momentum conservation is guaranteed, if

$$\int_{\mathbb{R}^n} d\mathbf{x}_1 d\mathbf{x}_2 \int_C d\bar{z} \mathbf{r}_1 \times \left[\Sigma(\mathbf{x}_1 z_1, \mathbf{x}_2 \bar{z}) \nabla_1 G(\mathbf{x}_2 \bar{z}, \mathbf{x}_1 z_1^+) - G(\mathbf{x}_1 z_1, \mathbf{x}_2 \bar{z}) \nabla_1 \Sigma(\mathbf{x}_2 \bar{z}, \mathbf{x}_1 z_1^+) \right] = 0, \quad (2.47)$$

and energy is conserved if

$$\int_{\mathbb{R}^n} d\mathbf{x}_1 d\mathbf{x}_2 \int_C d\bar{z} \left\{ \frac{1}{4} \frac{d}{dz_1} \left[\Sigma(\mathbf{x}_1 z_1, \mathbf{x}_2 \bar{z}) G(\mathbf{x}_2 \bar{z}, \mathbf{x}_1 z_1^+) + G(\mathbf{x}_1 z_1, \mathbf{x}_2 \bar{z}) \Sigma(\mathbf{x}_2 \bar{z}, \mathbf{x}_1 z_1^+) \right] \right. \\ \left. - \left[\Sigma(\mathbf{x}_1 z_1, \mathbf{x}_2 \bar{z}) \left(\frac{d}{dz_1} G(\mathbf{x}_2 \bar{z}, \mathbf{x}_1 z_1^+) \right) + \left(\frac{d}{dz_1} G(\mathbf{x}_1 z_1, \mathbf{x}_2 \bar{z}) \right) \Sigma(\mathbf{x}_2 \bar{z}, \mathbf{x}_1 z_1^+) \right] \right\} = 0. \quad (2.48)$$

Fortunately, *Baym* found a large class of approximations that already fulfill all these conditions, the Φ -derivable approximations, cf. Ref. [51]. Consider an arbitrary functional of G that we call Φ . Then

$$\Sigma_{ij}(z, z') = \frac{\delta \Phi[G]}{\delta G_{ji}(z', z^+)}, \quad (2.49)$$

i.e. the functional derivative of Φ with respect to G , is a conserving selfenergy approximation. The *Second Order Approximation* (SOA) and the *GW Approximation* (GWA), that will both be explained in this chapter, are Φ -derivable, and thus conserving approximations. The Hartree-Fock approximation can be cast into a selfenergy form that is also Φ -derivable.

Contour algebra can greatly be visualized using Feynman diagrams, but they can even be used to derive approximations. Every diagram, e.g. in Eq. (2.55), represents a formula consisting of Green functions, interactions and products of convolution type, cf. Eq. (2.37). Prefactors are usually included into the rules how to interpret a given diagram. In diagrammatic formalism, the Φ functional is a so called *vacuum diagram*, i.e. all Green function lines and interaction lines are closed. Functional derivatives are computed by cutting every Green function line once and adding up the resulting diagrams, as is demonstrated in practice in Ref. [48]. Diagrams can be classified by order of interaction or by similarities in the structure. Resummation techniques have been found to treat entire series of certain types of diagrams (*GW*, T-matrix approximations) at once. A detailed introduction into diagrammatic techniques unfortunately is beyond the scope of this thesis. The interested reader is referred to the book by Stefanucci and Van Leeuwen, Ref. [44], which gives a thorough introduction into these methods.

In the following the three approximations that are the most important for this work are introduced:

- The Hartree–Fock approximation is the simplest approximation and forms the basis for the later discussed HF-GKBA.
- The SOA is the simplest approximation which goes beyond mean-field.
- The GWA is the simplest approximation that includes dynamical screening and treats plasmons in a similar way as particles. Since dynamical screening is an important mechanism in dense plasmas, here the *GW* Approximation is by far the best out of these three.

Hartree–Fock Approximation

The Hartree–Fock (HF) selfenergy can be found from the Hartree–Fock two-particle Green function,

$$G_{ijkl}^{(2),\text{HF}}(z_1, z_2, z_3, z_4) = G_{ik}(z_1, z_3) G_{jl}(z_2, z_4) \pm G_{il}(z_1, z_4) G_{jk}(z_2, z_3). \quad (2.50)$$

The first term, the Hartree term, describes two particles/holes propagating in time without interacting with each other. The second term, the Fock term, accounts for effects due to (anti-)symmetry of the wave functions, i.e. for exchange effects in the mean-field. Since it fulfills Eq. (2.43), we already know that it is conserving. We compute the collision integral from Eq. (2.21) and get

$$\pm i\hbar \sum_{kmn} w_{ikmn} G_{mnjk}^{(2),\text{HF}}(z, z, z', z^+) = \pm i\hbar \sum_{kmn} w_{ikmn} [G_{mj}(z, z') G_{nk}(z, z^+) \pm G_{mk}(z, z^+) G_{nj}(z, z')] \quad (2.51)$$

$$= \pm i\hbar \sum_{kmn} [w_{ikmn} \pm w_{iknm}] G_{nk}(z, z^+) G_{mj}(z, z') \quad (2.52)$$

$$= \sum_m \int_C d\bar{z} \Sigma_{im}^{\text{HF}}(z, \bar{z}) G_{mj}(\bar{z}, z'), \quad (2.53)$$

where we defined the HF selfenergy $\Sigma_{ik}^{\text{HF}}(z, \bar{z}) = \pm i\hbar \delta_C(z, \bar{z}) \sum_{kn} [w_{ikmn} \pm w_{iknm}] G_{nk}(z, z^+)$. We

identify the less Green function $G_{nk}^<(t) = G_{nk}(z, z^+)$, t being the real time corresponding to z , since the z^+ time argument makes sure that the contour ordering always yields the $<$ component.

The insertion of Eq. (2.50) into the adjoint first hierarchy equation, Eq. (2.22), leads to the same expression for the selfenergy. The diagrammatic expansion shows two properties of this approximation:

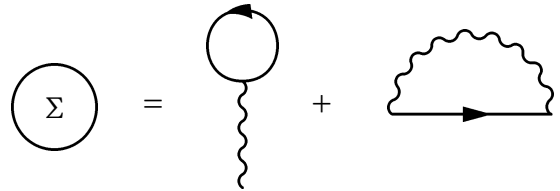
1. The HF approximation contains all diagrams with singular time dependence (contour δ). It follows that no memory integral occurs, which makes it inexpensive (but also inaccurate) in comparison to higher order approximations.
2. It contains all terms that are first order in the interaction.

Since the HF selfenergy is time-local, it is typically combined with the single-particle Hamiltonian, to find an effective HF Hamiltonian,

$$h_{ij}^{\text{HF}}(t) := h_{ij}^{(0)} \pm i\hbar \sum_{kn} [w_{ikjn} \pm w_{iknj}] G_{nk}^<(t, t), \quad (2.54)$$

and only the correlation part of selfenergy approximations is written into the collision integral on the right in Eqs. (2.25) and (2.26).

With regard to the aim to discuss spatially uniform gases, it is noteworthy that the Hartree–Fock approximation, as all mean-field theories, does not describe any collisions in this system. Algebraically, this is a consequence of the diagonality of G and Σ in its basis indices, as will be discussed in Sect. 2.3. The diagrams representing the Hartree–Fock approximation are



$$\Sigma = \text{Diagram 1} + \text{Diagram 2} \quad (2.55)$$

Solid lines with an arrow represent a Green function G , i.e. a particle. Wiggly lines represent the interaction w . In order to get some physical intuition about Feynman diagrams and the selfenergy, let us revisit the Dyson equation, Eq. (2.27), whose diagram representation is given by



$$\text{Solid line with arrow} = \text{Dashed line with arrow} + \text{Dashed line with arrow} \circ \Sigma \text{ Solid line with arrow} \quad (2.56)$$

Here, the dashed line with an arrow represents the noninteracting Green function, G_0 . The Dyson equation describes that the propagation amplitude of the particle (hole) from t_1 to t_2 represented by G has a contribution from the propagation without interactions inside the system (G_0), and a contribution that is divided into three steps: First, the particle (hole) is propagated freely to t_3 . Then it performs a few explicit collisions with other particles described by the selfenergy Σ during the time interval $[t_3, t_4]$. The last time interval, $[t_4, t_2]$ is propagated using the interacting Green function G . Each diagram in Σ corresponds to an individual scattering process. These processes can greatly be imagined for direct terms, e.g. Hartree, but are more counterintuitive for exchange diagrams, e.g. Fock. The Hartree term represents a direct interaction between two uncorrelated particles.

Second Order Approximation (SOA)

The SOA, as the name suggests, includes all diagrams up to second order in the interaction, i.e.

$$\Sigma = \text{diagram 1} + \text{diagram 2} + \text{diagram 3} + \text{diagram 4}. \quad (2.57)$$

The first two diagrams are the Hartree–Fock diagrams, which are of first order in the interaction. The third diagram is called the *second order direct diagram* and the fourth one is called the *second order exchange diagram*. The correlation diagrams translate into

$$\begin{aligned} \Sigma_{ij}^{\text{SOA}}(z, z') = \pm (i\hbar)^2 \sum_{mnpqrs} [G_{mn}(z, z') G_{pq}(z, z') w_{ispm}(z) w_{qnjr}(z') G_{rs}(z', z) \\ \pm w_{iqrm}(z) G_{mn}(z, z') w_{nsjp}(z') G_{pq}(z', z) G_{rs}(z', z)]. \end{aligned} \quad (2.58)$$

Being second order in the interaction, this approximation is suitable to describe weakly interacting systems. The second order diagrams, in contrast to Hartree–Fock, do not contain the contour δ , and the memory integral can thus not be simplified. The selfenergy at time (z, z') is dependent only on Green functions at the same or at transposed times, in contrast to higher selfenergy approximations. We will see in the context of the GKBA, how this leads to a strong computational simplification.

As we will see in the numerics section the second order exchange diagram is difficult to compute for uniform gases, which is why that diagram is usually neglected. The direct diagram by itself is conserving as well.

GW Approximation (GWA)

In general, the expansion of Σ in a power series of w is a bad approach: It is known to converge slowly, and in the case of metals it even is diverging. Lars Hedin [53] therefore proposed to include multiple diagram parts that end with interaction lines into an *effective, screened interaction* W , represented by a double wiggly line, cf. Eq. (2.59). In the GWA, that Hedin proposed, the Dyson equation of W is written as

$$\text{double wiggly line} = \text{single wiggly line} + \text{single wiggly line with loop} + \text{double wiggly line}, \quad (2.59)$$

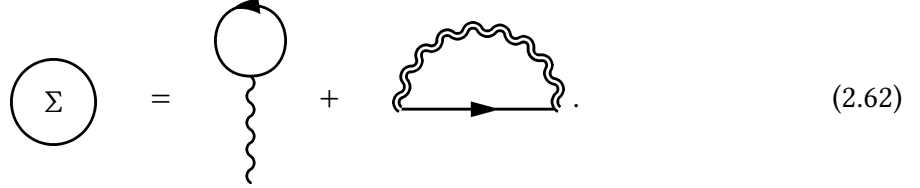
which is in full notation:

$$W_{ijkl}(z, z') = w_{ijkl}(z, z') \pm i\hbar \sum_{pqrs} w_{ipkq}(z) \int_C d\bar{z} G_{qr}(z, \bar{z}) G_{sp}(\bar{z}, z) W_{rjsl}(\bar{z}, z'). \quad (2.60)$$

The *loop*, the *GG* product, is also known as the zeroth order polarizability. The GWA is named after its expression for the exchange-correlation part of the selfenergy,

$$\Sigma_{ij}^{xc}(z, z') = i\hbar \sum_{kl} G_{kl}(z, z'^+) W_{ilkj}(z, z'), \quad (2.61)$$

or in Feynman diagrams,



The diagram shows a circle labeled Σ on the left, followed by an equals sign. To the right of the equals sign are two terms added together. The first term is a loop diagram consisting of a solid line with an arrow pointing up, forming a circle with a wavy line on the right side. The second term is a GW diagram consisting of a solid line with an arrow pointing right, and a wavy line above it forming a semi-circular shape.

The *GW* diagram is the Fock diagram, just with the screened interaction instead of the bare interaction. By iterating the Dyson equation, Eq. (2.59), in the *GW* diagram, we get



The diagram shows a circle labeled Σ^c on the left, followed by an equals sign. To the right of the equals sign are four terms added together. The first term is a loop diagram with a wavy line on the left and a solid line with an arrow pointing right on the bottom. The second term is a diagram with two loop structures connected by a wavy line. The third term is a diagram with three loop structures connected by wavy lines. The fourth term is an ellipsis followed by a plus sign.

The *GW* selfenergy contains an infinite amount of diagrams with increasing numbers of interactions. The restriction is that all diagrams are of the structure seen above. This diagrammatic expansion also demonstrates the physics that are described by the *GW* approximation: The first term describes a two-part collision: A particle (hole) interacts with an particle-hole pair at t_3 , creating a polarization. This polarization and the initial particle (hole) propagate in time until they interact a second time at t_4 . The second diagram describes an additional mechanism: The polarization induces another polarization, which then in turn interacts with the initial particle (hole). This process can be continued with arbitrary numbers of intermediate polarization steps and as such self-consistently describes dynamical screening. In a more pictorial manner: A test particle polarizes the environment, which in turn polarizes the environment a second time, which polarizes the environment a third time, and so on. This does not happen instantly, and the screening takes some time to adapt to changes in the system.

The screened interaction can also be regarded as the *plasmon Green function* [14], where $W^<$ describes the occupation of the plasmon modes. The dynamics of plasmons and particles are coupled in the *GW* approximation. The *GW* approximation is numerically quite demanding, since the Dyson equation (2.60) introduces memory into the dynamics of W , and some entry $W(z, z')$ cannot be solely computed from $G(z, z')$ and $G(z', z)$. Full two-time calculations using *GW* are not possible for uniform systems due to a divergence appearing in the $\mathbf{q} \rightarrow 0$ limit, cf. Ref. [54]. This divergence, however, is removed by using the GKBA, introduced in Sect. 2.1.6, also cf. Ref. [55] for a derivation.

Due to its high numerical cost, the *GW* approximation has often approximated in the past for an additional time by replacing G or W in the Dyson equation with a noninteracting one: The G_0W_0 approximation is the least costly one, cf. Refs. [56–58]. More expensive are G_0W and GW_0

[59]. The group of H. Haug used a relaxation time approximation to simplify the polarizability [60] which allowed an approximate solution of the equations. A fully self-consistent numerical implementation of the GW approximation with GKBA was used by Bányai et al. [61] to predict the buildup of screening of newly generated carriers following a laser pulse in GaAs on the time scale of the plasma period. This was later confirmed experimentally by Leitenstorfer et al., cf. Refs. [62, 63].

Hedin's equations [53] are a useful tool to construct better approximations than GW : This is achieved by using a better approximation to the so-called *vertex function*, Γ . Accordingly, these approximations are called *vertex corrected* or written GWT . To my knowledge, such approximations so far have only been applied to equilibrium.

Other approximations

The selfenergies discussed above are the ones relevant for this thesis. There are more commonly used approximations, cf. the review paper by *Schlünzen* [48], with their own advantages, that are only sketched in the following.

If one chooses to expand the selfenergy in powers of the interaction w , one finds the Born series, whereof the first order (HF) and the Second Order Approximation have been introduced. The Third Order Approximation [48] (TOA) contains 10 additional diagrams with 3 interaction lines. Summation techniques similar to that of GW (but with regard to a different type of diagrams) lead to the T -Matrix Approximations (TMA); In a similar manner to GW , in the T -matrix approaches a second integral equation has to be solved simultaneously, the *Lippmann-Schwinger equation* for the T -matrix [64]. Originating from scattering theory, the T -matrix selfenergies excel at describing strong coupling, multiple scatterings and bound states.

These selfenergies typically are not used for dynamics in uniform systems³. The TOA uses diagrams that are extremely difficult to compute. Due to long-range interactions in the electron gas, the T -matrix selfenergies are also very expensive to compute. The TMA shines in model systems with strongly localized interaction, such as the Hubbard model, cf. Sect. B.1.

2.1.6. Generalized Kadanoff–Baym ansatz (GKBA)

The time-diagonal values of $G^<$ are directly related to the 1pRDM, $\rho^{\lessgtr} = \pm i\hbar G^{\lessgtr}$, hence the time diagonal propagation is considered the most important for many applications. The time-diagonal KBE is acquired by combining the usual KBEs (2.38) and (2.39),

$$i\hbar \frac{d}{dt} G_{ij}^<(t, t) - [h^{\text{HF}}(t), G^<(t, t)]_{ij} = \sum_k \int_{t_0}^t d\bar{t} \{ \Sigma_{ik}^>(t, \bar{t}) G_{kj}^<(\bar{t}, t) - \Sigma_{ik}^<(t, \bar{t}) G_{kj}^>(\bar{t}, t) \} + h.c., \quad (2.64)$$

where the commutator $[h^{\text{HF}}(t) G^<(t, t)]_{ij} = \sum_k h_{ik}^{\text{HF}}(t) G_{kj}^<(t, t) - G_{ik}^<(t, t) h_{kj}^{\text{HF}}(t)$ is introduced. This equation is exact, if all the time off-diagonal values $G^{\lessgtr}(t, t')$ are known. The idea by Lipavský et al [32] was to reconstruct these values from the time-diagonal values of G^{\lessgtr} , making

³At least not in the present non-Markovian form, i.e. with memory integrals.

the approach *effectively* dependent on only one time. They derived an expression for the exact reconstruction, which for $t_1 \geq t_2$ is given by

$$G_{ij}^{\lessgtr}(t_1 \geq t_2) = -i\hbar \sum_k G_{ik}^{\mathcal{R}}(t_1, t_2) G_{kj}^{\lessgtr}(t_2, t_2) + \sum_{kl} \int_{t_2}^{t_1} d\bar{t} \int_{t_0}^{t_2} d\bar{t} G_{ik}^{\mathcal{R}}(t_1, \bar{t}) \Sigma_{kl}^{\lessgtr}(\bar{t}, \bar{t}) G_{lj}^{\mathcal{A}}(\bar{t}, t_2) \\ + \sum_{kl} \int_{t_2}^{t_1} d\bar{t} \int_{t_0}^{t_2} d\bar{t} G_{ik}^{\mathcal{R}}(t_1, \bar{t}) \Sigma_{kl}^{\mathcal{R}}(\bar{t}, \bar{t}) G_{lj}^{\lessgtr}(\bar{t}, t_2) \quad (2.65)$$

and for $t_1 < t_2$ is given by

$$G_{ij}^{\lessgtr}(t_1 < t_2) = +i\hbar \sum_k G_{ik}^{\lessgtr}(t_1, t_1) G_{kj}^{\mathcal{A}}(t_1, t_2) - \sum_{kl} \int_{t_2}^{t_1} d\bar{t} \int_{t_0}^{t_2} d\bar{t} G_{ik}^{\mathcal{R}}(t_1, \bar{t}) \Sigma_{kl}^{\lessgtr}(\bar{t}, \bar{t}) G_{lj}^{\mathcal{A}}(\bar{t}, t_2) \\ - \sum_{kl} \int_{t_2}^{t_1} d\bar{t} \int_{t_0}^{t_2} d\bar{t} G_{ik}^{\lessgtr}(t_1, \bar{t}) \Sigma_{kl}^{\mathcal{A}}(\bar{t}, \bar{t}) G_{lj}^{\mathcal{A}}(\bar{t}, t_2). \quad (2.66)$$

Since so far no explicit solution to these equations is known, the reconstruction is often approximated by dropping the integral terms, yielding

$$G_{ij}^{\lessgtr}(t_1, t_2) = -i\hbar \sum_k \left(G_{ik}^{\mathcal{R}}(t_1, t_2) G_{kj}^{\lessgtr}(t_2, t_2) - G_{ik}^{\lessgtr}(t_1, t_1) G_{kj}^{\mathcal{A}}(t_1, t_2) \right). \quad (2.67)$$

Of course, if one aims to use the spectral components computed from $G^{\lessgtr}(t_1, t_2)$, nothing is won, since we need the components we want to reconstruct for the reconstruction itself. Thus some kind of approximation has to be used and depending on it is the accuracy of the resulting simulation. Mainly due to efficiency reasons, the *free GKBA* and the *Hartree–Fock-GKBA*⁴ are very successful:

$$G_{ij}^{\mathcal{R}/\mathcal{A}, \text{HF}}(t_1, t_2) = \pm \frac{1}{i\hbar} \Theta(\pm[t_1 - t_2]) \exp \left\{ \frac{1}{i\hbar} \int_{t_2}^{t_1} d\bar{t} h^{\text{HF}}(\bar{t}) \right\}, \quad (2.68)$$

where for once the upper sign is for the \mathcal{R} component and the lower sign is for the \mathcal{A} component. The free GKBA is gotten from the HF case by neglecting the mean-field part. The reconstruction and thus propagation on the off-diagonal is a lot simpler than in the full two-time case, since no collision integral (and thus selfenergies) need to be computed there. Free

⁴In the interpretation of the Feynman diagrams, the interacting Green functions were used, i.e. between two explicit collisions, the particles are evolved in time under the full influence of all particles. GKBA results on the other hand have to be interpreted in such a way that basically the same collision processes happen (time-diagonal), but that between these explicit collisions described by the selfenergy, the particles evolve without two-particle interactions or in mean-field, instead of experiencing additional collisions in the meantime.

and HF-GKBA are still conserving and are in great parts equivalent to the *Reduced Density Matrix* formalism [14], but the NEGF approach allows a more systematic theory of selfenergy approximations. A GKBA calculation can be regarded as a standard NEGF calculation, where the collision integral is dropped in the off-diagonal propagation. Since the computation of the selfenergy is the most difficult part, this corresponds to a significant computational simplification. In free GKBA case, and if no explicit time dependence of $h^{(0)}$ is given, it simplifies even more. More sophisticated approaches to approximate $G^{\mathcal{R}/\mathcal{A}}$, constructed by approximating expressions from its Dyson equation, are described in Ref. [65], called *correlated GKBA*. The HF- and the free GKBA are undamped: Green functions do not decline towards the time off-diagonal, which they would do in most two-time calculations[66]. Dampening could be introduced using the correlated GKBA approach, effectively limiting the duration of memory effects.

The spectral function, given in Eq. (2.35), is computed from the time off-diagonal of G . Since the off-diagonal is reconstructed on HF-level, it cannot be expected to find a good spectral function in the HF-GKBA [67]. A different approach to finding the spectrum is to introduce some 'kick' perturbation ('kick spectrum') into the system and analyze the time-dependent response of the density to it using a Fourier transform, as was demonstrated in Ref. [54]: Since on the time-diagonal, the collision integral appears in the equation of motion, selfenergy effects beyond HF are included in the density dynamics.

2.2. The G1–G2 scheme

In this section a short introduction into the G1–G2 scheme is given without too much detail. This is due to the fact that most calculations in this thesis were not made using the G1–G2 scheme due to scaling difficulties, as discussed in Sect. 3.2.1.

Here and in the following we define $G_{ij}^{\geq}(t) := G_{ij}^{\geq}(t, t)$ for all bases. The time-diagonal KBE is given by

$$i\hbar \frac{d}{dt} G_{ij}^<(t, t) - [h^{\text{HF}}(t), G^<(t, t)]_{ij} = \sum_k \int_{t_0}^t d\bar{t} \left\{ \Sigma_{ik}^>(t, \bar{t}) G_{kj}^<(\bar{t}, t) - \Sigma_{ik}^<(t, \bar{t}) G_{kj}^>(\bar{t}, t) \right\} + h.c., \quad (2.69)$$

where the collision integral stems from some term of the form $\text{Tr}_2 w_{12} G_{12}^{(2)}$, cf. Eqs. (2.21) and (2.22). The idea [28, 29] now is to find a function $\mathcal{G}_{ijkl}(t)$ dependent on one real time, that restores this original structure of the hierarchy, i.e. that fulfills

$$I_{ij}(t) = \sum_k \int_{t_0}^t d\bar{t} \left\{ \Sigma_{ik}^>(t, \bar{t}) G_{kj}^<(\bar{t}, t) - \Sigma_{ik}^<(t, \bar{t}) G_{kj}^>(\bar{t}, t) \right\} = \pm i\hbar \sum_{klp} w_{klp}(t) \mathcal{G}_{lpjk}(t). \quad (2.70)$$

One then chooses a selfenergy approximation, inserts the expression into the formula above

and identifies some interaction part. For example, in SOA one finds

$$I_{ij}(t) = (i\hbar)^2 \sum_{kpqrsu} w_{iklp}(t) \int_{t_0}^t d\bar{t} w_{qrsu}^{\pm}(t) \left[G_{lq}^{\gt}(t, \bar{t}) G_{pr}^{\gt}(t, \bar{t}) G_{jk}^{\lt}(\bar{t}, t) G_{uj}^{\lt}(\bar{t}, t) - (> \leftrightarrow <) \right], \quad (2.71)$$

where the (anti-)symmetrized interaction $w_{ijkl}^{\pm} = w_{ijkl} \pm w_{ijlk}$ is used. Comparing this with Eq. (2.70), one readily finds that apart from prefactors, the integral is \mathcal{G} which we are looking for. Its equation of motion follows from Leibniz' rule and the application of GKBA to the G^{\lessgtr} under the integral. The derivation is more difficult for GW and the T-matrix selfenergies.

One finds different equations of motion for each selfenergy. The SOA result is

$$i\hbar \frac{d}{dt} \mathcal{G}_{ijkl}(t) - \left[h^{(2),\text{HF}}, \mathcal{G} \right]_{ijkl} = \Psi_{ijkl}^{\pm}(t), \quad (2.72)$$

where

$$\left[h^{(2),\text{HF}}, \mathcal{G} \right] = \sum_p \left\{ h_{ip}^{\text{HF}}(t) \mathcal{G}_{pjkl}(t) + h_{jp}^{\text{HF}}(t) \mathcal{G}_{ipkl}(t) - \mathcal{G}_{ijpl}(t) h_{pk}^{\text{HF}}(t) - \mathcal{G}_{ijkp}(t) h_{pl}^{\text{HF}}(t) \right\} \quad (2.73)$$

is a two-particle commutator and the source term Ψ^{\pm} is given by

$$\Psi_{ijkl}^{\pm}(t) = (i\hbar)^2 \sum_{pqrs} \left\{ G_{ip}^{\gt}(t) G_{jq}^{\gt}(t) w_{pqrs}^{\pm}(t) G_{rk}^{\lt}(t) G_{sl}^{\lt}(t) - (> \leftrightarrow <) \right\}. \quad (2.74)$$

The other selfenergies mentioned in Sect. 2.1.5 are represented by some small modifications:

GW: The (anti-)symmetrized interaction is replaced by the normal one, and we add $\Pi_{ijkl}(t) - [\Pi_{lkji}(t)]^*$ to the right, where

$$\Pi_{ijkl}(t) = \pm (i\hbar)^2 \sum_{pqrs} w_{rqs}(t) \left[G_{jr}^{\gt}(t) G_{sl}^{\lt}(t) - G_{jr}^{\lt}(t) G_{sl}^{\gt}(t) \right] \mathcal{G}_{ipkq}(t). \quad (2.75)$$

TPP: The particle-particle channel of the T-matrix is included by adding $\Lambda_{ijkl}^{\text{pp}} - [\Lambda_{klij}^{\text{pp}}(t)]^*$ to the right, where

$$\Lambda_{ijkl}^{\text{pp}}(t) = (i\hbar)^2 \sum_{pqrs} \left[G_{ir}^{\gt}(t) G_{js}^{\gt}(t) - G_{ir}^{\lt}(t) G_{js}^{\lt}(t) \right] w_{rspq}(t) \mathcal{G}_{pqkl}(t). \quad (2.76)$$

TPH: The particle-hole channel of the T-matrix is included by adding $\Lambda_{ijkl}^{\text{ph}} - [\Lambda_{klij}^{\text{ph}}(t)]^*$ to the right, where

$$\Lambda_{ijkl}^{\text{ph}}(t) = (i\hbar)^2 \sum_{pqrs} \left[G_{ir}^{\gt}(t) G_{sl}^{\lt}(t) - G_{ir}^{\lt}(t) G_{sl}^{\gt}(t) \right] w_{rpqs}(t) \mathcal{G}_{qjkp}(t). \quad (2.77)$$

All these terms are completely time-local and thus no explicit memory integral needs to be calculated, but instead the 4-index quantity \mathcal{G} must be handled. This linear time scaling of CPU time and memory usage, which is independent from the number of time steps, makes the G1–G2 scheme the preferred method for long simulations, if the computer can handle this large \mathcal{G} .

By adding all these bonus terms to the equation of motion, we find a new approximation, the *Dynamically Screened Ladder Approximation*, which contains all diagrams from the three approximations and thus includes both, dynamical screening and strong coupling effects. After fixing its instabilities using methods called purification and enforcing contraction consistency, cf. Ref. [27], the DSL was found to be the most precise out of these approximations, at least for 1D Hubbard chains [27], where exact reference data is available.

Being a component of $G^{(2)}$, through \mathcal{G} we have direct access to two-particle observables and the pair distribution function. The reconstruction of such quantities is also possible but difficult using the memory formalism, cf. Ref. [68] for a discussion of the SOA case.

2.3. Spatially uniform systems

In Subsect. 2.3.1, the second quantized Jellium Hamiltonian is derived, along the lines of the book by Giuliani and Vignale [69]. Jellium is one of the simplest models of uniform systems, describing electrons in front of a uniform positive background, and it is a good model for the description of metals. It is readily generalized to more complex systems, such as multi-component plasmas containing ions or electron-hole plasmas that can be excited in semiconductors. Jellium is thus the starting point. The ground state energy of the uniform electron has been computed using diffusion quantum Monte Carlo by Ceperley and Alder, cf. Ref. [70], which is the basis for one of the most important approximations to the DFT exchange-correlation functional, the *Local Density Approximation* (LDA) [71], and is thus also applied in approximate form to the inhomogeneous electron gas. The electron gas in equilibrium at warm dense matter conditions is a lot more complex and has successfully been studied using Path Integral Monte Carlo (PIMC), cf. Ref. [3] for a recent review. The application to nonequilibrium is far more challenging and has been done in an approximate matter using NEGF and RDM [14, 55], which opens a window to various applications such as plasmas or semiconductors in laser fields [54, 72] or carrier relaxation processes following a laser pulse [61, 73].

2.3.1. The Jellium Hamiltonian

Starting from a very clear first quantized Hamiltonian, a second quantized variant in momentum representation is derived. During the transition, the Coulomb interaction is regularized, which removes the diverging interaction term v_0 .

Consider a d -dimensional cubic box of length L containing n particles, where we define the

first quantized Hamiltonian

$$\hat{H} = \sum_{i=1}^N \frac{\hat{\mathbf{p}}_i^2}{2m} + \frac{1}{2} \sum_{i \neq j=1}^N \frac{e^2}{|\hat{\mathbf{r}}_i - \hat{\mathbf{r}}_j|} + \hat{H}_{e-b} + \hat{H}_{b-b}, \quad (2.78)$$

where the last two terms account for electron-background and background-background interaction. The background is assumed to be uniform and positive, which yields the electrostatic energy expressions

$$\hat{H}_{e-b} = -e^2 \int d\mathbf{r} \int d\mathbf{r}' \frac{\hat{n}(\mathbf{r}) n_b(\mathbf{r}')}{|\mathbf{r} - \mathbf{r}'|}, \quad (2.79)$$

$$\hat{H}_{b-b} = \frac{e^2}{2} \int d\mathbf{r} \int d\mathbf{r}' \frac{n_b(\mathbf{r}) n_b(\mathbf{r}')}{|\mathbf{r} - \mathbf{r}'|}, \quad (2.80)$$

where the local particle number operator is defined as $\hat{n}(\mathbf{r}) = \sum_{i=1}^N \delta(\mathbf{r} - \hat{\mathbf{r}}_i)$. To ensure convergence, we consider the statically screened Yukawa or Debye potential, $v(r, \kappa)$, and express it through a Fourier series, $w_{\mathbf{q}}(\kappa)$

$$w(r, \kappa) = e^2 \frac{\exp(-\kappa r)}{r} = \frac{1}{L^d} \sum_{\mathbf{q}} w_{\mathbf{q}}(\kappa) \exp(i\mathbf{r} \cdot \mathbf{q}), \quad w_{\mathbf{q}}(\kappa) = \int w(\mathbf{r}, \kappa) \exp(-i\mathbf{r} \cdot \mathbf{q}) d\mathbf{r}. \quad (2.81)$$

The Coulomb potential is regained by choosing the limit $\kappa \rightarrow 0$ at an appropriate point in the derivation. Using these relations and defining

$$\hat{n}_{\mathbf{q}} = \sum_{i=1}^N e^{-i\mathbf{q} \cdot \hat{\mathbf{r}}_i}, \quad (2.82)$$

the Hamiltonian can be cast into the form

$$\hat{H} = \sum_i \frac{\hat{\mathbf{p}}_i^2}{2m} + \frac{1}{2L^d} \sum_{\mathbf{q}} w_{\mathbf{q}}(\kappa) [\hat{n}_{-\mathbf{q}} \hat{n}_{\mathbf{q}} - \hat{N}] - w_0(\kappa) n_b \hat{N} + \frac{1}{2} w_0(\kappa) n_b^2 L^d, \quad (2.83)$$

where \hat{N} is the total particle number operator for the electrons. If the particle number density is fixated at n , we have the relation $\hat{N} = nL^d = n_b L^d$. Now in the $\mathbf{q} = 0$ case, we find that $\hat{n}_0 = \hat{N}$, and we can simplify that part of the Hamiltonian:

$$\frac{(\hat{H}_{e-b})_{\mathbf{q}=0} + (\hat{H}_{b-b})_{\mathbf{q}=0} + (\hat{H}_{e-e})_{\mathbf{q}=0}}{L^d} = -\frac{n w_0(\kappa)}{2L^d}, \quad (2.84)$$

which tends to zero in the thermodynamic limit, i.e. $L \rightarrow \infty$ while $n = \text{const}$. In the thermodynamic limit this term thus does not appear and cancels exactly with the background terms and we get

$$\hat{H} = \sum_i \frac{\hat{\mathbf{p}}_i^2}{2m} + \frac{1}{2L^d} \sum_{\mathbf{q} \neq 0} w_{\mathbf{q}}(\kappa) [\hat{n}_{-\mathbf{q}} \hat{n}_{\mathbf{q}} - \hat{N}]. \quad (2.85)$$

At this point, it is safe to perform the $\kappa \rightarrow 0$ limit, as the diverging term at $\mathbf{q} = 0$ is gone.

If we now insert the second quantized operators

$$\hat{n}_{\mathbf{q}} = \sum_i e^{-i\mathbf{q}\cdot\mathbf{r}_i} = \sum_{\mathbf{k}\sigma, \mathbf{k}'\sigma'} \langle \mathbf{k}\sigma | e^{-i\mathbf{q}\cdot\mathbf{r}} | \mathbf{k}'\sigma' \rangle \hat{a}_{\mathbf{k}\sigma}^\dagger \hat{a}_{\mathbf{k}'\sigma'} = \sum_{\mathbf{k}\sigma} \hat{a}_{\mathbf{k}-\mathbf{q},\sigma}^\dagger \hat{a}_{\mathbf{k},\sigma} \quad (2.86)$$

and

$$\hat{N} = \sum_{\mathbf{k}\sigma} \hat{a}_{\mathbf{k}\sigma}^\dagger \hat{a}_{\mathbf{k}\sigma} \quad (2.87)$$

as well as the second quantized expression for the kinetic energy, we arrive at

$$\hat{H} = \sum_{\mathbf{k}\sigma} \frac{\hbar^2 k^2}{2m} \hat{a}_{\mathbf{k},\sigma}^\dagger \hat{a}_{\mathbf{k},\sigma} + \frac{1}{2L^d} \sum_{\mathbf{q} \neq 0} w_{\mathbf{q}} \sum_{\mathbf{k}_1\sigma_1, \mathbf{k}_2\sigma_2} \hat{a}_{\mathbf{k}_1+\mathbf{q},\sigma_1}^\dagger \hat{a}_{\mathbf{k}_2-\mathbf{q},\sigma_2}^\dagger \hat{a}_{\mathbf{k}_2,\sigma_2} \hat{a}_{\mathbf{k}_1,\sigma_1}. \quad (2.88)$$

This is the result for some electron gas with a uniform positive background that exactly cancels the electronic charge. The generalization to semiconductors works similarly, but the band structure must be taken into account:

$$\hat{H} = \sum_{\mathbf{k}\sigma\alpha} \epsilon_\alpha(\mathbf{k}) \hat{a}_{\mathbf{k},\sigma,\alpha}^\dagger \hat{a}_{\mathbf{k},\sigma,\alpha} + \frac{1}{2L^d} \sum_{\mathbf{q} \neq 0} \sum_{\substack{\mathbf{k}_1\sigma_1\alpha_1\beta_1 \\ \mathbf{k}_2\sigma_2\alpha_2\beta_2}} w_{\mathbf{k}_1\mathbf{k}_2\mathbf{q}}^{\beta_1\beta_2,\alpha_1\alpha_2} \hat{a}_{\mathbf{k}_1+\mathbf{q},\sigma_1\beta_1}^\dagger \hat{a}_{\mathbf{k}_2-\mathbf{q},\sigma_2\beta_2}^\dagger \hat{a}_{\mathbf{k}_2,\sigma_2\alpha_2} \hat{a}_{\mathbf{k}_1,\sigma_1\alpha_1}. \quad (2.89)$$

Here, $\epsilon_\alpha(\mathbf{k})$ describes quasiparticle energy in band α and crystal momentum \mathbf{k} . The interaction is now dependent on all momenta and the bands involved.

The multi-component case is derived similarly to the Jellium case: instead of considering $n_b(\mathbf{r})$ to be a function that is in fact not really dependent on its argument, we consider it to be an operator like $\hat{n}(\mathbf{r})$ for the electrons. The $\mathbf{q} = 0$ considerations can be worked out analogously to find

$$\hat{H} = \sum_{\mathbf{k}\sigma\alpha} \frac{\hbar^2 k^2}{2m_\alpha} \hat{a}_{\mathbf{k},\sigma,\alpha}^\dagger \hat{a}_{\mathbf{k},\sigma,\alpha} + \frac{1}{2L^d} \sum_{\mathbf{q} \neq 0} \sum_{\substack{\mathbf{k}_1\sigma_1\alpha_1 \\ \mathbf{k}_2\sigma_2\alpha_2}} w_{\mathbf{q}}^{\alpha_1\alpha_2} \hat{a}_{\mathbf{k}_1+\mathbf{q},\sigma_1,\alpha_1}^\dagger \hat{a}_{\mathbf{k}_2-\mathbf{q},\sigma_2,\alpha_2}^\dagger \hat{a}_{\mathbf{k}_2,\sigma_2,\alpha_2} \hat{a}_{\mathbf{k}_1,\sigma_1,\alpha_1}, \quad (2.90)$$

where the third index describes the particle species. Since particle spin and particle species enter this Hamiltonian with the same structure (diagonal in kinetic energy, no flips or particle conversion during interaction), the spin index σ_i from now on also includes the particle species index and the sums have to be interpreted to also go over all particle species.

Statically screened interaction

The expressions for the gas particles are in the basis of momentum eigenstates,

$$\langle \mathbf{r}\sigma' | \mathbf{k}\sigma \rangle = \delta_{\sigma\sigma'} \frac{1}{\sqrt{L^d}} \exp\left(-\frac{i}{\hbar} \mathbf{k} \cdot \mathbf{r}\right), \quad (2.91)$$

where σ is a combined index that includes spin and the particle species, and \mathbf{k} is chosen in such a way that the function fulfills periodic boundary positions at the box ends. We compute the interaction matrix element for a 3D box of length L ,

$$\begin{aligned}
& \langle \mathbf{k}_1\sigma_1, \mathbf{k}_2\sigma_2 | \hat{w} | \mathbf{k}_3\sigma_3, \mathbf{k}_4\sigma_4 \rangle \\
&= \frac{\delta_{\sigma_1\sigma_3}\delta_{\sigma_2\sigma_4}}{L^6} \int_{\mathbb{R}^3} \int_{L^3} \exp\left\{\frac{i}{\hbar}(\mathbf{k}_3 - \mathbf{k}_1) \cdot \mathbf{r}_1 + (\mathbf{k}_4 - \mathbf{k}_2) \cdot \mathbf{r}_2\right\} \frac{Z_1 Z_2 e^2 e^{-\kappa|\mathbf{r}_1 - \mathbf{r}_2|}}{|\mathbf{r}_1 - \mathbf{r}_2|} d\mathbf{r}_1 d\mathbf{r}_2 \\
&= \frac{\delta_{\sigma_1\sigma_3}\delta_{\sigma_2\sigma_4}}{L^3} \underbrace{\frac{4\pi Z_1 Z_2 e^2}{|\mathbf{k}_3 - \mathbf{k}_1| + \kappa^2}}_{w_{|\mathbf{k}_3 - \mathbf{k}_1|}^{\sigma_1\sigma_2} :=} \delta_{\mathbf{k}_1 + \mathbf{k}_2, \mathbf{k}_3 + \mathbf{k}_4}. \tag{2.92}
\end{aligned}$$

We see that the interaction potential, through its homogeneity in space, conserves the momentum in each collision, does not change spins of the particles, and is only dependent on the amount of momentum transferred.

While in the *GW* approximation screening is handled by the Dyson equation, i.e. we must use the bare Coulomb potential $\kappa = 0$, this would drastically overestimate the effective interaction between particles in SOA calculations. Hence in this thesis, for SOA calculations, static *Thomas–Fermi* screening will be used, cf. Sect. 2.3.6.

2.3.2. Plasma parameters

Equilibrium plasmas are completely specified by the density and the energy per particle, and maybe the ion composition. There are however dimensionless parameters that are mostly used instead, which better characterize the plasma and describe the dominant effects.

Wigner–Seitz radius r_s

The *Wigner–Seitz radius* (or *Brückner parameter*) r_s is the radius of that sphere that contains exactly one electron, in units of the Bohr radius $a_B = \frac{\hbar^2}{me^2}$. In 3 dimensions it is given by

$$r_s = \left(\frac{3}{4\pi n}\right)^{\frac{1}{3}} \frac{1}{a_B}. \tag{2.93}$$

It is often called *coupling parameter*, since it not only directly describes the density, but also whether the kinetic energy term or the interaction term dominates. It can be shown that for small r_s , i.e. high density, the kinetic term dominates the interaction term, and thus it is then a weakly coupled plasma, and vice versa.

In Alkali metals r_s typically has values between 3 and 6. Since semiconductors can be weakly excited, we can find far greater r_s values there. In the warm dense matter (WDM) regime, which in parts is also accessible in inertial confinement fusion (ICF) experiments, r_s values around 1 can be found, in astrophysical objects even lower.

Quantum Degeneracy Parameter Θ

The second dimensionless parameter that will be used in this thesis is the *quantum degeneracy parameter* Θ . It is given by $\Theta = \frac{k_B T}{\epsilon_F}$, where $\epsilon_F = p_F^2/2m$ is the Fermi energy of the free gas. The Fermi momentum p_F is only dependent on the density and in 3D it can be computed as follows:

$$\frac{\overset{\text{spin}}{\downarrow} 4\pi}{3} \frac{p_F^3}{(2\pi\hbar)^3} = n \quad \Rightarrow \quad p_F = \pi\hbar \left(\frac{3n}{\pi} \right)^{\frac{1}{3}}. \quad (2.94)$$

A higher Θ corresponds to a broader Fermi function, which means that Pauli blocking and thus degeneracy become weaker.

2.3.3. NEGF for the uniform electron gas

The Jellium Hamiltonian in a box of length L acts on the Hilbert space of all wave functions that are periodic on the box boundaries, but they can in principle still be non-uniform. If the correlation length of the gas is small compared to the length scale of inhomogeneities, it is a reasonable approach to model the gas to be uniform locally. In a uniform system, only relative coordinates are relevant for one-particle quantities, i.e. the 1pNEGF in spatial coordinate representation has the form

$$G_{\sigma\sigma'}(\mathbf{r}z, \mathbf{r}'z') = G_{\sigma\sigma'}(\mathbf{r} - \mathbf{r}', zz'). \quad (2.95)$$

We now take the Fourier transform with respect to the spatial coordinates [14], which yields the momentum representation (basis transformation to plain waves) variant of the 1pNEGF,

$$\begin{aligned} G_{\mathbf{p}\sigma, \mathbf{p}'\sigma'}(z, z') &= \frac{1}{L^d} \int_{L^d} d\mathbf{r} d\mathbf{r}' e^{-\frac{i}{\hbar}(\mathbf{p}\mathbf{r} - \mathbf{p}'\mathbf{r}')} G_{\sigma\sigma'}(\mathbf{r} - \mathbf{r}', z, z') \\ &= \frac{1}{L^d} \int_{L^d} d\mathbf{r}' e^{-\frac{i}{\hbar}(\mathbf{p} - \mathbf{p}')\mathbf{r}'} \int_{L^d} d(\mathbf{r} - \mathbf{r}') G_{\sigma\sigma'}(\mathbf{r} - \mathbf{r}', z, z') = \delta_{\mathbf{p}\mathbf{p}'} G_{\mathbf{p}, \sigma\sigma'}(z, z'). \end{aligned} \quad (2.96)$$

Since the Hamiltonian does not allow spin flips or the conversion of the particle species, we can conclude that G is also diagonal in that index. This means that our 'final' Green function assumes the reduced form $G_{\mathbf{p}\sigma}(zz')$.

Now we can show that Σ has the same reduced form: Since we postulate spatial uniformity, the KBE, Eqs. (2.25),(2.26), take the form

$$\begin{aligned} i\hbar \frac{\partial}{\partial z} G_{\mathbf{p}\sigma}(z, z') &= \delta_C(z, z') + \sum_k h_{\mathbf{p}\sigma}^{(0)}(z) G_{\mathbf{p}\sigma}(z, z') + \sum_{\mathbf{k}\lambda} \int_C d\bar{z} \Sigma_{\mathbf{p}\sigma, \mathbf{k}\lambda}(z, \bar{z}) G_{\mathbf{k}\lambda}(\bar{z}, z') \delta_{\mathbf{k}\mathbf{p}} \delta_{\sigma, \lambda} \\ &= \delta_C(z, z') + \sum_k h_{\mathbf{p}\sigma}^{(0)}(z) G_{\mathbf{p}\sigma}(z, z') + \underbrace{\int_C d\bar{z} \Sigma_{\mathbf{p}\sigma, \mathbf{p}\sigma}(z, \bar{z}) G_{\mathbf{p}\sigma}(\bar{z}, z')}_{I_{\mathbf{p}\sigma}(z, z')}, \end{aligned} \quad (2.97)$$

i.e. we also only consider the momentum/spin-diagonal of the selfenergy, $\Sigma_{\mathbf{p}\sigma}(z, z')$. We see that some summations become trivial due to the diagonality of G (and the momentum conserving structure of w), which reduces the computational cost in momentum representation.

The 'loop' diagram, the zeroth order polarization function, is another quantity that is diagonal, and a key building block for direct SOA and the GW approximation:

$$\begin{array}{c} \circlearrowleft \\ \circlearrowright \end{array} = \pi_{\mathbf{q}}(z, z') = i\hbar \sum_{\mathbf{p}\sigma} (\pm)_{\sigma} G_{\mathbf{p}+\mathbf{q},\sigma}(z, z') G_{\mathbf{p},\sigma}(z', z), \quad (2.98)$$

where \pm_{σ} takes into account that the multiple particle species can be a mix of Fermions and Bosons. The sum is of the form of a convolution, which can be computed extremely fast using the convolution theorem and a Fourier transform, significantly simplifying the numerical cost of such integrations. The details about the practical realization of this is explained in the numerics chapter. Also, the momentum representation expression will be presented in that chapter, where efficient evaluation methods are also discussed.

2.3.4. Thermodynamic limit

The momenta appearing under the sums are dependent on the box length: Given a d -dimensional cubic box of length L , momenta can only assume the values $2\pi\hbar L^{-1}\mathbb{Z}^d$ due to the boundary conditions. This means that each momentum value takes a volume of $(2\pi\hbar/L)^d$ in momentum space. In the thermodynamic limit, $L \rightarrow \infty$, we thus find the transition

$$\sum_{\mathbf{p}} \rightarrow \int \frac{d\mathbf{p}}{(2\pi\hbar)^d}. \quad (2.99)$$

In the thermodynamic limit, momenta can assume continuous values. Momentum dependencies of functions are thus written in the form $f(\mathbf{p})$ instead of $f_{\mathbf{p}}$ in the thermodynamic limit⁵.

2.3.5. Observables in uniform systems using NEGF

Expectation values of s -particle operators $\hat{A}^{(s)}$ can be acquired from reduced density matrices $\hat{F}^{(s)}$ [14] by

$$\langle \hat{A}^{(s)} \rangle = \frac{1}{s!} \text{Tr} \left(\hat{F}^{(s)} \hat{A}^{(s)} \right). \quad (2.100)$$

⁵In numerical applications the momentum space needs to be discretized. This discretization implicitly corresponds to a transition back to finite box sizes. In fact, it even implicitly corresponds to a transition to a lattice system, since a discretized momentum grid also does not reach infinities. Many uniform gas calculations can thus be mapped on lattice systems with a dense Hamiltonian matrix and long-range interaction.

Since $F^{(1)}(t) = \pm i\hbar G^<(t, t)$, and because of the diagonal structure of G , single particle expectation values are given by

$$\langle \hat{A}^{(1)} \rangle (t) = \pm i\hbar \sum_{\mathbf{p}\sigma} G_{\mathbf{p}\sigma}^<(t, t) A_{\mathbf{p}\sigma}^{(1)} = \sum_{\mathbf{p}\sigma} f_{\mathbf{p}\sigma}(t) A_{\mathbf{p}\sigma}^{(1)}, \quad (2.101)$$

where the single-particle distribution function f has been introduced. Its values are the occupation numbers of the states $|\mathbf{p}\sigma\rangle$. Important examples for matrix elements of single-particle observables are the moments of \mathbf{p} :

- 0th moment, density: $A_{\mathbf{p}\sigma}^{(1)} = 1$
- 1st moment, momentum: $A_{\mathbf{p}\sigma}^{(1)} = \mathbf{p}$
- 2nd moment, kinetic energy: $A_{\mathbf{p}\sigma}^{(1)} = p^2/2m_\sigma$

The two-particle expressions in the thermodynamic limit are given by

$$F^{(2),\alpha\beta}(\mathbf{k}, \mathbf{p}, \mathbf{q}) = (i\hbar)^2 \left[(\pm)_\alpha (\pm)_\beta G_\alpha^<(\mathbf{k}) G_\beta^<(\mathbf{p}) \delta(\mathbf{q}) \pm G_\alpha^<(\mathbf{k}) G_\beta^<(\mathbf{p}) \delta(\mathbf{k} - \mathbf{q} - \mathbf{p}) \delta_{\alpha\beta} + \mathcal{G}_{\alpha\beta}(\mathbf{k}, \mathbf{p}, \mathbf{q}) \right], \quad (2.102)$$

$$\langle \hat{A}^{(2)} \rangle^H (t) = \frac{1}{2} (i\hbar)^2 \sum_{\alpha\beta} (\pm)_\alpha (\pm)_\beta \int \frac{d\mathbf{k}}{(2\pi\hbar)^d} \frac{d\mathbf{p}}{(2\pi\hbar)^d} G_\alpha^<(\mathbf{k}, t) G_\beta^<(\mathbf{p}, t) A_{\alpha\beta}^{(2)}(\mathbf{k}, \mathbf{p}, 0), \quad (2.103)$$

$$\langle \hat{A}^{(2)} \rangle^F (t) = \frac{1}{2} (i\hbar)^2 \sum_\alpha (\pm)_\alpha \int \frac{d\mathbf{k}}{(2\pi\hbar)^d} \frac{d\mathbf{p}}{(2\pi\hbar)^d} G_\alpha^<(\mathbf{k}, t) G_\alpha^<(\mathbf{p}, t) \left[A_{\alpha\alpha}^{(2)}(\mathbf{k}, \mathbf{p}, \mathbf{k} - \mathbf{p}) \right]^*, \quad (2.104)$$

$$\langle \hat{A}^{(2)} \rangle^c (t) = \frac{1}{2} (i\hbar)^2 \sum_{\alpha\beta} \int \frac{d\mathbf{k}}{(2\pi\hbar)^d} \frac{d\mathbf{p}}{(2\pi\hbar)^d} \frac{d\mathbf{q}}{(2\pi\hbar)^d} \mathcal{G}_{\alpha\beta}(\mathbf{k}, \mathbf{p}, \mathbf{q}, t) \left[A_{\alpha\beta}^{(2)}(\mathbf{k}, \mathbf{p}, \mathbf{q}) \right]^*, \quad (2.105)$$

where the first term of $\hat{F}^{(2)}$ represents the Hartree GF, the second term the Fock GF, and the third term the correlation part of the two particle GF, the pivotal quantity of the G1–G2 scheme. The expectation value of $\hat{A}^{(2)}$ has three contributions, stemming from the three parts of $\hat{F}^{(2)}$. A general two-particle observable might demand knowledge of \mathcal{G} , but this is not the case for the interaction energy: Here, the Hartree part vanishes due to assumed charge neutrality of the system. The two remaining parts are given by

$$\begin{aligned} \langle \hat{w} \rangle^F (t) &= \frac{1}{2} (i\hbar)^2 \sum_\alpha (\pm)_\alpha \int \frac{d\mathbf{k}}{(2\pi\hbar)^d} \frac{d\mathbf{p}}{(2\pi\hbar)^d} Z_\alpha^2 G_\alpha^<(\mathbf{k}, t) G_\alpha^<(\mathbf{p}, t) w(\mathbf{k} - \mathbf{p}) \\ &= \frac{1}{2} i\hbar \sum_\alpha (\pm)_\alpha \int \frac{d\mathbf{k}}{(2\pi\hbar)^d} h_\alpha^{\text{HF}}(\mathbf{k}, t) G_\alpha^<(\mathbf{k}, t) - \frac{1}{2} \langle \hat{T} \rangle (t), \end{aligned} \quad (2.106)$$

$$\langle \hat{w} \rangle^c (t) = \frac{1}{2} (i\hbar)^2 \sum_{\alpha\beta} Z_\alpha Z_\beta \int \frac{d\mathbf{k}}{(2\pi\hbar)^d} \frac{d\mathbf{p}}{(2\pi\hbar)^d} \frac{d\mathbf{q}}{(2\pi\hbar)^d} \mathcal{G}^{\alpha\beta}(\mathbf{k}, \mathbf{p}, \mathbf{q}, t) w(\mathbf{q}) = \frac{1}{2} i\hbar \sum_\alpha \int \frac{d\mathbf{p}}{(2\pi\hbar)^d} I_\alpha(\mathbf{p}, t), \quad (2.107)$$

where \hat{T} is the kinetic energy operator, $h_\alpha^{\text{HF}}(\mathbf{p}, t)$ is the (Hartree-)Fock Hamiltonian given by

$$h_\alpha^{\text{HF}}(\mathbf{p}, t) = \frac{p^2}{2m_\alpha} + i\hbar \int \frac{d\mathbf{k}}{(2\pi\hbar)^d} Z_\alpha^2 w(\mathbf{k} - \mathbf{p}) G_\alpha^<(\mathbf{p}, t), \quad (2.108)$$

and $I_\alpha(\mathbf{p}, t)$ is the time-diagonal collision integral given by

$$I_\alpha(\mathbf{p}, t) = \int_{t_0}^t d\bar{t} [\Sigma_\alpha^>(\mathbf{p}, t, \bar{t}) G_\alpha^<(\mathbf{p}, \bar{t}, t) - \Sigma_\alpha^<(\mathbf{p}, t, \bar{t}) G_\alpha^>(\mathbf{p}, \bar{t}, t)]. \quad (2.109)$$

This shows that the interaction energy is also directly accessible without the G1–G2 scheme.

2.3.6. Lindhard theory for static screening

The Yukawa potential is dependent on the screening constant κ . One way to obtain an estimate for κ is Lindhard's theory, thoroughly described in Ref. [74]. Lindhard's theory describes the response of the uniform gas in first order perturbation theory and yields the expression

$$\epsilon(\mathbf{q}, \omega) = 1 - \sum_{\mathbf{k}\sigma} w_{\mathbf{q}}^{\sigma\sigma} \frac{f_{\mathbf{k}-\mathbf{q},\sigma} - f_{\mathbf{k},\sigma}}{\hbar(\omega + i\delta) + E_{\mathbf{k}-\mathbf{q},\sigma} - E_{\mathbf{k},\sigma}}, \quad (2.110)$$

where $f_{\mathbf{k},\sigma}(t) = G_{\mathbf{k},\sigma}^<(t, t)$ is the momentum distribution function and $E_{\mathbf{k},\sigma}$ are the single-particle energies. Here we approximate these by the kinetic energies, i.e. $E_{\mathbf{k},\sigma} = k^2/2m_\sigma$.

In order to find a screening *constant*, we first take the static limit, i.e. $\omega \rightarrow 0$, which yields

$$\epsilon(\mathbf{q}, 0) = 1 - \sum_{\mathbf{k}\sigma} w_{|\mathbf{q}|}^{\sigma\sigma} \frac{f_{\mathbf{k}-\mathbf{q},\sigma} - f_{\mathbf{k},\sigma}}{E_{\mathbf{k}-\mathbf{q},\sigma} - E_{\mathbf{k},\sigma}}. \quad (2.111)$$

Now we consider the long wavelength limit, $\mathbf{q} \rightarrow 0$, where we can write the differences in terms of gradients

$$\epsilon(\mathbf{q}, 0) = 1 - \sum_{\mathbf{k}\sigma} w_{|\mathbf{q}|}^{\sigma\sigma} \frac{-\mathbf{q} \cdot \nabla f_{\mathbf{k},\sigma}}{-\frac{1}{2m_\sigma} 2\mathbf{q} \cdot \mathbf{k}}. \quad (2.112)$$

Now we focus on the isotropic 3D case in the continuum limit, i.e. $\sum_{\mathbf{k}} \rightarrow \int d\mathbf{k} (2\pi\hbar)^{-3}$. Without loss of generality, we assume $\mathbf{q} \parallel \mathbf{e}_z$. Since $\nabla f_\sigma(k) \parallel \mathbf{k}$, the expression becomes

$$\begin{aligned} \epsilon(\mathbf{q}, 0) &= 1 - \sum_{\sigma} w_{|\mathbf{q}|}^{\sigma\sigma} \int \frac{dk d\vartheta d\varphi}{(2\pi\hbar)^3} \frac{q \partial_k f_\sigma(k) \cos(\vartheta)}{\frac{1}{m_\sigma} q k \cos(\vartheta)} k^2 \sin(\vartheta) \\ &= 1 - \frac{4\pi\hbar e^2}{q^2} \sum_{\sigma} Z_\sigma^2 \int \frac{dk d\vartheta d\varphi}{(2\pi\hbar)^3} m_\sigma f_\sigma(k) \sin(\vartheta) = 1 + \frac{(4\pi)^2 \hbar e^2}{q^2} 4\pi \sum_{\sigma} Z_\sigma^2 \int \frac{dk}{(2\pi\hbar)^3} m_\sigma f_\sigma(k). \end{aligned} \quad (2.113)$$

In the last step integration by parts was used. If we define

$$\kappa^2 = \frac{2e^2}{\pi\hbar^2} \sum_{\sigma} Z_{\sigma}^2 m_{\sigma} \int dk f_{\sigma}(k), \quad (2.114)$$

the dielectric function can be cast in the form $\epsilon(\mathbf{q}, 0) = \frac{q^2 + \kappa^2}{q^2}$, and consequently we have

$$w(\mathbf{q}, \kappa) = \frac{w(\mathbf{q}, \kappa = 0)}{\epsilon(\mathbf{q}, 0)} = \frac{\frac{4\pi e^2}{q^2}}{\frac{q^2 + \kappa^2}{q^2}} = \frac{4\pi e^2}{\kappa^2 + q^2}, \quad (2.115)$$

the expression for the Yukawa potential, but with an estimate for κ . In an anisotropic system an approach to use this result is to average f over all angles first, and then apply the formula, as was applied in Ref. [75]. Since this approach can also be applied to time-dependent distribution functions, the screening constant can be adapted, too. A time-dependent screening constant however makes the simulation non-energy-conserving and should not be used, if energies are the focus of the calculation.

2.3.7. G1–G2 equations for the uniform multi-component gas

Since the HF-Hamiltonian is diagonal (single-particle Green function is diagonal, and the interaction conserves momentum), the commutator $[h^{\text{HF}}, G^{\gtrless}]$ vanishes, and the single-particle equation takes the simple form [29]

$$i\hbar \frac{d}{dt} G_{\mathbf{p}\sigma}^{\gtrless}(t) = \pm i\hbar \sum_{\mathbf{k}\mathbf{q}} \sum_{\lambda} w_{|\mathbf{q}|}^{\lambda\sigma}(t) \mathcal{G}_{\mathbf{k}\mathbf{p}\mathbf{q}}^{\lambda\sigma}(t) + h.c., \quad (2.116)$$

where $\mathcal{G}_{\mathbf{k}\mathbf{p}\mathbf{q}}^{\lambda\sigma}(t)$ is short for

$$\mathcal{G}_{\mathbf{k}\mathbf{p}\mathbf{q}}^{\lambda\sigma}(t) := \mathcal{G}_{\mathbf{k}-\mathbf{q}, \mathbf{p}+\mathbf{q}, \mathbf{k}, \mathbf{p}}^{\lambda\sigma\lambda\sigma}(t). \quad (2.117)$$

These 'momentum conserving' components of \mathcal{G} are sufficient to describe the correlations, since their equations of motion only couple to components with the same 'momentum conserving' structure. In the same way as in the general basis, Eq. (2.72), we start with the SOA equation

$$\begin{aligned} i\hbar \frac{d}{dt} \mathcal{G}_{\mathbf{k}\mathbf{p}\mathbf{q}}^{\lambda\sigma} - \mathcal{G}_{\mathbf{k}\mathbf{p}\mathbf{q}}^{\lambda\sigma} \overbrace{\left(h_{\mathbf{k}-\mathbf{q}, \lambda}^{\text{HF}}(t) + h_{\mathbf{p}+\mathbf{q}, \sigma}^{\text{HF}}(t) - h_{\mathbf{k}, \lambda}^{\text{HF}}(t) - h_{\mathbf{p}, \sigma}^{\text{HF}}(t) \right)}^{\Delta_{\mathbf{k}\mathbf{p}\mathbf{q}, \lambda\sigma}^{\text{HF}, (2)} :=} \\ = (i\hbar)^2 \underbrace{\left[w_{|\mathbf{q}|}^{\lambda\sigma} \pm \delta_{\sigma\lambda} w_{|\mathbf{k}-\mathbf{p}-\mathbf{q}|}^{\sigma\sigma}(t) \right] \left\{ G_{\mathbf{k}-\mathbf{q}, \lambda}^{\gtrless}(t) G_{\mathbf{p}+\mathbf{q}, \sigma}^{\gtrless}(t) G_{\mathbf{k}, \lambda}^{\lessgtr}(t) G_{\mathbf{p}, \sigma}^{\lessgtr}(t) - (\leftrightarrow \leftrightarrow \leftarrow) \right\}}_{\Psi_{\mathbf{k}\mathbf{p}\mathbf{q}}^{\lambda\sigma} :=} \end{aligned} \quad (2.118)$$

with the Hartree–Fock Hamiltonian given in Eq. (2.108). The modifications that represent advanced selfenergy approximations are given by:

GW Drop the $\pm\delta_{\sigma\lambda}w_{|\mathbf{k}-\mathbf{p}-\mathbf{q}|}^{\sigma\sigma}(t)$ on the right side, and add $\Pi_{\mathbf{k}\mathbf{p}\mathbf{q}}^{\lambda\sigma}(t) - [\Pi_{\mathbf{p}+\mathbf{q},\mathbf{k}-\mathbf{q},\mathbf{q}}^{\sigma\lambda}(t)]^*$ to the right side, where

$$\Pi_{\mathbf{k}\mathbf{p}\mathbf{q}}^{\lambda\sigma} = (\pm)_{\sigma} (i\hbar)^2 \left[G_{\mathbf{p}+\mathbf{q},\sigma}^{\lambda}(t) G_{\mathbf{p},\sigma}^{\lambda}(t) - G_{\mathbf{p}+\mathbf{q},\sigma}^{\lambda}(t) G_{\mathbf{p},\sigma}^{\lambda}(t) \right] \sum_{\mathbf{p}'\alpha} w_{|\mathbf{q}|}^{\lambda\alpha}(t) \mathcal{G}_{\mathbf{k}\mathbf{p}'\mathbf{q}}^{\lambda\alpha}(t). \quad (2.119)$$

TPP Add $\Lambda_{\mathbf{k}\mathbf{p}\mathbf{q}}^{\text{pp},\lambda\sigma}(t) - [\Lambda_{\mathbf{k}-\mathbf{q},\mathbf{p}+\mathbf{q},-\mathbf{q}}^{\text{pp},\lambda\sigma}(t)]^*$ to the right side, where

$$\Lambda_{\mathbf{k}\mathbf{p}\mathbf{q}}^{\text{pp},\lambda\sigma}(t) = (i\hbar)^2 \left[G_{\mathbf{k}-\mathbf{q},\lambda}^{\lambda}(t) G_{\mathbf{p}+\mathbf{q},\sigma}^{\lambda}(t) - G_{\mathbf{k}-\mathbf{q},\lambda}^{\lambda}(t) G_{\mathbf{p}+\mathbf{q},\sigma}^{\lambda}(t) \right] \sum_{\mathbf{q}'} w_{|\mathbf{q}'-\mathbf{q}|}^{\lambda\sigma}(t) \mathcal{G}_{\mathbf{k}\mathbf{p}\mathbf{q}'}^{\lambda\sigma}(t). \quad (2.120)$$

TPH Add $\Lambda_{\mathbf{k}\mathbf{p}\mathbf{q}}^{\text{ph},\lambda\sigma}(t) - [\Lambda_{\mathbf{k}-\mathbf{q},\mathbf{p}+\mathbf{q},-\mathbf{q}}^{\text{ph},\lambda\sigma}(t)]^*$ to the right side, where

$$\Lambda_{\mathbf{k}\mathbf{p}\mathbf{q}}^{\text{ph},\lambda\sigma}(t) = (i\hbar)^2 \left[G_{\mathbf{k}-\mathbf{q},\lambda}^{\lambda}(t) G_{\mathbf{p},\sigma}^{\lambda}(t) - G_{\mathbf{k}-\mathbf{q},\lambda}^{\lambda}(t) G_{\mathbf{p}+\mathbf{q},\sigma}^{\lambda}(t) \right] \sum_{\mathbf{q}} w_{|\mathbf{q}'|}^{\lambda\sigma}(t) \mathcal{G}_{\mathbf{k},\mathbf{p}-\mathbf{q}',\mathbf{q}+\mathbf{q}'}^{\lambda\sigma}(t). \quad (2.121)$$

We see that indeed only the 'momentum conserving' components of \mathcal{G} are relevant for the dynamics. We also see that all these approximations need the same order of memory, where objects of the size of \mathcal{G} are the largest. It is less evident that TPP and TPH are in fact slower than *GW* or *SOA* by one order of the number of basis states, N_B : While they have one sum over momentum states, just as *GW*, the TPP and TPH sums have 3 external momentum indices, meaning $\mathcal{O}(N_B^3)$ such sums must be computed, whereas *GW*'s sum only has two external indices. In fact, a *GW* code runs at a similar speed as an *SOA* code, since the sum (or a symmetry equivalent) is computed for the collision integral anyway and can be reused. The *SOA* exchange diagram is by no means harder to compute than the direct diagram in the G1–G2 scheme. In conclusion: *If* computer memory is sufficient to support these large tensor quantities, all these selfenergy approximations become viable at once. A discussion of the viability of the G1–G2 scheme with the *GW* approximation, with a comparison to the standard and an intermediate approach, is given in Sect. 3.

2.3.8. Initial correlations, adiabatic switching

In principle, $\mathcal{G}(t_0)$ can be chosen arbitrarily and the system (G^{\geq}, \mathcal{G}) can still be propagated. The question which initial correlations correspond to situations that are physical has been discussed before in the formalism of reduced density matrices [65, 76, 77]. Any binary correlations $\mathcal{G}(t_0)$ certainly can serve as initial correlatios, if they are result of some preceding time propagation. This in particular includes initial correlations that were generated by adiabatic switching, but also applies to arbitrary nonequilibrium situations. Calculations in the G1–G2 scheme are suitable to be interrupted at some point of time, have the current G^{\geq} and \mathcal{G} data stored, and be

restarted at the later time. These stored G^{\lessgtr} , \mathcal{G} values then serve as initial correlations for the continued calculation.

In the memory formalism, arbitrary initial correlations [77] can be included by a function $c(\mathbf{k}, \mathbf{p}, \mathbf{q}, t_0)$. The collision integral due to c is computed according to

$$I^{IC}(\mathbf{k}, t, t') = -2i\hbar^5 L^d \int \frac{d\mathbf{p}}{(2\pi\hbar)^d} \int \frac{d\mathbf{q}}{(2\pi\hbar)^d} w(\mathbf{q}) \times \\ \times G^{\mathcal{R}}(\mathbf{k} - \mathbf{q}, t, t_0) G^{\mathcal{R}}(\mathbf{p} + \mathbf{q}, t, t_0) c(\mathbf{k}, \mathbf{p}, \mathbf{q}, t_0) G^{\mathcal{A}}(\mathbf{p}, t_0, t') G^{\mathcal{A}}(\mathbf{k}, t_0, t'). \quad (2.122)$$

In the case that we want to compute c from a preceding propagation, for SOA we set

$$c(\mathbf{k}, \mathbf{p}, \mathbf{q}, t_0) = \frac{i\hbar}{L^d} \int_{t_-}^{t_0} d\bar{t} w(\mathbf{q}) [G^>(\mathbf{k} - \mathbf{q}, t_0, \bar{t}), G^>(\mathbf{p} + \mathbf{q}, t_0, \bar{t}) G^<(\mathbf{k}, \bar{t}, t_0) G^<(\mathbf{p}, \bar{t}, t_0) - (>\leftrightarrow<)] . \quad (2.123)$$

The expressions above are valid in full two-time calculations. In the GKBA case it is not a practical approach: Since c has the same index structure and thus the same memory demand as \mathcal{G} , the approach above combined with memory integrals contains the difficult parts of both worlds: difficult basis scaling with c/\mathcal{G} and difficult scaling with number of time steps from the memory integral. The G1–G2 scheme can be regarded as pushing the initial correlations idea to the extreme: After every time step, the 'new' correlations are included into the initial correlations, for which the \mathcal{G} equation was found, and thus only this term needs to be evaluated for the propagation of G^{\lessgtr} .

The condition 'must be obtainable through physical processes' for initial correlations is a criterion that is difficult to check for a given $\mathcal{G}(t_0)$. For example, in the SOA case in a uniform gas, we can choose an arbitrary G^{\lessgtr} , and find a \mathcal{G} that freezes the single-particle distribution (and 2p-correlations):

$$\underbrace{i\hbar \frac{d}{dt} \mathcal{G}_{\mathbf{k}\mathbf{p}\mathbf{q}}^{\lambda\sigma}(t)}_{\text{set to 0}} - \mathcal{G}_{\mathbf{k}\mathbf{p}\mathbf{q}}^{\lambda\sigma} \Delta_{\mathbf{k}\mathbf{p}\mathbf{q},\lambda\sigma}^{\text{HF},(2)} = \Psi_{\mathbf{k}\mathbf{p}\mathbf{q}}^{\lambda\sigma} \quad (2.124)$$

$$\Leftrightarrow \mathcal{G}_{\mathbf{k}\mathbf{p}\mathbf{q}}^{\lambda\sigma} = -\frac{\Psi_{\mathbf{k}\mathbf{p}\mathbf{q}}^{\lambda\sigma}}{\Delta_{\mathbf{k}\mathbf{p}\mathbf{q},\lambda\sigma}^{\text{HF},(2)}}, \quad (2.125)$$

where the abbreviations from Eq. (2.118), dependent on G^{\lessgtr} , were used. The expression on the right is understood as limit, if $\Delta_{\mathbf{k}\mathbf{p}\mathbf{q},\lambda\sigma}^{\text{HF},(2)} = 0$. Since Ψ and $\Delta^{\text{HF},(2)}$ are both real, we conclude that \mathcal{G} is real, too. Since the single particle equation of motion is given by

$$i\hbar \frac{d}{dt} G_{\mathbf{p}\sigma}^{\lessgtr}(t) = \pm i\hbar \sum_{\mathbf{k}\mathbf{q}} \sum_{\lambda} w_{|\mathbf{q}|}^{\lambda\sigma}(t) \mathcal{G}_{\mathbf{k}\mathbf{p}\mathbf{q}}^{\lambda\sigma}(t) + h.c., \quad (2.126)$$

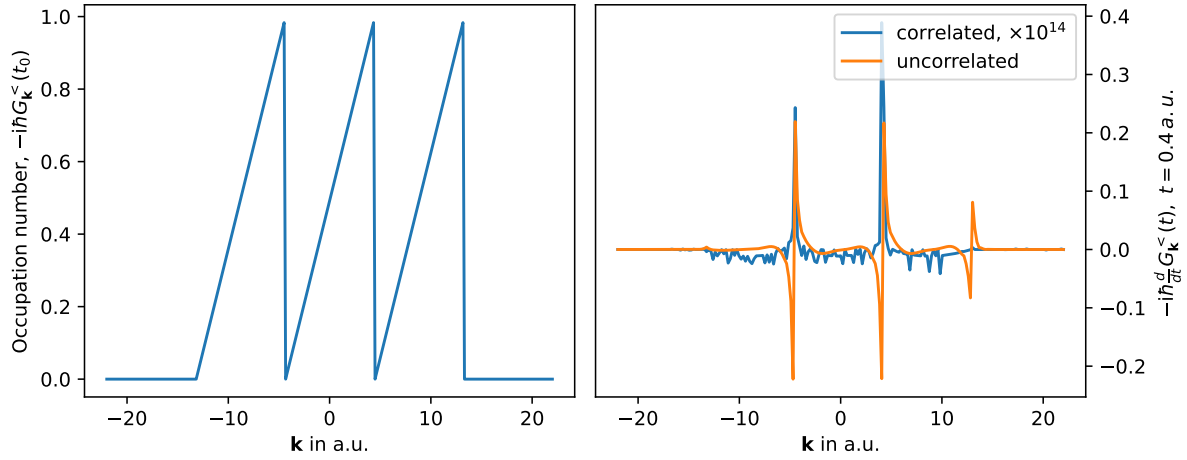


Figure 2.4.: Some exotic distribution function on the left. Time derivative of the distribution function after 4.0 a.u. for some uncorrelated initial state and some initial correlations according to Eq. (2.125). The derivative for the correlated initial state is on the order of machine precision and thus confirms that these initial correlations make the distribution stationary.

i.e. only the imaginary part of \mathcal{G} contributes to the dynamics of $G^>$, the system is stationary. In Fig. 2.4 this is demonstrated for a 1D quantum wire⁶: A very exotic distribution is chosen and the dynamics of an uncorrelated start and a correlated start according to Eq. (2.125) are compared. The initial correlations make the distribution indeed stationary. It is questionable if this distribution function can ever be achieved in an experiment, let alone be made stationary. This suggests that many initial correlations are unattainable through physical processes, but a rigorous proof is still missing.

Initial correlations through adiabatic switching

A suitable choice for initial correlations can be computed using the *adiabatic switching method* with an extended contour which has already been discussed in Fig. 2.3. NEGF calculations without the G1–G2 scheme however have high computational costs proportional to N_t^3 (except SOA with GKBA: N_t^2) and RAM demand of N_t^2 (except SOA with GKBA: N_t^1). These nonlinear scalings make the adiabatic switching process quite costly; especially, since long switching times are desirable according to the adiabatic connection.

In practical calculations one chooses a process that is the object of the study. The simulation of this process requires a certain amount of in-simulation time and a certain size and resolution of the momentum grid (cf. numerics section). The switching time then is chosen as long as possible with regard to resources to reduce perturbations caused by the switching process. Skipping the switching process corresponds to an uncorrelated start which is only suitable

⁶The model and interaction potential are derived in Ref. [69], Appendix A. Convergence parameters: 207 k points in the range $[-22 a_B^{-1}, 22 a_B^{-1}]$, Time step length is $0.0015 a.u. \approx 0.0364$ as, static $\kappa = 0.5 a_B^{-1}$, and wire radius (harmonic trap) is $0.5 a_B$

to describe a system where the charge carriers are newly generated. This is e.g. the case in semiconductors after an ultrashort laser pulse.

3. Simulation variants for spatially uniform systems

Abstract: This chapter is devoted to finding the best computational method for SOA and GW calculations of uniform systems. First, the numerical scalings with convergence parameters for uniform systems of various dimensions and symmetries are discussed. A 2D test calculation shows that the RAM demand of the G1–G2 scheme is very high and extrapolation of the scalings lead to the conclusion that 3D calculations (especially without isotropy) demand too much RAM for today’s computers. 3D cylinder symmetric GW calculations are best done in the ‘normal way’, i.e. by solution of the Dyson equation. The last part of this chapter discusses the scalings of the methods again, this time in view of aliasing.

3.1. Another reformulation of GW

In this subsection the reconstruction of \mathcal{G} from $W^{\geq}(t, t')$ and $G^{\geq}(t, t')$ is described, where an auxiliary quantity, a ‘decomposition components’ of the inverse dielectric function, $\epsilon_{\mathbf{k}\mathbf{q}\alpha}^{-1, \geq}(t, t')$ is defined. After that, a new, fully equivalent GW propagation scheme is introduced, which makes use of the simpler equations of these components, and whose scalings with time step numbers N_t and basis size N_B lie between those of the G1–G2 scheme and the traditional memory integral method.

Reconstruction of \mathcal{G}

The derivation of the G1–G2 scheme for the GW approximation in arbitrary basis [29] starts with the equation

$$\mathcal{G}_{ijkl}(t) = \pm \sum_{pq} \int_{t_0}^t d\bar{t} \left[\epsilon_{lpjq}^{-1, >}(t, \bar{t}) \mathcal{G}_{iqkp}^{\text{F}, >}(t, \bar{t}) - \epsilon_{lpjq}^{-1, <}(t, \bar{t}) \mathcal{G}_{iqkp}^{\text{F}, <}(t, \bar{t}) \right], \quad (3.1)$$

where $\mathcal{G}_{ijkl}^{\text{F}, \geq}(t, t') = G_{il}^{\geq}(t, t') G_{jk}^{\leq}(t', t)$ and $\epsilon_{ijkl}^{-1, \geq}(t, t')$ fulfills the Dyson equation

$$\epsilon_{ijkl}^{-1, \geq}(t, t') = \pm i\hbar \sum_{pq} w_{pq} \mathcal{G}_{kqip}^{\text{F}, \geq}(t, t') \quad (3.2)$$

$$\pm i\hbar \sum_{pqrs} w_{jrsl}(t') \left[\int_{t_0}^t d\bar{t} \left(\mathcal{G}_{kqip}^{\text{F}, >}(t, \bar{t}) - \mathcal{G}_{kqip}^{\text{F}, <}(t, \bar{t}) \right) \epsilon_{rpsq}^{-1, \leq}(t', \bar{t}) + \int_{t_0}^{t'} d\bar{t} \mathcal{G}_{kqip}^{\text{F}, \geq}(t, \bar{t}) \left(\epsilon_{rpsq}^{-1, >}(t', \bar{t}) - \epsilon_{rpsq}^{-1, <}(t', \bar{t}) \right) \right].$$

From the Dyson equation in momentum representation,

$$\begin{aligned} \varepsilon_{\mathbf{k}\mathbf{q}\alpha}^{-1,\gtrless}(t,t') &= \pm i\hbar w_{\mathbf{q}} G_{\mathbf{k}+\mathbf{q},\alpha}^{\gtrless}(t,t') G_{\mathbf{k},\alpha}^{\lesseqgtr}(t',t) \\ &\pm i\hbar w_{\mathbf{q}} \int_{t_0}^{t'} d\bar{t} G_{\mathbf{k}+\mathbf{q},\alpha}^{\gtrless}(t,\bar{t}) G_{\mathbf{k},\alpha}^{\lesseqgtr}(\bar{t},t) \left[\varepsilon_{\mathbf{q}}^{-1,<}(\bar{t},t') - \varepsilon_{\mathbf{q}}^{-1,>}(\bar{t},t') \right] \\ &\pm i\hbar w_{\mathbf{q}} \int_{t_0}^t d\bar{t} \left[G_{\mathbf{k}+\mathbf{q},\alpha}^>(t,\bar{t}) G_{\mathbf{k},\alpha}^<(\bar{t},t) - G_{\mathbf{k}+\mathbf{q},\alpha}^<(t,\bar{t}) G_{\mathbf{k},\alpha}^>(\bar{t},t) \right] \varepsilon_{\mathbf{q}}^{-1,\gtrless}(\bar{t},t'), \end{aligned} \quad (3.3)$$

we find that $\varepsilon_{\mathbf{k}\alpha,\mathbf{p}\beta,\mathbf{k}'\alpha',\mathbf{p}'\alpha'}^{-1,\gtrless} \sim \delta_{\mathbf{k}+\mathbf{p}',\mathbf{k}+\mathbf{p}} \delta_{\alpha,\alpha'} \delta_{\beta\beta'}$, and that apart from the δ 's it has no further dependence on $\mathbf{p}, \mathbf{p}', \alpha, \alpha'$. We thus write $\varepsilon_{\mathbf{k}\mathbf{q}\alpha}^{-1,\gtrless}(t,t') \equiv \varepsilon_{\mathbf{k},\alpha,\mathbf{p},\beta,\mathbf{k}+\mathbf{q},\alpha,\mathbf{p}+\mathbf{q},\beta}^{-1,\gtrless}(t,t')$. By tracing out \mathbf{k} and α , we get the usual inverse dielectric function, that was already used in the expression above:

$$\frac{W_{\mathbf{q}}^{\gtrless}(t,t')}{w_{\mathbf{q}}(t)} = \varepsilon_{\mathbf{q}}^{-1,\gtrless}(t,t') = \sum_{\mathbf{k}\alpha} \varepsilon_{\mathbf{k}\mathbf{q}\alpha}^{-1,\gtrless}(t,t'). \quad (3.4)$$

With this generalized inverse dielectric function we can write \mathcal{G} as

$$\mathcal{G}_{\mathbf{k}\mathbf{p}\mathbf{q}}^{\alpha\beta}(t) = \pm \int d\bar{t} \left[\varepsilon_{\mathbf{p}\mathbf{q}\beta}^{-1,>}(t,\bar{t}) G_{\mathbf{k}-\mathbf{q},\alpha}^>(t,\bar{t}) G_{\mathbf{k},\alpha}^<(\bar{t},t) - \varepsilon_{\mathbf{p}\mathbf{q}\beta}^{-1,<}(t,\bar{t}) G_{\mathbf{k}-\mathbf{q},\alpha}^<(t,\bar{t}) G_{\mathbf{k},\alpha}^>(\bar{t},t) \right]. \quad (3.5)$$

While the reconstruction of \mathcal{G} itself is often too difficult to carry out, these formulas are useful as a starting point to find formulas for two-particle quantities. For example, the pair distribution function g is given by

$$g_{\alpha\beta}(\mathbf{r}) = (i\hbar)^2 \sum_{\mathbf{k}\mathbf{p}\mathbf{q}} \exp(i\mathbf{q} \cdot \mathbf{r}) \left(G_{\mathbf{k}\alpha}^< G_{\mathbf{p}\beta}^< \delta_{\mathbf{q}} \pm G_{\mathbf{k}\alpha}^< G_{\mathbf{p}\beta}^< \delta_{\mathbf{k}-\mathbf{q}-\mathbf{p}} \delta_{\alpha\beta} + \mathcal{G}_{\mathbf{k}\mathbf{p}\mathbf{q}}^{\alpha\beta} \right). \quad (3.6)$$

By inserting the reconstruction of \mathcal{G} into this formula, we find the following expression for the correlation part of the pair distribution function, only dependent on W^{\gtrless} and π^{\gtrless} :

$$g^{\text{corr}}(\mathbf{r}) = \frac{(i\hbar)^2}{i} \int \frac{d\mathbf{q}}{(2\pi\hbar)^n} \exp(i\mathbf{q} \cdot \mathbf{r}) \int d\bar{t} \left[\frac{W^>(\mathbf{q},t,\bar{t})}{w(\mathbf{q},t)} \pi^>(-\mathbf{q},t,\bar{t}) - \frac{W^<(\mathbf{q},t,\bar{t})}{w(\mathbf{q},t)} \pi^<(-\mathbf{q},t,\bar{t}) \right]. \quad (3.7)$$

A new scheme involving $\varepsilon_{\mathbf{k}\mathbf{q}\alpha}^{-1,\gtrless}$

We differentiate Eq. (3.3) with respect to t_1 using the GKBA. In total 6 terms appear from partial derivatives of G^{\gtrless} , and one from the differentiation of the integral boundary. The 6 terms can easily be combined and we find the compact formula

$$\begin{aligned} i\hbar \frac{\partial}{\partial t} \varepsilon_{\mathbf{k}\mathbf{q}\alpha}^{-1,\gtrless}(t \geq t') &= \left[h_{\mathbf{k}+\mathbf{q},\alpha}^{\text{HF}}(t) - h_{\mathbf{k},\alpha}^{\text{HF}}(t) \right] \varepsilon_{\mathbf{k}\mathbf{q}\alpha}^{-1,\gtrless}(t,t') \\ &\pm i\hbar w_{\mathbf{q}} \left[G_{\mathbf{k}+\mathbf{q}}^>(t,t) G_{\mathbf{k}}^<(t,t) - G_{\mathbf{k}+\mathbf{q}}^<(t,t) G_{\mathbf{k}}^>(t,t) \right] \varepsilon_{\mathbf{q}}^{-1,\gtrless}(t,t'). \end{aligned} \quad (3.8)$$

This equation can be used to do the off-diagonal propagation of $\varepsilon^{-1, \gtrless}$ more efficiently, since no memory integral goes into this propagation. The time-diagonal propagation follows from the Dyson equation (3.3) on the time-diagonal:

$$\begin{aligned} \varepsilon_{\mathbf{k}\mathbf{q}\alpha}^{-1, \gtrless}(t, t) &= \pm i\hbar w_{\mathbf{q}} G_{\mathbf{k}+\mathbf{q}, \alpha}^{\gtrless}(t, t) G_{\mathbf{k}, \alpha}^{\lesseqgtr}(t, t) \\ &\pm i\hbar w_{\mathbf{q}} \int_{t_0}^t d\bar{t} \left[G_{\mathbf{k}+\mathbf{q}, \alpha}^{\gtrless}(t, \bar{t}) G_{\mathbf{k}, \alpha}^{\lesseqgtr}(\bar{t}, t) \varepsilon_{\mathbf{q}}^{-1, <}(\bar{t}, t) - G_{\mathbf{k}+\mathbf{q}, \alpha}^{\lesseqgtr}(t, \bar{t}) G_{\mathbf{k}, \alpha}^{\gtrless}(\bar{t}, t) \varepsilon_{\mathbf{q}}^{-1, >}(\bar{t}, t) \right]. \end{aligned} \quad (3.9)$$

A direct solution of this equation is rather difficult, since on the r.h.s. the (traced) inverse dielectric function appears which couples different components of $\varepsilon_{\mathbf{k}\mathbf{q}\alpha}^{-1, \gtrless}$. We differentiate it with respect to t . This yields many terms that are all simple to compute:

$$\begin{aligned} i\hbar \frac{d}{dt} \varepsilon_{\mathbf{k}\mathbf{q}\alpha}^{-1, \gtrless}(t, t) &= \pm i\hbar w_{\mathbf{q}} \left[\left(\frac{d}{dt} G_{\mathbf{k}+\mathbf{q}, \alpha}^{\gtrless}(t, t) \right) G_{\mathbf{k}, \alpha}^{\lesseqgtr}(t, t) + G_{\mathbf{k}+\mathbf{q}, \alpha}^{\gtrless}(t, t) \left(\frac{d}{dt} G_{\mathbf{k}, \alpha}^{\lesseqgtr}(t, t) \right) \right] \\ &\pm (i\hbar)^2 w_{\mathbf{q}} G_{\mathbf{k}+\mathbf{q}, \alpha}^{\gtrless}(t, t) G_{\mathbf{k}, \alpha}^{\lesseqgtr}(t, t) \varepsilon_{\mathbf{q}}^{-1, <}(t, t) - (>\leftrightarrow<) \\ &\pm i\hbar w_{\mathbf{q}} \left(h_{\mathbf{k}+\mathbf{q}, \alpha}^{\text{HF}}(t) - h_{\mathbf{k}, \alpha}^{\text{HF}}(t) \right) \int_{t_0}^t d\bar{t} \left[G_{\mathbf{k}+\mathbf{q}, \alpha}^{\gtrless}(t, \bar{t}) G_{\mathbf{k}, \alpha}^{\lesseqgtr}(\bar{t}, t) \varepsilon_{\mathbf{q}}^{-1, <}(\bar{t}, t) - (>\leftrightarrow<) \right] \\ &\pm i\hbar w_{\mathbf{q}} \int_{t_0}^t d\bar{t} G_{\mathbf{k}+\mathbf{q}, \alpha}^{\gtrless}(t, \bar{t}) G_{\mathbf{k}, \alpha}^{\lesseqgtr}(\bar{t}, t) \left[i\hbar \frac{\partial}{\partial t} \varepsilon_{\mathbf{q}}^{-1, <}(t, \bar{t}) \right]^* - (>\leftrightarrow<). \end{aligned} \quad (3.10)$$

Eqs. (3.8) and (3.10) are sufficient to propagate ε^{-1} or rather the screened interaction W in time. Memory integrals only appear in the time-diagonal propagation, which leads to a CPU scaling of $\mathcal{O}(N_t^2)$ with the time step number N_t , which lies inbetween $\mathcal{O}(N_t^3)$ for the standard method and $\mathcal{O}(N_t)$ in the G1–G2 scheme.

3.2. Uniform plasmas

Plasmas of various dimensions and symmetries exist in different fields of physics. 1D plasmas, i.e. plasmas with negligible radial extent, are quite exotic. These so-called quantum wires can be generated by combining different types of semiconductors and thereby producing well. Also, the thin filament produced via magnetic confinement by the Z machine [7] can be regarded 1-dimensional. An application of the G1–G2 scheme to dense 1D plasmas has been studied by F. Borges-Fajardo et al [78].

2D plasmas, in comparison, are a lot more common. Similarly to quantum wires they can be generated using different semiconductor layers. However, most applications include Honeycomb lattices of some kind: Since the discovery of graphene monolayers [79], extensive research went into the question how to adjust its properties, which led to the discussion of Graphene nanoribbons (GNRs). GNRs have been a hot research topic in the past decade, as they became widely available experimentally [80, 81]. Computationally, GNRs have also been treated using the Hubbard model and extensions with a focus on strong correlations using NEGF, cf.

Refs. [30, 31, 82]. Today the focus has shifted again towards macroscopic 2D systems, such as graphene monolayers but especially towards transition metal dichalcogenides (TMDCs)[83, 84] and (twisted) bilayers of these [85, 86]. These layers have the structure of a honeycomb lattice, which are discussed in Sect. B.2. The description of such systems using the Hubbard model is better done in momentum representation, as it reduces the complexity of the equations that arise, if the system is uniform. An introduction into the Hubbard systems and its application to uniform lattice systems is given in Appendix B.

The usual gaseous plasmas are the most obvious example of a 3D plasma. These span many magnitudes of densities and temperatures, from the interstellar space to warm dense matter. Bulk semiconductors contain the so-called electron-hole plasma. Without external fields many system quickly become isotropic. If the system is perturbed in a preferred direction, e.g. by an external particle beam or external linearly polarized laser field (\mathbf{B} part neglected), it assumes cylindrical symmetry, making this symmetry assumption sufficient for a lot of interesting physics. The fully anisotropic also often appears, but of course is the most expensive.

Symmetries usually allow a simplification of the equations. Different methods profit to a different degree. To what extent this happens, and which method is preferred for which system, is the topic of this section.

3.2.1. Scaling of SOA, GW in different dimensions, symmetries, reformulations

In this subsection, the CPU and RAM scalings for the SOA and GWA are discussed.

Symmetries in 1D, 2D and 3D

There are many possible symmetries in \mathbf{k} space that could be considered. However, most of them have identical scaling orders. So in the following only 1D anisotropic systems, 2D isotropic and anisotropic systems, and 3D isotropic and cylinder symmetric systems, and 3D systems without \mathbf{k} space symmetry will be discussed. Systems with other symmetries, such as inversion symmetry or mirror symmetry have the scaling orders of the anisotropic systems, but lower coefficients. In that sense the choice of symmetries is representative for all possible symmetries.

If the system is invariant under a symmetry operation S , and we have a quantity f dependent on an n -tuple of \mathbf{k} space vectors $(\mathbf{k}_1, \dots, \mathbf{k}_n)$, we can conclude that

$$f(S\mathbf{k}_1, \dots, S\mathbf{k}_n) = f(\mathbf{k}_1, \dots, \mathbf{k}_n). \quad (3.11)$$

This will be used, e.g. for $\mathcal{G}_{\mathbf{k}\mathbf{p}\mathbf{q}}$, to find a lower dimensional tuple \mathbf{k} space and by doing so reducing the CPU and RAM demand of such calculations by some orders.

Isotropic systems are invariant under any rotation (and any mirror). By using a rotation S_1 , the tuple of \mathbf{k} vectors can be represented by a symmetry equivalent tuple, where $\mathbf{k}_1 \parallel \mathbf{e}_i$ and \mathbf{e}_i is an arbitrary direction vector (in 3D we choose w.l.o.g. $\mathbf{e}_i = \mathbf{e}_z$). This already reduces the effective dimension for the tuple by 2 in 3D and by 1 in 2D. In 3D, a further dimension reduction

is possible: Suppose $\mathbf{k}_1 \parallel \mathbf{e}_z$, then we can apply a rotation S_2 around the z axis in such a way, that $S_2 \mathbf{k}_2 \in \{\mathbf{k} \in \mathbb{R}^3 \mid k_x \geq 0, k_y = 0\}$. S_2 does not change \mathbf{k}_1 , since it is on the z axis. For \mathbf{k}_3 another symmetry can reduce the size of the tuple \mathbf{k} space: the mirror symmetry, where the $x - z$ plane is the mirror, can be used to represent the tuple by a symmetry equivalent tuple where $(\mathbf{k}_3)_y \geq 0$, thus halving the tuple \mathbf{k} space. This is only a minor reduction, since the dimension stays the same. The last step in a similar form can be applied to 2D and \mathbf{k}_2 .

Cylinder symmetric systems are invariant under any rotations around the z axis and any mirror that include the z axis. Consider again a tuple $(\mathbf{k}_1, \dots, \mathbf{k}_n)$, we can in the first step only rotate in such a way that \mathbf{k} lies in the $x - z$ plane, reducing the effective dimension of the tuple \mathbf{k} space by 1. Using a mirror, we find a symmetry equivalent tuple where $(\mathbf{k}_2)_y \geq 0$.

Systems **without symmetry** do not allow such dimensional reductions.

It becomes apparent, that symmetries are especially useful, if the quantities depend only on very few \mathbf{k} vectors. For example, in an isotropic system we have $G_{\mathbf{k}\alpha}^{\geq}$, which is effectively described by a 1D quantity, instead of 3D or 2D. $\varepsilon_{\mathbf{k}q\alpha}^{-1, \geq}$ and $\mathcal{G}_{\mathbf{k}p\mathbf{q}}^{\alpha\beta}$ have more dependencies, and their dimensions cannot be reduced as efficiently.

Computational scalings

In this subsection the computational scalings are discussed. The \mathbf{k} point grid is assumed to be cartesian, but the implications from the scalings listed below also apply to other coordinate systems. Let N_x be the number of \mathbf{k} space grid points in one dimension, and N_t be the number of time steps for the whole simulation. The scalings for the G1–G2 scheme and the intermediate scheme follow quite straightforwardly from the formulas. The scalings for the standard GKBA follow from numerical tweaks that are discussed in chapter 4.

Table 3.1 shows the CPU and RAM scalings occurring in the GKBA and the G1–G2 method for the SOA. The GKBA method has an additional factor N_t in all scalings, compared to the G1–G2 scheme, but scales a lot better with N_x . This is due to the fact that all quantities necessary for SOA GKBA simulations are only dependent on one momentum, which excels at using symmetries.

		CPU		RAM	
		GKBA	G1–G2	GKBA	G1–G2
1D		$\mathcal{O}(N_t^2 N_x \ln N_x)$	$\mathcal{O}(N_t N_x^3)$	$\mathcal{O}(N_t N_x)$	$\mathcal{O}(N_x^3)$
2D	isotropic	$\mathcal{O}(N_t^2 N_x^2)$	$\mathcal{O}(N_t N_x^5)$	$\mathcal{O}(N_t N_x)$	$\mathcal{O}(N_x^5)$
	anisotropic	$\mathcal{O}(N_t^2 N_x^2 \ln(N_x))$	$\mathcal{O}(N_t N_x^6)$	$\mathcal{O}(N_t N_x^2)$	$\mathcal{O}(N_x^6)$
3D	isotropic	$\mathcal{O}(N_t^2 N_x \ln N_x)$	$\mathcal{O}(N_t N_x^6)$	$\mathcal{O}(N_t N_x)$	$\mathcal{O}(N_x^6)$
	cylindric	$\mathcal{O}(N_t^2 N_x^3)$	$\mathcal{O}(N_t N_x^8)$	$\mathcal{O}(N_t N_x^2)$	$\mathcal{O}(N_x^8)$
	anisotropic	$\mathcal{O}(N_t^2 N_x^3 \ln N_x)$	$\mathcal{O}(N_t N_x^9)$	$\mathcal{O}(N_t N_x^3)$	$\mathcal{O}(N_x^9)$

Table 3.1.: Numerical scalings for direct SOA in different dimensions and symmetries. The GKBA CPU scalings are due to symmetry adapted convolution techniques, as discussed in Chap. 4.

		CPU			RAM		
		GKBA	$\varepsilon_{\mathbf{kq}\alpha}^{-1, \geq}$	G1-G2	GKBA	$\varepsilon_{\mathbf{kq}\alpha}^{-1, \geq}$	G1-G2
1D		$\mathcal{O}(N_t^3 N_x \ln N_x)$	$\mathcal{O}(N_t^2 N_x^2)$	$\mathcal{O}(N_t N_x^3)$	$\mathcal{O}(N_t^2 N_x)$	$\mathcal{O}(N_t N_x^2)$	$\mathcal{O}(N_x^3)$
2D	isotropic	$\mathcal{O}(N_t^3 N_x^2)$	$\mathcal{O}(N_t^2 N_x^3)$	$\mathcal{O}(N_t N_x^5)$	$\mathcal{O}(N_t^2 N_x)$	$\mathcal{O}(N_t N_x^3)$	$\mathcal{O}(N_x^5)$
	anisotropic	$\mathcal{O}(N_t^3 N_x^2 \ln(N_x))$	$\mathcal{O}(N_t^2 N_x^4)$	$\mathcal{O}(N_t N_x^6)$	$\mathcal{O}(N_t^2 N_x^2)$	$\mathcal{O}(N_t N_x^4)$	$\mathcal{O}(N_x^6)$
3D	isotropic	$\mathcal{O}(N_t^3 N_x \ln N_x)$	$\mathcal{O}(N_t^2 N_x^3)$	$\mathcal{O}(N_t N_x^6)$	$\mathcal{O}(N_t^2 N_x)$	$\mathcal{O}(N_t N_x^3)$	$\mathcal{O}(N_x^6)$
	cylindric	$\mathcal{O}(N_t^3 N_x^3)$	$\mathcal{O}(N_t^2 N_x^5)$	$\mathcal{O}(N_t N_x^8)$	$\mathcal{O}(N_t^2 N_x^2)$	$\mathcal{O}(N_t N_x^5)$	$\mathcal{O}(N_x^8)$
	anisotropic	$\mathcal{O}(N_t^3 N_x^3 \ln N_x)$	$\mathcal{O}(N_t^2 N_x^6)$	$\mathcal{O}(N_t N_x^9)$	$\mathcal{O}(N_t^2 N_x^3)$	$\mathcal{O}(N_t N_x^6)$	$\mathcal{O}(N_x^9)$

Table 3.2.: Numerical scalings for *GWA* in different dimensions and symmetries. The GKBA CPU scalings are due to symmetry adapted convolution techniques, as discussed in Chap. 4.

Table 3.2 also shows CPU and RAM scalings for the *GW* approximation. Here we have three methods to compare: GKBA, the method discussed above using $\varepsilon_{\mathbf{kq}\alpha}^{-1, \geq}$, and the G1–G2 scheme.

It depends on the ratio between N_x and N_t which method should be preferred. For very long calculations, the G1–G2 scheme is obviously the method of choice since the RAM usage does not depend on N_t . However, the high N_x scaling in 3D makes any G1–G2 calculations computationally extremely demanding and strongly limits its applicability. In fact, aliasing effects will always occur in sufficiently long simulations, and they can be postponed by increasing N_x (cf. also Sect. 3.3 about aliasing). This means: in order to compute long G1–G2 simulations reliably, a large N_x is necessary.

In the next subsection a 2D isotropic electron relaxation using the G1–G2 scheme and the *GW* approximation is presented to give an impression about the size of N_x and CPU time necessary.

3.2.2. Test simulation of G1–G2 in 2D, isotropic

Figure 3.1 shows the relaxation of an isotropic 2D electron gas¹ starting from an uncorrelated and spin-symmetric nonequilibrium distribution. Since *GW* does not explicit distinguish between spin $\uparrow\uparrow$ and $\uparrow\downarrow$ configurations, $\mathcal{G}_{\mathbf{k}\mathbf{p}\mathbf{q}}(t)$ (independent of spins) is sufficient to describe two-particle correlations. With $N_x = 64$ on a half axis, i.e. on the momentum range $[0, p_{\text{co}}]$, where the cutoff momentum is given by $p_{\text{co}} = 20 \hbar a_B^{-1}$, one fully symmetry reduced \mathcal{G} data structure includes

$$64 \times [(2 \times 64 - 1) \times 64] \times [(2 \times 64 - 1) \times (2 \times 64 - 1)] = 8,390,176,768 \quad (3.12)$$

complex numbers. Assuming complex numbers based on two double precision numbers which occupy 8 Byte each, we compute a memory demand of

$$8,390,176,768 \times 16 \text{ Byte} = 134,242,828,288 \text{ Byte} \quad (3.13)$$

¹2D slab model inside harmonic trap, as described in Ref. [69], Appendix A. Slab thickness is $0.2 a_B$. RK4 time stepper, time step length of 0.024188 as.

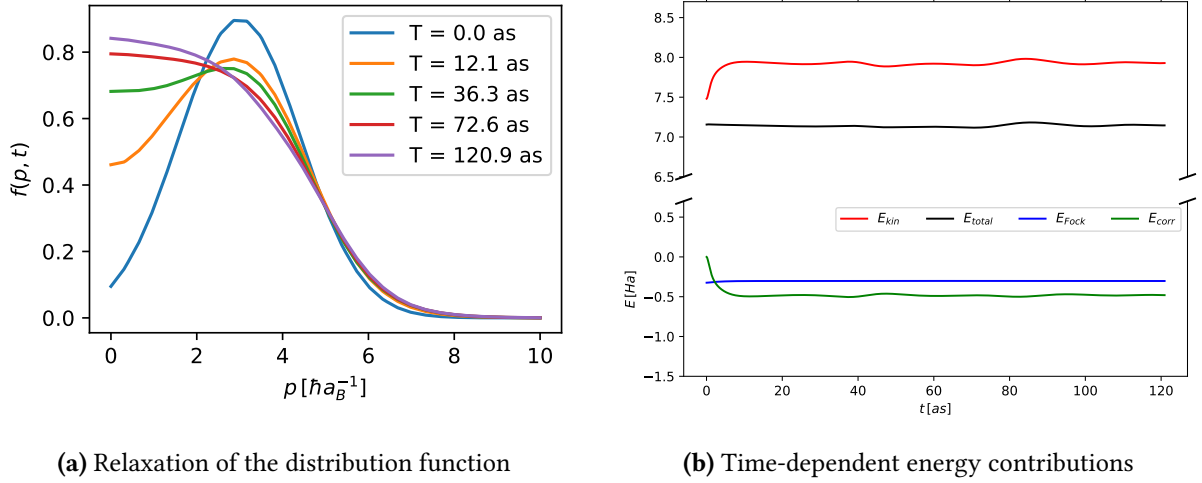


Figure 3.1.: 2D isotropic relaxation starting from an uncorrelated initial nonequilibrium distribution using *GW* selfenergy. The cutoff was chosen at $p_{co} = 20 \hbar a_B^{-1}$ with 64 basis vectors on the interval $[0, p_{co}]$.

for each instance of \mathcal{G} . Depending on the order of the propagation scheme, a different number of instances is needed: The Euler scheme uses two (current state and a derivative), Heun’s method can be implemented using three (current state and two derivatives) or the classical 4th-order Runge–Kutta (RK4) scheme can be implemented using four instances. The latter corresponds to a RAM demand of roughly 0.5 TB which are recalculated and rewritten multiple times in each time step. \mathcal{G} in a similar 3D isotropic or 2D anisotropic with the same number of k-points per coordinate axis would require $\approx 64 \times 0.5 \text{ TB} = 32 \text{ TB}$ which is not feasible on today’s computers. The G1–G2 scheme has thus not been used for 3D calculations in this thesis.

Figure 3.1b demonstrates that the energy conservation is weakly violated with these parameters, especially towards longer simulation times. Shown are 5000 time steps with a length of 0.001 *a.u.* using a semi-analytical propagation scheme. The calculation took 36 hours on a supercomputer using 128 cores on 8 nodes. The propagation scheme is described in Appendix C. It has been used instead of the classical Runge–Kutta scheme in order to reduce computational cost under the assumption that two particle correlations evolve on a shorter time scale than the one-particle distribution. Using an RK4 stepper, the energy conservation is better but the calculation is slower and the memory demand much higher.

In order to get better results we either have to use more expensive stepping methods, better convergence parameters, or even both. Both measures drastically increase the demand for RAM and computational power.

3.3. Dephasing and aliasing

Aliasing is a fundamental problem that arises in the discretization of some continuous function or signal f . The Nyquist-Shannon sampling theorem states that a angular frequency ω in the

spectrum of f that is sampled with a density of Δt can only be correctly identified if at least two sampling points per period exist, i.e.

$$\frac{2\pi}{\omega \cdot \Delta t} \geq 2. \quad (3.14)$$

If this condition is not fulfilled, Fourier transforms will wrongly identify a lower frequency, an 'alias', hence the name aliasing.

Uniform systems described in momentum representation (or in spatial representation, too) depend on continuous variables. In this section it is demonstrated how aliasing appears in GKBA-type algorithms, and how it appears in G1–G2 type algorithms. It is shown that longer calculations require a finer \mathbf{k} point grid, and thus revised scaling tables are presented in the final subsection.

3.3.1. Aliasing in GKBA-type algorithms

The time off-diagonal elements in GKBA can be written as

$$G_{\mathbf{k}\alpha}^{\geq}(t \geq t') = G_{\mathbf{k}\alpha}^{\geq}(t', t') \exp\left(\frac{1}{i\hbar} \int_{t'}^t d\bar{t} h_{\mathbf{k}\alpha}^{\text{HF}}(\bar{t})\right). \quad (3.15)$$

For fixed t, t' , consider $G_{\mathbf{k}\alpha}^{\geq}(t \geq t')$ as a signal in the variable \mathbf{k} . $G_{\mathbf{k}\alpha}^{\geq}(t', t')$ is purely imaginary, but the exponential function with imaginary argument evokes oscillations that are in general faster (faster in regard to \mathbf{k} variation) with larger time difference $|t - t'|$. Since in practice only a finite number of \mathbf{k} points can be considered, these oscillations can only be captured with finite sampling, i.e. with finite spacing Δk .

For some more detailed analysis, free GKBA is considered instead. The gradient of $G_{\mathbf{k}\alpha}^{\geq}(t \geq t')$ can be computed

$$\nabla G_{\mathbf{k}\alpha}^{\geq}(t \geq t') = \left[\nabla G_{\mathbf{k}\alpha}^{\geq}(t', t') + \frac{1}{i\hbar} G_{\mathbf{k}\alpha}^{\geq}(t', t') \frac{\mathbf{k}}{m_\alpha} (t - t') \right] \exp\left(\frac{1}{i\hbar} \frac{k^2}{2m} (t - t')\right). \quad (3.16)$$

The absolute value of the first term is independent of t , and is neglected in the following, since $t - t'$ is assumed to be large. We find

$$\nabla G_{\mathbf{k}\alpha}^{\geq}(t \geq t') = \frac{1}{i\hbar} \frac{\mathbf{k}}{m_\alpha} (t - t') G_{\mathbf{k}\alpha}^{\geq}(t \geq t'). \quad (3.17)$$

$G_{\mathbf{k}\alpha}^{\geq}(t \geq t')$ thus oscillates locally around \mathbf{k} with a 'frequency' of $\frac{\mathbf{k}(t-t')}{\hbar m_\alpha}$ with respect to variation of \mathbf{k} . We write down the Nyquist condition,

$$\left| \frac{2\pi}{\Delta k \cdot \frac{k(t-t')}{\hbar m_\alpha}} \right| = \frac{2\pi \hbar m_\alpha}{\Delta k \cdot |k|(t-t')} \geq 2, \quad (3.18)$$

which shows that for sufficiently large $t - t'$, undersampling appears in all \mathbf{k} points. Since the selfenergies used practically in this thesis make use of the convolution theorem and Fourier transforms, it is now plausible that aliasing appears at some point of time. Aliasing however is not limited to convolution type calculations, but also other integrations easily get perturbed by too coarse sampling.

The condition (3.18) can be used to find a rough estimate about the time scale, where aliasing has not occurred (too much) yet: Choose a characteristic momentum k . Near equilibrium this could be the Fermi momentum or thermal momentum. Then we find the estimate

$$t - t_0 \lesssim \frac{\pi \hbar m_\alpha}{\Delta k \cdot |k|}. \quad (3.19)$$

Since often a cutoff momentum k_{\max} is fixed, and the number of \mathbf{k} points per dimension, N_x , can be varied, this can be formulated as

$$t - t_0 \lesssim \frac{\pi \hbar m_\alpha}{2k_{\max} \cdot |k|} N_x. \quad (3.20)$$

In conclusion, in order to simulate a long physical time using some uncorrelated GKBA, N_x must be chosen sufficiently large, making the long-time scaling of this method effectively even worse.

It should be noted that in two-time calculations this problem is drastically reduced, as the correlation selfenergy includes an imaginary part that dampens the off-diagonal NEGF. Correlated GKBA approaches are expected to express similar behaviour, but this remains to be checked.

3.3.2. Aliasing in G1–G2 type algorithms

The G1–G2 scheme elegantly avoids two-time dependent Green functions that express oscillatory behaviour. Being equivalent to the GKBA, similar oscillations appear in another location, namely in \mathcal{G} . In this section the SOA case is discussed. Other selfenergy approximations also contain the SOA terms, and the additional terms further obfuscate the following analysis. It remains an open question if higher selfenergy terms reduce aliasing.

The \mathcal{G} equation in SOA with free GKBA is given by

$$i\hbar \frac{d}{dt} \mathcal{G}_{\mathbf{k}\mathbf{p}\mathbf{q}}^{\alpha\beta}(t) - \Delta E_{\mathbf{k}\mathbf{p}\mathbf{q}}^{\alpha\beta} \cdot \mathcal{G}_{\mathbf{k}\mathbf{p}\mathbf{q}}^{\alpha\beta}(t) = \Psi_{\mathbf{k}\mathbf{p}\mathbf{q}}^{\alpha\beta}(t). \quad (3.21)$$

The dynamics of different index combinations are coupled only indirectly through their influence on the single-particle GF G . In order to further analyze this highly nontrivial equation it is assumed that $G^{\lessgtr}(t)$ has negligible time-dependence. The resulting differential equation has a stationary solution that has been discussed in Sect. 2.3.8, and it will be called $\mathcal{G}_{\mathbf{k}\mathbf{p}\mathbf{q}}^{\alpha\beta,\text{stat}}$ here.

Suppose initial values $\mathcal{G}_{\mathbf{k}\mathbf{p}\mathbf{q}}^{\alpha\beta}(t_0)$ are given, then the solution of the differential equation is given by

$$\mathcal{G}_{\mathbf{k}\mathbf{p}\mathbf{q}}^{\alpha\beta}(t) \approx \mathcal{G}_{\mathbf{k}\mathbf{p}\mathbf{q}}^{\alpha\beta,\text{stat}} + \left[\mathcal{G}_{\mathbf{k}\mathbf{p}\mathbf{q}}^{\alpha\beta}(t_0) - \mathcal{G}_{\mathbf{k}\mathbf{p}\mathbf{q}}^{\alpha\beta,\text{stat}} \right] \exp\left(\frac{1}{i\hbar} \Delta E_{\mathbf{k}\mathbf{p}\mathbf{q}}^{\alpha\beta} \cdot [t - t_0]\right), \quad (3.22)$$

if $\Delta E_{\mathbf{k}\mathbf{p}\mathbf{q}}^{\alpha\beta} \neq 0$. Again, oscillations with respect to \mathbf{k} , \mathbf{p} or \mathbf{q} variation appear, whose phase factor increases with $t - t_0$, i.e. in long calculations.

Now we again consider a gradient, with respect to \mathbf{k} (or \mathbf{p}). Since

$$\Delta E_{\mathbf{k}\mathbf{p}\mathbf{q}}^{\alpha\beta} = \frac{1}{2m_\alpha} [(\mathbf{k} - \mathbf{q})^2 - \mathbf{k}^2] + \frac{1}{2m_\beta} [(\mathbf{p} + \mathbf{q})^2 - \mathbf{p}^2] = \frac{1}{m_\beta} \mathbf{p} \cdot \mathbf{q} - \frac{1}{m_\alpha} \mathbf{k} \cdot \mathbf{q} + 2 \left[\frac{1}{2m_\alpha} + \frac{1}{2m_\beta} \right] q^2, \quad (3.23)$$

the gradient of the energy difference is $\nabla_{\mathbf{k}} \Delta E_{\mathbf{k}\mathbf{p}\mathbf{q}}^{\alpha\beta} = -\mathbf{q}/m_\alpha$. Thus the total gradient becomes

$$\begin{aligned} \nabla_{\mathbf{k}} \mathcal{G}_{\mathbf{k}\mathbf{p}\mathbf{q}}^{\alpha\beta}(t) &= \nabla_{\mathbf{k}} \mathcal{G}_{\mathbf{k}\mathbf{p}\mathbf{q}}^{\alpha\beta, \text{stat}} + \exp\left(\frac{1}{i\hbar} \Delta E_{\mathbf{k}\mathbf{p}\mathbf{q}}^{\alpha\beta} \cdot [t - t_0]\right) \nabla_{\mathbf{k}} \left[\mathcal{G}_{\mathbf{k}\mathbf{p}\mathbf{q}}^{\alpha\beta}(t_0) - \mathcal{G}_{\mathbf{k}\mathbf{p}\mathbf{q}}^{\alpha\beta, \text{stat}} \right] \\ &\quad - \mathbf{q} \frac{1}{i\hbar m_\alpha} [t - t_0] \left[\mathcal{G}_{\mathbf{k}\mathbf{p}\mathbf{q}}^{\alpha\beta}(t_0) - \mathcal{G}_{\mathbf{k}\mathbf{p}\mathbf{q}}^{\alpha\beta, \text{stat}} \right] \exp\left(\frac{1}{i\hbar} \Delta E_{\mathbf{k}\mathbf{p}\mathbf{q}}^{\alpha\beta} \cdot [t - t_0]\right). \end{aligned} \quad (3.24)$$

Neglecting the first two terms, since for large $[t - t_0]$ the third term dominates, we find

$$\nabla_{\mathbf{k}} \mathcal{G}_{\mathbf{k}\mathbf{p}\mathbf{q}}^{\alpha\beta}(t) \approx \frac{-\mathbf{q}}{i\hbar m_\alpha} [t - t_0] \left(\mathcal{G}_{\mathbf{k}\mathbf{p}\mathbf{q}}^{\alpha\beta}(t) - \mathcal{G}_{\mathbf{k}\mathbf{p}\mathbf{q}}^{\alpha\beta, \text{stat}} \right). \quad (3.25)$$

This approximate differential equation has a solution that oscillates with a frequency of $q[t - t_0]/\hbar m_\alpha$. This is a similar frequency to that in the GKBA case, where k instead of q appeared.

In the collision integral,

$$I_{\mathbf{p}\beta} = \pm i\hbar \sum_{\mathbf{k}\mathbf{q}} \sum_{\alpha} v_{|\mathbf{q}|}^{\alpha\beta}(t) \mathcal{G}_{\mathbf{k}\mathbf{p}\mathbf{q}}^{\alpha\beta}(t) \longrightarrow \pm i\hbar \sum_{\alpha} \int \frac{d\mathbf{k}}{(2\pi\hbar)^d} \frac{d\mathbf{q}}{(2\pi\hbar)^d} v_{|\mathbf{q}|}^{\alpha\beta}(t) \mathcal{G}_{\mathbf{k}\mathbf{p}\mathbf{q}}^{\alpha\beta}(t), \quad (3.26)$$

this fast oscillating function \mathcal{G} appears under the momentum integrals. In order to accurately compute these integrals from a discretized \mathcal{G} , the sampling theorem has to be fulfilled: Simple integrals are the 0 component of the Fourier spectrum. If the signal is undersampled, this 0 component gets changed by aliases, which corresponds to integral errors. We get the estimates

$$t - t_0 \lesssim \frac{\pi\hbar m_\alpha}{2k_{\max} \cdot |q|} N_x, \quad (3.27)$$

$$t - t_0 \lesssim \frac{\pi\hbar}{2k_{\max} \cdot (|p|/m_\beta + |k|/m_\alpha)} N_x, \quad (3.28)$$

where the second estimate stems from a similar analysis with regard to the \mathbf{q} gradient. Small q are more relevant than large q , since $w_{\mathbf{q}}$ becomes large only at small q . Thus the second estimate, with the characteristic p and k , is smaller and in general the relevant estimate.

3.3.3. A revision of the scalings for long simulation durations

In the previous two subsections it was established that a simulation with a long duration requires a sufficiently fine \mathbf{k} point grid. It was found that the maximum simulation time is proportional to N_x , the number of \mathbf{k} space vectors along one axis. For long simulation times we thus have $N_x \sim N_t$ and all N_x can be converted into N_t in the tables from subsection 3.2.1, yielding the two tables below.

		CPU		RAM	
		GKBA	G1-G2	GKBA	G1-G2
1D		$\mathcal{O}(N_t^3 \ln N_t)$	$\mathcal{O}(N_t^4)$	$\mathcal{O}(N_t^2)$	$\mathcal{O}(N_t^3)$
2D	isotropic	$\mathcal{O}(N_t^4)$	$\mathcal{O}(N_t^6)$	$\mathcal{O}(N_t^2)$	$\mathcal{O}(N_t^5)$
	anisotropic	$\mathcal{O}(N_t^4 \ln(N_t))$	$\mathcal{O}(N_t^7)$	$\mathcal{O}(N_t^3)$	$\mathcal{O}(N_t^6)$
3D	isotropic	$\mathcal{O}(N_t^3 \ln N_t)$	$\mathcal{O}(N_t^7)$	$\mathcal{O}(N_t^2)$	$\mathcal{O}(N_t^6)$
	cylindric	$\mathcal{O}(N_t^5)$	$\mathcal{O}(N_t^9)$	$\mathcal{O}(N_t^3)$	$\mathcal{O}(N_t^8)$
	anisotropic	$\mathcal{O}(N_t^5 \ln N_t)$	$\mathcal{O}(N_t^{10})$	$\mathcal{O}(N_t^4)$	$\mathcal{O}(N_t^9)$

Table 3.3.: Effective SOA scalings for large N_t with consideration of aliasing, $N_x \sim N_t$.

		CPU			RAM		
		GKBA	$\varepsilon_{\mathbf{kq}\alpha}^{-1, \geq}$	G1-G2	GKBA	$\varepsilon_{\mathbf{kq}\alpha}^{-1, \geq}$	G1-G2
1D		$\mathcal{O}(N_t^4 \ln N_t)$	$\mathcal{O}(N_t^4)$	$\mathcal{O}(N_t^4)$	$\mathcal{O}(N_t^3)$	$\mathcal{O}(N_t^3)$	$\mathcal{O}(N_t^3)$
2D	isotropic	$\mathcal{O}(N_t^5)$	$\mathcal{O}(N_t^5)$	$\mathcal{O}(N_t^6)$	$\mathcal{O}(N_t^3)$	$\mathcal{O}(N_t^4)$	$\mathcal{O}(N_t^5)$
	anisotropic	$\mathcal{O}(N_t^5 \ln(N_t))$	$\mathcal{O}(N_t^6)$	$\mathcal{O}(N_t^7)$	$\mathcal{O}(N_t^4)$	$\mathcal{O}(N_t^5)$	$\mathcal{O}(N_t^6)$
3D	isotropic	$\mathcal{O}(N_t^4 \ln N_t)$	$\mathcal{O}(N_t^5)$	$\mathcal{O}(N_t^7)$	$\mathcal{O}(N_t^3)$	$\mathcal{O}(N_t^4)$	$\mathcal{O}(N_t^6)$
	cylindric	$\mathcal{O}(N_t^6)$	$\mathcal{O}(N_t^7)$	$\mathcal{O}(N_t^9)$	$\mathcal{O}(N_t^4)$	$\mathcal{O}(N_t^6)$	$\mathcal{O}(N_t^8)$
	anisotropic	$\mathcal{O}(N_t^6 \ln N_t)$	$\mathcal{O}(N_t^8)$	$\mathcal{O}(N_t^{10})$	$\mathcal{O}(N_t^5)$	$\mathcal{O}(N_t^7)$	$\mathcal{O}(N_t^9)$

Table 3.4.: Effective GWA scalings for large N_t with consideration of aliasing, $N_x \sim N_t$.

4. Numerical implementation (cylinder symmetric plasma)

Abstract: This chapter covers numerical considerations regarding convolution-based self-energy approximations. First, 3D Fourier transforms are rewritten as a combination of a 1D Fourier transform and a Hankel transform, which has been implemented in the Gnu Scientific Library (GSL). After an introduction the necessary discretizations in time and momentum space, the algorithms for SOA and GWA calculations are explained in detail. For didactic reasons, first the SOA algorithm is explained. The GW algorithm agrees in a few parts and is then introduced as a more complex modification of the SOA algorithm.

4.1. Fourier transformation in cylindric symmetry

In the direct SOA term and in the GW approximation only convolution type momentum integrals appear, cf. Sects. 4.4 and 4.5. This type of momentum integrals are favorable, since their numerical cost can be drastically reduced using the convolution theorem: Let $A(\mathbf{k})$ and $B(\mathbf{k})$ be functions in momentum space. Then the convolution $[A * B](\mathbf{k})$ is given by

$$(A * B)_{\mathbf{k}} = \int d\mathbf{q} A(\mathbf{k} - \mathbf{q}) B(\mathbf{q}). \quad (4.1)$$

The Fourier transform of the convolution is given by

$$\mathcal{F}[A * B](\mathbf{r}) = \mathcal{F}[A](\mathbf{r}) \cdot \mathcal{F}[B](\mathbf{r}), \quad (4.2)$$

where the conventional prefactor 1 for the forward transform and $(2\pi)^{-d}$ for the backward transform was used. The convolution can thus be computed as

$$[A * B](\mathbf{k}) = \mathcal{F}^{-1}[\mathcal{F}[A] \cdot \mathcal{F}[B]](\mathbf{k}). \quad (4.3)$$

The numerical advantage of this formulation is that for functions A, B on a discretized grid a very efficient algorithm Fourier transform algorithm exists, the *Fast Fourier transform* (FFT) algorithm [87]. Fortunately, today many libraries offering optimized FFT algorithms exist, e.g. the FFTW library [88] and variants optimized for Intel[®] CPUs in the Intel[®] *Math Kernel Library*[89] (MKL) or cuFFT[90], a library optimized for use on NVIDIA GPUs. In fact, these three libraries have highly compatible interfaces which allows the optimized portation of code to new machines.

For a d dimensional grid of N grid points per dimension, the FFT has a complexity of $\mathcal{O}(N^d \log N)$. However, if the functions to be transformed fulfill symmetries, the grid dimension can be reduced (cf. Sect. 3.2.1), and sometimes, e.g. in cylindric symmetry, algorithms can be derived that are even more efficient than the d -dimensional FFT.

4.1.1. Fourier-Hankel transform

Let $f(\mathbf{k}) = f(k_z, k_\rho)$ be a cylinder symmetric function. The Fourier transform then is cylinder symmetric, too, and we can write

$$\begin{aligned} \mathcal{F}_{xyz}[f](r_z, r_\rho) &= \int_{-\infty}^{\infty} dk_z \int_0^{\infty} dk_\rho \int_0^{2\pi} dk_\varphi k_\rho f(k_z, k_\rho) \exp(-i[k_z r_z + k_\rho r_\rho \cos k_\varphi]) \\ &= \int_{-\infty}^{\infty} dk_z \exp(-ik_z r_z) \int_0^{\infty} dk_\rho k_\rho f(k_z, k_\rho) \underbrace{\int_0^{2\pi} dk_\varphi \exp(-ik_\rho r_\rho \cos k_\varphi)}_{=2\pi J_0(k_\rho r_\rho)} \\ &= 2\pi \mathcal{F}_z [\mathcal{H}_\rho^0[f]](r_z, r_\rho) = 2\pi \mathcal{H}_\rho^0[\mathcal{F}_z[f]](r_z, r_\rho), \end{aligned} \quad (4.4)$$

where the Bessel function of first kind J_0 was identified as the angular integral. The remaining k_ρ integral is then identified as the zeroth order Hankel transform, whose general expression is

$$\mathcal{H}^\nu[f](r) = \int_0^{\infty} dk f(k) k J_\nu(kr). \quad (4.5)$$

The Fourier transform with respect to the z coordinate/momentum is efficiently treated with the FFT algorithm. For the Discrete Hankel transform (DHT) a lot of approaches exist with their own advantages and disadvantages. In particular, there are faster but less accurate [91, 92], and slower but more accurate methods. In the following section, a highly precise algorithm will be presented. As the applications show, CPU time is currently seldom the computational bottleneck, but RAM demand is, so the choice is well met.

4.1.2. Discrete Hankel transform, k-point grid

The DHT method used in this thesis for cylinder symmetric problems has been developed by H. Fisk Johnson [93] and D. Lemoine [94]. Its derivation is sketched here to give an impression about its strengths and weaknesses (what is exact, what is approximated, and how). Let $f : \mathbb{R}_+ \rightarrow \mathbb{C}$ be a Hankel transformable function, i.e.

$$F_\nu(R) = \int_0^{\infty} f(x) J_\nu(xR) x dx \quad (4.6)$$

exists for all $R \geq 0$, which is fulfilled if and only if

$$\int_0^{\infty} f(x) \sqrt{x} dx \quad (4.7)$$

converges absolutely and exists. The inverse transform is given by the same expression, but $x \leftrightarrow R$. An underlying assumption of the discrete method proposed by the authors above is that $f(t)$ for $t \geq T$ for some $T \in \mathbb{R}_+$. Choose an $N \in \mathbb{N}$ and let j_N be the N -th zero of $J_\nu(x)$. Using the variable $r = RT/j_n$, the transformations can be written as

$$F_\nu(rj_n/T) = T^2 \int_0^1 f(xT) J_\nu(xrj_n) x \, dx, \quad (4.8)$$

$$f(xT) = \frac{j_N^2}{T^2} \int_0^\infty F_\nu(rj_N/T) J_\nu(xrj_N) r \, dr. \quad (4.9)$$

$f(xT)$ is expanded in a series of Bessel functions,

$$f(xT) = \begin{cases} \sum_{m=1}^{\infty} \frac{2C_m}{J_{\nu+1}^2(j_m)} J_\nu(j_m x), & 0 \leq x \leq 1 \\ 0, & 1 < x < \infty \end{cases}, \quad (4.10)$$

$$C_m = \int_0^1 x f(xT) J_\nu(j_m x) \, dx, \quad (4.11)$$

where all terms $m \geq N$ are dropped, i.e. $C_m = 0$ is assumed. Using the property

$$F_\nu(j_m/T) = T^2 C_m, \quad (4.12)$$

Eq. (4.10) becomes

$$f(xT) = \begin{cases} \sum_{m=1}^{N-1} \frac{2F_\nu(j_m/T)}{J_{\nu+1}^2(j_m)T^2} J_\nu(j_m x), & 0 \leq x \leq 1 \\ 0 & 1 < x < \infty \end{cases}. \quad (4.13)$$

In particular for $x = j_i/j_N$, we find a discrete backward transform,

$$f(j_i T/j_N) = \frac{1}{T^2} \sum_{m=1}^{N-1} Y_\nu(m, i) F_\nu(j_m/T), \quad (4.14)$$

with the matrix $Y_\nu(m, i) = 2J_\nu(j_i j_m/j_N)/J_{\nu+1}^2(j_m)$. Using the orthogonality relation (ref. [93])

$$\frac{4}{J_{\nu+1}^2(j_m)j_N^2} \sum_{p=1}^{N-1} \frac{J_\nu(j_m j_p/j_N) J_\nu(j_i j_p/j_N)}{J_{\nu+1}^2(j_p)} = \delta_{m,i}, \quad \text{for } m, i < N, \quad (4.15)$$

the discrete forward transform can be found,

$$F_\nu(j_m/T) = \frac{T^2}{j_N^2} \sum_{i=1}^{N-1} Y_\nu(m, i) f(j_i T/j_N). \quad (4.16)$$

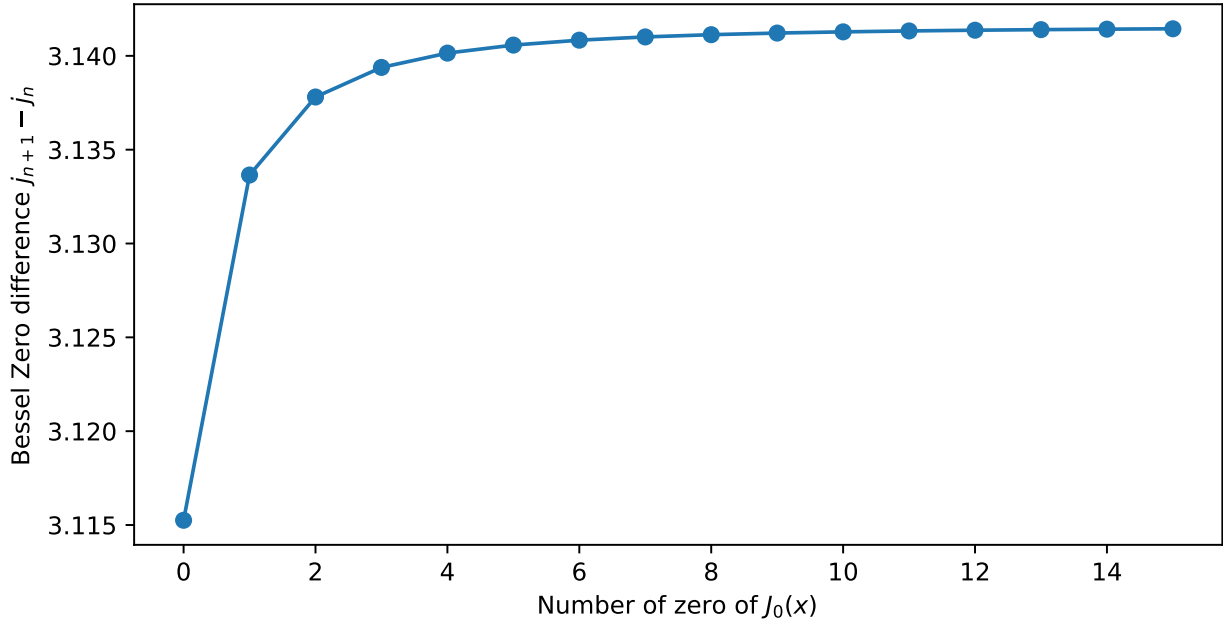


Figure 4.1.: Distance between neighboring zeros of $J_0(x)$

In conclusion: this discrete transformation is exact on the space of truncated Fourier-Bessel series, Eq. (4.10). Even if the transformed function is not of this type, its discrete values are implicitly interpolated using a Fourier-Bessel expansion, and the interpolant is then transformed exactly. This behavior is in fact analogous to that of discrete Fourier transforms. The orthogonality relation, Eq. (4.15), guarantees that in the discrete case a successive forward and backward transform always yield unity.

The expressions above dictate how the discretization has to be done, if one aims to use these equations: Let T be the 'cutoff', i.e. for $t \geq T$ the function to be transformed is 0, and we wish to use $N - 1$ grid points between 0 and T for $N > 2$, we have to choose

$$t_n = \frac{T j_n}{j_N}, \quad (4.17)$$

i.e. a non-equidistant grid. In the case $\nu = 0$ the first Bessel zero is not in $x = 0$. Figure 4.1 shows the first distances between neighboring Bessel zeros. The distance quickly converges towards π , and the deviations from an equidistant grid of spacing π start at less than 1% and become quickly even smaller.

4.1.3. A library for Discrete Hankel transforms

Luckily, the method from the subsection before is implemented in the *Gnu Scientific Library* (GSL) [95] and is declared in the header file `gsl_dht.h`. The library offers constructors of a DHT object, `gsl_dht *gsl_dht_new(size_t size, double nu, double xmax)`, an application method `int gsl_dht_apply(const gsl_dht *t, double *f_in, double *f_out)`, and some

utility to identify the sampling points, `double gsl_dht_x_sample(const gsl_dht *t, int n)` (starting domain) and `double gsl_dht_k_sample(const gsl_dht *t, int n)` (Fourier domain). It should be noted that the application method applies the coefficients of the forward transform. The backward transform is gotten by using the forward transform and applying an additional prefactor of $T^4/j_{\nu,M}^2$. The DHT method uses whatever optimized linear algebra packages it can find, e.g. the Intel MKL BLAS. Since the method is based on matrix-vector multiplications, the runtime for the transform of a vector of length N_x is $\mathcal{O}(N_x^2)$. In order to have similar spacings in z directions and in ρ direction, the z axis is discretized by $\mathcal{O}(N_x)$ samples. For a cylinder symmetric Fourier transform, thus $\mathcal{O}(N_x)$ such DHTs are needed, yielding a total scaling of $\mathcal{O}(N_x^3)$. Fast Fourier transform along the z axis has a runtime of $\mathcal{O}(N_x \log(N_x))$ and is thus not the expensive part of a cylinder symmetric Fourier transform.

4.2. Discretization in momentum space and time

4.2.1. Discretization in momentum space

The phase space of uniform gases is infinite and continuous and can be parametrized by \mathbb{R}^d . Computers however, cannot deal with an infinite number of data, and thus coarser model is necessary, i.e. a finite \mathbf{k} -point grid¹. The first simplification is the assumption that for large momentum values the states are approximately unoccupied and that scattering processes do not occupy them. In short, all momentum values above or below a certain threshold are neglected, introducing a *cutoff momentum* k_{co} . This finite phase volume still contains an infinite number of \mathbf{k} -points. It must thus be discretized to achieve a finite grid.

The discretization used here is rectilinear, i.e. the z and the ρ axis each are discretized yielding a number of samples $\{z_0, \dots, z_{N_z}\}$ and $\{\rho_0, \dots, \rho_{N_\rho}\}$ respectively. The $\rho - z$ plane is discretized using the cartesian product, $\{z_0, \dots, z_{N_z}\} \times \{\rho_0, \dots, \rho_{N_\rho}\}$. Since in z direction a standard Fourier transform has to be approximated, and the method of choice is the FFT, the z axis is discretized equidistantly. The ρ axis is discretized using the Bessel zeros from the section before to allow the usage of the DHT method.

While in principle it is possible to choose cutoff and number of \mathbf{k} -points separately for the two axes, it is plausible that often the demands in the two dimensions are similar. The cutoff k_{co} is thus chosen identically on both axes (because of cylinder symmetry this describes a cylinder of length $2k_{\text{co}}$ and radius k_{co}). Between 0 and k_{co} on both axes, N_x values are chosen according to the requirements for the transformation. An exemplary grid is shown in Fig. 4.2.

The usage of FFT to do the transform in z direction implies that a $2k_{\text{co}}$ -periodicity is assumed, and $G_{k_\rho, k_z + 2k_{\text{co}}, \alpha}^{\geq} = G_{k_\rho, k_z, \alpha}^{\geq}$. In practice, only one of the borders, $\pm k_{\text{co}}$, needs to be stored because of this translation symmetry. The cutoff in turn must be chosen large enough to prevent artifacts of this unwanted periodicity.

¹Some problems of such finite grids were already discussed in Sect. 3.3.

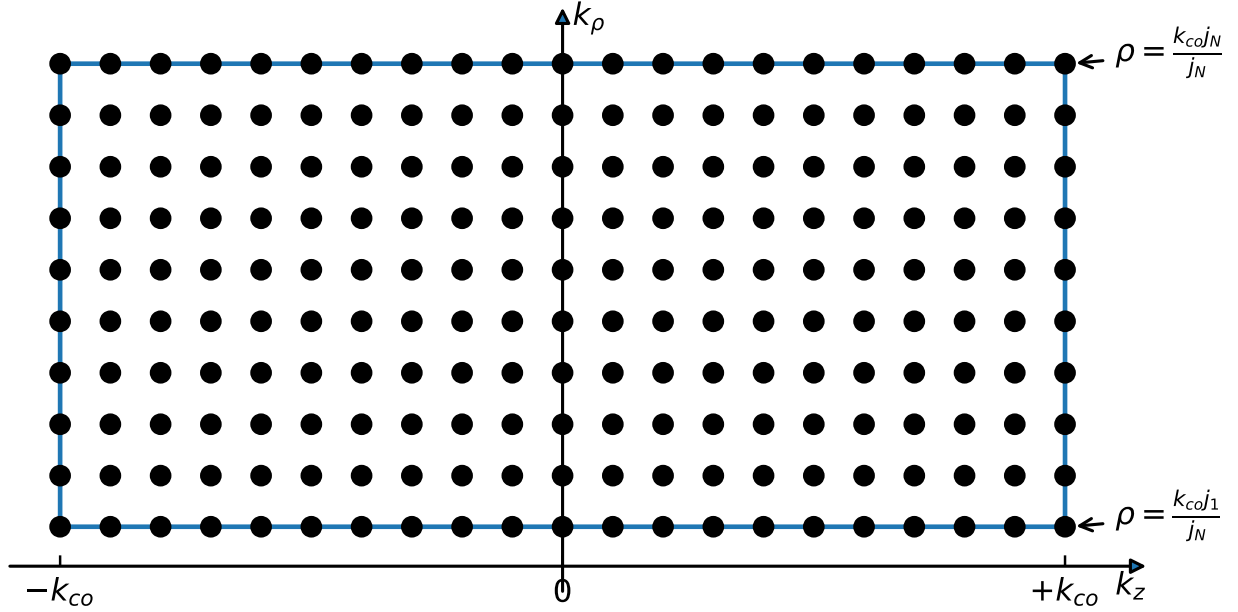


Figure 4.2.: Exemplary grid suitable for the GSL DHT in combination with FFT for $N_x = 10$.

Discretized expectation value integrals

Expectation values of single-particle observables \hat{A} with matrix elements $A_{\mathbf{k}\alpha}$ in the thermodynamic limit can be computed according to

$$\begin{aligned} \langle \hat{A} \rangle(t) &= \pm i \hbar \sum_{\alpha} \int \frac{d\mathbf{k}}{(2\pi\hbar)^3} A_{\alpha}(\mathbf{k}) G_{\alpha}^{\lessdot}(\mathbf{k}, t, t) \\ &= \pm i \frac{2\pi\hbar}{(2\pi\hbar)^3} \sum_{\alpha} \int dk_z \int dk_{\rho} A_{\alpha}(k_{\rho}, k_z) G_{\alpha}^{\lessdot}(k_{\rho}, k_z, t, t) k_{\rho}. \end{aligned} \quad (4.18)$$

In order to perform these integrals on the discrete grid, suitable quadrature formulas are needed. Integration along the z axis can be done using the weights k_{ci}/N_x , which are the weights that correspond to the exact integration of a Fourier interpolant, the 0 component of the transform. Integration in ρ direction involves nonequal integrations weights due to the grid points not being equidistant.

In particular, integrations of the form

$$\int_0^{\infty} f(x) x dx \quad (4.19)$$

are needed. Luckily, C. Frappier and P. Olivier [96] have found a quadrature formula for this type of integral with samples at the same x values as the DHT method above, which makes it suitable in this situations. It is given by

$$\int_0^{\infty} [f(x) + f(-x)] x dx \approx \frac{2T^2}{j_N^2} \sum_{k=1}^{\infty} \frac{1}{[J_0'(j_k)]^2} \left[f\left(\frac{j_k T}{j_N}\right) + f\left(-\frac{j_k T}{j_N}\right) \right]. \quad (4.20)$$

In order to apply this quadrature to the problems at hand, f is set to zero at negative values or equivalently, assume f to be symmetric and apply the factor $1/2$ afterwards. Since all functions are assumed to be zero at x values beyond the cutoff, the sum can be truncated after the first $N - 1$ terms. The quadrature formula is exact for all entire functions of exponential type that decay fast enough [96]. An entire function that is set to 0 in an open subset is 0 everywhere (Taylor expansion is valid everywhere for entire functions). The expression above thus can in our situation only be exact in the case that $f \equiv 0$, but nevertheless gives excellent integration results that are based on an implicit Fourier-Bessel expansion, similar to the ideas that led to the DHT.

4.2.2. Discretization in time, stepper and quadrature

In addition to quadratures suitable for momentum integrals, quadrature formulas for the memory integrals are needed. Depending on the propagation method of the differential equations (also called *stepper* in the following), G^{\geq} and Σ^{\geq} values are available only at certain points of time. While error control of the integration of the differential equations is possible through so-called *embedded Runge–Kutta formulae* [97], these methods vary the step size. Quadrature formulas can in principle be derived for unevenly distributed time samples, but make the procedure a lot more complicated.

In this thesis the versatile 4th order Runge–Kutta (RK4) stepper in combination with a versatile time integral quadrature were used. The time integration quadrature is based on the exact integration of Lagrange polynomials, that was used in the Master theses by N. Schlünzen [98] and J.-P. Joost [67] before. Let x_1, \dots, x_n sample points of a function f with values f_1, \dots, f_n at these points. The Lagrange polynomials are given by

$$L_i(x) = \prod_{m \neq i} \frac{x - x_m}{x_i - x_m} \quad (4.21)$$

with the property that $L_i(x_n) = \delta_{in}$. The polynomial interpolation of f is thus given by

$$\mathfrak{F}[f](x) := \sum_{m=1}^n f_m L_m(x). \quad (4.22)$$

As a polynomial, this expression is straightforward to integrate, which yields linear combination of the f_m ,

$$\int_{t_0}^{t_1} f(x) dx \approx \int_{t_0}^{t_1} \mathfrak{F}[f](x) dx = \sum_{m=1}^n f_m \int_{t_0}^{t_1} L_m(x) dx. \quad (4.23)$$

If the x_i are equidistant and setting $t_0 = x_1$, $t_1 = x_n$, one finds the famous closed Newton–Cotes formulas. These quadrature formulas are able to integrate polynomials of degree n exactly. If the function f is not a polynomial, the usage of high-order polynomial integration often leads to large errors (cf. "Runge's phenomenon" [99]). It is thus wise to use composite schemes (large

interval is distributed into many smaller intervals) and lower order polynomial interpolation. The most famous composite scheme is the *trapezoidal rule*. Following a code sample by N. Schlünzen and J.-P. Joost [100] an *overlapping composite scheme* is used: For up to 7 sampling points, the standard Newton–Cotes formulas from the literature are used.

Number of samples	w_1	w_2	w_3	w_4	w_5	w_6	w_7
1	0						
2	$\frac{1}{2}$	$\frac{1}{2}$					
3	$\frac{1}{3}$	$\frac{4}{3}$	$\frac{1}{3}$				
4	$\frac{3}{8}$	$\frac{9}{8}$	$\frac{9}{8}$	$\frac{3}{8}$			
5	$\frac{28}{90}$	$\frac{128}{90}$	$\frac{48}{90}$	$\frac{128}{90}$	$\frac{28}{90}$		
6	$\frac{95}{288}$	$\frac{375}{288}$	$\frac{250}{288}$	$\frac{250}{288}$	$\frac{375}{288}$	$\frac{95}{288}$	
7	$\frac{246}{840}$	$\frac{1296}{840}$	$\frac{162}{840}$	$\frac{1632}{840}$	$\frac{162}{840}$	$\frac{1296}{840}$	$\frac{246}{840}$

Table 4.1.: Newton–Cotes integration weights for up to 7 samples. The spacing factor is omitted in the weights above.

For $n \geq 8$ sampling points, consider the following: 5 points are needed to determine the coefficients of a fourth-order interpolation polynomial. Let $I_m(x)$, $1 \leq m \leq n-4$ be the interpolation polynomial based on the samples with numbers $m, m+1, m+2, m+3, m+4$. The interval $[x_m, x_{m+1}]$ is interpolated by a different number of polynomials, depending on m : $[x_1, x_2]$ by one, $[x_2, x_3]$ by two, $[x_3, x_4]$ by three, $[x_4, x_5]$ by four polynomials, and analogously at the other 'end' of the integration interval. The 'inner' intervals are interpolated by 5 different polynomials. The idea now is for each such interval to average between the integrals of all interpolation polynomials. For example, the first weights are given by

$$w_1 = \int_1^2 I_1(x) dx = \frac{17}{48}, \quad (4.24)$$

$$w_2 = \frac{1}{2} \left(\int_2^3 I_1(x) + I_2(x) dx \right) = \frac{59}{48}, \quad (4.25)$$

$$w_3 = \frac{1}{3} \left(\int_3^4 I_1(x) + I_2(x) + I_3(x) dx \right) = \frac{43}{48}. \quad (4.26)$$

The result of this procedure are the following weights (without the spacing factor):

Runge–Kutta fourth order stepper

Consider an ordinary differential equation

$$\frac{d}{dt}y(t) = f(t, y(t)) \quad (4.27)$$

w_1	w_2	w_3	w_4	w_5 to w_{n-5}	w_{n-3}	w_{n-2}	w_{n-1}	w_n
$\frac{17}{48}$	$\frac{59}{48}$	$\frac{43}{48}$	$\frac{49}{48}$	1	$\frac{49}{48}$	$\frac{43}{48}$	$\frac{59}{48}$	$\frac{17}{48}$

Table 4.2.: Integration weight factors for more than $n > 7$ equidistant sampling points, based on overlapping fourth order polynomial interpolation.

and suppose y is known at time t . We want to compute the function value $y(t + \Delta t)$. We can write

$$y(t + \Delta t) = y(t) + \int_t^{t+\Delta t} \frac{dy}{dt}(\bar{t}) d\bar{t} = f(t) + \Delta t \frac{dy}{dt}(t') \quad (4.28)$$

for some $t' \in [t, \Delta t]$, if y' is continuous. The aim of advanced steppers is to find a good estimate for the average derivative $\frac{dy}{dt}(t')$. In the classical Runge–Kutta scheme, this is computed as follows:

$$\frac{dy}{dt}(t') \approx \frac{1}{6} (k_1 + 2k_2 + 2k_3 + k_4), \quad \text{where} \quad (4.29)$$

$$k_1 = f(t, y(t)) \quad (4.30)$$

$$k_2 = f\left(t + \frac{1}{2}\Delta t, y(t) + \frac{1}{2}\Delta t k_1\right) \quad (4.31)$$

$$k_3 = f\left(t + \frac{1}{2}\Delta t, y(t) + \frac{1}{2}\Delta t k_2\right), \quad (4.32)$$

$$k_4 = f(t + \Delta t, y(t) + \Delta t k_3). \quad (4.33)$$

This method has a consistency error of fourth order: This means that the error of one step is of order $\mathcal{O}((\Delta t)^5)$. Since the number of steps necessary to compute a fixed interval $[t_0, t_1]$ grows with $\sim \frac{1}{\Delta t}$, and errors accumulate, the error of the final value, $y(t_1)$, (neglecting the higher order terms, arising from error propagation) is of order $\mathcal{O}((\Delta t)^4)$.

4.3. Real-time equations of motion for GW in the uniform gas

In this section it is assumed that the species-dependence of the interaction factorizes, $w_{\mathbf{q}}^{\alpha\beta} = Z_\alpha Z_\beta w_{\mathbf{q}}$ as it is the case for the Coulomb potential. The charge numbers Z_α, Z_β are arranged in the following expressions in such a way that the quantities and formulas become more compact. The expressions for SOA and GW A from Sect. 2.1.5 in the case of uniform gases after applying

the Langreth rules and using GKBA can be cast into the following form:

$$i\hbar \frac{\partial}{\partial t} G_{\mathbf{k}\alpha}^{\geq}(t \geq t') = h_{\mathbf{k}\alpha}^{\text{HF}}(t) G_{\mathbf{k}\alpha}^{\geq}(t, t'), \quad (4.34)$$

$$-i\hbar \frac{\partial}{\partial t'} G_{\mathbf{k}\alpha}^{\geq}(t \leq t') = h_{\mathbf{k}\alpha}^{\text{HF}}(t') G_{\mathbf{k}\alpha}^{\geq}(t, t'), \quad (4.35)$$

$$h_{\mathbf{k}\alpha}^{\text{HF}}(t) = \frac{k^2}{2m_\alpha} + i\hbar Z_\alpha^2 \sum_{\mathbf{p}} w_{\mathbf{k}-\mathbf{p}} G_{\mathbf{p}\alpha}^{\leq}(t, t). \quad (4.36)$$

These two equations stem from the GKBA and are used to propagate $G^{\geq}(t, t')$ away from the time-diagonal. The expression for the Hartree–Fock potential only includes the Fock contribution, since in uniform charge-neutral systems the Hartree contribution vanishes. On the time-diagonal, the commutator of G^{\geq} with h^{HF} is 0 (both are diagonal), but the collision integral I enters the equation of motion:

$$i\hbar \frac{d}{dt} G_{\mathbf{k}\alpha}^{\geq}(t, t) = [I + I^\dagger]_{\mathbf{k}\alpha}(t), \quad (4.37)$$

$$I_{\mathbf{k}\alpha}(t) = \int_{t_0}^t \Sigma_{\mathbf{k}\alpha}^{\geq}(t, \bar{t}) G_{\mathbf{k}\alpha}^{\leq}(\bar{t}, t) - \Sigma_{\mathbf{k}\alpha}^{\leq}(t, \bar{t}) G_{\mathbf{k}\alpha}^{\geq}(\bar{t}, t) d\bar{t}, \quad (4.38)$$

$$\Sigma_{\mathbf{k}\alpha}^{\geq}(t_1, t_2) = i\hbar Z_\alpha^2 \sum_{\mathbf{k}'} W_{\mathbf{k}'-\mathbf{k}}^{\geq}(t_1, t_2) G_{\mathbf{k}'\alpha}^{\geq}(t_1, t_2), \quad (4.39)$$

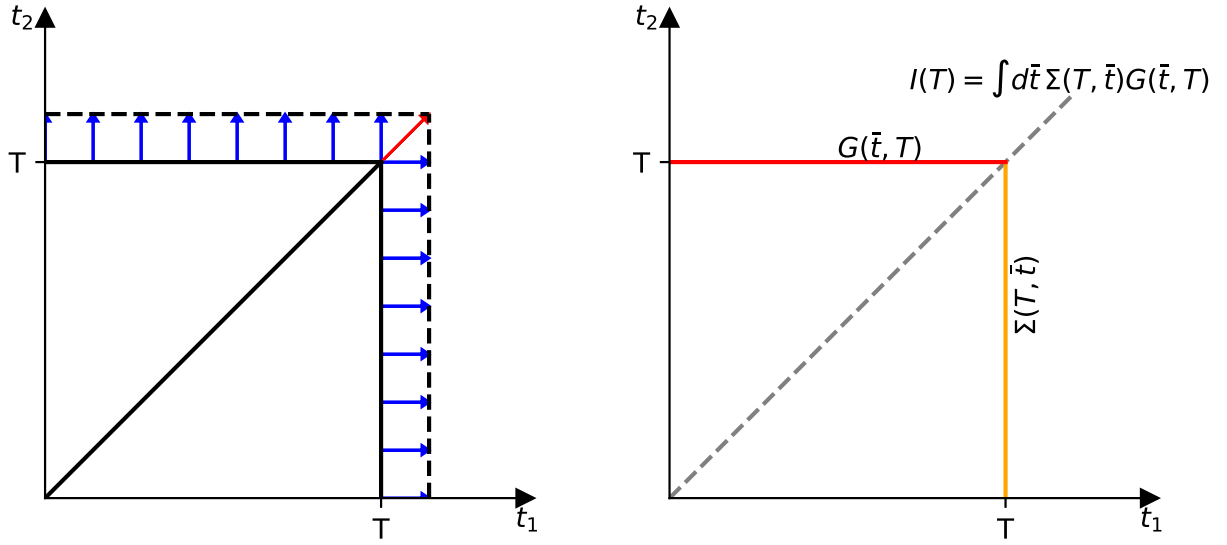
$$\begin{aligned} W_{\mathbf{q}}^{\geq}(t_1, t_2) &= \pi_{\mathbf{q}}^{\geq}(t_1, t_2) w_{\mathbf{q}}(t_1) w_{\mathbf{q}}(t_2) + w_{\mathbf{q}}(t_1) \int_{t_0}^{t_1} \pi_{\mathbf{q}}^{\mathcal{R}}(t_1, \bar{t}) W_{\mathbf{q}}^{\geq}(\bar{t}, t_2) d\bar{t} \\ &\quad + w_{\mathbf{q}}(t_1) \int_{t_0}^{t_2} \pi_{\mathbf{q}}^{\geq}(t_1, \bar{t}) W_{\mathbf{q}}^{\mathcal{A}}(\bar{t}, t_2) d\bar{t}, \end{aligned} \quad (4.40)$$

$$\pi_{\mathbf{q}}^{\geq}(t_1, t_2) = i\hbar \sum_{\mathbf{k}'\beta} (\pm)_{\beta} Z_{\beta}^2 G_{\mathbf{k}'+\mathbf{q},\beta}^{\geq}(t_1, t_2) G_{\mathbf{k}',\beta}^{\leq}(t_2, t_1). \quad (4.41)$$

Given above are the *GWA* equations. The direct *SOA* equations are gotten if the two integral terms in Eq. (4.40) are dropped. It is noteworthy that in the equations above only the non-singular part of $W(t, t') \rightarrow W(t, t') - w\delta(t, t')$ is written and used. The singular part is instead included in the Fock contribution of the Hartree–Fock Hamiltonian, and thus only contributes to the off-diagonal propagation.

4.4. Second-Order Approximation

In this section an algorithm for the *SOA* is presented. *SOA* calculations already contain many of the steps that *GW* calculations use. It is thus discussed first in order to make it easier to understand the *GW* algorithm, Sect. 4.5.



(a) Propagation in the two-time plane: Off-diagonal (blue) using a HF-propagator, time-diagonal (red) includes the collision integral I . (b) Computation of the collision integral I at time T is dependent on G and Σ values where one time argument is the current time T each.

Figure 4.3.: Sketch of the G, Σ values necessary to propagate by one time step in GKBA.

SOA GKBA calculations consist of two parts each time step: off-diagonal propagation using a Hartree–Fock Hamiltonian, and time-diagonal propagation using the collision integral. In this section it is discussed how these two can be computed efficiently. The following numerics are inspired by the book by M. Bonitz and D. Semkat, Ref. [101], and by Ref. [102].

4.4.1. Necessary data structures

NEGF, as a function depending on two times, the 'two-time plane', are usually propagated by gradually extending the 'area' of known G values. The area of known G values is extended away from the time-diagonal and along the time-diagonal. The GKBA can be understood as a simplification of the off-diagonal propagation, depicted by blue arrows in Fig. 4.3a and given by Eqs. (4.34) and (4.35). For the propagation from T to $T + \Delta T$, only the HF-Hamiltonian at the time T is needed. The off-diagonal propagation does not have any dependencies apart from the edges $\{T\} \times [0, T]$ and $[0, T] \times \{T\}$. The collision integral only enters the time-diagonal propagation. Figure 4.3b shows that G^{\lessgtr} and Σ^{\lessgtr} are only needed with time arguments on the same very two edges. A look at the SOA equations shows that Σ^{\lessgtr} on the edge again only depends on G^{\lessgtr} on the edges. (This changes in GWA .)

In Appendix A a few very useful time transposition properties for G, π, W and relations between $\pi^>, W^>$ and $\pi^<, W^<$ are derived. Since

$$G^{\lessgtr}(t_1, t_2) = -[G^{\lessgtr}(t_2, t_1)]^* \quad (4.42)$$

it is sufficient to explicitly store $G^>(t_1, t_2)$ for $t_1 \geq t_2$ and $G^<(t_1, t_2)$ for $t_1 \leq t_2$. These times allow the immediate computation of $\pi^>(t_1 \geq t_2)$. Using the property

$$\pi_{\mathbf{q}}^{\geq}(t_1, t_2) = -[\pi_{\mathbf{q}}^{\geq}(t_2, t_1)]^* = -[\pi_{-\mathbf{q}}^{\leq}(t_1, t_2)]^* = \pi_{-\mathbf{q}}^{\leq}(t_2, t_1) \quad (4.43)$$

we immediately get the $<$ component and all time transpositions as well, and can thus compute I from the knowledge of the edges only.

4.4.2. Computing HF energies

Since the Hartree–Fock energy of uniform 3D Coulomb gases takes the form

$$h_{\mathbf{k}\alpha}^{\text{HF}}(t) = \frac{k^2}{2m_\alpha} + i\hbar \int \frac{d\mathbf{p}}{(2\pi\hbar)^3} [w_{\mathbf{k}-\mathbf{p}}^{\alpha\alpha} G_{\mathbf{p}\alpha}^<(t, t)] , \quad (4.44)$$

the Fock potential can be written as

$$\varepsilon_{\mathbf{k}\alpha}^F(t) = \frac{i\hbar}{(2\pi\hbar)^3} [w^{\alpha\alpha} * G_\alpha^<(t, t)](\mathbf{k}), \quad (4.45)$$

where $*$ denotes the convolution operation. The efficient numerical evaluation of the Fock energy $\varepsilon_\alpha^F(t)$, by making use of the convolution theorem, is thus as follows:

$$\varepsilon_\alpha^F(t) = \frac{i\hbar}{(2\pi\hbar)^3} \text{IFT} [\text{FT}(w^{\alpha\alpha})\text{FT}(G_\alpha^<(t, t))] , \quad (4.46)$$

where FT and IFT are the numerical Fourier transform and inverse Fourier transform explained in Sect. 4.1. This procedure computes the Fock energies on the whole \mathbf{k} -point grid at once.

4.4.3. Computing collision integrals

Let S be the inversion operator, i.e. $Sf(\mathbf{k}) = f(-\mathbf{k})$. The inversion operator commutes with the Fourier transform. π^{\geq} can be written as a convolution,

$$\pi_{\mathbf{q}}^{\geq}(t_1, t_2) = i\hbar \sum_{\beta} (\pm)_{\beta} \int \frac{d\mathbf{k}'}{(2\pi\hbar)^3} G_{\mathbf{k}'+\mathbf{q},\beta}^{\geq}(t_1, t_2) S G_{-\mathbf{k}',\beta}^{\leq}(t_2, t_1) \quad (4.47)$$

$$= \frac{i\hbar}{(2\pi\hbar)^3} \sum_{\beta} (\pm)_{\beta} Z_{\beta}^2 [G^{\geq}(t_1, t_2) * S G^{\leq}(t_2, t_1)]_{\mathbf{q}} . \quad (4.48)$$

The first integrand of the collision integral, $\Sigma^>(T \geq \bar{t})G^<(\bar{t} \leq T)$, can thus be computed using the following recipe (omitting the momentum index in the following; quantities with a tilde $\tilde{}$ denote Fourier transformed quantities, i.e. in real space instead of momentum space):

1. Transform G : $\tilde{G}^>(T, \bar{t}) = \text{FT} [G^>(T, \bar{t})]$, $\tilde{G}^<(\bar{t}, T) = \text{FT} [G^<(\bar{t}, T)]$ for all species/spins.
2. Compute $\tilde{\pi}^>(T, \bar{t})$ as sum over $(\pm)_{\beta} Z_{\beta}^2 \tilde{G}^>(T, \bar{t}) S \tilde{G}^<(\bar{t}, T)$ for all species/spins β .

3. Transform $\tilde{\pi}^>$ back: $\pi^>(T, \bar{t}) = \frac{i\hbar}{(2\pi\hbar)^3} \text{IFT} [\tilde{\pi}^>(T, \bar{t})]$.
4. Multiply $\pi^>$ by the interactions: $W^>(T, \bar{t}) = \pi^>(T, \bar{t}) w(T) w(\bar{t})$.
5. Transform $\tilde{W}^>$: $\tilde{W}^>(T, \bar{t}) = \text{FT} [W^>(T, \bar{t})]$.
6. Multiply and find $\tilde{\Sigma}^>(T, \bar{t}) = \tilde{W}^>(T, \bar{t}) \tilde{G}^>(T, \bar{t})$ for all species/spins.
7. Transform Σ back: $\Sigma^>(T, \bar{t}) = Z_\alpha^2 \frac{i\hbar}{(2\pi\hbar)^3} \text{IFT} [\tilde{\Sigma}^>(T, \bar{t})]$ for all species/spins.
8. Multiply by $G^<(\bar{t}, T)$ for all species/spins.

For the calculation of $\Sigma^<(T \geq \bar{t}) G^>(\bar{t} \leq T)$, it can be reused that $\tilde{W}^>(T, \bar{t})$ has already been computed. Since $W^<(T, \bar{t}) = -[SW^>(T, \bar{t})]^*$, we get with the rule for Fourier transforms of complex conjugate functions (i.e. $\mathcal{F}[f^*](u) = \mathcal{F}[f]^*(-u)$, i.e. $\mathcal{F}[f^*] = S\mathcal{F}[f]^*$):

9. Compute $\tilde{W}^<(T, \bar{t}) = -[\tilde{W}^>(T, \bar{t})]^*$.
10. Multiply and find $\tilde{\Sigma}^<(T, \bar{t}) = \tilde{W}^<(T, \bar{t}) \tilde{G}^<(T, \bar{t})$, where $\tilde{G}^<(T, \bar{t}) = -S[\tilde{G}^>(\bar{t}, T)]^*$ for all species/spins.
11. Transform Σ back: $\Sigma^<(T, \bar{t}) = Z_\alpha^2 \frac{i\hbar}{(2\pi\hbar)^3} \text{IFT} [\tilde{\Sigma}^<(T, \bar{t})]$ for all species/spins.
12. Multiply by $G^>(\bar{t}, T) = -[G^>(T, \bar{t})]^*$ for all species/spins.

The steps above are repeated for all $\bar{t} \leq T$.

After that, use the integration weights introduced in Sect. 4.2.2 to compute

$$I_\alpha(T) = \int_{t_0}^T [\Sigma_\alpha^>(T, \bar{t}) G_\alpha^<(\bar{t}, T) - \Sigma_\alpha^<(T, \bar{t}) G_\alpha^>(\bar{t}, T)] d\bar{t}. \quad (4.49)$$

4.4.4. Application of h^{HF} and I

Eqs. (4.34) and (4.35) can in principle be solved using stepper methods, but for large momenta \mathbf{k} , the Hartree–Fock energies can become very large, and the oscillations thus very fast. Time steps must be sufficiently small to properly compute these oscillations, otherwise the amplitude increases infinitely or is dampened, depending on the exact stepping method. It is then efficient to make use of the very slow changes of h^{HF} over time:

$$G_{\mathbf{k}\alpha}^>(t + \Delta t \geq t') = G_{\mathbf{k}\alpha}^>(t, t') \exp\left(\frac{1}{i\hbar} \int_t^{t+\Delta t} h_{\mathbf{k}\alpha}^{\text{HF}}(\bar{t}) d\bar{t}\right) \approx G_{\mathbf{k}\alpha}^>(t, t') \exp\left(\frac{1}{i\hbar} h_{\mathbf{k}\alpha}^{\text{HF}}(t) \Delta t\right), \quad (4.50)$$

$$G_{\mathbf{k}\alpha}^<(t' \leq t + \Delta t) = G_{\mathbf{k}\alpha}^<(t', t) \exp\left(-\frac{1}{i\hbar} \int_t^{t+\Delta t} h_{\mathbf{k}\alpha}^{\text{HF}}(\bar{t}) d\bar{t}\right) \approx G_{\mathbf{k}\alpha}^<(t', t) \exp\left(-\frac{1}{i\hbar} h_{\mathbf{k}\alpha}^{\text{HF}}(t) \Delta t\right). \quad (4.51)$$

This complex exponential can directly be calculated by the computer, and the absolute value stays constant, as it should be. This method thus increases the stability.

The collision integral can straightforwardly be applied,

$$G_{\mathbf{k}\alpha}^{\geq}(T + \Delta t, T + \Delta t) = G_{\mathbf{k}\alpha}^{\geq}(T, T) + \frac{\Delta t}{i\hbar} 2\Re e(I_{\mathbf{k}\alpha}(T)). \quad (4.52)$$

These are of course the formulas for the explicit Euler method, but it is readily generalized to the RK4 scheme. The only unusual part is the propagation to the off-diagonal: Here we have to average between the four HF-energies from the four substeps according to the RK4 weights. This, however, has little impact, since the dynamics on the time-diagonal are slow compared to the off-diagonal dynamics.

4.5. GW Approximation

In this section numerical aspects of *GW* calculations are discussed. The first two subsections describe the discretization and solution of the *W* Dyson equation. The third subsection sketches the procedure of the program quite detailed, which is depicted in the flowcharts of the fourth subsection.

4.5.1. Discretization of the Dyson Equation

The *GW* propagation is widely similar to that of SOA calculations, just the screened potential *W* obeys a more difficult equation. The Dyson equation,

$$\begin{aligned} W_{\mathbf{q}}^{\geq}(t_1, t_2) &= \pi_{\mathbf{q}}^{\geq}(t_1, t_2) w_{\mathbf{q}}(t_1) w_{\mathbf{q}}(t_2) + w_{\mathbf{q}}(t_1) \int_{t_0}^{t_1} \pi_{\mathbf{q}}^{\mathcal{R}}(t_1, \bar{t}) W_{\mathbf{q}}^{\geq}(\bar{t}, t_2) d\bar{t} \\ &+ w_{\mathbf{q}}(t_1) \int_{t_0}^{t_2} \pi_{\mathbf{q}}^{\geq}(t_1, \bar{t}) W_{\mathbf{q}}^{\mathcal{A}}(\bar{t}, t_2) d\bar{t}, \end{aligned} \quad (4.53)$$

is discretized by approximating the integrals using a quadrature formula. This means that the integral is replaced by a sum over discrete points, multiplied by weight factors $w_n^{(1)/(2)}$ for the first and second integral. Let $W_{\mathbf{q}}^{\geq}(i, j)$ be the discretized version of $W_{\mathbf{q}}^{\geq}(t_1, t_2)$, i.e. $t_1 = i \cdot \text{DT}$, $t_2 = j \cdot \text{DT}$ for $i, j \in \mathbb{N}_0$, and with the time step length DT . This yields for the $>$ component:

$$\begin{aligned} W_{\mathbf{q}}^>(i, j) &= \pi_{\mathbf{q}}^>(i, j), w_{\mathbf{q}}(i), w_{\mathbf{q}}(j) + w_{\mathbf{q}}(i) \sum_{n=0}^i w_n^{(1)} \{ \pi_{\mathbf{q}}^>(i, n) - \pi_{\mathbf{q}}^<(i, n) \} W_{\mathbf{q}}^>(n, j) \\ &+ w_{\mathbf{q}}(i) \sum_{n=0}^j w_n^{(2)} \pi_{\mathbf{q}}^>(i, n) \{ W_{\mathbf{q}}^<(n, j) - W_{\mathbf{q}}^>(n, j) \}. \end{aligned} \quad (4.54)$$

The solution of this form is inconvenient since the computation of unknown $W^>$ values includes the knowledge of $W^<$ values (second sum), of which some are unknown, too. Bányai et al. [61] used the symmetry $W_{\mathbf{q}}^<(i, j) = W_{-\mathbf{q}}^>(j, i)$ to remove the dependence on $W^<$ in the Dyson equation. This works very well, even if parallelized (different times computed in parallel, cf. Sect. 4.5.5), especially on a single computation node. A different way to annihilate the $W^<$ -dependence is to make use of the symmetry $W_{\mathbf{q}}^<(i, j) = -[W_{-\mathbf{q}}^>(i, j)]^*$. This approach is convenient because the times are not transposed, which means the computation of such sums does not demand access to additional times than those appearing in Eq. (4.54), i.e. memory can be better distributed among the computation nodes. The resulting expression,

$$W_{\mathbf{q}}^>(i, j) = \pi_{\mathbf{q}}^>(i, j) w_{\mathbf{q}}(i) w_{\mathbf{q}}(j) + w_{\mathbf{q}}(i) \sum_{n=0}^i w_n^{(1)} \{ \pi_{\mathbf{q}}^>(i, n) - \pi_{\mathbf{q}}^<(i, n) \} W_{\mathbf{q}}^>(n, j) - w_{\mathbf{q}}(i) \sum_{n=0}^j w_n^{(2)} \pi_{\mathbf{q}}^>(i, n) \{ [W_{-\mathbf{q}}^>(n, j)]^* + W_{\mathbf{q}}^>(n, j) \}, \quad (4.55)$$

can be solved for the unknown values.

4.5.2. Numerical solution scheme for the Dyson equation

Assuming $W_{\mathbf{q}}^>(i, j)$ is known on the square $\{0, 1, \dots, m\} \times \{0, 1, \dots, m\}$, and G is known on the square $\{0, 1, \dots, m+1\} \times \{0, 1, \dots, m+1\}$, the aim is to extend the $W^>$ square to $\{0, 1, \dots, m+1\} \times \{0, 1, \dots, m+1\}$ for the computation of the collision integral.

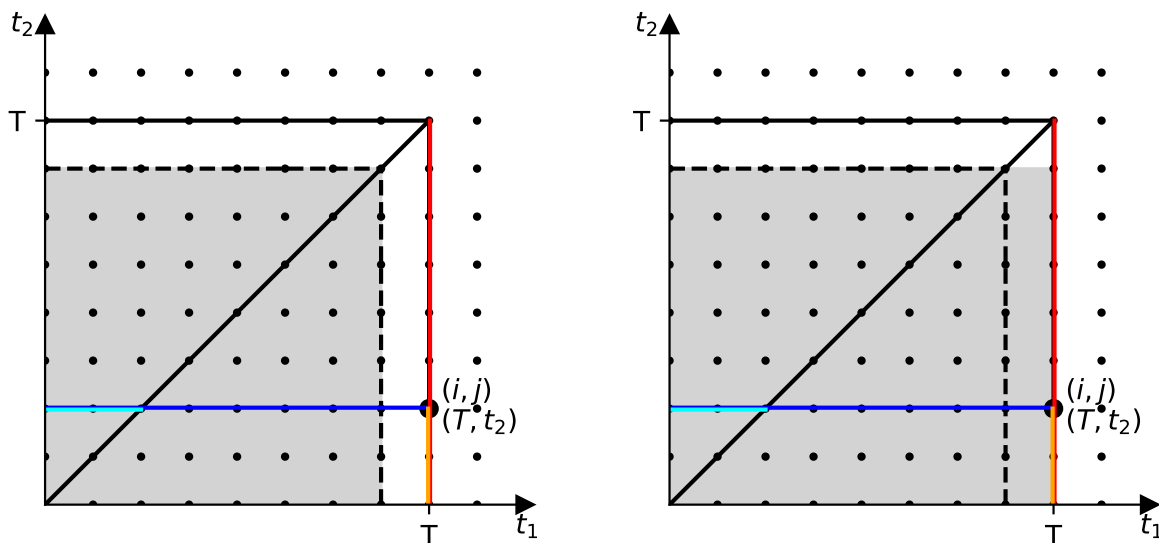
If $m+1 = i > j$, the explicit solution is given by

$$W_{\mathbf{q}}^>(i > j) = \frac{1}{1 + w_{\mathbf{q}}(i) w_i^{(1)} \{ \pi_{\mathbf{q}}^>(i, i) - \pi_{\mathbf{q}}^<(i, i) \}} \times \left[\pi^>(i, j) w_{\mathbf{q}}(i) w_{\mathbf{q}}(j) + w_{\mathbf{q}}(i) \sum_{n=0}^{i-1} w_n^{(1)} \{ \pi_{\mathbf{q}}^>(i, n) - \pi_{\mathbf{q}}^<(i, n) \} W_{\mathbf{q}}^>(n, j) - w_{\mathbf{q}}(i) \sum_{n=0}^j w_n^{(2)} \pi_{\mathbf{q}}^>(i, n) \{ [W_{-\mathbf{q}}^>(n, j)]^* + W_{\mathbf{q}}^>(n, j) \} \right]. \quad (4.56)$$

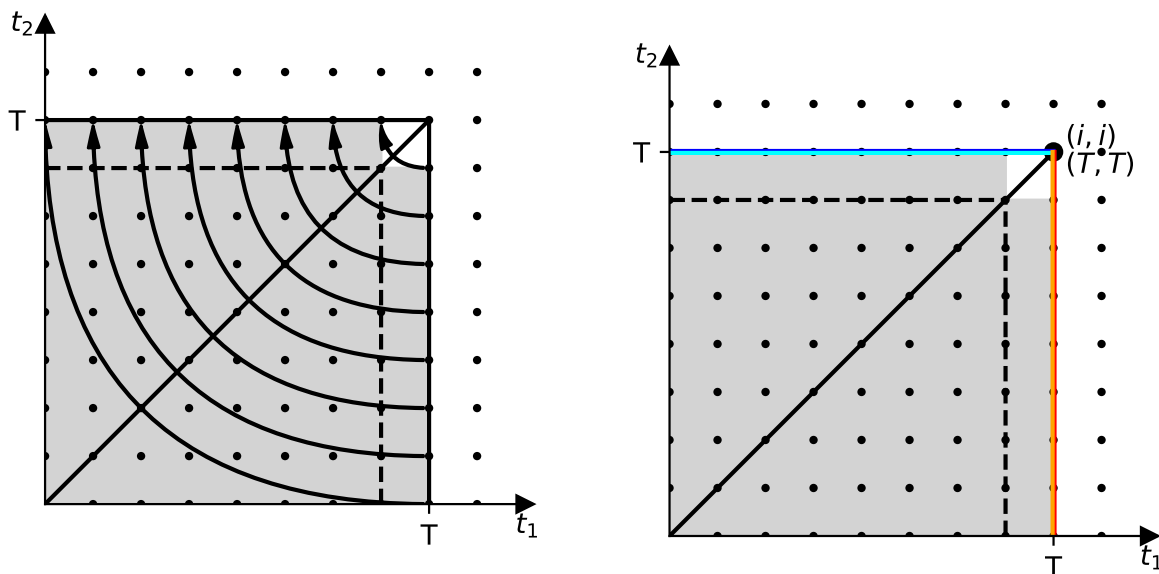
This is used to extend the square of known $W^>$ values to $\{0, 1, \dots, m+1\} \times \{0, 1, \dots, m\}$, as demonstrated in Figs. 4.4a and 4.4b.

This progress then can be mirrored using $W_{\mathbf{q}}^>(t_1, t_2) = -[W_{\mathbf{q}}^>(t_2, t_1)]^*$, and thus the values at times $\{0, 1, \dots, m+1\} \times \{0, 1, \dots, m+1\} \setminus (m+1, m+1)$ are known, depicted in Fig. 4.4c.

In order to find the corner value at $(m+1, m+1)$, the formula (4.56) must be modified, since $W_{\mathbf{q}}^>(m+1, m+1)$ appears in both sums. In fact, since the integration boundaries are the same, the integration weights become identical, and we find the discretized 'time-diagonal' Dyson



(a) The discretized Dyson equation for $t_2 \leq T - \Delta t$ only contains one unknown value. (b) By solving the discretized Dyson equation, the square is extended to the right.



(c) By using time transposition symmetry, the newly acquired $W^>$ values are used to extend the square to the top. (d) Only one entry of the larger square is unknown. It can be found in a similar way to substep (a)

Figure 4.4.: Sketch of the strategy to extend the square of known $W^>(i, j)$ values. The shaded area shows the known values at each substep. $\pi^{\lessgtr}(t, t')$ is known on the outer edges from G^{\lessgtr} , with one time argument being T . Blue, cyan, red and orange lines depict the integration paths: Bluish colors for $W^>$, reddish colors for π^{\lessgtr} . Dark colors: first integral term $\pi^{\mathcal{R}}W^>$; light colors: second integral term $\pi^>W^{\mathcal{A}}$.

equation

$$W_{\mathbf{q}}^{\gt}(i, i) = \pi_{\mathbf{q}}^{\gt} w_{\mathbf{q}}(i)^2 + w_{\mathbf{q}}(i) \sum_{n=0}^i w_n^{(1)} \left\{ -\pi_{\mathbf{q}}^{\gt}(i, n) \left[W_{-\mathbf{q}}^{\gt}(n, i) \right]^* - \pi_{\mathbf{q}}^{\lt}(i, n) W_{\mathbf{q}}^{\gt}(n, i) \right\}. \quad (4.57)$$

Since $W_{\mathbf{q}}^{\gt}(i, i)$ is purely imaginary, we have $-\left[W_{-\mathbf{q}}^{\gt}(i, i) \right]^* = W_{-\mathbf{q}}^{\gt}(i, i)$. In this equation, in contrast to the nondiagonal case before, the unknown $W_{\mathbf{q}}^{\gt}(i, i)$ and $W_{-\mathbf{q}}^{\gt}(i, i)$ values are coupled, i.e. the Dyson equation above is a 2×2 inhomogeneous equation system for $W_{\pm\mathbf{q}}^{\gt}(i, i)$:

$$\begin{pmatrix} A_{\mathbf{q}} & B_{\mathbf{q}} \\ B_{-\mathbf{q}} & A_{-\mathbf{q}} \end{pmatrix} \begin{pmatrix} W_{\mathbf{q}}^{\gt}(i, i) \\ W_{-\mathbf{q}}^{\gt}(i, i) \end{pmatrix} = \begin{pmatrix} C_{\mathbf{q}} \\ C_{-\mathbf{q}} \end{pmatrix}, \quad (4.58)$$

where the coefficients $A_{\mathbf{q}}, B_{\mathbf{q}}$ and the inhomogeneity $C_{\mathbf{q}}$ are given by

$$A_{\mathbf{q}} = 1 + w_{\mathbf{q}}(i) w_i^{(1)} \pi_{\mathbf{q}}^{\lt}(i, i), \quad (4.59)$$

$$B_{\mathbf{q}} = -w_{\mathbf{q}}(i) w_i^{(1)} \pi_{\mathbf{q}}^{\gt}(i, i), \quad (4.60)$$

$$C_{\mathbf{q}} = \pi_{\mathbf{q}}^{\gt} w_{\mathbf{q}}(i)^2 + w_{\mathbf{q}}(i) \sum_{n=0}^{i-1} w_n^{(1)} \left\{ -\pi_{\mathbf{q}}^{\gt}(i, n) \left[W_{-\mathbf{q}}^{\gt}(n, i) \right]^* - \pi_{\mathbf{q}}^{\lt}(i, n) W_{\mathbf{q}}^{\gt}(n, i) \right\}. \quad (4.61)$$

By virtue of Cramer's rule, this can be solved to find

$$W_{\mathbf{q}}^{\gt}(i, i) = \frac{C_{\mathbf{q}} A_{-\mathbf{q}} - B_{\mathbf{q}} C_{-\mathbf{q}}}{A_{\mathbf{q}} A_{-\mathbf{q}} - B_{\mathbf{q}} B_{-\mathbf{q}}}, \quad (4.62)$$

depicted in Fig. 4.4d. With this, the extension to the larger square is complete²³.

4.5.3. Computing collision integrals and HF energies

The Hartree–Fock Hamiltonian and off-diagonal propagation are the same as described in the SOA section. Apart from the significantly more involved computation of W^{\lessgtr} , the GW propagation is similar to the SOA propagation:

For all $\bar{t} \leq T$ do:

1. Transform G : $\tilde{G}^{\gt}(T, \bar{t}) = \text{FT} [G^{\gt}(T, \bar{t})]$, $\tilde{G}^{\lt}(\bar{t}, T) = \text{FT} [G^{\lt}(\bar{t}, T)]$ for all species/spins.
2. Compute $\tilde{\pi}^{\gt}(T, \bar{t})$ as sum over $(\pm)_{\beta} Z_{\beta}^2 \tilde{G}^{\gt}(T, \bar{t}) S \tilde{G}^{\lt}(\bar{t}, T)$ for all species/spins β .

²Of course, one can try and solve the Dyson equation of the 'upper' edge instantly – which yields a dense equation system for W^{\gt} on the edge. However, this approach is slower by one order of N_t (utilizing QR or LU factorization), and has equal memory demand (π^{\lessgtr} values on the whole plane are needed in this approach). It is thus not viable.

³In higher order propagation schemes, it is only necessary to replace the outer edge repeatedly for the substeps. The 'completed' earlier steps can be kept.

3. Transform $\tilde{\pi}^>$ back: $\pi^>(T, \bar{t}) = \frac{i\hbar}{(2\pi\hbar)^3} \text{IFT} [\tilde{\pi}^>(T, \bar{t})]$.

These three steps must be completed before continuing, as substep 4a) depends on all of these values of $\pi^>$.

4. Propagate W according to previous section:
- Extend to the right.
 - Use time transposition symmetry.
 - Compute corner value.

Now continue computing $\Sigma^>(T, \bar{t}) G^<(\bar{t}, T)$ for $\bar{t} \leq T$:

- Transform $\tilde{W}^>$: $\tilde{W}^>(T, \bar{t}) = \text{FT} [W^>(T, \bar{t})]$.
- Multiply and find $\tilde{\Sigma}^>(T, \bar{t}) = \tilde{W}^>(T, \bar{t}) \tilde{G}^>(T, \bar{t})$ for all species/spins.
- Transform Σ back: $\Sigma^>(T, \bar{t}) = Z_\alpha^2 \frac{i\hbar}{(2\pi\hbar)^3} \text{IFT} [\tilde{\Sigma}^>(T, \bar{t})]$ for all species/spins.
- Multiply by $G^<(\bar{t}, T)$ for all species/spins.

For the calculation of $\Sigma^<(T \geq \bar{t}) G^>(\bar{t} \leq T)$, use the $>\leftrightarrow<$ symmetry of W :

- Compute $\tilde{W}^<(T, \bar{t}) = -[\tilde{W}^>(T, \bar{t})]^*$.
- Multiply and find $\tilde{\Sigma}^<(T, \bar{t}) = \tilde{W}^<(T, \bar{t}) \tilde{G}^<(T, \bar{t})$, where $\tilde{G}^<(T, \bar{t}) = -S[\tilde{G}(\bar{t}, T)]^*$ for all species/spins.
- Transform Σ back: $\Sigma^<(T, \bar{t}) = Z_\alpha^2 \frac{i\hbar}{(2\pi\hbar)^3} \text{IFT} [\tilde{\Sigma}^<(T, \bar{t})]$ for all species/spins.
- Multiply by $G^>(\bar{t}, T) = -[G^>(T, \bar{t})]^*$ for all species/spins.

After that, as in SOA, integrate

$$I_\alpha(T) = \int_{t_0}^T [\Sigma_\alpha^>(T, \bar{t}) G_\alpha^<(\bar{t}, T) - \Sigma_\alpha^<(T, \bar{t}) G_\alpha^>(\bar{t}, T)] d\bar{t} \quad (4.63)$$

(all \mathbf{p} at once), using a quadrature formula.

4.5.4. Flowchart of the program

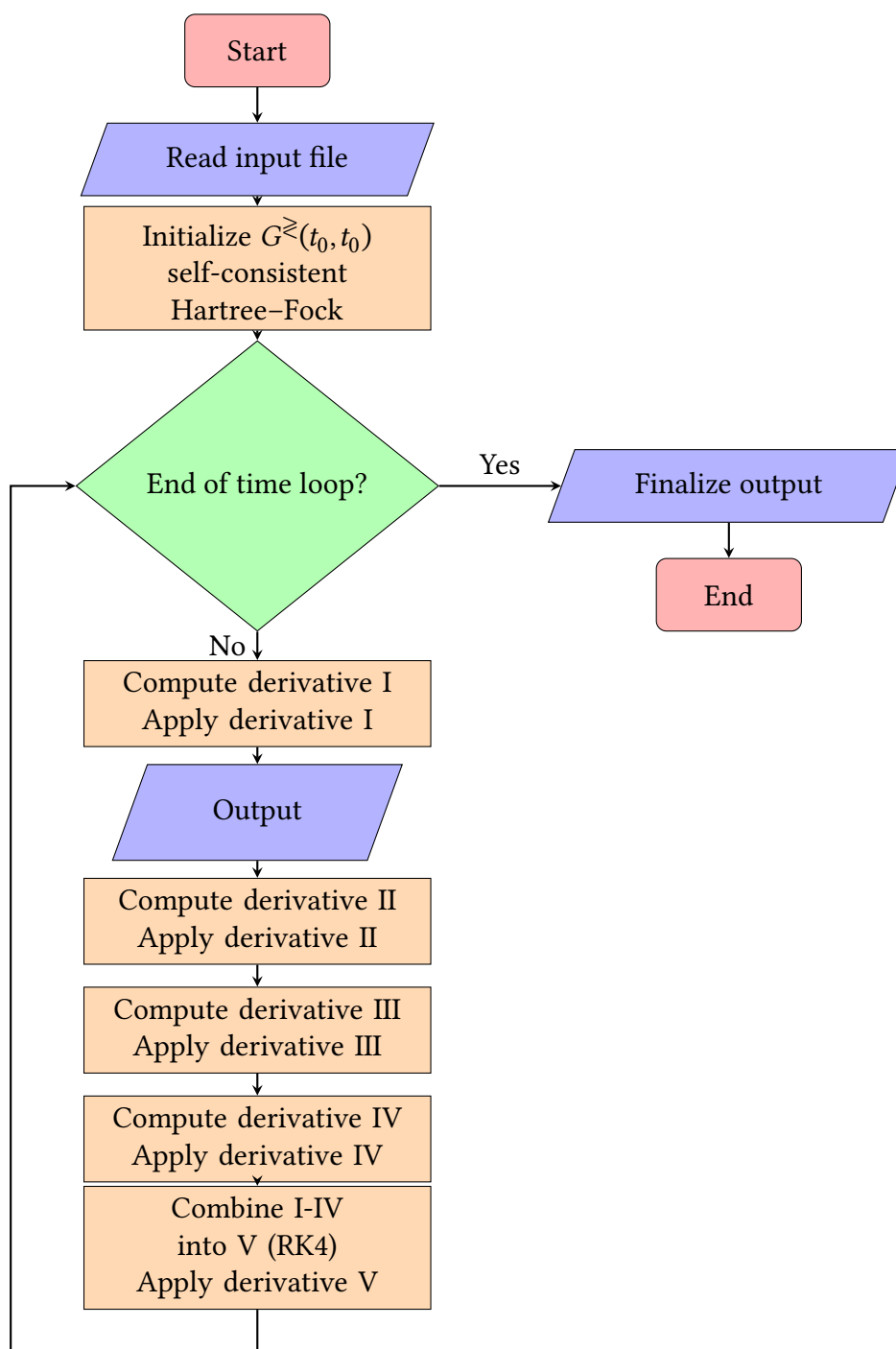


Figure 4.5.: Flowchart for the simulation program 'JelliumCyl' on large scale. Flowcharts of the parts are on the next pages.

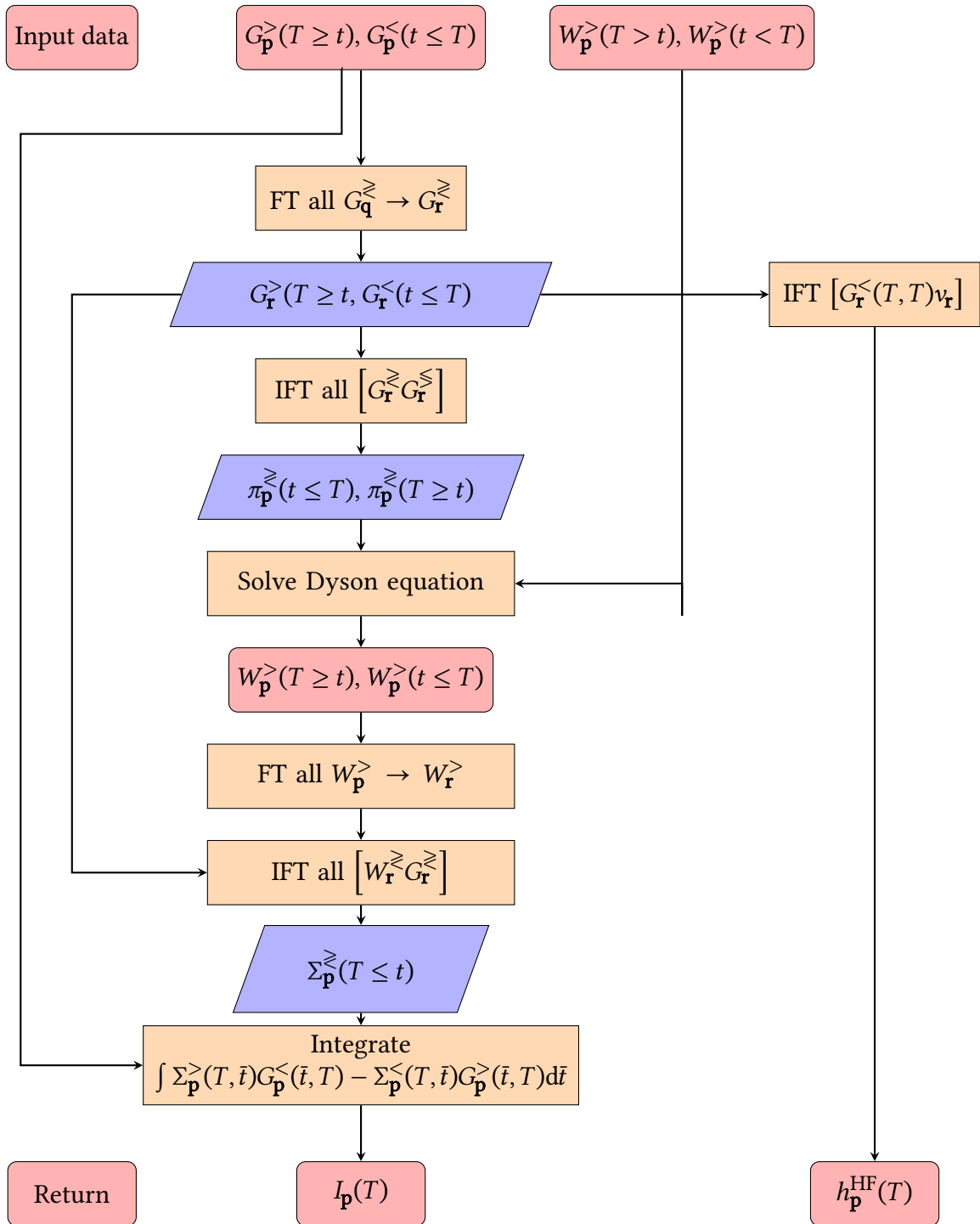


Figure 4.6.: Flowchart for 'Compute derivative'. Prefactors are omitted in this depiction. Blue parallelograms indicate temporary quantities, red rectangles indicate data that are needed in subsequent steps.

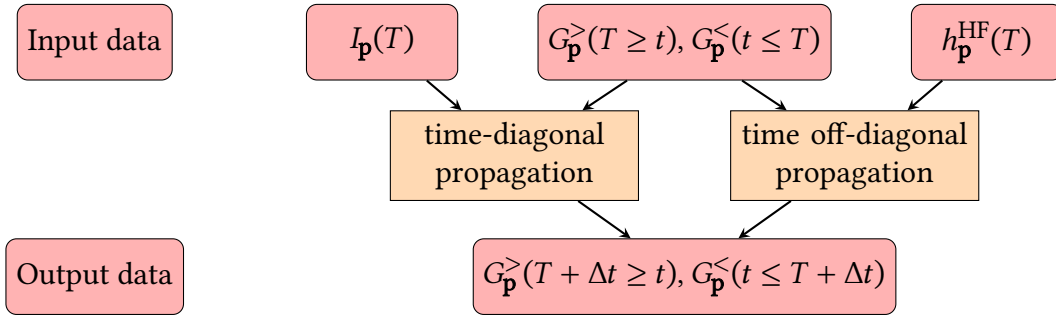


Figure 4.7.: Flowchart for 'Apply derivative'.

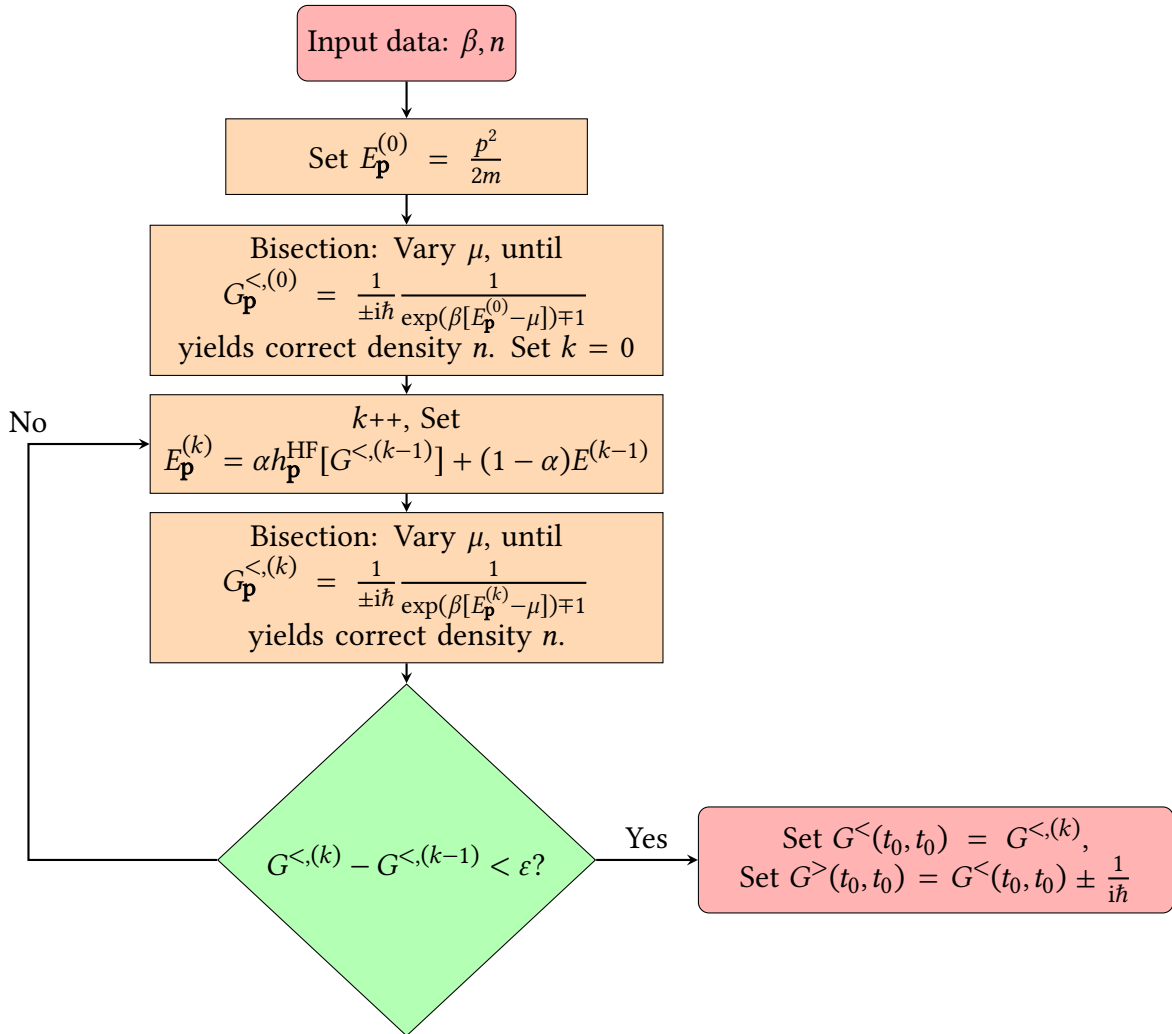


Figure 4.8.: Flowchart for self-consistent Hartree-Fock initialization of $G^<$.

4.5.5. Parallelization

The program has to manage large amounts of data and do a lot of computational work. Parallelization for the use with distributed memory on multiple computation nodes and the use of many CPU cores is thus advisable. Two important principles in parallelization are:

- Distribute workload evenly among nodes (minimize downtime of nodes).
- Minimize communication needed between nodes.

The largest data structure by far is $W_{q_z, q_\rho}^>(t_1, t_2)$, a 2D array in time and a 2D array in momentum, i.e. in total a 4D array. The only one step that induces the $\mathcal{O}(N_t^3)$ scaling is substep (b) of the solution of Dyson's equation. It is thus most important to find a good distribution of $W^>$ on the multiple nodes, and then parallelize this substep.

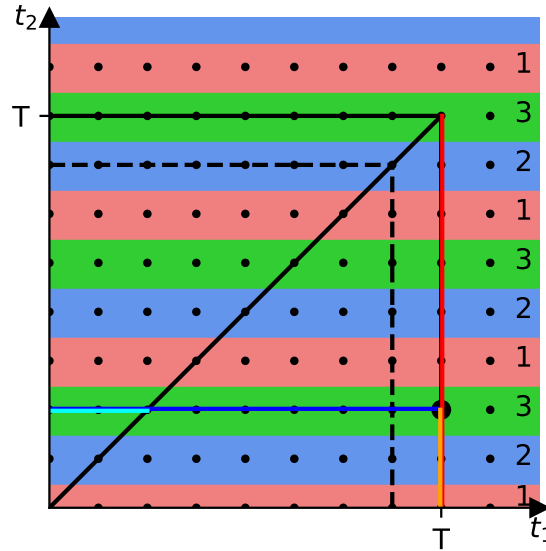


Figure 4.9.: Distribution of $W^>$ onto multiple computation threads, demonstrated for exemplary 3 threads. The numbers on the right represent the thread responsible for the solution of the Dyson equation on the given slice. Some exemplary integration paths are also sketched, cf. Fig. 4.4b

Considering the algorithm to solve the Dyson equation as shown above, it is efficient to distribute $W^>(t_1, t_2)$ into disjunct slices with constant t_2 (horizontal slices), such that the integrals in the Dyson equation can be computed on one node. This distribution is pictured in Fig. 4.9. Each node needs access to $W^>$ on the whole slice and $\pi^>$ on the edge: $\pi^>$ is thus stored multiple times, on each node.

For simpler steps, such as the computation of π , it is not always clear whether it is useful to parallelize it: Exchanging data between nodes takes time, and for smaller tasks it is more efficient to just let each node do the computation themselves than to distribute the work and share

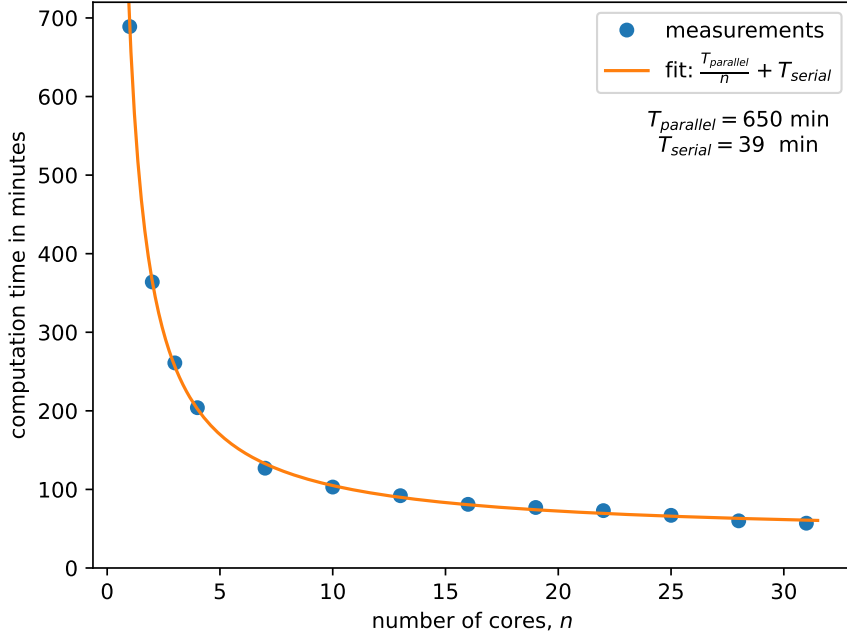


Figure 4.10.: Computation time of a GW calculation as a function of number of threads. Simulation parameters: 500 time steps, and 80 grid points in radial, 160 grid points in z direction, one particle species.

the results afterwards. The code used in this thesis however does parallelize the computation of π . So far, no tests were made to compare this to the non-distributed idea, it should however not matter that much, as it is not the bottleneck.

Figure 4.9 suggests that the nodes acquire new slices in always the same order. This is chosen in order to distribute the work evenly:

1. The number of slices each node is responsible for differs only by maximum 1.
2. The solution of the Dyson equation on one slice uses two integrals: one with a long integration interval (same length for all slices), and one with a shorter length. During the propagation, when the Dyson equation must be solved on a 'new' slice, this slice gets assigned to the node that up to this point had the shortest integration intervals. The node with the least work load thus gets the new slice.

The program has been tested with different numbers of MPI threads in a relatively small setup, which yields the times computation times in Fig. 4.10. They show that this small simulation is already 94.3% parallelized, a quota which should only increase with longer calculations: In short calculations, non-parallelized computational work necessary for initialization and overhead from data exchange matter more in relation to the parallelized parts of the propagation.

4.6. Convergence parameters

In order to keep the descriptions of simulation parameters short in the following chapter, the numerical convergence parameters are defined in this section. Their names are written in typewriter font, since they are also the names of input parameters of the program.

The momentum grid is rectangular. It spans a rectangle of

$$[-\text{CUTOFFMOMENTUM} + \text{E_GOFFSET}, \text{CUTOFFMOMENTUM} + \text{E_GOFFSET}] \times [0, \text{CUTOFFMOMENTUM}], \quad (4.64)$$

in the $p_z \times p_\rho$ plane, where CUTOFFMOMENTUM is the momentum cut-off in atomic units $[\hbar a_B^{-1}]$, and E_GOFFSET is a parameter that shifts the whole grid for the electrons. There is a second offset parameter, I_GOFFSET , which describes the same for the ions⁴. This parameter is necessary to construct a momentum grid that is able to support the large momenta of ion projectiles.

This rectangle of momentum values is sampled according to section 4.2.1 using $2 \times \text{NKR}$ values in z direction and NKR values in ρ direction. The momentum spacing in z direction, $\text{DKR} = \text{CUTOFFMOMENTUM}/\text{NKR}$ is implicitly defined by the other two grid parameters. The momentum spacing in ρ is roughly of the same magnitude, but it is not equidistant, as described in section 4.2.1.

The time stepping is defined by the time step length in atomic units $[\hbar/E_H] \approx [24.188 \text{ as}]$, DT , and the number of time steps, PROPT .

The memory demand of a calculation can be estimated to be roughly

$$\text{RAM demand} \approx 2\text{NKR}^2 \times \text{PROPT}^2 \times 16 \text{ Byte} \quad (4.65)$$

for the dynamically screened potential W which is by far the most memory consuming quantity in a GW calculation (in comparison GKBA Green functions are rather cheap). A calculation with $\text{NKR} = 100$ and $\text{PROPT} = 1000$, for example, already uses 320 GiB with quadratic scaling in both, PROPT and NKR .

⁴These parameters can be set to change dynamically by setting E_FLOATINGGRID or I_FLOATINGGRID to true: Then the program shifts the grid position if the mean momentum of the distribution supported by the grid deviates too much from the grid's center.

5. Application to stopping power

Abstract: This section is devoted to the stopping power of dense plasmas acting on proton and electron projectiles. First, the simulation setup is explained. Second, rather raw simulation results are presented and discussed: time-dependent projectile distribution functions and their time-derivatives. From the time-dependent observables the stopping power can be extracted. Finally, the computed non-Markovian results are compared with Markovian RPA results. The agreement of proton results and the disagreement of the electron results is discussed analytically.

5.1. Simulation setup

5.1.1. Plasma target velocity scale separation

A gaseous plasma, the 'target', consists of unbound electrons and at least one ion species. It is known from classical Lenard-Balescu equation[103–105],

$$\frac{\partial f(\mathbf{v}, t)}{\partial t} = -\frac{8\pi^4 n_0}{m_e^2} \nabla_{\mathbf{v}} \cdot \int d\mathbf{k} \int d\mathbf{v}' \mathbf{k} \otimes \mathbf{k} \frac{\varphi^2(k)}{|\varepsilon(\mathbf{k}, \mathbf{k} \cdot \mathbf{v})|^2} \cdot \delta(\mathbf{k} \cdot [\mathbf{v} - \mathbf{v}']) [f(\mathbf{v}) \nabla_{\mathbf{v}'} f(\mathbf{v}') - f(\mathbf{v}') \nabla_{\mathbf{v}} f(\mathbf{v})] , \quad (5.1)$$

that the conservation of kinetic energy described by the δ -function is especially fulfilled for particles of identical velocity, $\mathbf{v} = \mathbf{v}'$. A consequence is, that particles of similar velocity collide especially intensively. Similar conclusions can be drawn from the Markov limit of the second-order approximation in the reduced-density matrix formalism, cf. Ref. [14] and Sect. 5.4.2.

These δ -functions only become sharp in the long-time limit and if single-particle distributions are weakly time-dependent. On short time-scales the δ -functions are smoothed and temporarily allow non-conserving collisions, but are still peaked in such a way that collisions which preserve single-particle energies (high density \rightarrow exchange energies are small compared to kinetic energies) are preferred. The conclusion that mainly particles of identical velocity collide thus remains valid in non-Markovian short-time dynamics.

From the Maxwellian distribution function,

$$f(\mathbf{v}) = n \left(\frac{m}{2\pi k_B T} \right)^{3/2} \exp \left(-\frac{mv^2}{2k_B T} \right) , \quad (5.2)$$

it can be seen that the velocity scale of a nondegenerate plasma goes as $v \sim m^{-1/2}$, or goes as $v \sim m^{-1}$ in the highly degenerate case (Fermi distribution, 0 K). In fully ionized isothermal

two-component plasma consisting of electrons (' e ') and ions (' i ') with a mass ratio of at least 1836 (proton), the velocity scales of the two components are thus strongly separated¹. For the application to stopping power calculations this means, that

- collisions between the projectile and target ions are negligible on electronic velocity scales,
- on ionic velocity scales electronic contributions to stopping power are small and only v -linear (friction, cf. [106]).

In this thesis the focus is on the electronic velocity scales. Target ions are thus neglected in the calculations and only target electrons are considered.

5.1.2. Simulation procedure to compute stopping powers

In the following the setup to compute the stopping power of the electron gas felt by a projectile of a given mass m_i and momentum $\mathbf{p}^{\text{projectile}}$ is described.

First, a correlated electron gas is created: In order to do this, the gas is first initialized self-consistently on Hartree–Fock level. After that, the interaction in the correlation part is slowly turned on (Adiabatic Switching, Sect. 2.3.8), which yields a correlated electron gas. The gas is assumed to be spin-symmetric. The ionic distribution function is initialized to be 0 everywhere and its propagation can thus be skipped in this part of the simulation.

Now, at time $T = t_b$, a narrow and flat Gaussian $\Phi^{\text{projectile}}$ is added to the ionic distribution function, i.e. $G_{\mathbf{p}\sigma i}^{\geq}(T, T) \rightarrow G_{\mathbf{p}\sigma i}^{\geq}(T, T) \mp \frac{i}{\hbar} \Phi_{\mathbf{p}}^{\text{projectile}}$, the Green function at earlier times remains unchanged. The Gaussian is chosen to be so narrow that it represents only projectiles of a single velocity. The height of the Gaussian on the order of 10^{-12} represents the limit of single projectiles being stopped by the target plasma, where projectile-projectile interactions can be neglected.

After the introduction of projectiles into the system, their distribution function starts to evolve over time. The stopping power in media is usually described as the energy loss per units distance. Since the Gaussian was chosen to be narrow (monochromatic), it can be expressed as (n_b is the projectile number density)

$$\frac{dE_{\text{kin}}}{dx} = \frac{1}{n_b} \left(\frac{dx}{dt} \right)^{-1} \frac{d}{dt} \langle E_{\text{kin}} \rangle = \frac{1}{vn_b} \frac{d}{dt} \langle E_{\text{kin}} \rangle . \quad (5.3)$$

Ion projectiles carry huge amounts of kinetic energy compared to the energy loss on the time scale of a few correlation times. This implies that the approach to compute the stopping power using Eq. (5.3) and finite differences is badly conditioned and leads to large errors in standard double precision. This problem can be bypassed by swapping the order of expectation value computation and time derivative, which yields the formula taken from Ref. [107],

$$\frac{dE_{\text{kin}}}{dx} = \pm i\hbar \frac{1}{n_b} \sum_{\sigma} \int \frac{d\mathbf{p}}{(2\pi\hbar)^3} \frac{\mathbf{p} \cdot \mathbf{v}}{v} \frac{d}{dt} G_{\sigma i}^{\leq}(\mathbf{p}, t, t) . \quad (5.4)$$

¹In an electron-hole plasma the mass ratio usually is smaller and the velocity scales cannot always be separated as clearly.

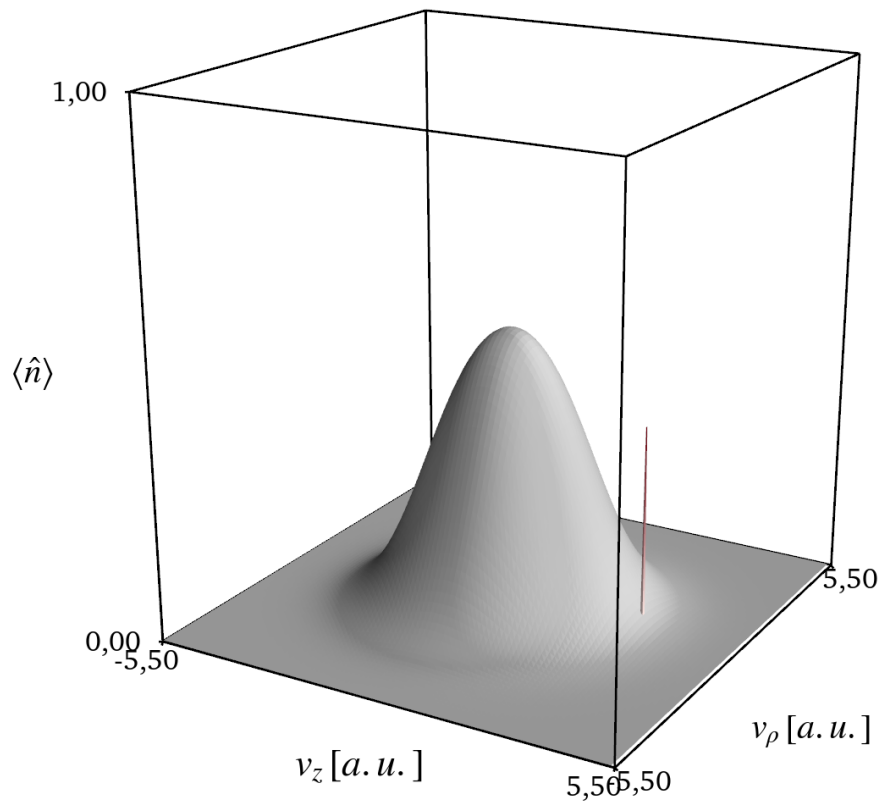


Figure 5.1.: Exemplary stopping setup. The grey distribution function represents the target's electronic velocity distribution. The very sharp red distribution represents the projectiles which are stopped by the target plasma. The plotted projectile distribution function above is multiplied by $4 \cdot 10^7$ to make it visible on the scale of the electronic distribution function. Shown is the setup for electron projectiles, the peak for proton projectiles is slimmer by a factor of $1/1836$.

The numerical condition of this computation can be improved even further: Since the particle number is conserved, the substitution $\mathbf{p} = \tilde{\mathbf{p}} + \langle \mathbf{p} \rangle$ yields

$$\frac{dE_{\text{kin}}}{dx} = \pm i\hbar \frac{1}{n_b} \sum_{\sigma} \int \frac{d\tilde{\mathbf{p}}}{(2\pi\hbar)^3} \frac{\tilde{\mathbf{p}} \cdot \mathbf{v}}{v} \frac{d}{dt} G_{\sigma i}^{\leq}(\tilde{\mathbf{p}} + \langle \mathbf{p} \rangle, t, t), \quad (5.5)$$

where the integrand now is magnitudes smaller, differences in the integrand can be resolved better, and the computation is thus better conditioned.

Strictly speaking, these formulas only describe the loss of kinetic energy in the z direction. As will be shown in section 5.3, this is the only relevant part in calculations with proton projectiles: Even after some relaxation of the distribution function, the z momentum is of the order of several $1000 \hbar a_B^{-1}$, whereas the relevant ϱ momenta are below $3 \hbar a_B^{-1}$. The ϱ contributions of the kinetic energy are thus negligible for heavy projectiles.

In contrast, the distribution function of lightweight projectiles such as electrons quickly broadens significantly. The ϱ component then also notably contributes to the kinetic energy and this formula is not adequate to compute the stopping power there. Luckily, the numerical condition of numerical derivatives is much better for lightweight projectiles, since they lose a notable portion of their kinetic energy, and we can compute the stopping power using usual numerical differentiation.

5.2. Distinction between projectile and target electrons

We are not only interested in the stopping power acting on protons which are heavier than electrons by a mass ratio of 1836, but also the stopping power acting on projectile electrons. Quantum mechanical electrons however are not distinguishable. The separation of the electrons into target and projectiles thus does not make sense in a strict quantum mechanical sense. However, the approximations used in this thesis, i.e. direct SOA and GWA, allow a distinction², just as one can do in classical plasma simulations. This is demonstrated in the following.

We separate a distribution function $f_{\alpha}(\mathbf{p}, t)$ into two 'groups',

$$f_{\alpha}(\mathbf{p}, t) = f_{\alpha}^{(1)}(\mathbf{p}, t) + f_{\alpha}^{(2)}(\mathbf{p}, t). \quad (5.6)$$

We need equations of motion of $f_{\alpha}^{(1)}(\mathbf{p}, t)$ and $f_{\alpha}^{(2)}(\mathbf{p}, t)$ that fulfill

$$\frac{d}{dt} f_{\alpha}(\mathbf{p}, t) = \frac{d}{dt} f_{\alpha}^{(1)}(\mathbf{p}, t) + \frac{d}{dt} f_{\alpha}^{(2)}(\mathbf{p}, t), \quad (5.7)$$

since then all time-dependent single-particle observables are identical between the undivided approach and the two-groups approach, a necessary condition. This can be achieved by making a few modifications to the GKBA and the usual two-component equations of motion:

²Indirect terms would allow the exchange of particles between the two groups. They would retain their particle numbers. In the approach described here, they would quickly adapt their distribution functions until they are identical, $f_{\alpha}^{(1)}(\mathbf{p}, t) = g f_{\alpha}^{(2)}(\mathbf{p}, t)$, up to a rescaling factor g .

- The single-particle energies in the HF-GKBA must remain the same. This means $h_{\alpha}^{\text{HF}}(\mathbf{p}, t)$ is computed from $f_{\alpha}^{(1)}(\mathbf{p}, t) + f_{\alpha}^{(2)}(\mathbf{p}, t)$ instead of from only one group (compared to the two-component case)
- If both groups partially occupy a quantum state, scattering into this state is reduced by Pauli blocking. Pauli blocking is described by the factors $G^>$ which on the time-diagonal is given by (fermion) $G_{\alpha}^>(\mathbf{p}, t, t) = \frac{1}{i\hbar} [1 - f_{\alpha}(\mathbf{p}, t)]$. Here, again, the sum of the contribution of the two groups is used to compute the time-diagonal $G^>$.

A straightforward calculation shows that using these modification the polarization function $\pi(\mathbf{q}, t, t')$ is identical in the two approaches, given that (5.6). It follows that W is also identical. One can then show that Eq. (5.7) is fulfilled. Since initially, at $t = t' = t_0$, Eq. (5.6) is fulfilled, the derivatives match, too, at t_0 . Analogously to a mathematical induction follows that the two approaches give identical (total) expectation values. The two groups approach however allows to consider observables of the 'projectile' group separated from the target group.

Figure 5.2 demonstrates the equality of total ensemble expectation values on the example of the time-dependent kinetic energy.

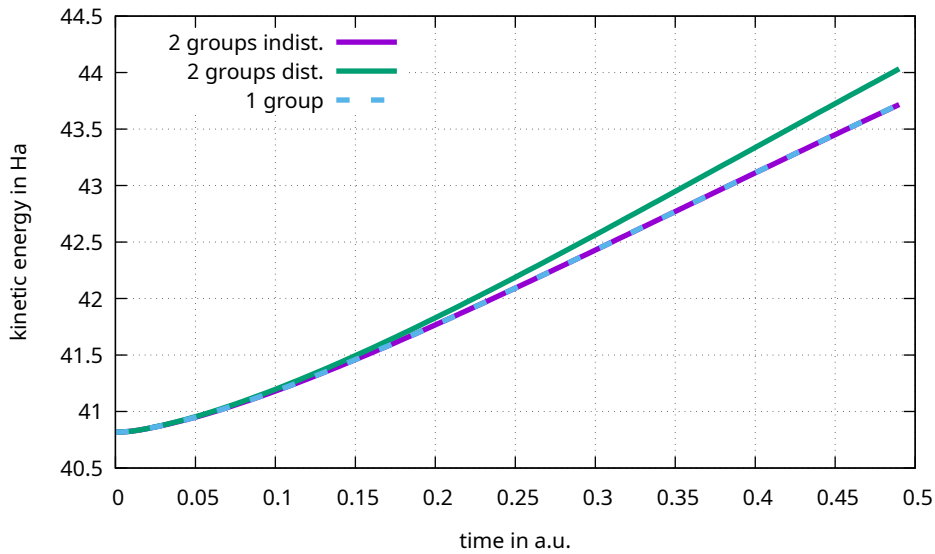


Figure 5.2.: Time-dependent kinetic energy per particle in a nonequilibrium setup. 1 group: Gaussian initial distribution (height 0.6, $\sigma^2 = 2$ Ha), uncorrelated start without adiabatic switching. 2 groups indist.: Gaussian separated into two identical Gaussians of half height, 0.3, and propagated according to the modifications from Sect. 5.2. 2 groups dist.: Same separation, but without modifications. 1 group and 2 groups indist. yield identical observables up to rounding errors. It is significantly different from the calculation with distinguishable particles, demonstrating numerically the correctness of the two groups approach.

5.3. Relaxation of the projectile momentum distribution function

Figure 5.3 shows time-dependent projectile distribution functions for the two considered projectile types, protons and electrons. The convergence parameters are given $DT = 0.005$, $CUTOFFMOMENTUM = 12$ with $NKR = 80$ for the electron calculations and $NKR = 100$ for the ion calculations³. It is visible that the projectiles scatter in all directions but prefer scattering towards the momentum 0. This corresponds to stopping in average and is visible from the final distributions that are stretched and slightly shifted towards 0. Energy and momentum loss of these particular simulations are also shown in Fig. 5.4. These figures show that the difference in mass and therefore in momentum or kinetic energy carried plays a significant role in the amount of dynamics appearing: Over the course of the simulation, the ion projectiles lost around 150 eV of its kinetic energy of roughly 522, 850 eV, approximately 0.029%. The electrons lost around 100 eV of its roughly 280 eV of kinetic energy, i.e. approximately 35.7%. Over the time, the situation of the electron projectiles has changed fundamentally, whereas the proton distribution broadened and stretched a bit but the situation (velocity distribution) stayed essentially the same. A consequence of these barely changing conditions for the proton projectiles is the nearly linear loss of kinetic energy and momentum over time, cf. also Sect. 5.4.3. Such behaviour cannot be observed to this extent with the electron projectiles. It is hence straightforward to define the stopping power for the ion projectiles. Since the energy loss of electron projectiles is changing over time it is not fully characterizable using one parameter.

Figure 5.5 gives a more detailed look into the time-dependent distribution functions via their time-derivatives, for three different mean velocities for the two projectile types each. The derivatives show the drift of the distribution function towards 0 more clearly. Two features stand out: First, the scattering of slow projectiles is less directed than the scattering of fast projectiles. Second, the scattering of electron projectiles is reduced in comparison to proton projectiles of similar velocity. This is especially true for slow projectiles. In this case this can be explained by the influence of Pauli blocking: Electron projectiles primarily scatter into states of a momentum similar to the original momentum. However, if the projectiles are slow, these states are already partially occupied by the target electrons. Since fermionic states can only be occupied once, the scattering into these states is thus reduced. This effect diminishes towards higher projectile velocities.

³The degree of energy conservation achieved for the given parameters is shown in Appendix D.

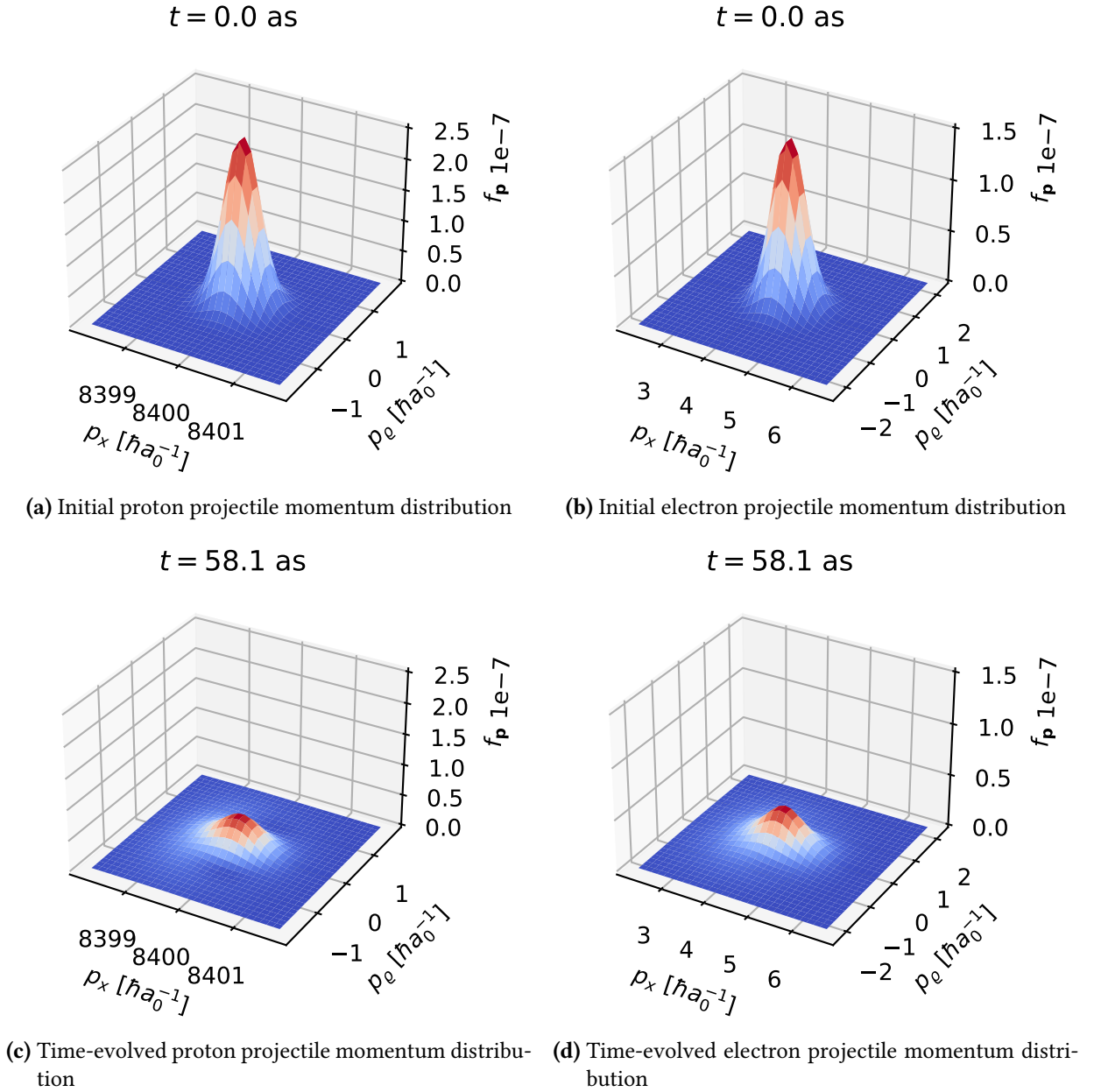


Figure 5.3.: Time-evolution of the projectile distribution functions for proton and electron projectiles of similar velocity: Proton average velocity is $8400 \cdot (m_e/m_p) \approx 4.57 \hbar(a_B m_e)^{-1}$, electron average velocity is $4.5 \hbar(a_B m_e)^{-1}$. Both distribution functions relax in a similar way: they become broader but are stretched towards 0 indicating momentum and kinetic energy loss. $t = 0$ corresponds to the time when the projectile distribution is introduced into the system, after the adiabatic switching.

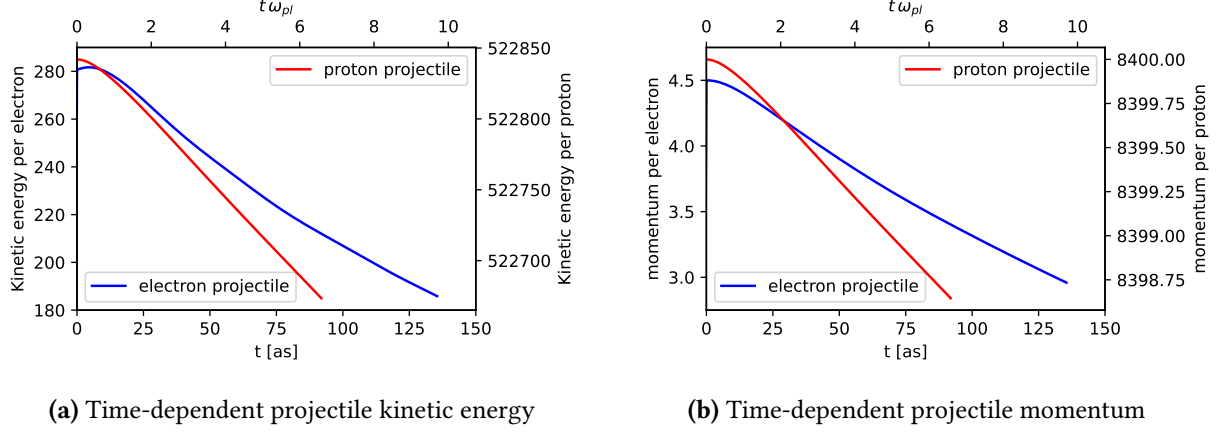


Figure 5.4.: Time-dependent observables from the calculations shown in Fig. 5.3. The electron projectile transfers a larger portion of its kinetic energy and momentum to the target electrons, compared to the proton projectile.

5.4. Non-Markovian and time-dependent stopping power

5.4.1. Description of the findings, comparison between proton and electron projectiles

Figs. 5.6 and 5.7 show the time-dependent stopping powers (Eq. (5.3)) for an array of different projectile velocities. While the ion data are available far beyond the Bragg peak (stopping maximum), this has not been possible for the electrons due to numerical constraints: In order to account for indistinguishability effects (via $G^> \rightarrow \pi$ and h^{HF}), the projectile distribution must be carried by an identical momentum grid as the target electronic distribution. If the projectile distribution is too close to the grid borders, errors will occur: The projectiles partially scatter away from the 0 momentum. Due to the discrete Fourier techniques used for convolutions, a particle that crosses the border of the finite grid in $\pm z$ direction reenters the calculation on the other end of the grid. This is unphysical in plasmas (such effects can be physical in solids when crossing Brillouin zone borders) and thus greatly perturb the results.

Indistinguishability effects however diminish for high-velocity electron projectiles: Since projectiles primarily scatter into states with similar momentum as the original state the target states are then unoccupied by the target plasma. This implies that Pauli-blocking is negligible in this limit. On the other hand, the change of single-particle HF-energies (needed for the HF-GKBA) becomes negligible, if the projectiles are fast. This can be seen from the formula of h^{HF} ,

$$h_{\alpha}^{\text{HF}}(\mathbf{p}, t) = \frac{p^2}{2m} + i\hbar \sum_{\mathbf{k}} \frac{4\pi Z_{\alpha}^2 e^2}{|\mathbf{k} - \mathbf{p}|^2} G_{\alpha}^{<}(\mathbf{k}, t, t). \quad (5.8)$$

An electron only affects the exchange energy of states with similar momentum. If the distributions are separated this effect between them diminishes. It is thus justified to compute stop-

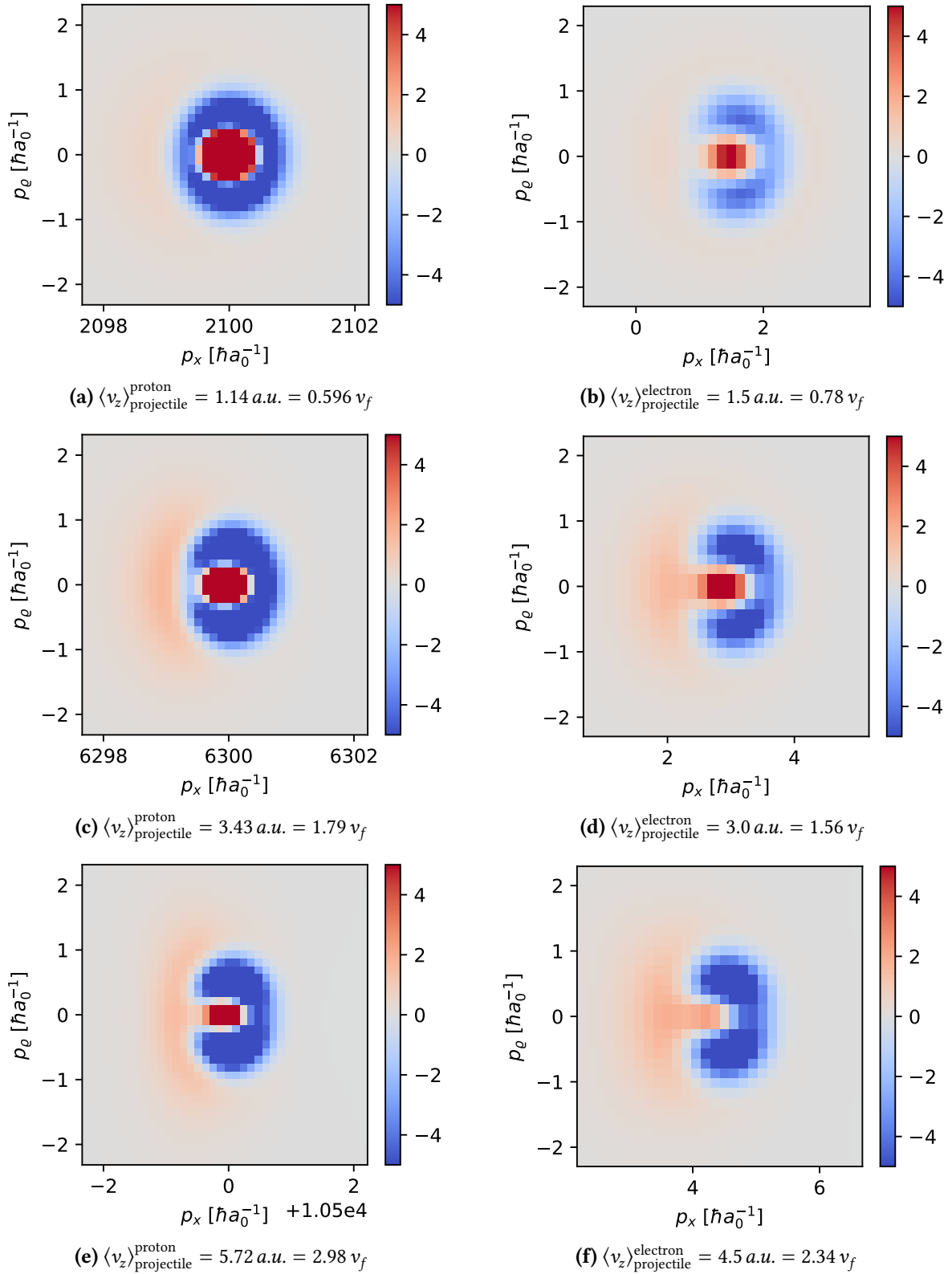


Figure 5.5.: $\partial_t f_{\text{projectile}}(\mathbf{p}, t)/n_{\text{projectile}}$ for the two projectile types and different projectile velocities. Target parameters: $r_s = 1$, $\Theta = 1$. The point of time is 29 as after the introduction of the projectiles into the system. The division by the density normalizes the derivatives, since the projectile densities are slightly different. Dynamics of slow electrons, cf. Fig. 5.5b, is significantly reduced due to Pauli blocking, compared to protons, cf. Fig. 5.5a.

ping powers for electron projectiles in the high-velocity limit using 'distinguishable' electrons: These particles follow the same numerics as proton projectiles, just with a differently signed charge (which only appears squared anyway) and with the mass of an electron⁴. Stopping powers of these fictional particles in the low velocity limit are also of interest: They separate effects due to small mass from the effects due to indistinguishability and allow a better understanding. The stopping power as a function of time and velocity is shown in Fig. 5.8.

In the case of proton projectiles of high velocity, Fig. 5.6, the stopping power quickly builds up and then is constant, as has already been noted in the previous section. If the projectiles are slow, however, the buildup process takes longer and does not reach a constant value during these calculations, but is oscillating instead, with roughly twice the plasma frequency⁵. The findings are qualitatively different in the case of electron projectiles, cf. Fig. 5.7: For high velocities, the stopping power temporarily reaches a maximum and then slowly declines again. Oscillations in the low-velocity region can be found here, too, with the same frequency. The maximum stopping power is found at higher velocities compared to the case of proton projectiles. This is especially visible in the distinguishable 'electron' plot, Fig. 5.8, where higher projectile velocities can be included.

5.4.2. Quantum Lenard-Balescu equation

The nonequilibrium *GW* equations are difficult to handle analytically. One often considers the so-called *Markov-limit* of quantum kinetic equations (cf. [14], chapter 10.3.1), which bans the memory-dependence from the equations in two steps

1. The memory integral at time t is dependent on the distribution function $f(t')$ at all earlier times, $t' \leq t$. Under the assumption that f changes slowly during a correlation time, one can approximate $f(t') \approx f(t)$. The resulting collision integral only depends on $f(t)$ and the initial time t_0
2. The dependence on the initial time, t_0 , is removed by assuming the limit $t_0 \rightarrow -\infty$.

This way, one finds the **quantum Lenard-Balescu collision integral** (which in this context is complete time derivative of the distribution function, $\partial_t f = I$),

$$I_\alpha^{LB}(\mathbf{p}_1, t) = \frac{2\pi}{\hbar} \sum_\beta \int \frac{d\mathbf{p}_2}{(2\pi\hbar)^3} \int \frac{d\mathbf{q}}{(2\pi\hbar)^3} \left| \frac{Z_\alpha^2 w(\mathbf{q})}{\varepsilon(\mathbf{q}, E_{\mathbf{p}_1}^\alpha - E_{\mathbf{p}_1 - \mathbf{q}}^\alpha + i\delta, t)} \right|^2 \delta(E_{\mathbf{p}_1}^\alpha + E_{\mathbf{p}_2}^\beta - E_{\mathbf{p}_1 - \mathbf{q}}^\alpha - E_{\mathbf{p}_2 + \mathbf{q}}^\beta) \times \\ \times \left\{ f_\alpha(\mathbf{p}_1 - \mathbf{q}) f_\beta(\mathbf{p}_2 + \mathbf{q}) [1 \pm f_\alpha(\mathbf{p}_1)] [1 \pm f_\beta(\mathbf{p}_2)] \right. \\ \left. - f_\alpha(\mathbf{p}_1) f_\beta(\mathbf{p}_2) [1 \pm f_\alpha(\mathbf{p}_1 - \mathbf{q})] [1 \pm f_\beta(\mathbf{p}_2 + \mathbf{q})] \right\} \Big|_t. \quad (5.9)$$

⁴Since the signs of the charges do not appear in these calculations, this can also be interpreted as the stopping of positrons, where pair annihilation is neglected.

⁵This is also the frequencies at which the long wavelength plasmon distribution oscillates due to rather short switching times, cf. Appendix E. This should be fixed if the switching time is sufficiently long.

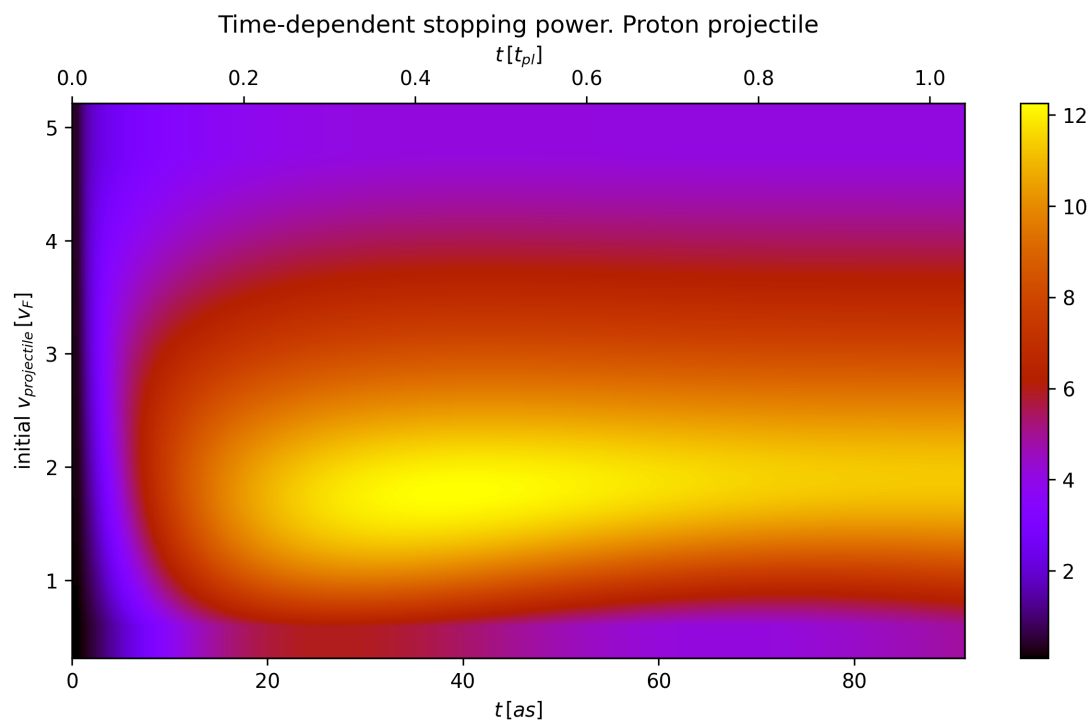


Figure 5.6.: Stopping power of proton projectiles as function of time and projectile velocity

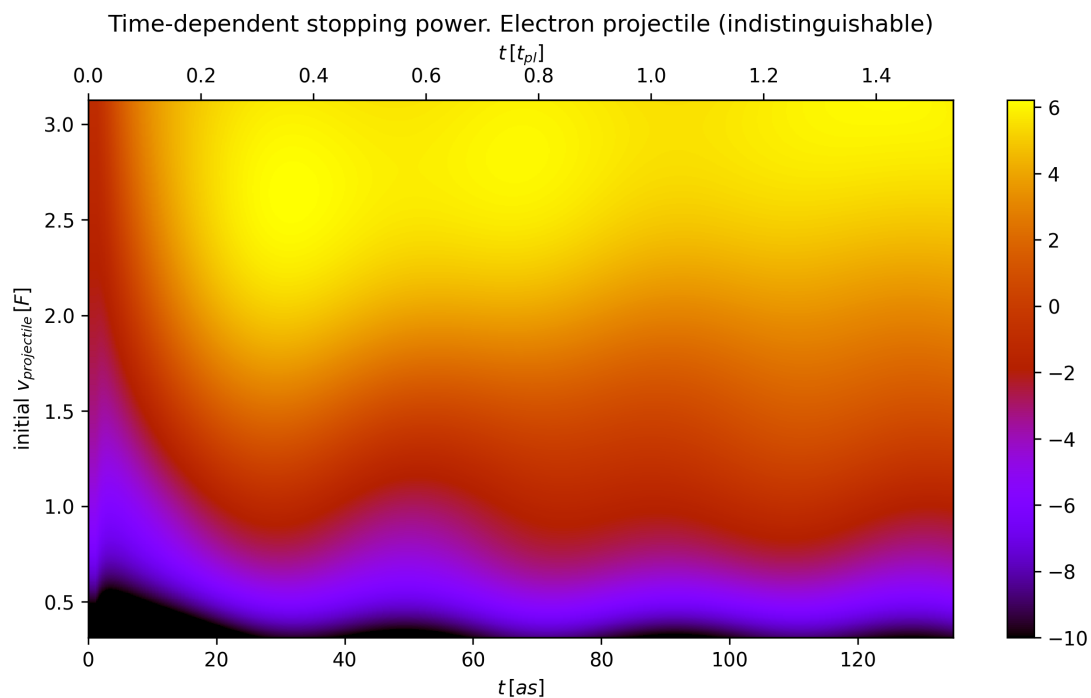


Figure 5.7.: Stopping power of electron projectiles as function of time and projectile velocity

In the Markov-limit it contains the same single-particle energy conserving δ function as the MQL. The inverse dielectric function in the Markov limit is given by the RPA result, the Lindhard formula,

$$\varepsilon_{\text{RPA}}(\mathbf{q}, \omega + i\delta, t) = 1 - w_{\mathbf{q}} \sum_{\beta} Z_{\beta}^2 \int \frac{d\mathbf{k}}{(2\pi\hbar)^3} \frac{f_{\beta}(\mathbf{k}, t) - f_{\beta}(\mathbf{k} + \mathbf{q}, t)}{E_{\mathbf{k}}^{\beta} - E_{\mathbf{k}+\mathbf{q}}^{\beta} + \hbar\omega + i\delta}. \quad (5.10)$$

Markovian quantum kinetic equations have been used before to study stopping power. In particular, the expression derived from the Quantum Lenard-Balescu, cf. Refs. [107, 108], is given by

$$\frac{dE_{\text{kin}}}{dt} = \frac{2Z_b^2 e^2}{\pi v^2} \int_0^{\infty} \frac{dk}{k} \int_{\hbar k^2/2m_b - kv}^{\hbar k^2/2m_b + kv} d\omega \left[\omega - \frac{\hbar k^2}{2m_b} \right] \text{Im} \varepsilon_{\text{RPA}}^{-1}(k, \omega) n_B(\omega), \quad (5.11)$$

where $n_B(\omega) = [\exp(\hbar\omega/k_B T)]^{-1}$ is the plasmon Bose distribution. This expression does not include modifications necessary to describe Pauli-blocking effects arising from indistinguishability of projectile electrons.

5.4.3. Comparisons

Given a plasma, stopping power is usually written as a simple function of the projectile velocity, $S(v)$. In order to compare to other methods, the time-dependent data must be condensed into single stopping values. Fig. 5.9 demonstrates the strategy used in this thesis. First of all, the proton stopping power quickly reaches saturation (apart from some smaller oscillations) after a short buildup time. The z component of the stopping power acting on an electron projectile quickly builds up but then steadily declines. This reflects the quick changes to the projectile distribution function. The full stopping power, i.e. \dot{E}_{kin}/v , is more stable over time and includes the relevant z component of the kinetic energy. Velocity dependent stopping values are then estimated by computing average and standard deviation of the time-dependent stopping power over a period of time. The corresponding velocity value is computed from the average velocity during the same time window.

The stopping values using this approach are given in Fig. 5.10. Also included are data using the RPA Markov limit [109] (linear response), given by Eq. (5.11). The RPA stopping formula has been evaluated for an ideal dispersion of the target electrons. Also given in the figure are statically screened SOA stopping values which are significantly lower than their *GW* counterparts.

GW and SOA

The SOA yielding smaller stopping values than the RPA is an effect that has been observed in previous Markovian calculations before as well [110]. This effect becomes especially strong in the high density range, such as it is the case here. The time-dependent SOA stopping power

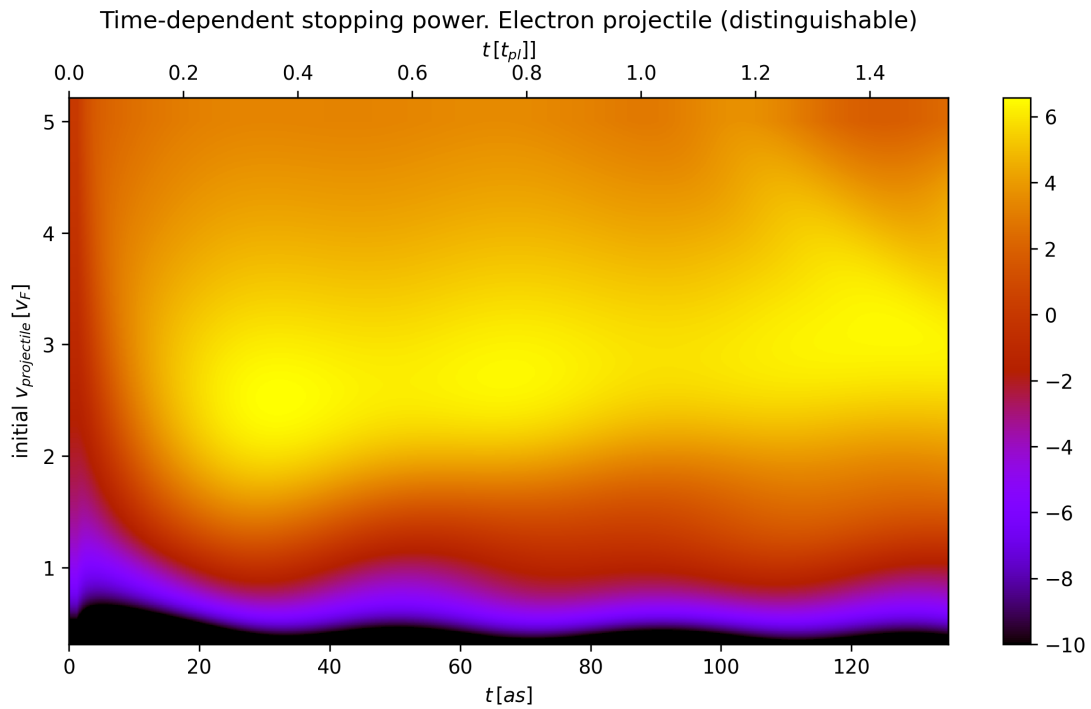


Figure 5.8.: Stopping power of distinguishable 'electron' projectiles as function of time and projectile velocity

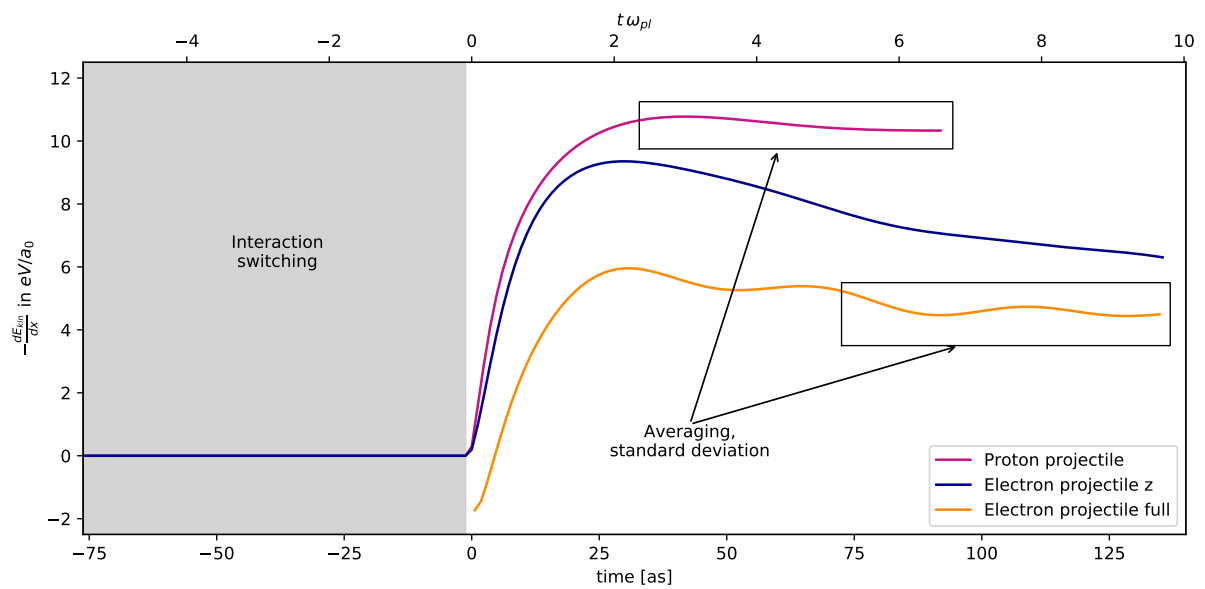


Figure 5.9.: Time-dependent stopping power. The stopping power acting on the proton quickly reaches a nearly constant value. Regarding the electron projectile, it is notable that the z component of the stopping power changes more over time than the 'full' stopping power.

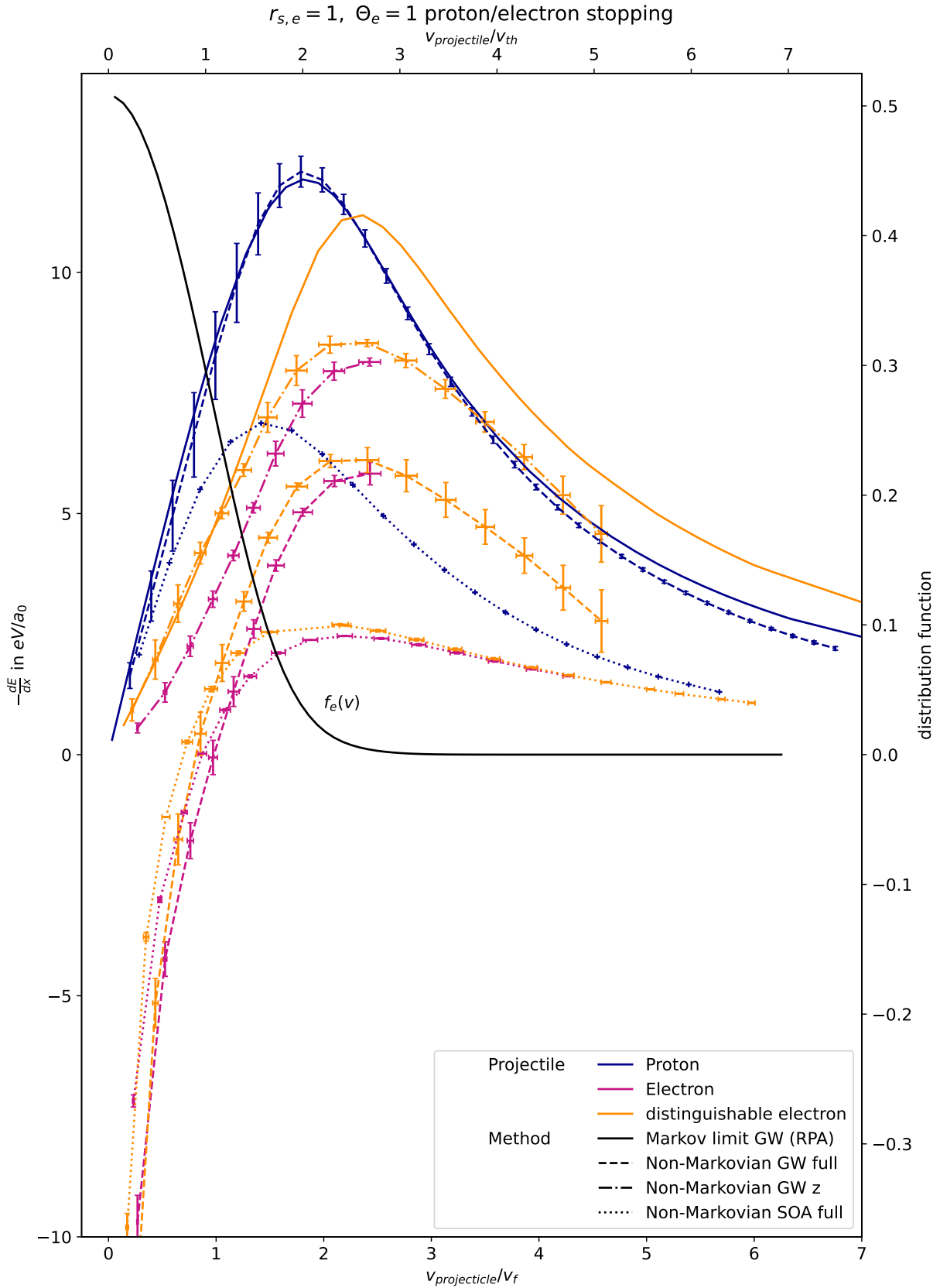


Figure 5.10.: Stopping powers for various projectile types and methods. Note, that the z component of the GW stopping power is always positive, whereas the full stopping power becomes negative for projectiles that are both slow and lightweight. $v_{th} = \sqrt{3k_B T/m_e}$ is used as definition of the thermal velocity in the upper velocity scale.

does not oscillate, cf. Appendix F, which reinforces the assumption that it is the oscillations of the plasmon occupation that leads to the fluctuation of the *GW* stopping power.

Negative stopping values at low velocities

The full *GW* stopping powers of lightweight particles becomes negative at low projectile velocities while they stay positive for proton projectiles. This, too, has been observed in static RPA calculations, cf. Ref. [108]. At a given velocity v , a proton has significantly more kinetic energy than an electron. The full electron stopping power changes its sign around the thermal velocity⁶: Below that, the projectiles are heated up by the target, which manifests itself as negative stopping power. For a proton to carry less kinetic energy than an average target electron, it must have a velocity that is smaller by a factor of roughly $\sqrt{1836} \approx 43$. Such velocities are not included in this figure and will be investigated in the future⁷.

Differences between 'distinguishable' and indistinguishable electron projectiles

The calculations of electron projectiles and 'distinguishable electrons' are different in the low-velocity range but converge in the high-velocity limit. This is due to the fact that the projectiles scatter via the coulomb interaction $w(\mathbf{q}) = 4\pi/q^2$, which clearly prefers scattering into states with small changes of the projectile momentum. This means, that if the incoming electron projectile has a momentum well beyond a few fermi momenta, the states it will scatter into are unoccupied. On the other hand, if its momentum is small, its 'neighbouring momenta' are occupied and the scattering will be inhibited by the Pauli principle. Generally, since the target distribution is maximal at $\mathbf{p} = 0$, scattering towards $\mathbf{p} = 0$ becomes less efficient than scattering away from $\mathbf{p} = 0$: This means that the heating up of the electron projectile distribution is enhanced compared to the distinguishable counterpart. In other words, the stopping power is lowered (and heating increased).

Comparison of *GW* with static RPA

The proton results of *GW* and RPA agree very well, at least in the range $[0, 3 v_F]$. Beyond this range, we observe increasing deviations. These are consequences of different requirements: Since the dispersion around high-velocity protons becomes steeper, a finer momentum grid is necessary. It is expected that a reduction of the grid spacing cures these deviations and that they are just a numerical error.

The 'electronic' RPA data in Fig. 5.10 are given for the case of 'distinguishable electrons'. The RPA data and the *GW* data disagree strongly at all velocities.

So why does the static limit of *GW*, the RPA agree well for proton projectiles, but disagrees strongly for the lightweight particles? Over the course of the simulation, the projectile distribution functions broaden. The assumption of slowly changing distribution functions, one of the

⁶Here, the Maxwellian RMS thermal velocity, $v_{th} = \sqrt{3k_B T/m_e}$, is used as a scale. Of course this only represents the kinetic energy of particles well in the low-degeneracy limit.

⁷At these velocities the radial kinetic energy change will matter. This means that the 'full' stopping power and the z component will not agree well anymore, and we have to resort to the 'full' method.

core assumption of the static limit, is thus not justified. As we have seen from the simplified collision integrals in Sect. 5.4.2, the efficiency at which a collision between two particles can happen depends on the energy balance. Energy offsets do not matter, but the slope $\nabla E_{\mathbf{p}}^a$ and the second derivative, $\nabla \otimes \nabla E_{\mathbf{p}}^a$ do. Over the course of a calculation, the proton projectiles change their momentum \mathbf{p} slightly to $\mathbf{p} + \Delta\mathbf{q}$ with $|\Delta\mathbf{q}| \ll |\mathbf{p}|$. Since $\nabla E_{\mathbf{p}}^p = \mathbf{v}^p \approx \mathbf{v}^p + \frac{\Delta\mathbf{q}}{m_p} = \nabla E_{\mathbf{p}+\Delta\mathbf{q}}^p$, the single particle energy slope around the momenta occupied by projectiles before and after first collisions is nearly the same.

The *GW* equations discussed in this thesis up until now are given in a form that is useful for numerical solutions. Eq. (10.38) in Ref. [14] uses three nested time integrals to equivalently express the collision integral in terms of $W^{\mathcal{R}/\mathcal{A}}$ instead of W^{\lessgtr} . The generalization to multiple components is given in the form

$$I_{\alpha}(\mathbf{p}, t) = \frac{1}{\hbar^4} \sum_{\mathbf{q}} Z_{\alpha}^2 \int_{t_0}^t dt_2 \int_{t_0}^{t_2} dt_4 U_{\alpha}^{0,\mathcal{R}}(\mathbf{p} - \mathbf{q}, \mathbf{p}, t, t_2) \Phi_{\alpha}^{\lessgtr}(\mathbf{p} - \mathbf{q}, \mathbf{p}, t_2) \Psi_{\beta}^{\lessgtr}(\mathbf{q}, t, t_2, t_4) + \text{c.c.} - (>\leftrightarrow<), \quad (5.12)$$

where Ψ , which contains the parts of the formula not further relevant for this discussion, is given by

$$\Psi(\mathbf{q}, t, t_2, t_4) = \sum_{\mathbf{k}\beta} Z_{\beta}^2 W^{\mathcal{A}}(\mathbf{q}, t_4, t_2) \left[\int_{t_0}^{t_4} dt_3 W^{\mathcal{R}}(\mathbf{q}, t, t_3) U_{\beta}^{0,\mathcal{A}}(\mathbf{k} + \mathbf{q}, \mathbf{k}, t_3, t_4) \Phi_{\beta}^{\lessgtr}(\mathbf{k} + \mathbf{q}, \mathbf{k}, t_3) + \int_{t_4}^t dt_3 W^{\mathcal{R}}(\mathbf{q}, t, t_3) U_{\beta}^{0,\mathcal{A}}(\mathbf{k} + \mathbf{q}, \mathbf{k}, t_3, t_4) \Phi_{\beta}^{\lessgtr}(\mathbf{k} + \mathbf{q}, \mathbf{k}, t_4) \right], \quad (5.13)$$

and the short forms $\Phi_{\alpha}^{\lessgtr}(\mathbf{p} - \mathbf{q}, \mathbf{p}, t_2) = f_{\alpha}^{\lessgtr}(\mathbf{p} - \mathbf{q}, t) f_{\alpha}^{\lessgtr}(\mathbf{p}, t)$ and $f^{\lessgtr} = f$, $f^{\lessgtr} = (1 \pm f)$ and the free retarded electron-hole propagator $U^{0,\mathcal{R}}$ is given by

$$U_{\alpha}^{0,\mathcal{R}}(\mathbf{p} - \mathbf{q}, \mathbf{p}, t, t_2) = \Theta[(t - t_2)] \exp \left\{ -\frac{i}{\hbar} \int_{t_2}^t d\bar{t} \left[\frac{(\mathbf{p} - \mathbf{q}^2)}{2m_{\alpha}} - \frac{\mathbf{p}^2}{2m_{\alpha}} \right] \right\} \quad (5.14)$$

$$= \Theta[(t - t_2)] \exp \left\{ -\frac{i}{\hbar} \int_{t_2}^t d\bar{t} \left[-\mathbf{q} \cdot \mathbf{v} + q^2/2m_{\alpha} \right] \right\}, \quad (5.15)$$

and analogously for the β species. The contribution of the projectiles to Ψ (through $W^{\mathcal{R}/\mathcal{A}}$) is negligible due to low density. Now we write the energy loss over time using this form of the

collision integral,

$$\begin{aligned} \frac{d}{dt} \langle \hat{T}_\alpha \rangle(t) &= \sum_{\mathbf{p}} \frac{\mathbf{p}^2}{2m_\alpha} I_\alpha(\mathbf{p}, t) \\ &= \frac{1}{\hbar^4} Z_\alpha^2 \sum_{\mathbf{p}\mathbf{q}} \frac{\mathbf{p}^2}{2m_\alpha} \int_{t_0}^t dt_2 \int_{t_0}^{t_2} dt_4 U_\alpha^{0,\mathcal{R}}(\mathbf{p} - \mathbf{q}, \mathbf{p}, t, t_2) \Phi_\alpha^<(\mathbf{p} - \mathbf{q}, \mathbf{p}, t_2) \Psi_\beta^<(\mathbf{q}, t, t_2, t_4) \\ &+ \text{c.c.} - (>\leftrightarrow<) \end{aligned} \quad (5.16)$$

$$\begin{aligned} &= \frac{1}{\hbar^4} Z_\alpha^2 \sum_{\mathbf{p}\mathbf{q}} \frac{1}{2} \left[\frac{\mathbf{p}^2 - (\mathbf{p} - \mathbf{q})^2}{2m_\alpha} \right] \int_{t_0}^t dt_2 \int_{t_0}^{t_2} dt_4 U_\alpha^{0,\mathcal{R}}(\mathbf{p} - \mathbf{q}, \mathbf{p}, t, t_2) \Phi_\alpha^<(\mathbf{p} - \mathbf{q}, \mathbf{p}, t_2) \\ &\times \Psi_\beta^<(\mathbf{q}, t, t_2, t_4) + \text{c.c.} - (>\leftrightarrow<), \end{aligned} \quad (5.17)$$

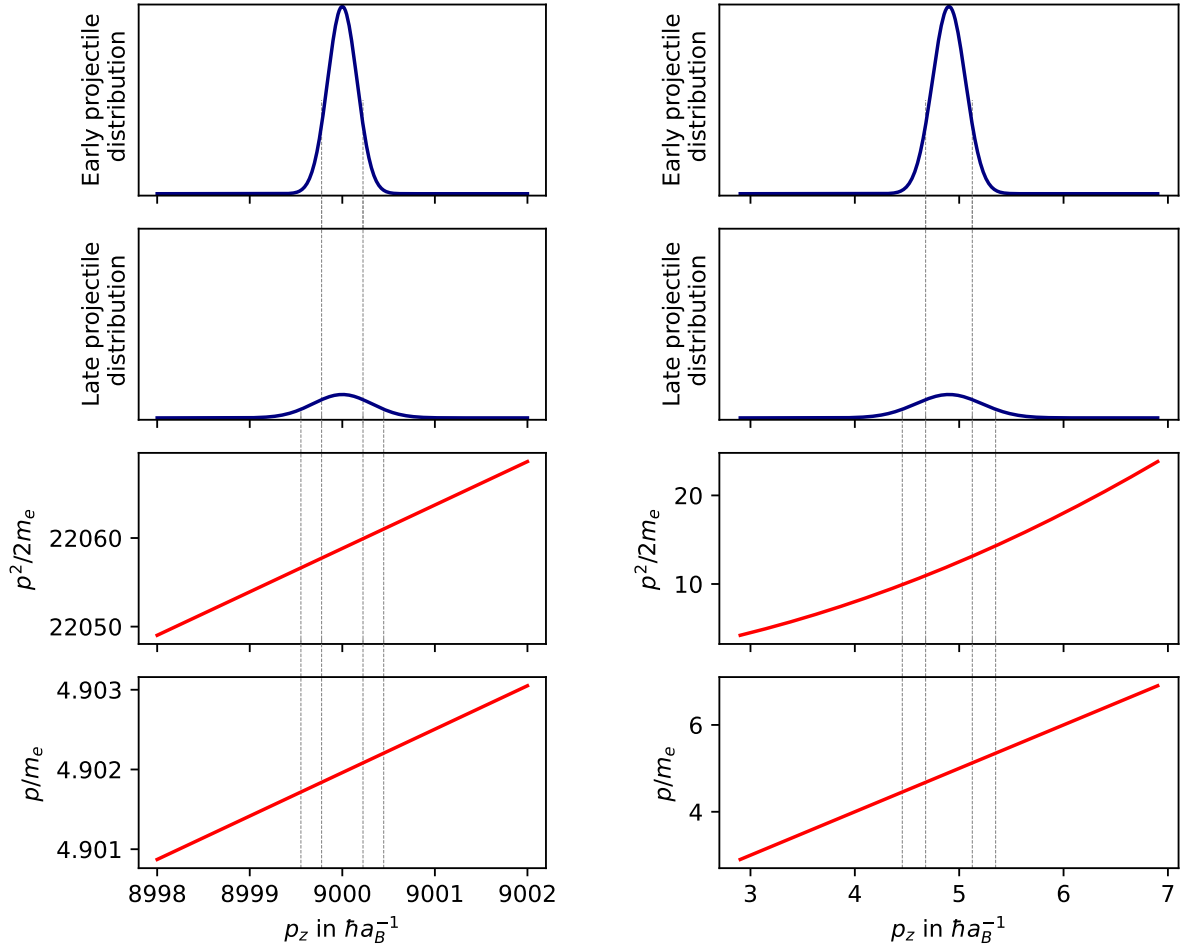
where the kinetic energy expression has been symmetrized in order to fit the expression in the electron hole propagator $U^{0,\mathcal{R}}$. Since the projectile distribution is assumed to be negligibly flat, we use $f^> \equiv 1$, and the kinetic energy loss takes the form

$$\begin{aligned} \frac{d}{dt} \langle \hat{T}_\alpha \rangle(t) &= \frac{1}{\hbar^4} Z_\alpha^2 \sum_{\mathbf{p}\mathbf{q}} \frac{1}{2} \left[\frac{\mathbf{q}^2 - 2\mathbf{q} \cdot \mathbf{p}}{2m_\alpha} \right] \int_{t_0}^t dt_2 \int_{t_0}^{t_2} dt_4 \exp \left\{ -\frac{i}{\hbar} \int_{t_2}^t d\bar{t} \left[\frac{\mathbf{q}^2 - 2\mathbf{q} \cdot \mathbf{p}}{2m_\alpha} \right] \right\} \\ &\times f_\alpha^<(\mathbf{p} - \mathbf{q}, t_2) \Psi_\beta^<(\mathbf{q}, t, t_2, t_4) + \text{c.c.} - (>\leftrightarrow<), \end{aligned} \quad (5.18)$$

As discussed before, $f_\alpha^<$ only is occupied in the vicinity of the mean projectile momentum, $\bar{\mathbf{p}}$. In this range, $(\mathbf{q}^2 - \mathbf{q} \cdot \mathbf{p})/2m_\alpha$ is nearly constant with regard to the \mathbf{p} integration, and we find

$$\begin{aligned} \frac{d}{dt} \langle \hat{T}_\alpha \rangle(t) &= \frac{1}{\hbar^4} Z_\alpha^2 \sum_{\mathbf{q}} \frac{1}{2} \left[\frac{\mathbf{q}^2 - \mathbf{q} \cdot \bar{\mathbf{p}}}{2m_\alpha} \right] \int_{t_0}^t dt_2 \int_{t_0}^{t_2} dt_4 \exp \left\{ -\frac{i}{\hbar} \int_{t_2}^t d\bar{t} \left[\frac{\mathbf{q}^2 - \mathbf{q} \cdot \bar{\mathbf{p}}}{2m_\alpha} \right] \right\} \\ &\times \sum_{\mathbf{p}} f_\alpha^<(\mathbf{p} - \mathbf{q}, t_2) \Psi_\beta^<(\mathbf{q}, t, t_2, t_4) + \text{c.c.} - (>\leftrightarrow<). \end{aligned} \quad (5.19)$$

Here, the time-dependent distribution function does not explicitly enter the stopping power, as long as $\bar{\mathbf{p}}/m_\alpha$ is a good approximation to \mathbf{p}/m_α . With this we have an analytical explanation why even though the proton projectile distribution function changes over time, static methods still agree well. In a more pictorial manner, e.g. Fig. 5.11: The protons start scattering during the correlation time with the target and exchange tiny amounts of momentum, barely changing the velocity. When transferring momentum, the particles transfer kinetic energy given by $(\mathbf{q}^2 - 2\mathbf{q} \cdot \mathbf{p})/2m_\alpha = \mathbf{q}^2/2m_\alpha - \mathbf{v} \cdot \mathbf{q}$. The energy transfer rate stays the same for the first consecutive collisions (after a long time, of course, thermalization will occur) and it turns out, that this is enough to justify taking the static limit. On the other hand, for the lightweight electron projectiles, we find similar broadening of the projectile distribution in momentum space. This however corresponds to a significant change of velocity of the particle, and consecutive collisions transfer a different amount of energy. The free propagators can thus not be approximated by using the mean momentum, since different parts of the projectile distribution function behave very differently. The stationarity assumption of the projectile distribution which leads to the quantum Lenard-Balescu equation, eq. (5.9), is thus not justified for electron projectiles.



(a) Exemplary sketch of the mechanism for proton projectiles

(b) Exemplary sketch of the mechanism for electron projectiles

Figure 5.11.: The different curvatures of the dispersion, experienced by proton and by electron projectiles. The mean velocity in both subfigures is the same. After some initial broadening during correlation buildup, the electron distribution function spans a range where the gradient of the dispersion changes, thereby changing the scattering properties of the different particles at different 'ends' of the distribution. In contrast, the slope for proton projectiles is nearly constant. Even after some initial scatterings, the proton projectiles continue to perceive the target electrons in a similar way and to build up energy loss until the static result is reached.

6. Conclusion and outlook

This thesis studied two topics: The viability and scalings of similar up to equivalent GKBA Green function/reduced density matrix methods for uniform systems, and the non-Markovian effects of GW on the stopping power in uniform warm dense plasmas.

The G1–G2 scheme was hoped to tackle the scaling problem with the number of time steps, N_t , that occurs in long-time simulations using NEGF and the GKBA. While it does in principle allow arbitrary long simulations, it turns out that its base memory demand is extraordinary high for uniform systems in 2 or 3 dimensions, especially if isotropy is not assumed. This is worsened by the fact that aliasing occurs in the usual free or HF-GKBA.

Correlated GKBA and therefore off-diagonal damping methods could cure the aliasing and allows an increase in efficiency by memory truncation [111, 112]. This would benefit both, the G1–G2 scheme and especially the usual memory integral methods, for both numerical and for physical reasons. It is therefore of high future interest. The scalings discussed concern only the SOA and the GWA . Since the TMA or the DSLA are currently not feasible in the memory integral approach (or in the DSLA case, not even known) and their memory demand is not higher in the G1–G2 scheme (compared to SOA and GWA), the latter might be the method of choice which makes these approximations accessible in the future.

First tests have shown that the G1–G2 scheme can also be applied to uniform honeycomb lattice models with extraordinary stability, even with rather small convergence parameters. This stability is expected to be a property of the chosen Brillouin zone samples, so it should also be given in the older formalism. This is of relevance since the aliasing problems in principle also exist here. For future applications to TMDCs the method of choice thus depends on the selfenergy approximation: SOA and GW are preferably used in the memory integral approach, the other selfenergies are more accessible in the G1–G2 scheme.

Many physical questions, e.g. the one-directional particle beams studied in this thesis, or the electric field part of linearly polarized lasers, can be studied using a cylinder symmetric description. Due to scaling difficulties of the G1–G2 scheme the memory integral approach has been used to study cylinder symmetric plasmas using the GWA and the SOA. In order to do so, a variety of numerical procedures has been combined in a simulation program. GW calculations contain two expensive parts: Fourier transforms and time integrals. Previous implementations [102] used a 3D grid \mathbf{k} point grid where symmetry equivalent grid points are identified, and 3D Fourier transforms are utilized. The implementation in this thesis reduces the number of stored \mathbf{k} points even further (they are all in a plane) by use of a Hankel transform. Integrations have been employed via quadrature formulas that have proven to be accurate in the past. A comparison with alternative numerical methods, on the other hand, so far has not been made. In

particular, there are better quadrature formulas that yield more precise time integrals, e.g. using spline integration. Regarding Fourier transforms, or rather in cylindric symmetry, discrete Hankel transforms: Of the methods known to me the most precise method has been used.

There are faster methods and for practical reasons it would be interesting to see in future developments, how much speed up of the whole program is possible (time integrals are not accelerated) and how large the accuracy losses might be. Simulation time is usually limited by the memory needed to store the screened potential W , so a speed up of the calculation would not allow us to reach longer in-simulation times. Speed-ups would however give the user more flexibility to explore new functionalities of the program or to quickly get an overview about new physical situations, before more expensive and precise simulations can be performed to secure the results.

Another promising approach to reduce memory demand and accelerate full two-time NEGF calculations has recently been employed by Jason Kaye and Denis Golež [113]. The basic idea is to identify the relevant contributions in the two-time quantities using a singular value decomposition and compress the data cleverly. Similar ideas might be suitable to improve future GW-GKBA calculations.

A newly written program utilizing discrete Hankel transformations has been used to investigate non-Markovian effects on the stopping power in the GW approximation. In order to model this, the electronic part of a target plasma has been simulated. Correlations are introduced using adiabatic switching before projectiles represented by a small monochromatic distribution function are added to the system. This distribution function (and the target distribution as well, even though its time-dependence is negligible due to small projectile densities) is propagated in time, giving access to the time-dependent kinetic energy per particle and other observables. In particular, the stopping power, i.e. kinetic energy loss per distance, is accessible this way. Three different projectile types are investigated: Protons, electrons and an artificial particle type with the mass of an electron but distinguishable from one ('distinguishable electron'). The proton stopping power has been found to agree very well with results within the static limit of the GW approximation. It turns out that the reason for this are the rather small changes of projectile velocity with each collision, which is a necessary assumption in its analytical explanation. In contrast, the lightweight projectiles exchange the same magnitude of momentum as protons do, which on the other hand corresponds to significant changes in the velocity of the projectiles: The assumption of a static monochromatic distribution of lightweight projectiles hence is not realistic. The static limit is thus not applicable here, which is also confirmed by the numerical results: The non-Markovian GW stopping values are significantly reduced compared to the static limit, where only data for 'distinguishable electrons' are currently available¹. The stopping power of the electrons is even more reduced compared to 'distinguishable electrons' which is due to Pauli-blocking caused by target electrons, which weakens scattering towards $\mathbf{p} = 0$.

Particularly for low projectile velocities, oscillations with double the plasma frequency in the time-dependent stopping power are observed, but whose time average is well explained by the

¹An extension of the static formula to indistinguishable projectile/particle systems is work in progress.

analysis. So far, the physical meaning of this is not clear. This could be an artifact of rather short switching times, which were used since longer times make the calculations significantly more expensive. In particular, the plasmon occupations oscillate a bit in these calculations, with the double plasma frequency in the long wavelength limit. This conjecture is further reinforced by the fact that oscillations of such kind do not appear in SOA, which does not treat plasmons dynamically. To investigate this, next calculations will thus include a reduction of the basis size and in turn an increase of the time step number to let the plasmon dynamics relax more before the projectiles are added.

So far, the ionic target background has been neglected due to numerical reasons and since its influence is only expected at very low velocities, which can be seen from the Markov limit. Apart from collisions such a background can affect the dynamics of the screened potential. The ion background can efficiently be included in a static and classical manner, of which the influence should be studied in the future.

The projectile densities in the simulations presented in this thesis are many magnitudes smaller than target particle densities in order to model single projectiles being stopped in the plasma. However, high density particle beams are of interest in context of the fast ignition fusion, a type of inertial confinement fusion where the particle beam is used to compress and heat up the hydrogen target capsule. In this situation, the beam particles significantly contribute to the plasmon dynamics which can significantly change the outcome. However, the *GW* method presented in this thesis *can* take these effects into account and should be applied to dense particle beams in the future.

Appendices

A. Useful NEGF relations in uniform systems

This appendix contains a collection of formulas and relations for Green functions and related quantities in uniform systems that are useful in either analytical investigations or numerical implementations.

A.1. Relations for one-particle Green function

Time transposition symmetry of G^{\gtrless}

$$G_{\mathbf{k}\alpha}^{\gtrless}(t, t') = -[G_{\mathbf{k}\alpha}^{\gtrless}(t', t)]^* \quad (\text{A.1})$$

Time diagonal relation between $G^>$ and $G^<$

$$G_{\mathbf{k}\alpha}^>(t, t') = G_{\mathbf{k}\alpha}^<(t, t') + \frac{1}{i\hbar} \quad (\text{A.2})$$

Generalized Kadanoff–Baym ansatz

$$G_{\mathbf{k}\alpha}^{\gtrless}(t, t') = i\hbar G_{\mathbf{k}\alpha}^{\mathcal{R}}(t, t') G_{\mathbf{k}\alpha}^{\gtrless}(t', t') - i\hbar G_{\mathbf{k}\alpha}^{\gtrless}(t, t) G_{\mathbf{k}\alpha}^{\mathcal{A}}(t, t')$$

with the approximate spectral components $G_{\mathbf{k}\alpha}^{\mathcal{R}/\mathcal{A}}$ which obey in HF-approximation

$$i\hbar \frac{\partial}{\partial t} G_{\mathbf{k}\alpha}^{\mathcal{R}/\mathcal{A}}(t, t') = h_{\mathbf{k}\alpha}^{\text{HF}}(t) G_{\mathbf{k}\alpha}^{\mathcal{R}/\mathcal{A}}(t, t') + \delta(t, t') \quad (\text{A.3})$$

$$-i\hbar \frac{\partial}{\partial t'} G_{\mathbf{k}\alpha}^{\mathcal{R}/\mathcal{A}}(t, t') = h_{\mathbf{k}\alpha}^{\text{HF}}(t') G_{\mathbf{k}\alpha}^{\mathcal{R}/\mathcal{A}}(t, t') + \delta(t, t') \quad (\text{A.4})$$

This implies the following off-diagonal equations of motion for G^{\gtrless} (informal)

$$i\hbar \frac{\partial}{\partial t} G_{\mathbf{k}\alpha}^{\gtrless}(t \geq t') = h_{\mathbf{k}\alpha}^{\text{HF}}(t) G_{\mathbf{k}\alpha}^{\gtrless}(t, t') \quad (\text{A.5})$$

$$-i\hbar \frac{\partial}{\partial t'} G_{\mathbf{k}\alpha}^{\gtrless}(t \leq t') = h_{\mathbf{k}\alpha}^{\text{HF}}(t') G_{\mathbf{k}\alpha}^{\gtrless}(t, t') \quad (\text{A.6})$$

A.2. Relations for zeroth order polarization function

Zero-order Polarization π^{\gtrless} is defined as

$$\pi_{\mathbf{q}}^{\gtrless}(t, t') = -i\hbar \sum_{\mathbf{k}\alpha} G_{\mathbf{k}+\mathbf{q},\alpha}^{\gtrless}(t, t') G_{\mathbf{k}\alpha}^{\lesseqgtr}(t', t) \quad (\text{A.7})$$

If we define $*$ as convolution operator and S as inversion operator, $Sf_{\mathbf{k}} = f_{-\mathbf{k}}$, we can write π^{\gtrless} as a **convolution** according to

$$\pi_{\mathbf{q}}^{\gtrless}(t, t') = -i\hbar \sum_{\alpha} [G^{\gtrless}(t, t') * SG^{\lesseqgtr}(t', t)]_{\mathbf{q}\alpha}, \quad (\text{A.8})$$

an expression, that can be computed via FFT.

Time transposition symmetry follows from the relation for G^{\gtrless}

$$\pi_{\mathbf{q}}^{\gtrless}(t', t) = -i\hbar \sum_{\mathbf{k}\alpha} G_{\mathbf{k}+\mathbf{q},\alpha}^{\gtrless}(t', t) G_{\mathbf{k}\alpha}^{\lesseqgtr}(t, t') = -i\hbar \sum_{\mathbf{k}\alpha} [G_{\mathbf{k}+\mathbf{q},\alpha}^{\gtrless}(t, t') G_{\mathbf{k}\alpha}^{\lesseqgtr}(t', t)]^* = -[\pi_{\mathbf{q}}^{\gtrless}(t, t')]^* \quad (\text{A.9})$$

Relation between $\pi^>$ and $\pi^<$

$$\begin{aligned} \pi_{\mathbf{q}}^>(t, t') &= -i\hbar \sum_{\mathbf{k}\alpha} G_{\mathbf{k}+\mathbf{q},\alpha}^>(t, t') G_{\mathbf{k}\alpha}^<(t', t) = -i\hbar \sum_{\mathbf{k}\alpha} [G_{\mathbf{k}\alpha}^<(t, t')]^* [G_{\mathbf{k}+\mathbf{q},\alpha}^>(t', t)]^* \\ &= -i\hbar \sum_{\mathbf{k}\alpha} [G_{\mathbf{k}-\mathbf{q},\alpha}^<(t, t')]^* [G_{\mathbf{k}\alpha}^>(t', t)]^* = -[\pi_{-\mathbf{q}}^<(t, t')]^* = -[S\pi_{\mathbf{q}}^<(t, t')]^* \end{aligned} \quad (\text{A.10})$$

All symmetries in conclusion:

$$\pi_{\mathbf{q}}^{\gtrless}(t, t') = -[\pi_{\mathbf{q}}^{\gtrless}(t', t)]^* = -[S\pi_{\mathbf{q}}^{\lesseqgtr}(t, t')]^* = S\pi_{\mathbf{q}}^{\lesseqgtr}(t', t) \quad (\text{A.11})$$

The generalization to particles with a charges q_{α}

$$\pi_{\mathbf{q}}^{\gtrless}(t, t') = -i\hbar \sum_{\mathbf{k}\alpha} q_{\alpha}^2 G_{\mathbf{k}+\mathbf{q},\alpha}^{\gtrless}(t, t') G_{\mathbf{k}\alpha}^{\lesseqgtr}(t', t) \quad (\text{A.12})$$

fulfills the same symmetries.

A.3. Relations for GW screened potential W

Dyson equations for non-singular part of W in multi-component systems

$$W_{\mathbf{q}}^{\geq}(t, t') = \mp w_{\mathbf{q}}(t) w_{\mathbf{q}}(t') \pi_{\mathbf{q}}^{\geq}(t, t') \\ \mp w_{\mathbf{q}}(t) \left[\int_{t_0}^t (\pi_{\mathbf{q}}^{\geq}(t, \bar{t}) - \pi_{\mathbf{q}}^{\leq}(t, \bar{t})) W_{\mathbf{q}}^{\geq}(\bar{t}, t') d\bar{t} + \int_{t_0}^{t'} \pi_{\mathbf{q}}^{\geq}(t, \bar{t}) (W_{\mathbf{q}}^{\leq}(\bar{t}, t') - W_{\mathbf{q}}^{\geq}(\bar{t}, t')) d\bar{t} \right] \quad (\text{A.13})$$

$$W_{\mathbf{q}}^{\geq}(t, t') = \mp w_{\mathbf{q}}(t) w_{\mathbf{q}}(t') \pi_{\mathbf{q}}^{\geq}(t, t') \\ \mp \left[\int_{t_0}^t (W_{\mathbf{q}}^{\geq}(t, \bar{t}) - W_{\mathbf{q}}^{\leq}(t, \bar{t})) \pi_{\mathbf{q}}^{\geq}(\bar{t}, t') d\bar{t} + \int_{t_0}^{t'} W_{\mathbf{q}}^{\geq}(t, \bar{t}) (\pi_{\mathbf{q}}^{\leq}(\bar{t}, t') - \pi_{\mathbf{q}}^{\geq}(\bar{t}, t')) d\bar{t} \right] w_{\mathbf{q}}(t') \quad (\text{A.14})$$

A function W is a solution to one of these equations then and only then, if it is also a solution to the other one.

Diagrams tell that W also has a dependence on the particle types interacting, but this factorizes for Coulomb type interactions:

$$W_{\mathbf{q}}^{\geq\alpha\beta}(t, t') = W_{\mathbf{q}}^{\geq}(t, t') q_{\alpha} q_{\beta} \quad (\text{A.15})$$

This was used in the Dyson equations above, but needs to be respected, when put into selfenergy formulas.

The second order term follows the relation (cf. Eq. (A.11))

$$W_{\mathbf{q}, \text{SOA}}^{\geq}(t, t') = -[W_{\mathbf{q}, \text{SOA}}^{\geq}(t', t)]^* \quad (\text{A.16})$$

Next we show, that this relation is also true for the whole W . We start with the first version of Dyson's equation:

$$- [W_{\mathbf{q}}^{\geq}(t', t)]^* \\ = \mp w_{\mathbf{q}}(t) w_{\mathbf{q}}(t') [-\pi_{\mathbf{q}}^{\geq}(t', t)]^* \mp w_{\mathbf{q}}(t') \left[- \int_{t_0}^{t'} (\pi_{\mathbf{q}}^{\geq}(t', \bar{t}) - \pi_{\mathbf{q}}^{\leq}(t', \bar{t})) W_{\mathbf{q}}^{\geq}(\bar{t}, t) d\bar{t} - \int_{t_0}^t \pi_{\mathbf{q}}^{\geq}(t', \bar{t}) (W_{\mathbf{q}}^{\leq}(\bar{t}, t) - W_{\mathbf{q}}^{\geq}(\bar{t}, t)) d\bar{t} \right]^* \quad (\text{A.17})$$

$$= \mp w_{\mathbf{q}}(t) w_{\mathbf{q}}(t') \pi_{\mathbf{q}}^{\geq}(t, t') \mp \left[\int_{t_0}^t \pi_{\mathbf{q}}^{\geq}(t', \bar{t}) (W_{\mathbf{q}}^{\geq}(\bar{t}, t) - W_{\mathbf{q}}^{\leq}(\bar{t}, t)) d\bar{t} + \int_{t_0}^{t'} \pi_{\mathbf{q}}^{\geq}(t', \bar{t}) (W_{\mathbf{q}}^{\leq}(\bar{t}, t) - W_{\mathbf{q}}^{\geq}(\bar{t}, t)) d\bar{t} \right]^* w_{\mathbf{q}}(t') \quad (\text{A.18})$$

Now we use Eq. (A.11) and use Eq. (A.16), which can be seen as initial condition for the Dyson equations at (t_0, t_0)

$$= \mp w_{\mathbf{q}}(t) w_{\mathbf{q}}(t') \pi_{\mathbf{q}}^{\geq}(t, t') \mp \left[\int_{t_0}^t (W_{\mathbf{q}}^{\geq}(t, \bar{t}) - W_{\mathbf{q}}^{\leq}(t, \bar{t})) \pi_{\mathbf{q}}^{\geq}(\bar{t}, t') d\bar{t} + \int_{t_0}^{t'} W_{\mathbf{q}}^{\geq}(t, \bar{t}) (\pi_{\mathbf{q}}^{\geq}(\bar{t}, t') - \pi_{\mathbf{q}}^{\leq}(\bar{t}, t')) d\bar{t} \right] w_{\mathbf{q}}(t') \quad (\text{A.19})$$

$$= W_{\mathbf{q}}^{\geq}(t, t') \quad (\text{A.20})$$

In the last line the second form of Dyson's equation has been used.

Similarly we directly see for the second order term (cf. Eq. (A.11))

$$W_{\mathbf{q},SOA}^>(t, t') = SW_{\mathbf{q},SOA}^<(t', t) \quad (\text{A.21})$$

For the complete W then follows similarly to the relation above

$$\begin{aligned} & SW_{\mathbf{q}}^<(t', t) \\ &= \mp w_{\mathbf{q}}(t') w_{\mathbf{q}}(t) S \pi_{\mathbf{q}}^<(t', t) \mp w_{\mathbf{q}}(t') S \left[\int_{t_0}^{t'} (\pi_{\mathbf{q}}^>(t', \bar{t}) - \pi_{\mathbf{q}}^<(t', \bar{t})) W_{\mathbf{q}}^<(\bar{t}, t) d\bar{t} + \int_{t_0}^t \pi_{\mathbf{q}}^<(t', \bar{t}) (W_{\mathbf{q}}^<(\bar{t}, t) - W_{\mathbf{q}}^>(\bar{t}, t)) d\bar{t} \right] \quad (\text{A.22}) \end{aligned}$$

$$= \mp w_{\mathbf{q}}(t) w_{\mathbf{q}}(t') \pi_{\mathbf{q}}^>(t, t') \mp \left[\int_{t_0}^t (W_{\mathbf{q}}^>(t, \bar{t}) - W_{\mathbf{q}}^<(t, \bar{t})) \pi_{\mathbf{q}}^>(\bar{t}, t') d\bar{t} + \int_{t_0}^{t'} W_{\mathbf{q}}^>(t, \bar{t}) (\pi_{\mathbf{q}}^>(\bar{t}, t') - \pi_{\mathbf{q}}^>(\bar{t}, t')) d\bar{t} \right] w_{\mathbf{q}}(t') \quad (\text{A.23})$$

$$= W_{\mathbf{q}}^>(t, t') \quad (\text{A.24})$$

In conclusion, the relations for W are completely analogous to those for π :

$$W_{\mathbf{q}}^{\gtrless}(t, t') = -[W_{\mathbf{q}}^{\gtrless}(t', t)]^* = -[SW_{\mathbf{q}}^{\lessgtr}(t, t')]^* = SW_{\mathbf{q}}^{\lessgtr}(t', t) \quad (\text{A.25})$$

In isotropic systems, the inversion operator can be dropped which yields the expressions that are found in Ref. [61].

B. Uniform lattice models

B.1. Homogeneous rectangular lattices

Rectangular lattices are a lot simpler to describe than honeycomb lattices, cf. Sect. B.2. This section serves to give a quick introduction into the Hubbard Model in momentum representation for this simpler system before it is applied to the more complex honeycomb lattice.

Hubbard Model

The Hubbard model [114] is a lattice model that was initially developed to describe electrons in a solid that are closely bound to lattice atoms ('sites') and that do not exert interaction with electrons on other sites. It is usually defined in a site-spin basis $|i\alpha\rangle$ where the overlap is neglected, i.e. $\langle i\alpha|j\beta\rangle = \delta_{ij}\delta_{\alpha\beta}$. The Hubbard Hamiltonian is given by

$$\hat{H} = -t \sum_{\langle ij \rangle, \alpha} \hat{a}_{i\alpha}^\dagger \hat{a}_{j\alpha} + U \sum_i \hat{n}_{i\uparrow} \hat{n}_{i\downarrow}, \quad (\text{B.1})$$

where $\langle ij \rangle$ denotes that sites i and j are nearest neighbours. The $U = 0$ limit yields the well-known tight binding model. The Hubbard model has been extended to models where hopping is also allowed to next-nearest neighbours and where orbital overlap is included [115]. Another important generalization is the Pariser–Parr–Pople model (PPP)[116–118] which accounts for long range interaction potentials that go beyond on-site. While these are not treated in this thesis explicitly, the derivations in these sections can easily be extended to go beyond the Hubbard model.

Basis states, first Brillouin zone

We consider an infinite square 2D lattice with lattice constant a spanning the xy plane, i.e. every site has an upper, a lower, a left and a right neighbour, and the hopping probability is the same for all directions. Now we assume the system to be periodic every N_x sites in x direction and every N_y sites in y direction and define a plane wave state $|\mathbf{k}\sigma\rangle$ according to

$$|\mathbf{k}, \sigma\rangle = \frac{1}{\sqrt{N_x N_y}} \sum_{l=1}^{N_x} \sum_{j=1}^{N_y} \exp[i(lak_x + jak_y)] |l, j, \sigma\rangle. \quad (\text{B.2})$$

ia and ja can be understood as x and y coordinate in the cell. The periodicity allows only \mathbf{k} vectors of the form $k_{x/y} = n_{x/y} \frac{2\pi}{aN_{x/y}}$, and where we choose $n_{x/y} \in \mathbb{Z}$ and $|n_{x/y}| \leq N_{x/y}/2$, the

symmetric range of \mathbf{k} vectors. Since

$$\hat{H}^{(0)} |\mathbf{k}, \sigma\rangle = -2t (\cos k_x a + \cos k_y a) |\mathbf{k}, \sigma\rangle, \quad (\text{B.3})$$

we see that it is the eigenbasis of the noninteracting Hamiltonian. In conclusion: This model has a square first Brillouin zone with edge length $2\pi/a$ and only one cosine band. The derivation of the cosine tight binding bands in 1D and 3D is analogous.

Matrix elements, G1–G2 equations

Now in order to describe the electron-electron dynamics, we need to find interaction matrix elements. Since the interaction $W_{ijkl}^{\sigma_1\sigma_2\sigma_3\sigma_4} = U \delta_{ij} \delta_{jk} \delta_{kl} \delta_{\sigma_1\sigma_3} \delta_{\sigma_2\sigma_4} (1 - \delta_{\sigma_1\sigma_2})$ is highly localized, we easily find (the δ 's from W are already applied in the following expression)

$$\begin{aligned} & \langle \mathbf{k}_1\sigma_1, \mathbf{k}_2\sigma_2 | \hat{W} | \mathbf{k}_3\sigma_3, \mathbf{k}_4\sigma_4 \rangle \\ &= \delta_{\sigma_1\sigma_3} \delta_{\sigma_2\sigma_4} (1 - \delta_{\sigma_1\sigma_2}) \frac{U}{(N_x N_y)^2} \sum_{i=1}^{N_x} \sum_{j=1}^{N_y} \exp[i\mathbf{a} \cdot (\mathbf{k}_3 + \mathbf{k}_4 - \mathbf{k}_1 - \mathbf{k}_2)] \\ &= \delta_{\sigma_1\sigma_3} \delta_{\sigma_2\sigma_4} (1 - \delta_{\sigma_1\sigma_2}) \frac{U}{N_x N_y} \delta_{\mathbf{k}_1+\mathbf{k}_2, \mathbf{k}_3+\mathbf{k}_4}^{\text{per}}, \end{aligned} \quad (\text{B.4})$$

with $\mathbf{a} = (a, a)^T$. $\delta_{\mathbf{k}_1+\mathbf{k}_2, \mathbf{k}_3+\mathbf{k}_4}^{\text{per}}$ is a modified Kronecker delta that is 1 if $\mathbf{k}_1 + \mathbf{k}_2 = \mathbf{k}_3 + \mathbf{k}_4 + G$ for a reciprocal lattice vector G and 0 else. This is a key difference to jellium, as in these lattice systems some collisions that do not conserve momentum, are allowed¹. 1D and 3D are analogous, only the factor $\frac{1}{N_x N_y}$ must be changed accordingly.

Now if we assume uniformity, i.e. shift symmetry with respect to every shift on the lattice, G has the same diagonal form as in the jellium case. The modified momentum δ does in fact not change much in the form of the equations: for a given pair of momenta, \mathbf{k} and \mathbf{p} and some transfer momentum \mathbf{q} , there is exactly one reciprocal lattice vector $G_{\mathbf{k}}$ such that $\mathbf{k} - \mathbf{q} + G_{\mathbf{k}}$ is in the first Brillouin zone and one reciprocal lattice vector $G_{\mathbf{p}}$ such that $\mathbf{p} + \mathbf{q} + G_{\mathbf{p}}$ is in the first Brillouin zone. This means that sums/differences between momentum vectors just have to be interpreted as that vector, that shifted by reciprocal lattice vector G , lies in the first Brillouin zone. This interpretation is assumed in the following.

\mathcal{G} gets even more sparse than the jellium \mathcal{G} : Since interaction only happens between a spin up and a spin down electron, we have $\mathcal{G}_{\mathbf{k}\mathbf{p}\mathbf{q}}^{\uparrow\uparrow} = \mathcal{G}_{\mathbf{k}\mathbf{p}\mathbf{q}}^{\downarrow\downarrow} = 0$. In the following, a barred spin index, e.g. $\bar{\alpha}$ is the opposite spin of α . The G1–G2 equations are thus a simplification of the jellium

¹Translation symmetry is discretized, hence the usual momentum symmetry is not valid anymore.

G1–G2 equations:

$$i\hbar \frac{d}{dt} G_{\mathbf{k}\alpha}^{\gtrless}(t, t) = \pm i\hbar \frac{U}{(N_x N_y)^2} \sum_{\mathbf{p}\mathbf{q}} \mathcal{G}_{\mathbf{k}\mathbf{p}\mathbf{q}}^{\alpha\bar{\alpha}}(t) + \text{h.c.} \quad (\text{B.5})$$

$$\begin{aligned} i\hbar \frac{d}{dt} \mathcal{G}_{\mathbf{k}\mathbf{p}\mathbf{q}}^{\alpha\bar{\alpha}}(t) - \mathcal{G}_{\mathbf{k}\mathbf{p}\mathbf{q}}^{\alpha\bar{\alpha}}(t) [E_{\mathbf{k}-\mathbf{q}}^{\text{kin}} + E_{\mathbf{p}+\mathbf{q}}^{\text{kin}} - E_{\mathbf{k}}^{\text{kin}} - E_{\mathbf{p}}^{\text{kin}}] \\ = (i\hbar)^2 U [\mathcal{G}_{\mathbf{k}-\mathbf{q},\alpha}^{\gtrless}(t) \mathcal{G}_{\mathbf{p}+\mathbf{q},\bar{\alpha}}^{\gtrless}(t) \mathcal{G}_{\mathbf{k},\alpha}^{\lessgtr}(t) \mathcal{G}_{\mathbf{p},\bar{\alpha}}^{\lessgtr}(t) - \mathcal{G}_{\mathbf{k}-\mathbf{q},\alpha}^{\lessgtr}(t) \mathcal{G}_{\mathbf{p}+\mathbf{q},\bar{\alpha}}^{\lessgtr}(t) \mathcal{G}_{\mathbf{k},\alpha}^{\gtrless}(t) \mathcal{G}_{\mathbf{p},\bar{\alpha}}^{\gtrless}(t)]. \end{aligned} \quad (\text{B.6})$$

The modifications for higher order selfenergies are found analogously. Note, that in the Hubbard model the exchange energy is a constant. In a uniform system, the Hartree energy is a constant, too, which is the reason why only the kinetic energy appears in the two-particle commutator above.

B.2. The honeycomb lattice

Defining the lattice and diagonalizing the Hamiltonian

Graphene and TMDCs are 2D materials whose atoms are not arranged in a square lattice, but in a honeycomb lattice. The honeycomb lattice is a hexagonal Bravais lattice with two sites per elementary cell. Let a be the distance between one site and its nearest neighbours. The honeycomb lattice, depicted in Fig. B.1, is defined by the following vectors:

$$\mathbf{a}_1 = \frac{a}{2}(3, \sqrt{3}), \quad \mathbf{a}_2 = \frac{a}{2}(3, -\sqrt{3}), \quad (\text{B.7})$$

$$\boldsymbol{\delta}_1 = \frac{a}{2}(1, \sqrt{3}), \quad \boldsymbol{\delta}_2 = \frac{a}{2}(1, -\sqrt{3}), \quad \boldsymbol{\delta}_3 = -a(1, 0). \quad (\text{B.8})$$

The lattice is divided into two hexagonal sublattices that we call A and B . Let $\hat{a}_i^{(\dagger)}, \hat{b}_i^{(\dagger)}$ be the ladder operators for an A or B site. The noninteracting Hubbard Hamiltonian is given by (the spin index is added in the end)

$$\hat{T} = -t \sum_{\langle ij \rangle} (\hat{a}_i^\dagger \hat{b}_j + \hat{b}_j^\dagger \hat{a}_i) = -t \sum_{i \in A} \sum_{\delta} (\hat{a}_i^\dagger \hat{b}_{i+\delta} + \hat{b}_{i+\delta}^\dagger \hat{a}_i), \quad (\text{B.9})$$

where $i+\delta$ denotes the neighbour of A site number i in δ direction. In order to find an eigenbasis of the Hamiltonian, we again choose a cell that consists of $N_1 \times N_2$ elementary cells, N_1 in \mathbf{a}_1 direction and N_2 in \mathbf{a}_2 direction, which now holds in total $2N_1 \times N_2$ sites. Let $\mathbf{a}_{\mathbf{k}}^{(\dagger)}, \mathbf{b}_{\mathbf{k}}^{(\dagger)}$ be the ladder operators for plane waves on the respective sublattices. Then we can write the site operators as a Fourier transform,

$$\hat{a}_i^\dagger = \frac{1}{\sqrt{N_1 N_2}} \sum_{\mathbf{k}} e^{i\mathbf{k} \cdot \mathbf{r}_{i,A}} \mathbf{a}_{\mathbf{k}}^\dagger, \quad \hat{a}_i = \frac{1}{\sqrt{N_1 N_2}} \sum_{\mathbf{k}} e^{-i\mathbf{k} \cdot \mathbf{r}_{i,A}} \mathbf{a}_{\mathbf{k}}, \quad (\text{B.10})$$

$$\hat{b}_i^\dagger = \frac{1}{\sqrt{N_1 N_2}} \sum_{\mathbf{k}} e^{i\mathbf{k} \cdot \mathbf{r}_{i,B}} \mathbf{b}_{\mathbf{k}}^\dagger, \quad \hat{b}_i = \frac{1}{\sqrt{N_1 N_2}} \sum_{\mathbf{k}} e^{-i\mathbf{k} \cdot \mathbf{r}_{i,B}} \mathbf{b}_{\mathbf{k}}. \quad (\text{B.11})$$

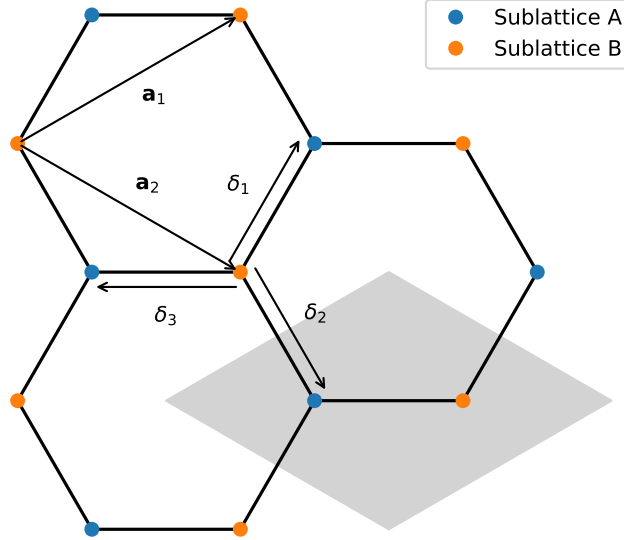


Figure B.1.: The honeycomb lattice and some common definitions: Each elementary cell (grey area) contains two sites, one of sublattice *A* and one of sublattice *B*. The lattice vectors are \mathbf{a}_1 and \mathbf{a}_2 . From a *B* site, the three neighbouring *A* sites are found by adding the vectors δ_1 , δ_2 and δ_3 to the *B* site coordinates. The length of these vectors is $|\delta_i| = a$.

These are used to rewrite the Hamiltonian in momentum representation:

$$\hat{T} = -t \sum_{\delta, \mathbf{k}} (e^{-i\mathbf{k}\cdot\delta} \hat{a}_{\mathbf{k}}^\dagger \hat{b}_{\mathbf{k}} + e^{i\mathbf{k}\cdot\delta} \hat{b}_{\mathbf{k}}^\dagger \hat{a}_{\mathbf{k}}) = -t \sum_{\mathbf{k}} \begin{pmatrix} \hat{a}_{\mathbf{k}}^\dagger & \hat{b}_{\mathbf{k}}^\dagger \end{pmatrix} \begin{pmatrix} 0 & \Delta_{\mathbf{k}} \\ \Delta_{\mathbf{k}}^* & 0 \end{pmatrix} \begin{pmatrix} \hat{a}_{\mathbf{k}} \\ \hat{b}_{\mathbf{k}} \end{pmatrix}, \quad (\text{B.12})$$

where $\Delta_{\mathbf{k}} \equiv \sum_{\delta} e^{i\mathbf{k}\cdot\delta}$. This matrix is easily diagonalized, which yields the energy eigenvalues

$$E_{\mathbf{k}}^{\pm} = \pm t \sqrt{\Delta_{\mathbf{k}} \Delta_{\mathbf{k}}^*} \quad (\text{B.13})$$

and the eigenstates

$$|\mathbf{k}\sigma\pm\rangle = \frac{\Delta_{\mathbf{k}}}{\sqrt{2}|\Delta_{\mathbf{k}}|} |\mathbf{k}\sigma, A\rangle \mp \frac{1}{\sqrt{2}} |\mathbf{k}\sigma, B\rangle, \quad (\text{B.14})$$

where the states on the r.h.s. are the sublattice plane waves. Another popular set of labels are c, v (conduction, valence band) instead of \pm for the two bands, but the sign \pm appears again in the computation of the interaction matrix. Thus the sign notation is used.

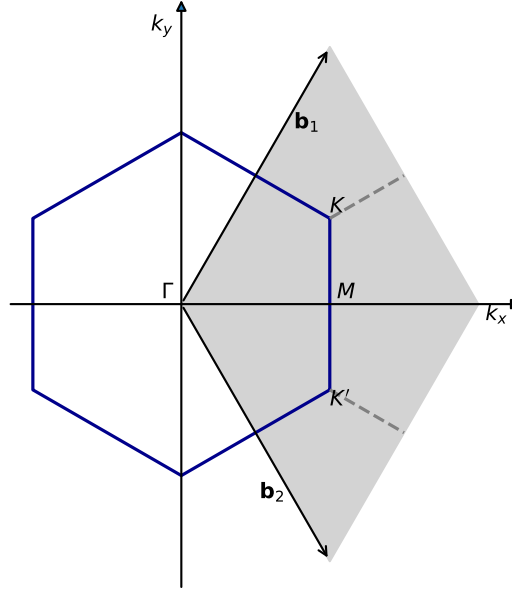


Figure B.2.: First Brillouin zone of the honeycomb lattice. The shaded area is the parallelogram spanned by the reciprocal lattice vectors. The hexagon is the rearranged Brillouin zone. Note that there are only two irreducible corners, K and K' , all others can be reached using a reciprocal lattice vector.

From the lattice vectors $\mathbf{a}_1, \mathbf{a}_2$ one finds the reciprocal lattice vectors

$$\mathbf{b}_1 = \frac{2\pi}{3a}(1, \sqrt{3}) \quad \mathbf{b}_2 = \frac{2\pi}{3a}(1, -\sqrt{3}) \quad (\text{B.15})$$

that span a parallelogram. This parallelogram shaped first Brillouin zone can be reshaped into a hexagon that has the point symmetry of the honeycomb lattice, as can be seen in Fig. B.2.

The kinetic energy can also be expressed as

$$E_{\mathbf{k}}^{\pm} = \pm t \sqrt{1 + 4 \cos\left(\frac{3}{2}k_x a\right) \cos\left(\frac{\sqrt{3}}{2}k_y a\right) + 4 \cos^2\left(\frac{\sqrt{3}}{2}k_y a\right)}, \quad (\text{B.16})$$

which is plotted in Fig. B.3.

Interaction matrix elements

The interaction matrix elements in honeycomb lattice momentum representation are derived in a similar manner to the square lattice if one makes use of the relation

$$\mathbf{a}_i \cdot \mathbf{b}_j = 2\pi\delta_{ij}. \quad (\text{B.17})$$

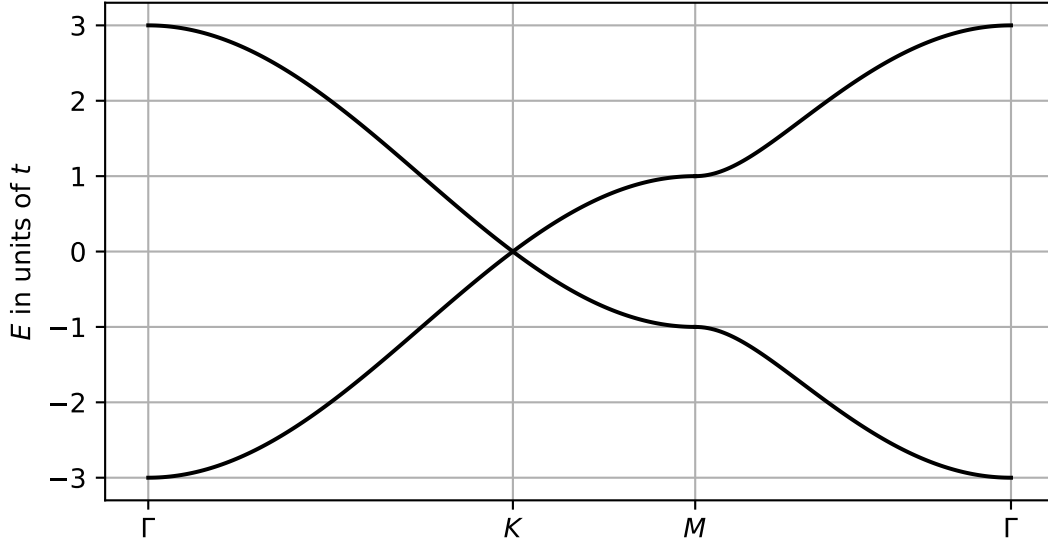


Figure B.3.: Dispersion in a tight binding honeycomb lattice. The two bands touch in the points K and K' , which are also referred to as *Dirac cones*.

We consider a cell spanned by $n_i \mathbf{a}_i$ for $n_i \in \{0, \dots, N_i - 1\}$. The first Brillouin zone then is discretized by the reciprocal vectors $n_i \mathbf{b}_i / N_i$ for $n_i \in \{0, \dots, N_i - 1\}$. Now we can write

$$\begin{aligned} \langle ij\sigma A | \mathbf{k}_{i,jk} \sigma A \rangle &= \frac{1}{\sqrt{N_1 N_2}} \exp(i[\mathbf{ia}_1 + \mathbf{ja}_2] \cdot [i_k \mathbf{b}_1 + j_k \mathbf{b}_2]) \\ &= \frac{1}{\sqrt{N_1 N_2}} \exp\left(i2\pi \left[\frac{ii_k}{N_1} + \frac{jj_k}{N_2} \right]\right). \end{aligned} \quad (\text{B.18})$$

The expression for the B sites only contains an additional phase factor $\exp(-i\mathbf{k} \cdot \delta_1)$ that cancels with its adjoint in the computation of the interaction matrix element. Let $\mathbf{k}_l = i_{k,l} \mathbf{b}_1 + j_{k,l} \mathbf{b}_2$ be the expansion of \mathbf{k}_l in the basis $\mathbf{b}_1, \mathbf{b}_2$. We find

$$\begin{aligned} &\langle \mathbf{k}_1 \sigma_1 \pm_1, \mathbf{k}_2 \sigma_2 \pm_2 | \hat{W} | \mathbf{k}_3 \sigma_3 \pm_3, \mathbf{k}_4 \sigma_4 \pm_4 \rangle \\ &= \delta_{\sigma_1 \sigma_3} \delta_{\sigma_2 \sigma_4} (1 - \delta_{\sigma_1 \sigma_2}) \frac{U}{(2N_1 N_2)^2} \left(\frac{\Delta_{\mathbf{k}_1}^* \Delta_{\mathbf{k}_2}^* \Delta_{\mathbf{k}_3} \Delta_{\mathbf{k}_4}}{|\Delta_{\mathbf{k}_1}^* \Delta_{\mathbf{k}_2}^* \Delta_{\mathbf{k}_3} \Delta_{\mathbf{k}_4}|} \pm_1 \pm_2 \pm_3 \pm_4 1 \right) \times \\ &\times \sum_{i=1}^{N_1} \sum_{j=1}^{N_2} \exp\left\{i2\pi \left([i_{k,3} + i_{k,4} - i_{k,1} - i_{k,2}] \frac{i}{N_1} + [j_{k,3} + j_{k,4} - j_{k,1} - j_{k,2}] \frac{j}{N_2} \right)\right\} \\ &= \delta_{\sigma_1 \sigma_3} \delta_{\sigma_2 \sigma_4} (1 - \delta_{\sigma_1 \sigma_2}) \frac{U}{4N_1 N_2} \left(\frac{\Delta_{\mathbf{k}_1}^* \Delta_{\mathbf{k}_2}^* \Delta_{\mathbf{k}_3} \Delta_{\mathbf{k}_4}}{|\Delta_{\mathbf{k}_1}^* \Delta_{\mathbf{k}_2}^* \Delta_{\mathbf{k}_3} \Delta_{\mathbf{k}_4}|} \pm_1 \pm_2 \pm_3 \pm_4 1 \right) \delta_{i_{k,1}+i_{k,2}, i_{k,1}+i_{k,2}}^{\text{per}} \delta_{j_{k,1}+j_{k,2}, j_{k,1}+j_{k,2}}^{\text{per}} \\ &= \delta_{\sigma_1 \sigma_3} \delta_{\sigma_2 \sigma_4} (1 - \delta_{\sigma_1 \sigma_2}) \frac{U}{4N_1 N_2} \left(\frac{\Delta_{\mathbf{k}_1}^* \Delta_{\mathbf{k}_2}^* \Delta_{\mathbf{k}_3} \Delta_{\mathbf{k}_4}}{|\Delta_{\mathbf{k}_1}^* \Delta_{\mathbf{k}_2}^* \Delta_{\mathbf{k}_3} \Delta_{\mathbf{k}_4}|} \pm_1 \pm_2 \pm_3 \pm_4 1 \right) \delta_{\mathbf{k}_1 + \mathbf{k}_2, \mathbf{k}_3 + \mathbf{k}_4}^{\text{per}} \end{aligned} \quad (\text{B.19})$$

and $\pm_1 \pm_2 \pm_3 \pm_4$ is the product of the energy signs of the four states. The matrix elements are 'momentum preserving' in the same way as in the case of the square lattice. In contrast to jellium or the square lattice this matrix element is dependent on all three (four minus one, because of the δ) momenta, and distinguishes between an even number of band changes and an uneven number (i.e. one band change, an Auger process).

To be somewhat consistent with formulas for similar systems, the following definition is used:

$$v_{\mathbf{k}\mathbf{p}\mathbf{q}}^s = \frac{U}{4} \left(\frac{\Delta_{\mathbf{k}-\mathbf{q}}^* \Delta_{\mathbf{p}+\mathbf{q}}^* \Delta_{\mathbf{k}} \Delta_{\mathbf{p}}}{|\Delta_{\mathbf{k}-\mathbf{q}}^* \Delta_{\mathbf{p}+\mathbf{q}}^* \Delta_{\mathbf{k}} \Delta_{\mathbf{p}}|} + s \right), \quad (\text{B.20})$$

where again sums and difference are understood as modulo reciprocal lattice vector. Here and in the following, s is the product of the four energy signs.

G1–G2 equations

The G1–G2 equations in a uniform honeycomb lattice are similar to those of the square lattice, but with some key differences: G has two additional band indices, and G is not diagonal in them. i.e. we have $G_{\mathbf{k}\alpha,ss'}^{\geq}$.

The single-particle SOA G1–G2 equation is

$$i\hbar \frac{d}{dt} G_{\mathbf{k}\alpha,ss'}^{\geq}(t) - [E_{\mathbf{k}}^s(t) - E_{\mathbf{k}}^{s'}(t)] G_{\mathbf{k}\alpha,ss'}^{\geq} = [I + I^\dagger]_{\mathbf{k}\alpha,ss'}, \quad (\text{B.21})$$

where

$$I_{\mathbf{k}\alpha,ss'} = \pm i\hbar \frac{1}{(N_x N_y)^2} \sum_{\substack{\mathbf{p}, \mathbf{q} \in \text{1st BZ} \\ \bar{s}_1, \bar{s}_2 \in \{-1, +1\}}} \left[v_{\mathbf{k}\mathbf{p}\mathbf{q}}^{\bar{s}_1 \bar{s}_2 s' \bar{s}} \right]^* \mathcal{G}_{\mathbf{k}\mathbf{p}\mathbf{q}, \alpha \bar{\alpha}}^{\bar{s}_1 \bar{s}_2 s' \bar{s}}(t). \quad (\text{B.22})$$

Again, no Hartree or Fock contributions exist due to spatial homogeneity and the short interaction range. For the components $G_{\mathbf{k}\alpha,ss}^{\geq}$ the commutator vanishes, as in the jellium case.

The \mathcal{G} equation of motion is given by

$$\begin{aligned} i\hbar \frac{d}{dt} \mathcal{G}_{\mathbf{k}\mathbf{p}\mathbf{q}, \alpha \bar{\alpha}}^{s_1 s_2 s_3 s_4}(t) - [E_{\mathbf{k}-\mathbf{q}}^{s_1} + E_{\mathbf{p}+\mathbf{q}}^{s_2} - E_{\mathbf{k}}^{s_3} + E_{\mathbf{p}}^{s_4}] \mathcal{G}_{\mathbf{k}\mathbf{p}\mathbf{q}, \alpha \bar{\alpha}}^{s_1 s_2 s_3 s_4}(t) \\ = (i\hbar)^2 \sum_{\substack{\bar{s}_1, \bar{s}_2, \bar{s}_3, \bar{s}_4 \\ \in \{-1, 1\}}} G_{\mathbf{k}-\mathbf{q}, \alpha, s_1 \bar{s}_1}^>(t) G_{\mathbf{p}+\mathbf{q}, \bar{\alpha}, s_2 \bar{s}_2}^>(t) v_{\mathbf{k}\mathbf{p}\mathbf{q}}^{\bar{s}_1 \bar{s}_2 \bar{s}_3 \bar{s}_4} G_{\mathbf{k}\alpha, \bar{s}_3 s_3}^<(t) G_{\mathbf{p}\bar{\alpha}, \bar{s}_4 s_4}^<(t) + (>\leftrightarrow<). \end{aligned} \quad (\text{B.23})$$

Equations for higher order selfenergies are derived similarly: They are jellium-like in the momentum index, only opposite spin interactions and \mathcal{G} contribute, and the equations have the structure known from arbitrary basis in regard to the band index. They are also generalized with minor changes to the PPP model or the extended Hubbard model. PPP yields modified interaction matrix elements that do not contain the $(1 - \delta_{\alpha_1 \alpha_2})$ term, which leads to the appearance of a Fock exchange term, and $\mathcal{G}_{\mathbf{k}\mathbf{p}\mathbf{q}, \alpha_1 \alpha_2}^{s_1 s_2 s_3 s_4}$ contributes for arbitrary combinations of α_1, α_2 . The extended Hubbard model only changes the single particle dispersion, but does not change the structure of the equations.

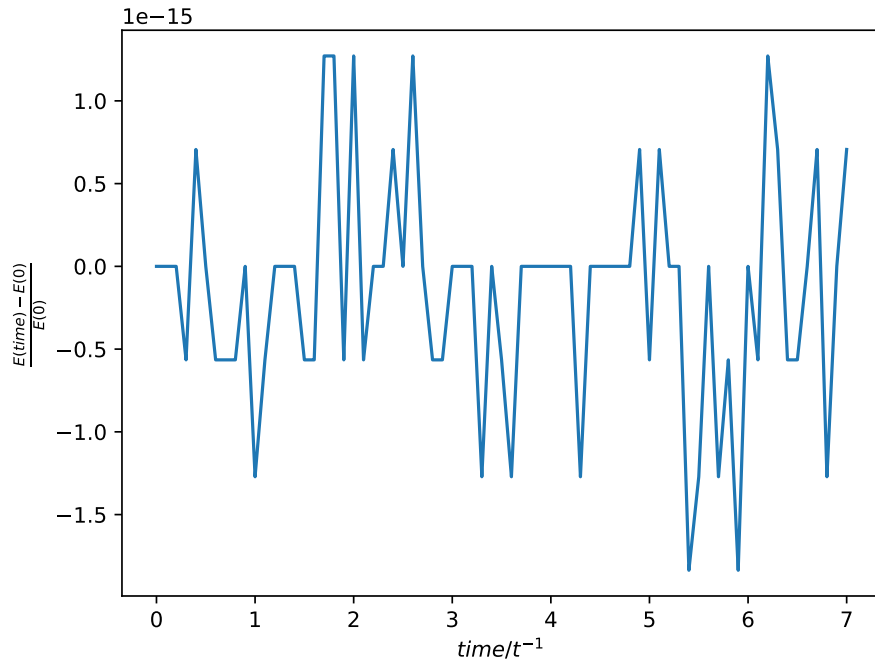


Figure B.4.: Energy conservation of an SOA calculation of a Hubbard honeycomb lattice

Test simulation

Figure B.4 shows the energy conservation of an SOA calculation of a Hubbard honeycomb lattice. The initial situation is a purely for test purposes: No initial correlations, the upper band is empty, and all states in the lower band is half filled. The energy conservation shown in the figure is on the scale of the machine precision, i.e. the best numerically possible conservation. In total 243 \mathbf{k} points have been used to sample the first Brillouin zone on a hexagonal grid. The time step length is $0.02 t^{-1}$, U is set to $U = 1t$, and an RK4 stepper is used.

The excellent stability is a property of the 'closed grid', also sketched in Fig. B.5. What this means becomes clear when considering an 'unclosed grid', cf. Chap. 4: The uniform gas in the thermodynamic limit has an infinite first Brillouin zone. This is approximated by a finite and discretized grid. Collisions can push a particle to receive a momentum that is beyond the largest momenta of the grid. This particle then vanishes from the simulation. Such effects cannot happen in closed grids: After every collision of particles with momenta given on the grid, where a momentum, that is also given on the grid, is transferred, the two particles end up on two new grid positions. No extrapolation or interpolation is needed (as in the jellium case), which increases the stability.

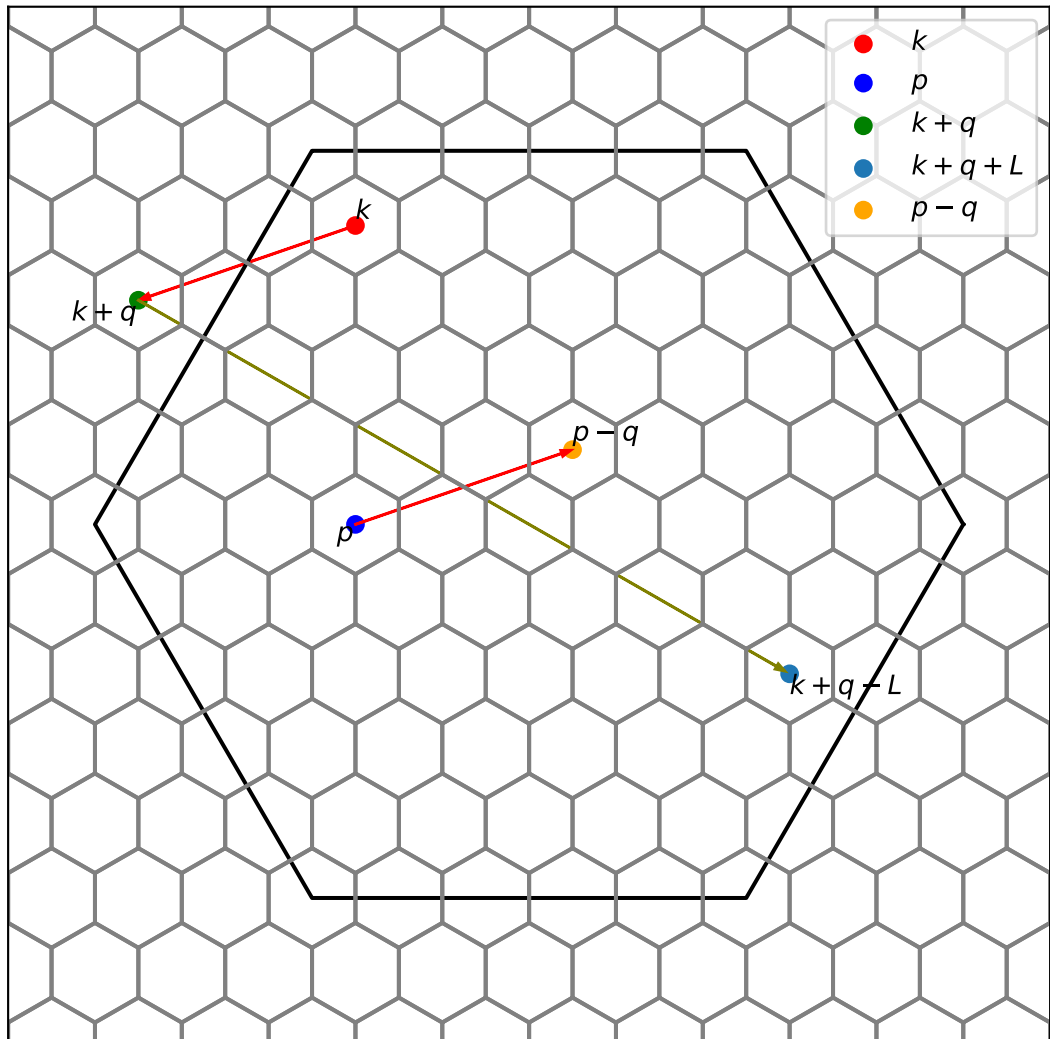


Figure B.5.: Sketch of the first Brillouin zone and its hexagonal sampling: each minor hexagon represents a sample, denoted by the momentum in its center. Particles of grid momenta \mathbf{k} and \mathbf{p} exchange a grid momentum \mathbf{q} , yielding the grid momenta $\mathbf{k} + \mathbf{q}$ and $\mathbf{p} - \mathbf{q}$. If one particle 'leaves' the first Brillouin zone that way, here e.g. $\mathbf{k} + \mathbf{q}$, it is mapped back into it and exactly onto a grid momentum via a lattice momentum \mathbf{L} .

C. Semianalytical Euler stepper

The *GW* equation of motion for \mathcal{G} is given by

$$i\hbar \frac{d}{dt} \mathcal{G}_{\mathbf{k}\mathbf{p}\mathbf{q}}^{\alpha\beta}(t) - \mathcal{G}_{\mathbf{k}\mathbf{p}\mathbf{q}}^{\alpha\beta}(t) \Delta_{\mathbf{k}\mathbf{p}\mathbf{q},\alpha\beta}^{\text{HF},(2)}(t) = \Psi_{\mathbf{k}\mathbf{p}\mathbf{q},\alpha\beta}(t) + \Pi_{\mathbf{k}\mathbf{p}\mathbf{q}}^{\alpha\beta}(t) - \left[\Pi_{\mathbf{p}+\mathbf{q},\mathbf{k}-\mathbf{q},\mathbf{q}}^{\beta\alpha}(t) \right]^*, \quad (\text{C.1})$$

where the terms are defined in section 2.3.7. The single particle energy difference $\Delta_{\mathbf{k}\mathbf{p}\mathbf{q},\alpha\beta}^{\text{HF},(2)}$ and the source term $\Psi_{\mathbf{k}\mathbf{p}\mathbf{q},\alpha\beta}$ are only dependent on $G^{\geq}(t)$, the polarization term contains G^{\geq} , but is also dependent on a \mathbf{k} or \mathbf{p} sum of $\mathcal{G}_{\mathbf{k}\mathbf{p}\mathbf{q}}^{\alpha\beta}$.

Let us at first neglect the Π terms. Under the assumption that G^{\geq} evolves slower than \mathcal{G} , we find the equation

$$i\hbar \frac{d}{dt} \mathcal{G}_{\mathbf{k}\mathbf{p}\mathbf{q}}^{\alpha\beta}(t) - \mathcal{G}_{\mathbf{k}\mathbf{p}\mathbf{q}}^{\alpha\beta}(t) \Delta_{\mathbf{k}\mathbf{p}\mathbf{q},\alpha\beta}^{\text{HF},(2)} = \Psi_{\mathbf{k}\mathbf{p}\mathbf{q},\alpha\beta} \quad (\text{C.2})$$

with the solution

$$\mathcal{G}_{\mathbf{k}\mathbf{p}\mathbf{q}}^{\alpha\beta}(t) = \mathcal{G}_{\mathbf{k}\mathbf{p}\mathbf{q},\text{stat}}^{\alpha\beta} + \left(\mathcal{G}_{\mathbf{k}\mathbf{p}\mathbf{q}}^{\alpha\beta}(t_0) - \mathcal{G}_{\mathbf{k}\mathbf{p}\mathbf{q},\text{stat}}^{\alpha\beta} \right) \exp \left((t - t_0) \frac{\Delta_{\mathbf{k}\mathbf{p}\mathbf{q},\alpha\beta}^{\text{HF},(2)}}{i\hbar} \right), \quad (\text{C.3})$$

where the stationary solution is given by

$$\mathcal{G}_{\mathbf{k}\mathbf{p}\mathbf{q},\text{stat}}^{\alpha\beta} = - \frac{\Psi_{\mathbf{k}\mathbf{p}\mathbf{q}}^{\alpha\beta}}{\Delta_{\mathbf{k}\mathbf{p}\mathbf{q},\alpha\beta}^{\text{HF},(2)}}. \quad (\text{C.4})$$

The usual problem with Runge-Kutta steppers and oscillations is that the time step length must be chosen in such a way that multiple time steps fit into one oscillation period. Since $\Delta_{\mathbf{k}\mathbf{p}\mathbf{q},\alpha\beta}^{\text{HF},(2)}$ can reach high oscillation frequencies, the step length must usually be chosen very short in order to avoid that quick oscillations grow due to numerical errors. Eq. (C.3) is robust in this regard: The exponential function describes harmonic oscillations without changing its amplitude and thereby avoiding the instabilities occurring in the Runge-Kutta methods.

The *GW*-defining term Π contains both – slowly evolving G^{\geq} functions and a fast evolving \mathcal{G} function. However, \mathcal{G} enters Π only in shape of a sum. Sums of \mathcal{G} , such as the collision integral in a sense, are expected to be slowly evolving functions. The proposed generalization is thus using

$$\mathcal{G}_{\mathbf{k}\mathbf{p}\mathbf{q},\text{stat}}^{\alpha\beta} = - \frac{\Psi_{\mathbf{k}\mathbf{p}\mathbf{q}}^{\alpha\beta} + \Pi_{\mathbf{k}\mathbf{p}\mathbf{q}}^{\alpha\beta}(t) - \left[\Pi_{\mathbf{p}+\mathbf{q},\mathbf{k}-\mathbf{q},\mathbf{q}}^{\beta\alpha}(t) \right]^*}{\Delta_{\mathbf{k}\mathbf{p}\mathbf{q},\alpha\beta}^{\text{HF},(2)}}, \quad (\text{C.5})$$

in the stepping formula, (C.3).

D. Numerical energy conservation

Figure D.1 shows the energy per particle as a function of time after the adiabatic switching process, i.e. $t = 0$ is set to be the end time of the switching. During the switching, the total energy changes strongly, and is therefore not included in the graphic.

Best convergence would be reached if basis parameter NKR is large time step length DT is small and the number of time steps PROPT is large. This is however not possible due to expensive scalings. A compromise thus has to be found. The proton calculations with $NKR = 100$ were done first. Since the electron stopping power is less stationary, NKR has been reduced to achieve longer simulations. After 50 as the energy conservation is violated by about 0.02 % in GW calculations. The cheaper and simpler SOA calculations with static screening conserve energy much better.

The energy conservation in the three GW calculations is fulfilled to a similar degree. It might be possible to decrease NKR even further and to increase the number of time steps, PROPT, instead. This could either be used to make the time step smaller, thereby increasing accuracy of the integrations, or to achieve longer simulation times.

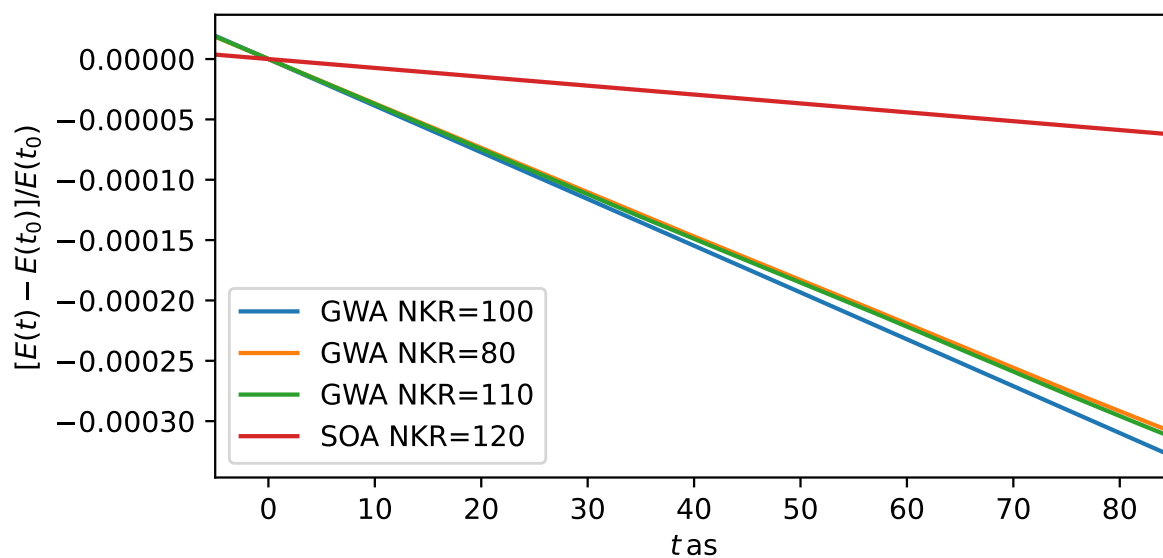


Figure D.1.: Energy conservation for a few different basis sizes. Time step length is $0.005 \text{ a.u.} \approx 0.0121 \text{ as}$ for all calculations. The time is shifted so that $t = 0$ denotes the point of time where the adiabatic switching is finished.

E. Time-dependent plasmon-occupation

Figure E.1 shows the time-dependent plasmon occupation numbers. Due to short switching times these occupations are strongly oscillating, with small- q plasmon occupation oscillating at roughly $2\omega_{pl} = 2\sqrt{3/r_s^3}$ (in atomic units). Towards later times the oscillation is damped. It is strongly suspected that the oscillations in stopping power are due to these varying plasmon occupations, as their frequencies are similar. More adequate results are thus expected if the projectiles are added to the system at much later times. This is only possible in combination with a smaller basis parameter NKR to counteract the increased costs of longer calculations. Figure E.2 shows analogous results with shorter switching times. In comparison, the plasmon oscillations are stronger than for longer switching times.

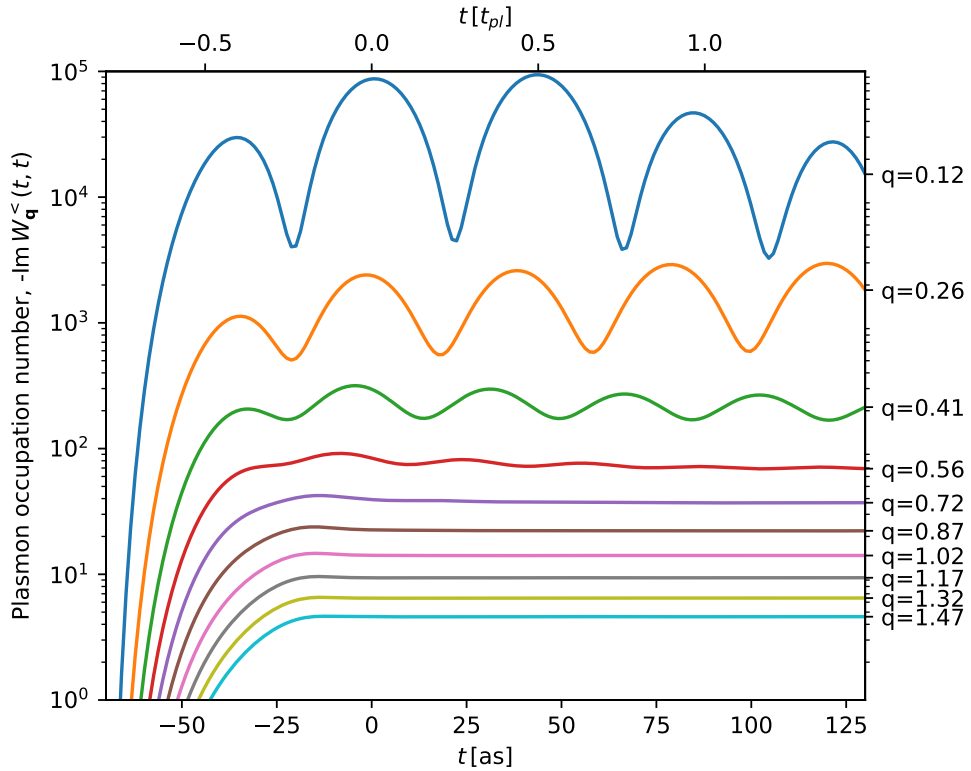


Figure E.1.: Time-dependent plasmon occupation in the presented simulations. $t = 0$ corresponds to the finishing time of the adiabatic switching of $3 a.u.$.

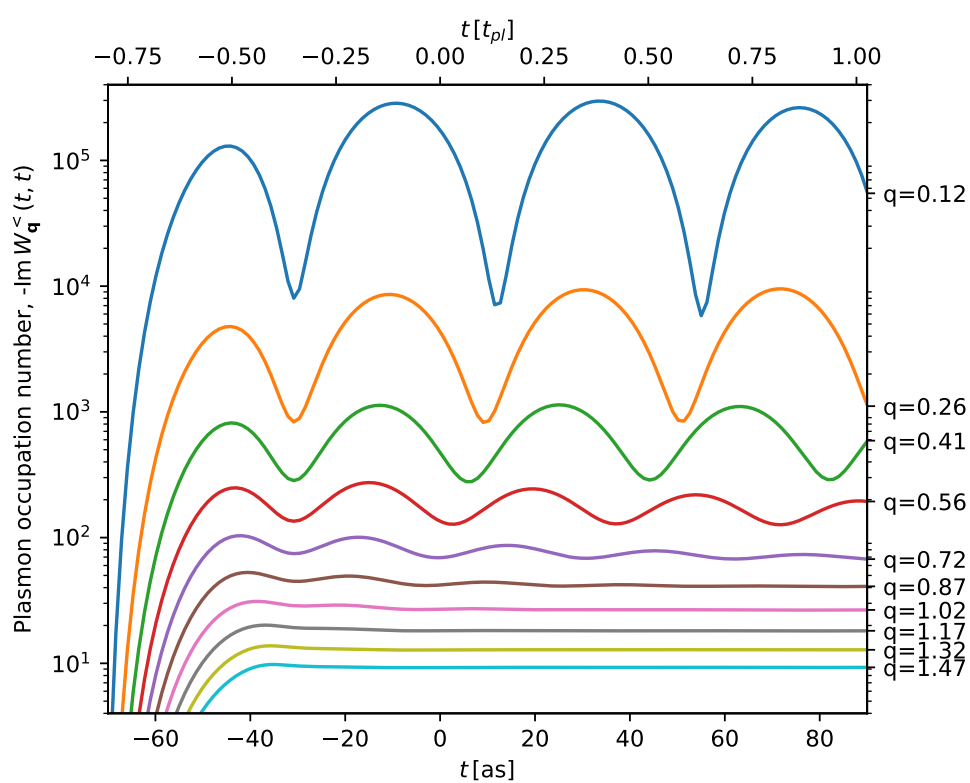


Figure E.2.: Same as in Fig. E.1, but with a switching time of $2 a.u.$.

F. Complete time-dependent stopping data in SOA

For completeness, this appendix contains heatmaps about stopping data in the second order approximation analogous to the *GW* heatmaps in Sect. 5.4. Plasma parameters are the same, i.e. $r_s = 1$ and $\Theta = 1$. In Figs. F.1, F.2 and F.3 it is visible that the oscillations, that were observed in *GW*, do not appear in SOA. Simulation parameters were (SOA is a lot less expensive than *GW*)

$$\text{NKR} = 120,$$

$$\text{CUTOFFMOMENTUM} = 12 \hbar a_B^{-1} \text{ and}$$

$$DT = 0.004 \text{ a.u.} \approx 0.09 \text{ as.}$$

The energy loss per distance quickly becomes constant which explains the small errorbars in Fig. 5.10.

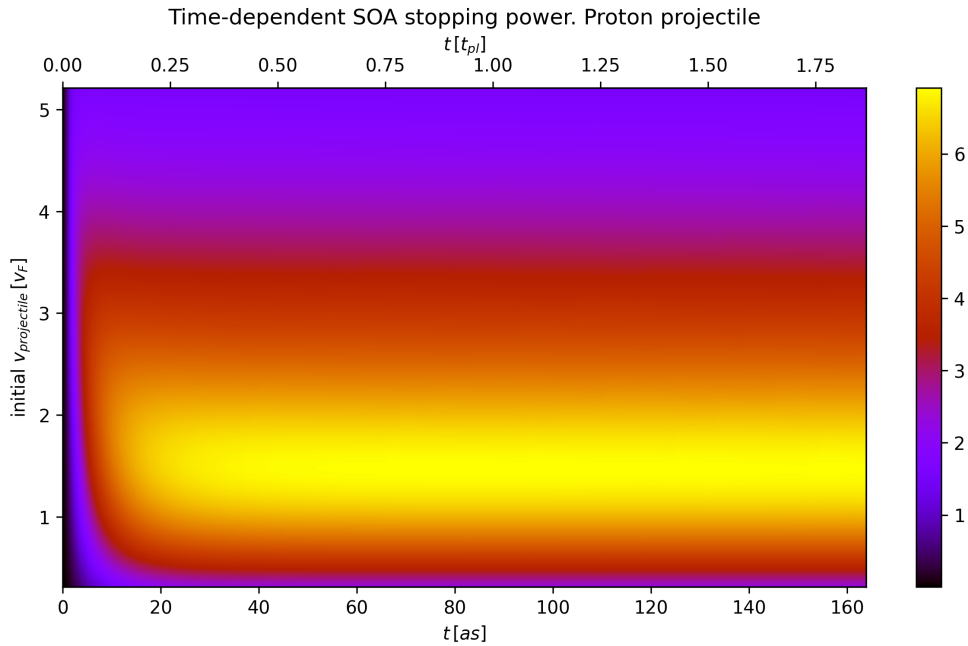


Figure F.1.: Time-resolved stopping power for a proton projectile in SOA

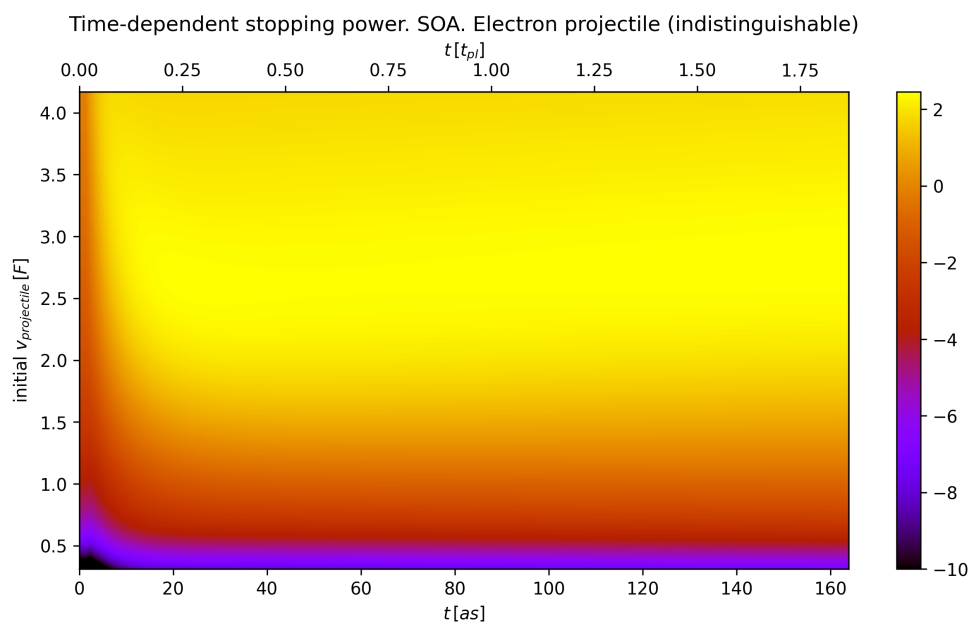


Figure F.2.: Time-resolved stopping power for an electron projectile in SOA

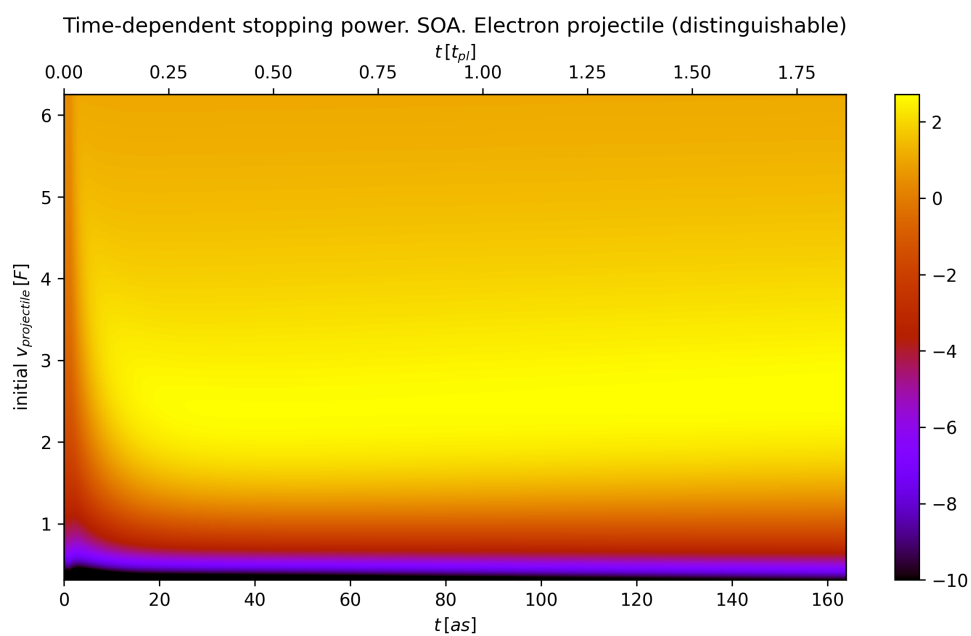


Figure F.3.: Time-resolved stopping power for a 'distinguishable electron' projectile in SOA

References

- [1] D. Riley, *Warm dense matter*, 2053-2563 (IOP Publishing, 2021).
- [2] F. Graziani, M. P. Desjarlais, R. Redmer, and S. B. Trickey, eds., *Frontiers and challenges in warm dense matter* (Springer, International Publishing, 2014).
- [3] T. Dornheim, S. Groth, and M. Bonitz, “The uniform electron gas at warm dense matter conditions”, *Physics Reports* **744**, 1–86 (2018).
- [4] A. Becker, W. Lorenzen, J. J. Fortney, N. Nettelmann, M. Schöttler, and R. Redmer, “Ab initio equations of state for hydrogen (h-REOS.3) and helium (he-REOS.3) and their implications for the interior of brown dwarfs”, *The Astrophysical Journal Supplement Series* **215**, 21 (2014).
- [5] R. Püstow, N. Nettelmann, W. Lorenzen, and R. Redmer, “H/He demixing and the cooling behavior of Saturn”, *Icarus* **267**, 323–333 (2016).
- [6] M. D. Knudson, M. P. Desjarlais, R. W. Lemke, T. R. Mattsson, M. French, N. Nettelmann, and R. Redmer, “Probing the interiors of the ice giants: shock compression of water to 700 GPa and 3.8 g/cm³”, *Phys. Rev. Lett.* **108**, 091102 (2012).
- [7] D. Yager-Elorriaga, M. Gomez, D. Ruiz, S. Slutz, A. Harvey-Thompson, C. Jennings, P. Knapp, P. Schmit, M. Weis, T. Awe, G. Chandler, M. Mangan, C. Myers, J. Fein, B. Galloway, M. Geissel, M. Glinsky, S. Hansen, E. Harding, D. Lamppa, W. Lewis, P. Rambo, G. Robertson, M. Savage, G. Shipley, I. Smith, J. Schwarz, D. Ampleford, K. Beckwith, K. Peterson, J. Porter, G. Rochau, and D. Sinars, “An overview of magneto-inertial fusion on the z machine at sandia national laboratories”, *Nuclear Fusion* **62**, 042015 (2022).
- [8] S. H. Glenzer, L. B. Fletcher, E. Galtier, B. Nagler, R. Alonso-Mori, B. Barbrel, S. B. Brown, D. A. Chapman, Z. Chen, C. B. Curry, F. Fiuza, E. Gamboa, M. Gauthier, D. O. Gericke, A. Gleason, S. Goede, E. Granados, P. Heimann, J. Kim, D. Kraus, M. J. MacDonald, A. J. Mackinnon, R. Mishra, A. Ravasio, C. Roedel, P. Sperling, W. Schumaker, Y. Y. Tsui, J. Vorberger, U. Zastra, A. Fry, W. E. White, J. B. Hasting, and H. J. Lee, “Matter under extreme conditions experiments at the linac coherent light source”, *Journal of Physics B: Atomic, Molecular and Optical Physics* **49**, 092001 (2016).
- [9] K. Voigt, M. Zhang, K. Ramakrishna, A. Amouretti, K. Appel, E. Brambrink, V. Cerantola, D. Chekrygina, T. Döppner, R. W. Falcone, K. Falk, L. B. Fletcher, D. O. Gericke, S. Göde, M. Harmand, N. J. Hartley, S. P. Hau-Riege, L. G. Huang, O. S. Humphries, M. Lokamani, M. Makita, A. Pelka, C. Prescher, A. K. Schuster, M. Šmíd, T. Toncian, J. Vorberger, U. Zastra, T. R. Preston, and D. Kraus, “Demonstration of an x-ray raman spectroscopy

- setup to study warm dense carbon at the high energy density instrument of european xfel”, *Physics of Plasmas* **28**, 082701 (2021).
- [10] R. S. Craxton, K. S. Anderson, T. R. Boehly, V. N. Goncharov, D. R. Harding, J. P. Knauer, R. L. McCrory, P. W. McKenty, D. D. Meyerhofer, J. F. Myatt, A. J. Schmitt, J. D. Sethian, R. W. Short, S. Skupsky, W. Theobald, W. L. Kruer, K. Tanaka, R. Betti, T. J. B. Collins, J. A. Delettrez, S. X. Hu, J. A. Marozas, A. V. Maximov, D. T. Michel, P. B. Radha, S. P. Regan, T. C. Sangster, W. Seka, A. A. Solodov, J. M. Soures, C. Stoeckl, and J. D. Zuegel, “Direct-drive inertial confinement fusion: a review”, *Physics of Plasmas* **22**, 110501 (2015).
- [11] R. S. Craxton, K. S. Anderson, T. R. Boehly, V. N. Goncharov, D. R. Harding, J. P. Knauer, R. L. McCrory, P. W. McKenty, D. D. Meyerhofer, J. F. Myatt, A. J. Schmitt, J. D. Sethian, R. W. Short, S. Skupsky, W. Theobald, W. L. Kruer, K. Tanaka, R. Betti, T. J. B. Collins, J. A. Delettrez, S. X. Hu, J. A. Marozas, A. V. Maximov, D. T. Michel, P. B. Radha, S. P. Regan, T. C. Sangster, W. Seka, A. A. Solodov, J. M. Soures, C. Stoeckl, and J. D. Zuegel, “Direct-drive inertial confinement fusion: a review”, *Physics of Plasmas* **22**, 110501 (2015).
- [12] H. Abu-Shawareb et al. (Indirect Drive ICF Collaboration), “Lawson Criterion for Ignition Exceeded in an Inertial Fusion Experiment”, *Phys. Rev. Lett.* **129**, 075001 (2022).
- [13] D. Kremp, M. Schlanges, and S. (service), *Quantum Statistics of Nonideal Plasmas*, Springer Series on Atomic, Optical, and Plasma Physics, (Springer Berlin Heidelberg, Berlin, Heidelberg : 2005).
- [14] M. Bonitz, *Quantum kinetic theory* (Springer International Publishing, 2015).
- [15] F. Graziani, Z. Moldabekov, B. Olson, and M. Bonitz, “Shock physics in warm dense matter: a quantum hydrodynamics perspective”, *Contributions to Plasma Physics* **62**, e202100170 (2022).
- [16] H. Zhang, S. Zhang, D. Kang, J. Dai, and M. Bonitz, “Finite-temperature density-functional-theory investigation on the nonequilibrium transient warm-dense-matter state created by laser excitation”, *Phys. Rev. E* **103**, 013210 (2021).
- [17] T. G. White, S. Richardson, B. J. B. Crowley, L. K. Pattison, J. W. O. Harris, and G. Gregori, “Orbital-free density-functional theory simulations of the dynamic structure factor of warm dense aluminum”, *Phys. Rev. Lett.* **111**, 175002 (2013).
- [18] A. D. Baczewski, L. Shulenburger, M. P. Desjarlais, S. B. Hansen, and R. J. Magyar, “X-ray thomson scattering in warm dense matter without the chihara decomposition”, *Phys. Rev. Lett.* **116**, 115004 (2016).
- [19] T. Dornheim, S. Groth, J. Vorberger, and M. Bonitz, “Ab initio path integral monte carlo results for the dynamic structure factor of correlated electrons: from the electron liquid to warm dense matter”, *Phys. Rev. Lett.* **121**, 255001 (2018).
- [20] K. P. Driver and B. Militzer, “All-electron path integral monte carlo simulations of warm dense matter: application to water and carbon plasmas”, *Phys. Rev. Lett.* **108**, 115502 (2012).

- [21] S. Atzeni, M. Temporal, and J. Honrubia, “A first analysis of fast ignition of precompressed ICF fuel by laser-accelerated protons”, *Nuclear Fusion* **42**, L1–L4 (2002).
- [22] A. Pukhov and J. Meyer-ter-Vehn, “Laser hole boring into overdense plasma and relativistic electron currents for fast ignition of icf targets”, *Phys. Rev. Lett.* **79**, 2686–2689 (1997).
- [23] W. Bang, B. J. Albright, P. A. Bradley, E. L. Vold, J. C. Boettger, and J. C. Fernández, “Uniform heating of materials into the warm dense matter regime with laser-driven quasimonoenergetic ion beams”, *Phys. Rev. E* **92**, 063101 (2015).
- [24] M. Schlanges, D. Gericke, W. Kraeft, and T. Bornath, “Stopping power of nonideal quantum plasmas”, *Nuclear Instruments and Methods in Physics Research Section A: Accelerators, Spectrometers, Detectors and Associated Equipment* **415**, 517–524 (1998).
- [25] Z. A. Moldabekov, T. Dornheim, M. Bonitz, and T. S. Ramazanov, “Ion energy-loss characteristics and friction in a free-electron gas at warm dense matter and nonideal dense plasma conditions”, *Physical Review E* **101**, 10.1103/physreve.101.053203 (2020).
- [26] A. White, L. Collins, K. Nichols, and S. Hu, “Mixed stochastic-deterministic time-dependent density functional theory: application to stopping power of warm dense carbon”, *Journal of Physics: Condensed Matter* **34**, 10.1088/1361-648X/ac4f1a (2022).
- [27] J.-P. Joost, N. Schlünzen, H. Ohldag, M. Bonitz, F. Lackner, and I. Březinová, *The dynamically screened ladder approximation: simultaneous treatment of strong electronic correlations and dynamical screening out of equilibrium*, 2022.
- [28] N. Schlünzen, J.-P. Joost, and M. Bonitz, “Achieving the scaling limit for nonequilibrium green functions simulations”, *Phys. Rev. Lett.* **124**, 076601 (2020).
- [29] J.-P. Joost, N. Schlünzen, and M. Bonitz, “G1-g2 scheme: dramatic acceleration of nonequilibrium green functions simulations within the hartree-fock generalized kadanoff-baym ansatz”, *Phys. Rev. B* **101**, 245101 (2020).
- [30] J.-P. Joost, A.-P. Jauho, and M. Bonitz, “Correlated topological states in graphene nanoribbon heterostructures”, *Nano Letters* **19**, PMID: 31735027, 9045–9050 (2019).
- [31] K. Balzer, M. R. Rasmussen, N. Schlünzen, J.-P. Joost, and M. Bonitz, “Doublon formation by ions impacting a strongly correlated finite lattice system”, *Phys. Rev. Lett.* **121**, 267602 (2018).
- [32] P. Lipavský, V. Špička, and B. Velický, “Generalized kadanoff-baym ansatz for deriving quantum transport equations”, *Phys. Rev. B* **34**, 6933–6942 (1986).
- [33] E. Schrödinger, “An undulatory theory of the mechanics of atoms and molecules”, *Phys. Rev.* **28**, 1049–1070 (1926).
- [34] P. A. M. Dirac and R. H. Fowler, “The quantum theory of the electron”, *Proceedings of the Royal Society of London. Series A, Containing Papers of a Mathematical and Physical Character* **117**, 610–624 (1928).

- [35] J. v. Neumann, “Wahrscheinlichkeitstheoretischer Aufbau der Quantenmechanik”, Nachrichten von der Gesellschaft der Wissenschaften zu Göttingen, Mathematisch-Physikalische Klasse **1927**, 245–272 (1927).
- [36] P. Hohenberg and W. Kohn, “Inhomogeneous electron gas”, Phys. Rev. **136**, B864–B871 (1964).
- [37] W. Kohn and L. J. Sham, “Self-consistent equations including exchange and correlation effects”, Phys. Rev. **140**, A1133–A1138 (1965).
- [38] N. D. Mermin, “Thermal properties of the inhomogeneous electron gas”, Phys. Rev. **137**, A1441–A1443 (1965).
- [39] E. Runge and E. K. U. Gross, “Density-functional theory for time-dependent systems”, Phys. Rev. Lett. **52**, 997–1000 (1984).
- [40] J. Yvon, *La théorie statistique des fluides et l’équation d’état, actualités scientifiques et industrielles*, Vol. 203 (Hermann, Paris, 1935).
- [41] N. N. Bogoliubov, “Kinetic Equations”, Journal of Physics USSR **10**, 265–274 (1946).
- [42] J. Schwinger, “On the Green’s functions of quantized fields. i”, Proceedings of the National Academy of Sciences **37**, 452–455 (1951).
- [43] J. Schwinger, “On the Green’s functions of quantized fields. ii”, Proceedings of the National Academy of Sciences **37**, 455–459 (1951).
- [44] G. Stefanucci and R. van Leeuwen, *Nonequilibrium many-body theory of quantum systems: a modern introduction* (Cambridge University Press, 2013).
- [45] V. Fock, “Konfigurationsraum und zweite Quantelung”, Z. Physik **75**, 622–647 (1932).
- [46] J. C. Slater, “The theory of complex spectra”, Phys. Rev. **34**, 1293–1322 (1929).
- [47] L. V. Keldysh, “Diagram technique for nonequilibrium processes”, Zh. Eksp. Teor. Fiz. **47**, 1515–1527 (1964).
- [48] N. Schlünzen, S. Hermanns, M. Scharnke, and M. Bonitz, “Ultrafast dynamics of strongly correlated fermions—nonequilibrium green functions and selfenergy approximations”, Journal of Physics: Condensed Matter **32**, 103001 (2019).
- [49] M. Gell-Mann and F. Low, “Bound states in quantum field theory”, Phys. Rev. **84**, 350–354 (1951).
- [50] D. C. Langreth and J. W. Wilkins, “Theory of spin resonance in dilute magnetic alloys”, Phys. Rev. B **6**, 3189–3227 (1972).
- [51] G. Baym, “Self-consistent approximations in many-body systems”, Phys. Rev. **127**, 1391–1401 (1962).
- [52] G. Baym and L. P. Kadanoff, “Conservation laws and correlation functions”, Phys. Rev. **124**, 287–299 (1961).
- [53] L. Hedin, “New method for calculating the one-particle green’s function with application to the electron-gas problem”, Phys. Rev. **139**, A796–A823 (1965).

- [54] N.-H. Kwong and M. Bonitz, “Real-time kadanoff-baym approach to plasma oscillations in a correlated electron gas”, *Phys. Rev. Lett.* **84**, 1768–1771 (2000).
- [55] H. Haug and S. Koch, *Quantum theory of the optical and electronic properties of semiconductors* (World Scientific, 2004).
- [56] B. I. Lundqvist, “Single-particle spectrum of the degenerate electron gas”, *Physik der kondensierten Materie* **6**, 193–205 (1967).
- [57] B. I. Lundqvist, “Single-particle spectrum of the degenerate electron gas”, *Physik der kondensierten Materie* **7**, 117–123 (1968).
- [58] B. Lundqvist, “Single-particle spectrum of the degenerate electron gas. iii. numerical results in the random phase approximation”, *Phys. Kondens. Mater* **7**, 117–23 (1968).
- [59] U. von Barth and B. Holm, “Self-consistent GW_0 results for the electron gas: fixed screened potential W_0 within the random-phase approximation”, *Phys. Rev. B* **54**, 8411–8419 (1996).
- [60] G. Manzke, K. Henneberger, J. Heeg, K. El Sayed, S. Schuster, and H. Haug, “Dynamics of screening and field fluctuations on ultrashort time scales”, *physica status solidi (b)* **188**, 395–403 (1995).
- [61] L. Bányai, Q. T. Vu, B. Mieck, and H. Haug, “Ultrafast quantum kinetics of time-dependent rpa-screened coulomb scattering”, *Phys. Rev. Lett.* **81**, 882–885 (1998).
- [62] R. Huber, F. Tauser, A. Brodschelm, M. Bichler, G. Abstreiter, and A. Leitenstorfer, “How many-particle interactions develop after ultrafast excitation of an electron–hole plasma”, *Nature* **414**, 286–289 (2001).
- [63] A. Leitenstorfer, R. Huber, F. Tauser, and A. Brodschelm, “How fast do charged particles get dressed?”, *physica status solidi (b)* **238**, 455–461 (2003).
- [64] B. A. Lippmann and J. Schwinger, “Variational principles for scattering processes. i”, *Phys. Rev.* **79**, 469–480 (1950).
- [65] M. Bonitz, K. Balzer, N. Schlünzen, M. R. Rasmussen, and J.-P. Joost, “Ion impact induced ultrafast electron dynamics in finite graphene-type hubbard clusters (phys. status solidi b 7/2019)”, *physica status solidi (b)* **256**, 1970028 (2019).
- [66] Bonitz, M., Semkat, D., and Haug, H., “Non-lorentzian spectral functions for coulomb quantum kinetics”, *Eur. Phys. J. B* **9**, 309–314 (1999).
- [67] J.-P. Joost, “Spectral Properties of Excited Hubbard Clusters: A Nonequilibrium Green Functions Approach”, MA thesis (CAU Kiel, December 2017).
- [68] M. Bonitz, S. Hermanns, K. Kobusch, and K. Balzer, “Nonequilibrium green function approach to the pair distribution function of quantum many-body systems out of equilibrium”, in *Journal of physics: conference series*, Vol. 427, 1 (IOP Publishing, 2013), p. 012002.
- [69] G. Giuliani and G. Vignale, *Quantum theory of the electron liquid* (Cambridge University Press, 2005).

- [70] D. M. Ceperley and B. J. Alder, “Ground state of the electron gas by a stochastic method”, *Phys. Rev. Lett.* **45**, 566–569 (1980).
- [71] J. P. Perdew and A. Zunger, “Self-interaction correction to density-functional approximations for many-electron systems”, *Phys. Rev. B* **23**, 5048–5079 (1981).
- [72] H. Haberland, M. Bonitz, and D. Kremp, “Harmonics generation in electron-ion collisions in a short laser pulse”, *Phys. Rev. E* **64**, 026405 (2001).
- [73] R. Binder, H. S. Köhler, M. Bonitz, and N. Kwong, “Green’s function description of momentum-orientation relaxation of photoexcited electron plasmas in semiconductors”, *Phys. Rev. B* **55**, 5110–5116 (1997).
- [74] N. W. Ashcroft and N. D. Mermin, *Solid State Physics* (Holt-Saunders, 1976).
- [75] R. Binder, H. S. Köhler, M. Bonitz, and N. Kwong, “Green’s function description of momentum-orientation relaxation of photoexcited electron plasmas in semiconductors”, *Phys. Rev. B* **55**, 5110–5116 (1997).
- [76] D. Kremp, D. Semkat, and M. Bonitz, “Short-time kinetics and initial correlations in quantum kinetic theory”, *Journal of Physics: Conference Series* **11**, 1 (2005).
- [77] D. Semkat, M. Bonitz, and D. Kremp, “Relaxation of a quantum many-body system from a correlated initial state. a general and consistent approach”, *Contributions to Plasma Physics* **43**, 321–325 (2003).
- [78] F. Borges-Fajardo, C. Makait, and M. Bonitz, “Time-dependent charged particle stopping in quantum plasmas: testing the g_1 – g_2 scheme for quasi-one-dimensional systems”, (2022).
- [79] K. S. Novoselov, A. K. Geim, S. V. Morozov, D. Jiang, Y. Zhang, S. V. Dubonos, I. V. Grigorieva, and A. A. Firsov, “Electric field effect in atomically thin carbon films”, *Science* **306**, 666–669 (2004).
- [80] J. Cai, C. A. Pignedoli, L. Talirz, P. Ruffieux, H. Söde, L. Liang, V. Meunier, R. Berger, R. Li, X. Feng, K. Müllen, and R. Fasel, “Graphene nanoribbon heterojunctions”, *Nature Nanotechnology* **9**, 896–900 (2014).
- [81] Y.-C. Chen, T. Cao, C. Chen, Z. Pedramrazi, D. Haberer, D. G. de Oteyza, F. R. Fischer, S. G. Louie, and M. F. Crommie, “Molecular bandgap engineering of bottom-up synthesized graphene nanoribbon heterojunctions”, *Nature Nanotechnology* **10**, 156–160 (2015).
- [82] L. Borkowski, N. Schlünzen, J.-P. Joost, F. Reiser, and M. Bonitz, “Doublon production in correlated materials by multiple ion impacts”, *physica status solidi (b)* **259**, 2100511 (2022).
- [83] D. Van Tuan, B. Scharf, I. Žutić, and H. Dery, “Marrying excitons and plasmons in monolayer transition-metal dichalcogenides”, *Phys. Rev. X* **7**, 041040 (2017).
- [84] A. Steinhoff, T. O. Wehling, and M. Rösner, “Frequency-dependent substrate screening of excitons in atomically thin transition metal dichalcogenide semiconductors”, *Phys. Rev. B* **98**, 045304 (2018).

- [85] F. Wu, T. Lovorn, E. Tutuc, and A. H. MacDonald, “Hubbard model physics in transition metal dichalcogenide moiré bands”, *Phys. Rev. Lett.* **121**, 026402 (2018).
- [86] H. Li, S. Li, E. C. Regan, D. Wang, W. Zhao, S. Kahn, K. Yumigeta, M. Blei, T. Taniguchi, K. Watanabe, S. Tongay, A. Zettl, M. F. Crommie, and F. Wang, “Imaging two-dimensional generalized Wigner crystals”, *Nature* **597**, 650–654 (2021).
- [87] J. Cooley and J. Tukey, “An algorithm for the machine calculation of complex fourier series”, *Mathematics of Computation* **19**, 297–301 (1965).
- [88] M. Frigo and S. G. Johnson, “The design and implementation of FFTW3”, *Proceedings of the IEEE* **93**, Special issue on “Program Generation, Optimization, and Platform Adaptation”, 216–231 (2005).
- [89] Intel[®], *Math Kernel Library FFT*, <https://www.intel.com/content/www/us/en/developer/articles/technical/onemkl-ipp-choosing-an-fft.html>, Accessed: June 3rd, 2022.
- [90] NVIDIA, *cuFFT*, <https://developer.nvidia.com/cufft>, Accessed: June 3rd, 2022.
- [91] V. Magni, G. Cerullo, and S. D. Silvestri, “High-accuracy fast hankel transform for optical beam propagation”, *J. Opt. Soc. Am. A* **9**, 2031–2033 (1992).
- [92] D. W. Zhang, X.-C. Yuan, N. Q. Ngo, and P. Shum, “Fast hankel transform and its application for studying the propagation of cylindrical electromagnetic fields”, *Opt. Express* **10**, 521–525 (2002).
- [93] H. Johnson, “An improved method for computing a discrete hankel transform”, *Computer Physics Communications* **43**, 181–202 (1987).
- [94] D. Lemoine, “The discrete bessel transform algorithm”, *The Journal of Chemical Physics* **101**, 3936–3944 (1994).
- [95] The GSL Team, *Discrete Hankel Transforms — GSL 2.7 documentation*, <https://www.gnu.org/software/gsl/doc/html/dht.html>, Accessed: June 8rd, 2022.
- [96] C. Frappier and P. Olivier, “A quadrature formula involving zeros of bessel functions”, *Mathematics of Computation - Math. Comput.* **60**, 303–316 (1993).
- [97] J. Dormand and P. Prince, “A family of embedded runge-kutta formulae”, *Journal of Computational and Applied Mathematics* **6**, 19–26 (1980).
- [98] N. Schlünzen, “Nonequilibrium Green functions analysis of electron dynamics in strongly correlated lattice systems”, MA thesis (CAU Kiel, September 2015).
- [99] O. Schlömilch, B. Witzschel, M. Cantor, E. Kahl, R. Mehmke, and C. Runge, *Zeitschrift für mathematik und physik*, Bd. 46 (B. G. Teubner., 1901).
- [100] J.-P. Joost and N. Schlünzen, personal communication, Nov. 19, 2019.
- [101] M. Bonitz and D. Semkat, *Introduction to computational methods in many body physics* (Rinton Press, 2006).

- [102] H. Köhler, N. Kwong, and H. A. Yousif, “A fortran code for solving the kadanoff–baym equations for a homogeneous fermion system”, *Computer Physics Communications* **123**, 123–142 (1999).
- [103] R. Balescu, “Irreversible processes in ionized gases”, *The Physics of Fluids* **3**, 52–63 (1960).
- [104] A. Lenard, “On bogoliubov’s kinetic equation for a spatially homogeneous plasma”, *Annals of Physics* **10**, 390–400 (1960).
- [105] D. Nicholson, *Introduction to plasma theory* (Wiley, 1983).
- [106] Z. A. Moldabekov, T. Dornheim, M. Bonitz, and T. S. Ramazanov, “Ion energy-loss characteristics and friction in a free-electron gas at warm dense matter and nonideal dense plasma conditions”, *Phys. Rev. E* **101**, 053203 (2020).
- [107] D. O. Gericke and M. Schlanges, “Beam-plasma coupling effects on the stopping power of dense plasmas”, *Phys. Rev. E* **60**, 904–910 (1999).
- [108] K. Morawetz and G. Röpke, “Stopping power in nonideal and strongly coupled plasmas”, *Phys. Rev. E* **54**, 4134–4146 (1996).
- [109] J. Vorberger, personal communication.
- [110] D. Gericke, M. Schlanges, and W. Kraeft, “Stopping power of a quantum plasma – t-matrix approximation and dynamical screening”, *Physics Letters A* **222**, 241–245 (1996).
- [111] M. Schüler, M. Eckstein, and P. Werner, “Truncating the memory time in nonequilibrium dynamical mean field theory calculations”, *Phys. Rev. B* **97**, 245129 (2018).
- [112] A. Picano and M. Eckstein, “Accelerated gap collapse in a slater antiferromagnet”, *Phys. Rev. B* **103**, 165118 (2021).
- [113] J. Kaye and D. Golež, “Low rank compression in the numerical solution of the nonequilibrium Dyson equation”, *SciPost Phys.* **10**, 091 (2021).
- [114] J. Hubbard and B. H. Flowers, “Electron correlations in narrow energy bands”, *Proceedings of the Royal Society of London. Series A. Mathematical and Physical Sciences* **276**, 238–257 (1963).
- [115] J.-P. Joost, N. Schlünzen, and M. Bonitz, “Femtosecond electron dynamics in graphene nanoribbons – a nonequilibrium green functions approach within an extended hubbard model”, *physica status solidi (b)* **256**, 1800498 (2019).
- [116] J. A. Pople, “Electron interaction in unsaturated hydrocarbons”, *Trans. Faraday Soc.* **49**, 1375–1385 (1953).
- [117] R. Pariser and R. G. Parr, “A semi-empirical theory of the electronic spectra and electronic structure of complex unsaturated molecules. i.”, *The Journal of Chemical Physics* **21**, 466–471 (1953).
- [118] R. Pariser and R. G. Parr, “A semi-empirical theory of the electronic spectra and electronic structure of complex unsaturated molecules. ii””, *The Journal of Chemical Physics* **21**, 767–776 (1953).

Important used tools

- Main simulations written in C++ using the following numerical libraries

- Eigen
- GSL
- boost
- FFTW
- Intel MPI

and the Intel C++ compiler

- Calculations were done on the NEC HPC-System ("nesh") of the Rechenzentrum CAU Kiel
- data postprocessing was done in Python
- Plottools: Matplotlib, mayavi, gnuplot
- Overleaf \LaTeX editor with graphical packages
 - FeynMF for Feynman diagrams
 - tikz for flowcharts

Danksagung

Zunächst möchte ich mich bei Herrn Professor Dr. Michael Bonitz für die Gelegenheit bedanken, unter seiner Leitung außerordentlich spannende Physik zu erforschen. Während er mir in der Ausgestaltung viel Freiraum gelassen hat, waren seine Anregungen zu aktuellen Entwicklungen sehr inspirierend und hilfreich und haben mir zu einem guten Verständnis der aktuellen Physik verholfen.

Als nächstes möchte ich meinen Bürokollegen, Dr. Niclas Schlünzen und Jan-Philip Joost, danken. Als ich in die Thematik der Greenfunktionen einstieg, standen sie mir stets bei Fragen zur Verfügung und haben mich gelegentlich mit aufmunternden Worten motiviert. Auch später noch waren unsere Diskussionen für mich sehr bereichernd.

Weiterhin gilt mein Dank Erik Schroedter für unsere zahlreichen Diskussionen zu verschiedensten physikalischen und nichtphysikalischen Themen.

Abschließend möchte ich mich bei der gesamten Arbeitsgruppe für die angenehme Atmosphäre und dafür bedanken, dass sie mich so freundlich aufgenommen hat.

Erklärung nach Prüfungsverfahrensordnung

Hiermit versichere ich gemäß § 10 Absatz 6 der Prüfungsverfahrensordnung, dass ich die Arbeit selbstständig verfasst und keine anderen als die abgegebenen Quellen und Hilfsmittel benutzt und die Arbeit in keinem anderen Prüfungsverfahren eingereicht habe.

Kiel, den